THE UNIVERSITY
of EDINBURGH

Design of a H_2 Pressure Swing Adsorption process at an advanced IGCC plant for cogenerating hydrogen and power with CO_2 capture

Mauro Luberti

For the degree of Doctor of Philosophy

School of Engineering

The University of Edinburgh

2015

Declaration of authorship

I declare that this thesis has been composed by myself, that the novel work here presented has been developed by myself and that the present thesis has not been submitted for any degree or professional qualification except for the one specified in the front page.

Mauro Luberti

Edinburgh, 18/04/2016

Lay Summary

Strong dependency on coal, crude oil and natural gas and the associated price and supply chain risk increase the need for efficient utilisation of existing non-renewable energy sources. Carbon capture and hydrogen purification technologies are expected to play a key role in the future low-carbonised energy matrix. Integrated Gasification Combined Cycles (IGCCs) are one of the emerging clean coal technologies which pave the way for producing power from coal with a higher net power efficiency than conventional PC-fired boiler power plants. The first part of this thesis has been devoted to a detailed process simulation of an IGCC with a Shell technology gasifier based on the DOE/NETL report in order to estimate the net plant efficiency when the carbon capture unit is equipped.

At the same time, the production of ultrapure hydrogen is both a sought target and an appropriate environmental solution because it is commonly utilised as feedstock in refineries' hydrotreaters and hydrocrackers as well as energy carrier in fuel cells.

An efficient way to produce hydrogen can be through coal gasification. Therefore, a novel hydrogen pressure swing adsorption (PSA) system has been designed and optimised that is applied to an advanced IGCC plant for cogenerating power and ultrapure hydrogen (99.99+ mol%) with pre-combustion CO_2 capture. An in-depth economic analysis was carried out and discussed in detail. The industrial advanced IGCC performances have also been improved by process integration between the H_2 PSA unit and other units in the plant.

Abstract

Strong dependency on fossil fuels and the associated price and supply chain risk increase the need for more efficient utilisation of existing non-renewable energy sources. Carbon capture and hydrogen purification technologies are expected to play a key role in the future low-carbonised energy matrix. Integrated Gasification Combined Cycles (IGCCs) are one of the emerging clean coal technologies which pave the way for producing power from coal with a higher net power efficiency than conventional PC-fired boiler power plants. It is also advantageous that in an IGCC power plant a carbon capture unit can be applied to a stream having a very high CO_2 partial pressure ahead of gas combustion that would not be available in case of a PC-fired boiler power plant, leading to less energy penalty involved in carbon capture.

At the same time, the production of ultrapure hydrogen is both a sought target and an appropriate environmental solution because it is commonly utilised as feedstock in refineries' hydrotreaters and hydrocrackers as well as energy carrier in fuel cells. A high purity of hydrogen has been commercially produced out of raw synthesis gas using a Hydrogen Pressure Swing Adsorption (H_2 PSA) process. In this thesis, it was aimed to design and optimise a bespoke H_2 PSA system tailored for a decarbonised syngas feed originating from a carbon capture unit. Therefore, a novel H_2 PSA has been studied that is applied to an advanced IGCC plant for cogenerating power and ultrapure hydrogen (99.99+ mol%) with pre-combustion CO_2 capture.

In designing the H_2 PSA, it is essential to increase the recovery of ultrapure hydrogen product to its maximum since the power consumption for compressing the H_2 PSA tail gas up to the gas turbine operating pressure should be minimised to save the total auxiliary power consumption. Hydrogen recovery was raised by increasing the complexity of the PSA step configuration that allows a PSA cycle to have a lower feed flow to one column being used for adsorption and more pressure equalisation steps. An in-depth economic analysis was carried out and discussed in detail. The industrial advanced IGCC performances have also been improved by process integration between the H_2 PSA unit and other units in the plant.

"The number measures reality and allows to penetrate its meaning"

PYTHAGORAS

"Felix, qui potuit rerum cognoscere causas"
[Fortunate who was able to know the causes of things]

VIRGIL (Georgica, II, 490)

Acknowledgements

It is arduous to express in just a few sentences my sincere gratitude for all the people who made possible this three-year PhD in Edinburgh.

First of all, I would like to profoundly thank my first supervisor Dr. Hyungwoong Ahn for his constant help, support and motivation in exploring new ideas and paths during my tenure. His continuous guidance has been fundamental for achieving all my research goals, for improving my critical thinking, for introducing me to the academic world in terms of how to write, improve and revise a paper, and how to successfully prepare a presentation. I am convinced that my engineering skills in general were greatly enhanced by this constant and daily exchange of opinions. A special thanks goes to my second supervisor, Prof. Stefano Brandani, for his precious advice and comments on my research during the weekly group meetings: his extensive knowledge in all the fields of Chemical Engineering opened my mind more than once, bringing me to solve problems from other perspectives.

I would like to express my gratitude to Dr. Daniel Friedrich for his support, especially in developing the numerical code for simulating PSA systems, and to Dr. Giulio Santori for the useful conversations on Adsorption Thermodynamics and for making me sympathetic of his research interests. I owe a lot of my knowledge on carbon capture and beyond to the CCS group at the University of Edinburgh: having shared the office with brilliant colleagues was a great pleasure. In particular I wish to thank the “old group” in the persons of Enzo, Zoe, Davide, Dursun, Francisco and Zhilin, and the “new group” comprising Eleni, Arran, Elsa, Nick, Pramatesh, Shreenath and Charithea. A special thanks is directed to Gabriel with whom I shared almost three years of the burdens and joys of academic life, always supporting each other like brothers.

My life in Edinburgh was much enlivened by the honest friendship of my successive flatmates Ruth and Roberto who helped me explore the city and build new life experiences. I wish also to thank George, Mike and Thomas for the scientific conversations, the sport activities and many nights out where a disconnection from the university was more than appreciated. I would like to heartily thank Nash who

has been my first and best friend here in Edinburgh and on whom I could always rely in any situation, especially at the beginning of this adventure.

I have always expressed in the past the willingness to do research but if I were asked who convinced me to undertake the PhD I would answer it was my family. My parents Rolando and Lucia and my brothers Tiziano and Dario, now both engineers, have always been my best supporters, encouraging me to face new life challenges, even abroad.

Eventually, I wish to dedicate this thesis work to my girlfriend Sarah, whose sincere love has accompanied me during these years in Edinburgh, helping to relieve me of the stress of research and highlighting all the good that life can bring.

List of papers / patents related to the Thesis

Luberti M, Friedrich D, Brandani S, Ahn H. Design of H_2 PSA for cogeneration of ultrapure hydrogen and power at an advanced integrated gasification combined cycle with pre-combustion capture. Adsorption 2014; 20: 511-524.

Luberti M, Friedrich D, Ozcan DC, Brandani S, Ahn H. A novel strategy to produce ultrapure hydrogen from coal with pre-combustion carbon capture. Energy Procedia 2014; 63: 2023-2030.

Ahn H, Brandani S, Luberti M, Lee CH. Hydrogen production processing. WO 2015/104532 A1, 2015.

Full list of papers / patents

Ahn H, Luberti M, Liu Z, Brandani S. Process configuration studies of the amine capture process for coal-fired power plants. International Journal of Greenhouse Gas Control 2013; 16: 29-40.

Ahn H, Luberti M, Liu Z, Brandani S. Process simulation of aqueous MEA plants for post-combustion capture from coal-fired power plants. Energy Procedia 2013; 37: 1523-1531.

Luberti M, Friedrich D, Brandani S, Ahn H. Design of H_2 PSA for cogeneration of ultrapure hydrogen and power at an advanced integrated gasification combined cycle with pre-combustion capture. Adsorption 2014; 20: 511-524.

Santori G, Luberti M, Ahn H. Ideal adsorbed solution theory solved with direct search minimisation. Computers and Chemical Engineering 2014; 71: 235-240.

Luberti M, Friedrich D, Ozcan DC, Brandani S, Ahn H. A novel strategy to produce ultrapure hydrogen from coal with pre-combustion carbon capture. Energy Procedia 2014; 63: 2023-2030.

Santori G, Luberti M, Brandani S. Common tangent plane in mixed-gas adsorption. Fluid Phase Equilibria 2015; 392: 49-55.

Oreggioni GD, Brandani S, Luberti M, Baykan Y, Friedrich D, Ahn H. CO_2 capture from syngas by an adsorption process from a biomass gasification CHP plant: Its comparison with amine-based CO_2 capture. International Journal of Greenhouse Gas Control 2015; 35: 71-81.

Barba D, Brandani F, Capocelli M, Luberti M, Zizza A. Process analysis of an industrial waste-to-energy plant: Theory and experiments. Process Safety and Environmental Protection 2015; 96: 61-73.

Luberti M, Kim YH, Lee CH, Ferrari MC, Ahn H. New momentum and energy balance equations considering kinetic energy effect for mathematical modelling of a fixed bed adsorption column. Adsorption 2015; 21: 353-363.

Ahn H, Brandani S, Luberti M, Lee CH. Hydrogen production processing. WO 2015/104532 A1, 2015.

List of symbols

a	Sorbate activity, (-)
AC	Cost of CO_2 avoided, ($/ton$_{CO2}$)
A_c	Internal column surface area, (m^2)
$A_{c,a}$	Internal column axial surface area, (m^2)
$A_{c,l}$	Internal column lateral surface area, (m^2)
A_p	Pellet surface area, (m^2)
B	Mobility of sorbate, ($mol \cdot m^2/J \cdot s$)
$b_{n,i}$	Adsorption equilibrium constant of site n for component i, (bar^{-1})
$b_{n,i,0}$	Pre-exponential adsorption equilibrium const. coeff. of site n for comp. i, (bar^{-1})
b_i	Adsorption equilibrium constant of component i, (bar^{-1})
$b_{i,0}$	Pre-exponential adsorption equilibrium constant of component i, (bar^{-1})
C	Gas phase concentration, (mol/m^3)
c_T	Total gas phase concentration, (mol/m^3)
c_i	Gas phase concentration of component i, (mol/m^3)
c_i^m	Gas phase concentration of component i in the macropore, (mol/m^3)
$c_{p,i}$	Heat capacity at constant pressure of component i, ($J/mol \cdot K$)
$c_{v,i}$	Heat capacity at constant volume of component i, ($J/mol \cdot K$)
$c_{p,s}$	Adsorbent specific heat capacity ($J/kg \cdot K$)
cv	Valve coefficient, (m^2)
D	Diffusivity, (m^2/s)
D_0	Corrected diffusivity, (m^2/s)
D_∞	Diffusivity at infinite temperature, (m^2/s)
D_c	Internal column diameter, (m)
$D_{c,ext}$	External column diameter, (m)
$D_{i,j}$	Molecular diffusivity of the component pair i and j, (m^2/s)
$D_{k,i}$	Knudsen diffusivity of component i, (m^2/s)

D_{lm} Diameter logarithmic mean, (m)

$D_{m,i}$ Molecular diffusivity of component i, (m^2/s)

$D_{p,i}$ Macropore diffusivity of component i, (m^2/s)

d_p Pellet averaged diameter, (m)

$D_{s,i}$ Surface diffusivity of component i, (m^2/s)

$D_{s0,i}$ Surface diffusivity at infinite temperature of component i, (m^2/s)

$D_{v,i}$ Viscous diffusivity of component i, (m^2/s)

D_z Mass axial dispersion, (m^2/s)

$D_{\mu,i}$ Effective micropore diffusivity, (m^2/s)

E Diffusional activation energy, (J/mol)

F Flowrate (mol/s)

f_i Fugacity of component i, (Pa)

H_f Enthalpy of the gas phase, (J/m^3)

$\tilde{H}_i$ Partial molar enthalpy in the gas phase of component i, (J/mol)

ΔH Heat of adsorption, absorption or reaction, (J/mol)

$(-\Delta H_i)$ Heat of adsorption of component i, (J/mol)

h_{int} Internal surface heat transfer coefficient, ($W/m^2 \cdot K$)

h_{ext} External surface heat transfer coefficient, ($W/m^2 \cdot K$)

h_w Heat transfer coefficient between the gas phase and the column wall, ($W/m^2 \cdot K$)

J Diffusive flux, ($mol/m^2 \cdot s$)

J_i Diffusive flux of component i, ($mol/m^2 \cdot s$)

J_T Thermal diffusive flux, (W/m^2)

K Dimensionless Henry's law constant, (-)

K_0 Pre-exponential dimensionless Henry's law constant, (-)

K' Henry's law adsorption constant defined in terms of sorbate pressure, ($mol/m^3 \cdot Pa$)

k_g Gas phase thermal conductivity, ($W/m \cdot K$)

$k_{g,i}$ Gas phase thermal conductivity of component i, ($W/m \cdot K$)

$K_{i,s}$ Henry's law constant of component i in solvent s, (Pa)

$k_i^p \cdot A_p/V_p$ LDF mass transfer coefficient of component i in the pellet, (s^{-1})

$k_i^{cr} \cdot 3/r_c$ LDF mass transfer coefficient of component i in the crystal, (s^{-1})

k_w Wall thermal conductivity, (W/m·K)

k_z Thermal axial dispersion, (W/m·K)

L, L_c Column length, (m)

LCOE Levelized cost of electricity, ($/MWh)

m_{ads} Adsorbent mass, (kg)

$\overline{M}$ Averaged molecular weight, (kg/mol)

M_i Molecular weight of component i, (g/mol)

N_c Number of components, (-)

P Total pressure in the gas phase, (bar)

P_i Partial pressure of component i, (bar)

P_{ads} Adsorption pressure, (bar)

P_{des} Desorption pressure, (bar)

Pr Prandtl number, (-)

q Adsorbed phase concentration, (mol/m^3)

$\overline{q}_i$ Averaged adsorbed phase concentration of component i in the crystal, (mol/m^3)

$\overline{Q_i}$ Averaged adsorbed concentration of component i in the pellet, (mol/m^3)

q_i^* Adsorbed phase concentration in the equilibrium state of component i, (mol/m^3)

$q_{s,i}$ Saturation adsorption capacity of component i, (mol/m^3)

$q_{s,n,i}$ Saturation adsorption capacity of site n for component i, (mol/m^3)

Q_{feed} Feed flowrate, (mol/s)

r Radial coordinate, (-)

R Ideal gas constant, (J/mol·K)

R_c Column radius, (m)

Re Reynolds number, (-)

r_c Crystal radius, (m)

r_p Pellet radius, (m)

Sc Schimdt number, (-)

t Time, (s)

t_{ads} Adsorption time, (s)

t_{cycle} Cycle time, (s)

T Temperature, (K)

T_{ref} Reference temperature, (K)

T_f Gas phase temperature, (K)

T_s Adsorbed phase temperature, (K)

T_{feed} Feed temperature, (K)

T_w Column wall temperature, (K)

u Interstitial velocity, (m/s)

U_f Internal energy in the gas phase, (J/m^3)

U_P Internal energy in the pellet, (J/m^3)

$U_{P,f}$ Internal energy in the macropores, (J/m^3)

$U_{P,s}$ Internal energy in the adsorbed phase, (J/m^3)

ΔU Internal energy change of adsorption, (J/mol)

V_c Column volume, (m^3)

v Superficial velocity, (m/s)

V_p Pellet volume, (m^3)

x Wall thickness, (m)

x_i Molar fraction of component i in the liquid or adsorbed phase, (-)

y_i Molar fraction of component i in the gas phase, (-)

z Axial coordinate, (m)

Greek letters

$\alpha_{i,j}$ Selectivity of component i over component j, (-)

ε Bed void fraction excluding macropores, (-)

ε_i Characteristic Lennard-Jones energy parameter of component i, $((kg/mol \cdot K)^{0.5})$

ε_{cry} Crystal void fraction, (-)

ε_p Pellet void fraction, (-)

μ Molar chemical potential, (J/mol)

μ^0 Molar chemical potential in the reference state, (J/mol)

μ Gas phase viscosity, (Pa·s)

μ_i Gas phase viscosity of component i, (Pa·s)

φ Pellet non-spherically coefficient, (-)

φ_i Fugacity coefficient of component i, (-)

$\Phi_{i,j}$ Characteristic Lennard-Jones viscosity parameter for the component pair i and j, (-)

ρ_{bulk} Gas bulk phase density, (kg/m^3)

ρ_{cry} Crystal density, (kg/m^3)

ρ_f, ρ_g Gas phase density, (kg/m^3)

ρ_p Pellet density, (kg/m^3)

ρ_{skel} Skeletal density, (kg/m^3)

$\sigma_{i,j}$ Characteristic Lennard-Jones length for the component pair i and j, (Å)

τ Gas residence time, (s)

τ_p Pellet tortuosity, (-)

$\Omega_{i,j}$ Characteristic Lennard-Jones energy parameter for the component pair i and j, (-)

Ω_μ Characteristic Lennard-Jones viscosity parameter, (-)

List of contents

Chapter 1: General introduction 1
1.1 Fossil fuels and global warming 1
1.2 Carbon dioxide global emissions and the need for CCS 3
1.3 Carbon capture systems 6
1.3.1 Post-combustion carbon capture 7
1.3.2 Pre-combustion carbon capture 8
1.3.3 Oxy-fuel combustion carbon capture 8
1.3.4 Capture from industrial process streams 9
1.4 Carbon capture technologies 9
1.4.1 Chemical absorption 10
1.4.2 Physical absorption 13
1.4.3 Adsorption 14
1.4.4 Membranes 15
1.4.5 Chemical looping 16
1.4.6 Cryogenic distillation 16
1.5 Carbon dioxide capture costs 17
1.6 Global hydrogen demand 18
1.7 Methods for producing hydrogen 20
1.8 Carbon capture from hydrogen plants: Research perspective 22
1.9 Carbon capture from hydrogen plants: Industrial perspective 25
1.10 The role of hydrogen in the future energy matrix 26
1.11 Objectives of the thesis 27
1.12 Outline of the thesis 30
References 31
Chapter 2: IGCC power plant design and simulation 39
2.1 IGCC power plants in the literature 40
2.2 Gasification process 43
2.3 Gasification technologies 45
2.4 Shell gasifier description and modelling 46
2.5 Gasifier and surroundings modification for carbon capture 50
2.6 Water gas shift reactors 52

2.7 Air separation unit 53
2.8 Dual-stage Selexol^{TM} 60
2.8.1 Thermodynamics of the process 62
2.8.2 Gas–liquid equilibrium in UniSim Design 65
2.8.3 Proposed configuration 67
2.9 CO_2 compression and dehydration 70
2.10 Claus plant 72
2.11 Gas turbine 77
2.12 Heat recovery steam generation 80
2.12.1 Main and reheat steam systems 81
2.12.2 Circulating water system 81
2.12.3 Raw water and cycle makeup water systems 82
2.13 Overall plant performances 85
2.14 Conclusions 88
References 89
Chapter 3: Fundamentals of adsorption and pressure swing adsorption processes 96
3.1 Adsorbents 96
3.1.1 Silica gel 99
3.1.2 Activated alumina 100
3.1.3 Activated carbon 100
3.1.4 Carbon molecular sieves 101
3.1.5 Polymeric resins 101
3.1.6 Mesoporous silica 102
3.1.7 Zeolites 102
3.1.8 Metal organic frameworks (MOFs) 104
3.2 Adsorption equilibrium 105
3.3 Adsorption kinetics 109
3.3.1 Diffusion in mesopores and macropores 110
3.3.2 Diffusion in micropores 112
3.4 Adsorption column model 113
3.4.1 Column dimensions 114
3.4.2 Mass balance 116
3.4.3 Energy balance 118

3.4.4 Momentum balance 120
3.4.5 Transport parameters and physical properties of gases 120
3.5 Industrial use of adsorption for gas separation 122
3.6 PSA process for hydrogen purification 128
3.7 Conclusions 136
References 137
Chapter 4: Design of a H_2 PSA applied to an IGCC with pre-combustion capture 142
4.1 Background of the study 142
4.2 Design basis of a H_2 PSA integrated with an IGCC power plant 144
4.3 Adsorption equilibria 145
4.4 Simulation of the H_2 PSA unit 150
4.5 Adsorption breakthrough results 154
4.6 PSA cycle simulation results 155
4.6.1 Four-column H_2 PSA 156
4.6.2 Six-column H_2 PSA 161
4.6.3 Polybed H_2 PSA (nine and twelve columns) 166
4.6.4 Sixteen-column H_2 PSA 171
4.6.5 Comparison among various PSA cycles 172
4.7 H_2 PSA simulation results with fixed total cycle time 175
4.8 Conclusions 177
References 178
Chapter 5: Process integration of the industrial H_2 PSA unit with the IGCC for cogenerating ultrapure hydrogen and electricity, cost analysis and process improvements 181
5.1 Retrofit of the H_2 PSA unit to the IGCC with pre-combustion capture 182
5.2 Design of an industrial H_2 PSA at the advanced IGCC 184
5.3 Industrial H_2 PSA economic analysis 195
5.4 Integrated IGCC cost analysis 198
5.5 Recycle of the H_2 PSA tail gas to shift reactors 204
5.6 Cogenerating IGCC process improvements 207
5.6.1 Case 1: H_2 PSA tail gas recycle to water gas shift reactors 208

5.6.2 Case 2: H_2 PSA tail gas recycle to dual-stage Selexol unit 209
5.6.3 Case 3: H_2 PSA tail gas recycle to coal dryer 209
5.6.4 Case 4: Multiple alterations with H_2 PSA tail gas recycle to WGSRs and coal dryer 210
5.6.5 Comparison for the proposed process modifications 211
5.7 Hydrogen plant process improvements 214
5.8 Conclusions 216
References 217
Chapter 6: Conclusions and directions for future work 220
6.1 IGCC power plant modelling 220
6.2 Design of a novel H_2 PSA unit applied to an IGCC H_2-rich feed 222
6.3 Retrofit of an industrial H_2 PSA unit to an IGCC 224
References 225
Appendix 1: DOE case 6 block flow diagram and data 226
Appendix 2: Design of H_2 PSA for cogeneration of ultrapure hydrogen and power at an advanced integrated gasification combined cycle with pre-combustion capture *by Luberti et al., 2014* 232
Appendix 3: A novel strategy to produce ultrapure hydrogen from coal with pre-combustion carbon capture *by Luberti et al., 2014* 247
Appendix 4: Hydrogen production processing *by Ahn et al., 2015* 256

List of Tables

Table 1.1: Carbon capture cross-referenced toolbox between systems and technologies (IPCC, 2005) 10
Table 1.2: Common solvents used in pre-combustion capture processes (IPCC, 2005)..... 13
Table 1.3: World hydrogen demand over years expressed in billion cubic meters (Freedonia Group, Inc., 2014) 19
Table 1.4: Summary of research works on carbon capture processes from hydrogen plants 22
Table 2.1: Categories of gasification processes (Simbeck et al., 1993) 46
Table 2.2: Illinois No. 6 proximate and ultimate analysis (DOE, 2007) 48
Table 2.3: Validation of the simulation approach with DOE (2007) data for Shell gasifier.. 50
Table 2.4: Simulation parameters and product specifications for ASU simulation 58
Table 2.5: Properties of physical solvents (Ranke and Mohr, 1985) 61
Table 2.6: Henry's law constants for H_2S and CO_2 in Selexol (Xu et al., 1992) 63
Table 2.7: Standard heats of absorption for H_2S and CO_2 in Selexol (Xu et al., 1992) 63
Table 2.8: Gas solubilities of some physical solvents relative to CO_2 (Burr and Lyddon, 2008) 65
Table 2.9: Original and regressed parameters of Henry's law equation for acid gases in Selexol 67
Table 2.10: Energy requirements for two-stage Selexol process 70
Table 2.11: Combustion turbine exhaust gas for carbon capture Shell IGCC compared with DOE report (2007) data 79
Table 2.12: Condenser outlet streams validation carbon capture Shell IGCC compared with DOE report (2007) data 82
Table 2.13: Comparison of DOE report (2007) data and simulation 87
Table 2.14: Simulated energy penalty in Shell IGCC with capture 87
Table 2.15: Auxiliary consumptions comparison between non-capture and carbon capture IGCCs (DOE, 2007) 88
Table 3.1: Classification of commercial adsorbents 97
Table 3.2: Physical properties of some common adsorbents and their industrial application (Yang, 1987; Ruthven et al., 1994) 99
Table 3.3: Summary of column and pellet dimensions, densities and void fractions 115
Table 3.4: Some dimensionless numbers used in the correlations 121
Table 3.5: Summary of research works on hydrogen purification by PSA processes 131
Table 4.1: Isotherm parameters of dual-site Langmuir model for zeolite 5A 146

Table 4.2: List of column parameters, particle parameters and operating conditions of H_2 PSA simulations (Luberti et al., 2014a) 153
Table 4.3: Performances of the four-column H_2 PSA system at different purge flow rates 158
Table 4.4: Performance of six-column H_2 PSA simulations 165
Table 4.5: Performance of nine- and twelve-column PSA simulations 170
Table 4.6: Performance of sixteen-column PSA simulations 172
Table 4.7: Effect of the one-column residence time during adsorption step on hydrogen purity, recovery and productivity at different H_2 PSA configurations 177
Table 5.1: List of column parameters and pressure drop evaluation for the industrial H_2 PSA simulations 185
Table 5.2: List of additional column parameters, particle parameters and operating conditions of the industrial H_2 PSA simulations for a one-column residence time of 120 s. Numbers in brackets represent transport parameters of lab-scale system 187
Table 5.3: Effect of the one-column residence time during adsorption step on hydrogen purity, recovery and bed productivity at different industrial H_2 PSA configurations with total cycle time of 420 s 190
Table 5.4: List of variables used to calculate the bed productivity for all the system configurations at 99.99+% H_2 purity 191
Table 5.5: Ultrapure hydrogen production rate and tail gas compression work at various industrial H_2 PSA configurations at the condition of 99.99+ mol% H_2 purity and total cycle time of 420 s, including IGCC overall plant performances 194
Table 5.6: Design and economic parameters utilised in the economic analysis 196
Table 5.7: Economic analysis comparison among the different PSA configurations including the comparison with the entire IGCC plant 197
Table 5.8: Nomenclature used to define levelised cost of electricity 200
Table 5.9: Economic and plant parameters used for the cost analysis among the three IGCC cases 201
Table 5.10: List of references for unit costs 201
Table 5.11: LCOE and AC results of various studies on hard coal IGCC with pre-combustion capture (ZEP, 2011) 204
Table 5.12: Simulation results for the cogenerating IGCC plant performances among the various cases 213
Table 5.13: Simulation results for the hydrogen plant (HP) performances for the various cases (Ahn et al., 2015) 215

List of Figures

Figure 1.1: World energy consumption by fuel type during the years 1990–2040 (quadrillion [10^{15}] Btu) (WEO/EIA, 2013) 2
Figure 1.2: World primary energy use by sector, 1971–2001 (IEA, 2003) 4
Figure 1.3: World CO_2 emissions from fossil fuel use by sector, 1971–2001 (IEA, 2003) 4
Figure 1.4: Relative importance of refinery greenhouse gas emission sources evaluated on CO_{2e} basis (EPA, 2008) 6
Figure 1.5: Overview of carbon capture systems (IPCC, 2005) 7
Figure 1.6: General schemes of the main processes relevant for CO_2 capture (IPCC, 2005) 10
Figure 1.7: Process flow diagram for CO_2 recovery from flue gas by chemical absorption (IPCC, 2005) 11
Figure 1.8: Levelised cost of electricity (LCOE) of PC and IGCC power plants (Hoffmann and Szlo, 2011) 17
Figure 1.9: Cost of CO_2 avoided of PC and IGCC power plants (Hoffmann and Szlo, 2011) 18
Figure 1.10: World hydrogen production and use (Evers, 2008) 19
Figure 1.11: Hydrogen sources and production processes (IGEM, 2012) 21
Figure 1.12: Block flow diagram of Port Arthur SMRs and integrated CO_2 capture facility (Baade et al., 2012) 26
Figure 2.1: Block flow diagram of the Shell IGCC with carbon capture 43
Figure 2.2: Simplified schematic of a gasification process showing options with CO_2 capture and electricity, hydrogen or chemical production (IPCC, 2005) 44
Figure 2.3: Shell gasifier schematic (DOE, 2007) 47
Figure 2.4: Variation of syngas composition with temperature at 40 bar (Higman and van der Burgt, 2003) 49
Figure 2.5: Shell Gasifier, syngas scrubber and COS hydrolysis reactor for non-capture mode (Kapetaki et al., 2013) 51
Figure 2.6: Shell Gasifier, syngas scrubber and water gas shift reactors for carbon capture mode (Kapetaki et al., 2013) 52
Figure 2.7: Technology comparison for nitrogen production systems 54
Figure 2.8: Cryogenic process for oxygen production by distillation of liquid air (Castle, 1991) 55
Figure 2.9: Simulation flowsheet of cryogenic air separation unit 56
Figure 2.10: Coal gasification and air separation unit schematic (Kapetaki, 2015) 59
Figure 2.11: Selexol process flow diagram for acid gas removal (Padurean et al., 2012) 62

Figure 2.12: Gas solubilities of H_2S and CO_2 in physical solvents (..... 64
Figure 2.13: Solubilities of CO_2 and H_2S in Selexol solvent at 25 °C. The Y-axis reports the gas partial pressure while the X-axis reports the component mole fraction in the liquid phase. Dotted lines represent UniSim original curves, continuous lines represent UniSim regressed curves, dots represent experimental obtained values by Xu et al. (1992) 67
Figure 2.14: Simplified schematic of the integrated Selexol process (Kapetaki, 2015) 69
Figure 2.15: Syngas clean-up schematic (Kapetaki, 2015) 71
Figure 2.16: Schematic of the Claus process with two converters (El-Bishtawi and Haimour, 2004) 73
Figure 2.17: Sulfur conversion to species with temperature (♦ S_2, ■ S_6, ▲ S_8) 75
Figure 2.18: Sulfur recovery and tail gas recycle schematic (Kapetaki, 2015) 76
Figure 2.19: Carbon capture Shell IGCC power block schematic 79
Figure 2.20: Combined cycle power generation schematic (Kapetaki, 2015) 83
Figure 2.21: Steam and feedwater schematic (Kapetaki, 2015) 84
Figure 2.22: Fully integrated IGCC simulation flow sheet in UniSim Design R400 environment 86
Figure 3.1: Pore size distribution for pelleted 5A zeolite (Ruthven et al., 1994) 98
Figure 3.2a: Representation of a sodalite cage or truncated octahedron (Manske, 2009) ... 103
Figure 3.2b: Representation of type A zeolite unit cell (left) and unit cell of types X and Y, or faujasite (right) (Averill and Eldredge, 2007) 104
Figure 3.3: X-ray crystal structure of indium soc-MOF, in which (a) is a cluster of metal ions, (b) is an organic linker, (c) and (d) are representations of a cuboidal cage of indium soc-MOF and (e) is a space filling representation of the framework viewed along the y-direction (Wang et al., 2011) 105
Figure 3.4: The IUPAC classification for adsorption isotherms (IUPAC, 1985) 106
Figure 3.5: Dimensionless equilibrium isotherms 107
Figure 3.6: The resistances to mass transfer in a composite adsorbent pellet 110
Figure 3.7: Model hierarchy for the adsorption column: in each stage the different options are only shown for one option of the previous stage but apply to all options of the previous stage 114
Figure 3.8: Schematic of an adsorption column showing the two inlets and the adsorbent pellets: the inset shows a schematic of an idealised adsorbent pellet including the spherical crystallites 115
Figure 3.9: Schematic isotherms showing pressure swing, thermal swing and combined pressure–temperature swing operation for an adsorption process (Ruthven et al., 1984).... 123

Figure 3.10: The basic two-bed pressure swing adsorption system (Skarstrom, 1960)..... 125
Figure 3.11: The sequence of steps in the basic Skarstrom cycle..... 126
Figure 3.12: UOP four-bed PSA system (Batta, 1971)..... 129
Figure 3.13: UOP Polybed process for hydrogen purification (Fuderer and Rudelstorfer, 1976)..... 130
Figure 4.1: A conceptual diagram to compare general approach to capture CO_2 from a SMR H_2 plant and a coal-fired power plant separately to an advanced IGCC process for cogenerating power and ultrapure hydrogen with carbon capture (Luberti et al., 2014a) ... 143
Figure 4.2: Block flow diagram of an advanced IGCC process for cogenerating power and ultrapure hydrogen..... 144
Figure 4.3: Adsorption equilibrium of hydrogen on 5A zeolite. Solid lines: dual-site Langmuir model. Experimental data by Lopes et al. (2009)..... 147
Figure 4.4: Adsorption equilibrium of carbon dioxide on 5A zeolite. Solid lines: dual-site Langmuir model. Experimental data by Lopes et al. (2009)..... 147
Figure 4.5: Adsorption equilibrium of carbon monoxide on 5A zeolite. Solid lines: dual-site Langmuir model. Experimental data by Lopes et al. (2009)..... 148
Figure 4.6: Adsorption equilibrium of nitrogen on 5A zeolite. Solid lines: dual-site Langmuir model Experimental data by Lopes et al. (2009) 148
Figure 4.7: Adsorption equilibrium of argon on 5A zeolite. Solid lines: dual-site Langmuir model. Experimental data by Miller et al. (1987) 149
Figure 4.8: Adsorption equilibrium comparison of hydrogen, carbon dioxide, carbon monoxide, nitrogen and argon on 5A zeolite at 303 K 150
Figure 4.9: Unibed CySim PSA flowsheet 152
Figure 4.10: Breakthrough simulation results of the shifted syngas stream on zeolite 5A bed at 303 K and 34 bar. Column size and feed condition are reported in Table 4.2..... 154
Figure 4.11: Step configuration of a four-column PSA cycle (AD: adsorption, DPE: depressurising pressure equalisation, PP: providing purge, BD: blowdown, PU: purge, PPE: pressurising pressure equalisation, PR: product pressurisation, $t_{AD} = t_{cycle}/4$; $t_{PR} = 3t_{cycle}/16$; $t_{PP} = t_{PU} = t_{cycle}/8$; $t_{BD} = t_{DPE} = t_{PPE} = t_{cycle}/16$) 156
Figure 4.12: Pressure profiles at the product end of a column over a cycle at the cyclic steady state of the four-column H_2 PSA unit: effect of the different amounts of purge flow 157
Figure 4.13: Component mole fraction profiles at the feed end of a column over a cycle at the cyclic steady state of the four-column H_2 PSA unit (Run 2)..... 159
Figure 4.14: Hydrogen mole fraction profile along the column at the end of adsorption step at the cyclic steady state of the four-column H_2 PSA unit (Run 2)..... 160

Figure 4.15: Impurities mole fraction profiles along the column at the end of adsorption step at the cyclic steady state of the four-column H_2 PSA unit (Run 2)..... 160
Figure 4.16: Evolution of hydrogen purity and recovery through the cycles (Run 2) 161
Figure 4.17: Step configurations of a six-column H_2 PSA cycle with two-stage pressure equalisation (AD: adsorption, DPE: depressurising pressure equalisation, ID: idle, PP: providing purge, BD: blowdown, PU: purge, PPE: pressurising pressure equalisation, PR: pressurisation, $t_{AD} = t_{cycle}/3$; $t_{PP} = t_{PU} = t_{PR} = t_{cycle}/9$; $t_{BD} = t_{DPE} = t_{PPE} = t_{cycle}/18$) 162
Figure 4.18: Step configurations of a six-column H_2 PSA cycle with three-stage pressure equalisations (AD: adsorption, DPE: depressurising pressure equalisation, PP: providing purge, BD: blowdown, PU: purge, ID: idle, PPE: pressurising pressure equalisation, PR: pressurisation, $t_{AD} = t_{cycle}/6$; $t_{PP} = t_{PU} = t_{PR} = t_{cycle}/9$; $t_{BD} = t_{DPE} = t_{PPE} = t_{ID} = t_{cycle}/18$) 163
Figure 4.19: Pressure profile at the product end of a column over a cycle at the cyclic steady state of six-column H_2 PSA simulation at PP/F = 0.3 with two-stage pressure equalisation (Run 6) 164
Figure 4.20: Pressure profile at the product end of a column over a cycle at the cyclic steady state of six-column H_2 PSA simulation at PP/F = 0.3 with three-stage pressure equalisation 164
Figure 4.21: Step configurations of a nine-column H_2 PSA cycle (AD: adsorption, DPE: depressurising pressure equalisation, PP: providing purge, BD: blowdown, PU: purge, PPE: pressurising pressure equalisation, PR: pressurisation, $t_{AD} = t_{cycle}/3$; $t_{PP} = t_{PU} = t_{cycle}/9$; $t_{BD} = t_{DPE} = t_{PPE} = t_{PR} = t_{cycle}/18$) 167
Figure 4.22: Pressure profiles at the product end of a column over a cycle at the cyclic steady state of a nine-column H_2 PSA at PP/F = 0.3 (Run 14) 168
Figure 4.23: Step configurations of a twelve-column H_2 PSA cycle (AD: adsorption, DPE: depressurising pressure equalisation, PP: providing purge, BD: blowdown, PU: purge, PPE: pressurising pressure equalisation, PR: pressurisation, $t_{AD} = t_{cycle}/4$; $t_{PP} = t_{PU} = t_{cycle}/6$; $t_{BD} = t_{DPE} = t_{PPE} = t_{PR} = t_{cycle}/24$) 169
Figure 4.24: Pressure profiles at the product end of a column over a cycle at the cyclic steady state of a twelve-column H_2 PSA at PP/F = 0.3 (Run 18)..... 169
Figure 4.25: Step configurations of a sixteen-column H_2 PSA cycle (AD: adsorption, DPE: depressurising pressure equalisation, PP: providing purge, BD: blowdown, PU: purge, PPE: pressurising pressure equalisation, PR: pressurisation, $t_{AD} = t_{cycle}/4$; tPP = $t_{PU} = 3t_{cycle}/16$; $t_{BD} = t_{DPE} = t_{PPE} = t_{PR} = t_{cycle}/32$) 171
Figure 4.26: Comparison of hydrogen purity and recovery at various H_2 PSA systems with the different number of columns and different step configurations 173

Figure 4.27: Hydrogen molar fraction profiles along the column at the end of the adsorption step in various H_2 PSA cycles at around 99.99% H_2 purity 174
Figure 4.28: Hydrogen molar fraction profiles along the column at the end of the blowdown step in various H_2 PSA cycles at around 99.99% H_2 purity 175
Figure 5.1: Block flow diagram of an advanced IGCC plant for cogenerating power and ultrapure hydrogen with pre-combustion capture 182
Figure 5.2: Overall mass balance around the industrial H_2 PSA unit of the cogenerating IGCC 183
Figure 5.3: Evolution of the pressure drops against one-column residence time for the industrial H_2 PSA simulations 186
Figure 5.4: Step configuration of the industrial four-column H_2 PSA cycle at PP/F = 0.2 (See Chapter 4 for configuration details) 187
Figure 5.5: Step configurations of the industrial six-column H_2 PSA cycle with two-stage pressure equalisation at PP/F = 0.3 (See Chapter 4 for configuration details) 188
Figure 5.6: Step configurations of the industrial nine-column H_2 PSA cycle at PP/F = 0.3 (See Chapter 4 for configuration details) 188
Figure 5.7: Step configurations of the industrial twelve-column H_2 PSA cycle at PP/F = 0.3 (See Chapter 4 for configuration details) 189
Figure 5.8: Comparison of hydrogen purity against recovery for various industrial H_2 PSA systems with different numbers of columns and different step configurations 192
Figure 5.9: Comparison of hydrogen purity against productivity for various industrial H_2 PSA systems with different numbers of columns and different step configurations 192
Figure 5.10: Weakly adsorbed impurities (nitrogen + argon) molar fraction profiles along a common dimensionless axial coordinate at the end of adsorption step at CSS and at 99.99+% H_2 purity among various industrial H_2 PSA configurations 193
Figure 5.11: Economic analysis summary for the different PSA configurations expressed in total installed cost ($ Millions) 198
Figure 5.12: LCOE calculation results for the three examined IGCC cases 203
Figure 5.13: Block flow diagram of an advanced IGCC plant with a recycle of H_2 PSA tail gas to water gas shift reactors 205
Figure 5.14: Variation of the hydrogen mole fraction percentage in the raw H_2 feed with the split ratio of the ‘tail gas recycle to shift reactors’ flow to total tail gas flow 205
Figure 5.15: Hydrogen molar fraction profile along the column at the end of adsorption step and at CSS for the nine-column PSA system 206
Figure 5.16: Block diagram of the Base case 207

Figure 5.17: Block diagram of the Case 1 with the H_2 PSA tail gas recycle to the water gas shift reactors 208
Figure 5.18: Block diagram of the Case 2 with the H_2 PSA tail gas recycle to the Selexol unit 209
Figure 5.19: Block diagram of the Case 3 with the H_2 PSA tail gas recycle to the coal dryer 210
Figure 5.20: Block diagram of the Case 4 with the H_2 PSA tail gas recycle to the water gas shift reactors and the coal dryer 211
Figure 5.21: Block diagram of the hydrogen plant (HP). Red arrows define the improved cases of Table 5.13 with different ways to recycle the H_2 PSA tail gas to the water gas shift reactor, the coal dryer and the CO_2 regenerator 215

Chapter 1: General introduction

Strong dependency on coal, crude oil and natural gas, as well as the associated costs and supply chain risks, increase the need for efficient utilisation of existing non-renewable energy sources. The rise in concentration of different pollutants in the atmosphere, especially greenhouse gases, has alerted the international community to evidence of possible climate change and has spurred on research to reduce anthropogenic carbon dioxide (CO_2) emissions.

Utilising more renewable sources and reducing the dependency on fossil fuels for energy production will ultimately lead to decarbonised and sustainable societies. However, renewable energy must be complemented by fossil fuel energy in the near future because its availability varies around the world and their production rates, varying depending on the natural environment, often give rise to supply and demand mismatches and their production costs are still more expensive than those of fossil fuel energies. Therefore, short-term measures, e.g. carbon capture and storage (CCS), must be taken to prevent the CO_2 concentration in the air from increasing while fossil fuels still take the position of major energy source.

This chapter introduces a brief discussion about fossil fuels, global warming and CO_2 emissions as well as the role of carbon capture and storage in the future low-carbonised energy matrix. The following sub-sections are devoted to the description of carbon capture systems and technologies, and the importance of hydrogen as both a sought target and an appropriate environmental solution. Subsequently, the motives, aims and outline of this thesis are presented and discussed.

1.1 Fossil fuels and global warming

Among fossil fuels, coal has long been considered the most conventional energy source for power generation due to its abundance – there is supply for more than 2,000 years at current consumption rates – and its relatively wide geographic distribution (Emun et al., 2010). By contrast, the CIA World Factbook (2010) estimated that oil and natural gas will run out in 2050 and 2060, respectively. The use of coal increased rapidly, mainly due to the industrial revolution, and has

continued to grow ever since, with only a few occasional temporary decreases. Coal was the dominant fuel during the 19th century and the first half of the 20th century (Encyclopaedia of Energy, 2004). The development that has occurred during the years in all societies is directly linked to the growth of the coal industry. Technological advancements closely associated with the use of coal have clearly influenced the modern definition of a developed society. Globally, coal is currently the dominant fuel in the power sector, accounting for 38% of electricity generated in 2000, with hydropower accounting for 17.5%, natural gas for 17.3%, nuclear for 16.8%, oil for 9% and non-hydro renewables for 1.6% (IPCC, 2005). The usage of coal as a primary fuel is expected to grow between 2010 and 2030 and the worldwide capacity of coal-fuelled power plants is expected to increase as well (Deb-Mondol et al., 2009). Moreover, according to the IPCC report (2005), coal is projected to remain the dominant fuel for power generation in 2020 (about 36%). Figure 1.1 exhibits the overall world energy consumption by fuel type during the years 1990–2040 expressed in quadrillions of Btu.

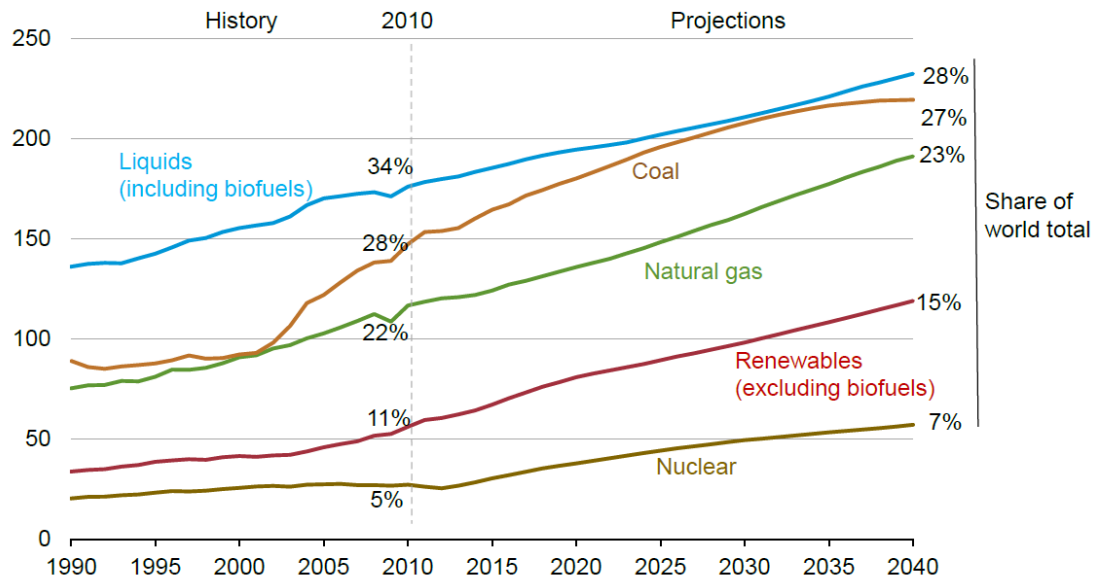

Figure 1.1: World energy consumption by fuel type during the years 1990–2040 (quadrillion [10^{15}] Btu) (WEO/EIA, 2013)

Nevertheless, burning coal and other fossil fuels leads to greenhouse gas emissions. Greenhouse gases (often abbreviated to GHG) are gaseous constituents of the atmosphere, both natural and anthropogenic, that absorb and emit radiation

within the thermal infrared range produced by solar warming of the Earth's surface. This property causes the greenhouse effect (IPCC, 2008). Water vapour (H_2O), carbon dioxide (CO_2), nitrous oxide (N_2O), methane (CH_4) and ozone (O_3) are the primary greenhouse gases in the Earth's atmosphere. Moreover, there are a number of entirely man-made greenhouse gases in the atmosphere, such as the halocarbons and other chlorine- and bromine-containing substances. Greenhouse gases greatly affect the temperature of the Earth; without them, the Earth's surface temperature would be approximately -18 ºC and under this condition most life as we know it would not be possible (Jacob, 1999). Since the Industrial Revolution began around 1750, the burning of fossil fuels and extensive clearing of native forests has contributed to a 43% increase in the atmospheric concentration of carbon dioxide, from 280 to 400 parts per million (ppm) in 2014 in the northern hemisphere (www.natureworldnews.com). Under ongoing greenhouse gas emissions, Earth System Models projected that the Earth's surface temperature would exceed historical analogues as early as 2047, affecting most ecosystems on Earth and the livelihoods of over 3 billion people worldwide (Mora et al., 2013). In addition, the International Panel on Climate Change (IPCC, 2007) as well as Mastandrea and Sneider (2005) have estimated that an increase of 2 °C in the global temperature would be extremely dangerous for the planet. Within this situation, there exists a concrete and substantial need to interrupt the trend of atmospheric change.

1.2 Carbon dioxide global emissions and the need for CCS

Carbon dioxide continued an upward trend in the early years of the 21st century. Fossil fuels are the dominant form of energy utilised in the world (86%), and account for about 75% of current anthropogenic CO_2 emissions (IPCC, 2005). The main sectors that contribute to energy consumption and CO_2 emissions are illustrated in Figures 1.2 and 1.3. Within the industrial sector, it is noteworthy that electricity production is responsible for approximately 30% of global CO_2 emissions (Chiesa et al., 2005). Regarding world energy source consumption and future predictions, several scenarios have been developed by different institutions based on different perspectives and techniques (Coates, 2002; Schiffer, 2008). Globally, the electricity and heat generation sectors rely heavily on coal. By 2035, the World

Energy Outlook (2013) projects that the demand for electricity will be more than 70% higher than the current demand (WEO, 2013). Therefore, the future development of CO_2 emissions intensity of this sector would depend strongly on the fuels used to generate electricity and on the share of fossil fuel plants equipped with CCS. This would be possible only if policy makers agreed with this direction.

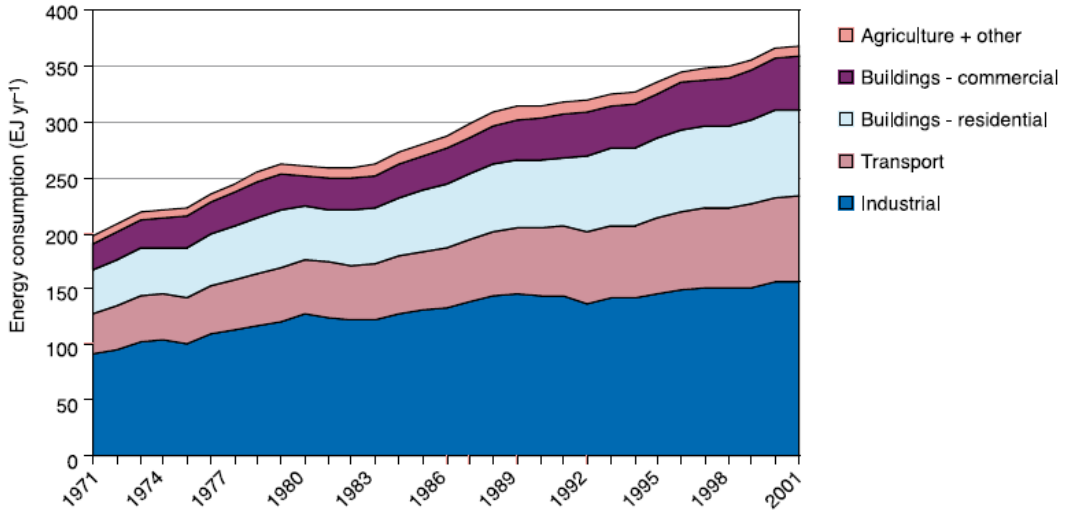

Figure 1.2: World primary energy use by sector, 1971–2001 (IEA, 2003)

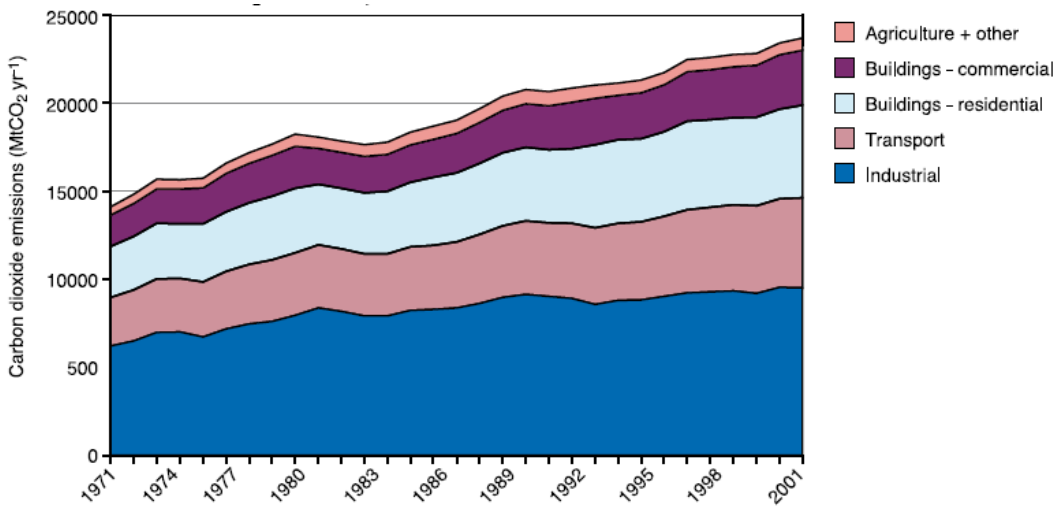

Figure 1.3: World CO_2 emissions from fossil fuel use by sector, 1971–2001 (IEA, 2003)

From a more local point of view, the UK (and similarly the EU) has set in its 2008 Climate Change Act a target to reduce its GHG emissions to 80% of the 1990 levels by 2050, achieving the allowed emissions of 150 Mt CO_{2e} (CO_2 equivalent)

per year. However, the figure also includes GHG emissions that are hard to reduce further, such as international aviation and shipping, and non-CO_2 emissions, both of which amount to 90 Mt CO_{2e}. Therefore, the net CO_2 emissions to be allowed in 2050 will be only 60 Mt CO_{2e} (Committee on Climate Change, 2011). To meet the target, it is essential to decarbonise all the industries, including refineries as well as power stations. Usually, the emission sources to be considered include all large stationary sources (>0.1 Mt CO_{2e} yr^{-1}). This threshold is selected because the sources emitting less than 0.1 Mt CO_{2e} yr^{-1} account for less than 1% of the emissions from all the stationary sources under consideration (IPCC, 2005). Eight refineries in the UK are currently emitting 14.9 Mt CO_{2e}, which accounts for around 3% of the total CO_2 emissions in the UK in 2009 (DECC, 2009). The INEOS refining plant in Grangemouth, for example, emits around 2.2 Mt CO_{2e} per annum, which is equivalent to 4% of total CO_2 emissions in Scotland (SEPA, 2008). The Committee on Climate Change (CCC) estimated that there will be a chance to curtail around 3.5 Mt CO_{2e} out of 14.9 Mt CO_{2e} from refineries in 2030 by improving their energy efficiency. The CCC also foresaw that, beyond this target of abatement, a further reduction would be possible by deploying carbon capture units on H_2 plants and replacing combustion fuels with carbon-neutral biomass (Committee on Climate Change, 2011). The petroleum refining industry is the nation's second-highest industrial consumer of energy.

Globally, the petroleum refining industry is a significant source of GHG emissions because nearly all of the energy consumed is fossil fuel for combustion. In addition to the combustion-related sources (e.g., process heaters and boilers), there are certain processes, such as fluid catalytic cracking units (FCCU), hydrogen production units and sulfur recovery plants, that have significant process emissions of carbon dioxide. Methane emissions from a typical petroleum refinery arise from process equipment leaks, crude oil storage tanks, asphalt blowing and delayed coking units. System blowdown and flaring of waste gas also contribute to the overall CO_2 and CH_4 emissions at the refinery. Figure 1.4 presents the breakdown of onsite GHG emissions by source. As seen in Figure 1.4, combustion sources, direct process emissions and flaring account for 99% of the onsite GHG emissions on a CO_{2e} basis (EPA, 2008).

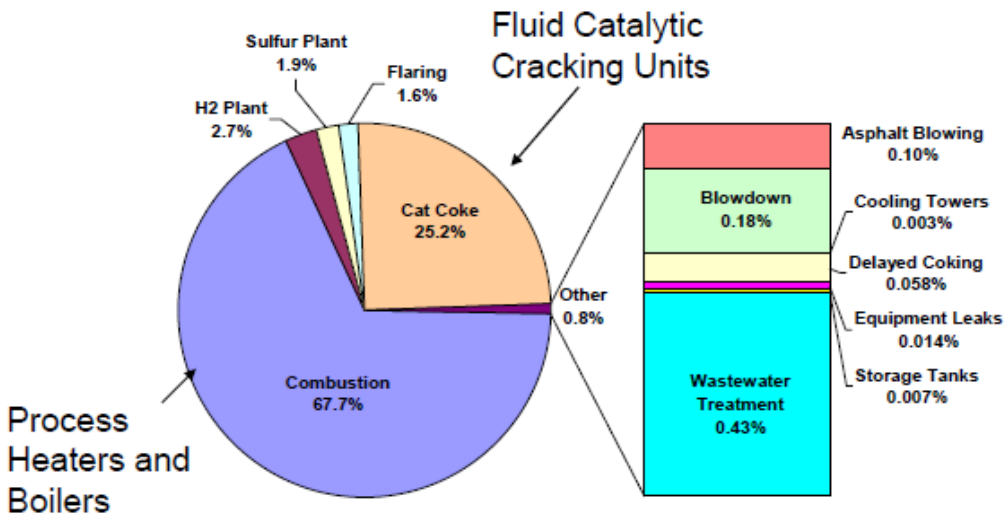

Figure 1.4: Relative importance of refinery greenhouse gas emission sources evaluated on CO_{2e} basis (EPA, 2008)

1.3 Carbon capture systems

Capturing CO_2 typically involves separating it from a gas stream. Suitable techniques were developed more than 80 years ago in connection with the production of town gas; these involve scrubbing the gas stream with a chemical solvent (Bottoms, 1931). This kind of technique is widely used today for separating CO_2 and other acid gases from natural gas streams. Horn and Steinberg (1982) and Hendriks et al. (1989) were among the firsts to discuss the application of this type of technology to carbon capture from power plants for the purpose of mitigation of climate change. The main application of CO_2 capture is likely to be at large point sources, as discussed in the previous sub-section. Capturing CO_2 directly from small and mobile sources in the transportation and residential and commercial building sectors is expected to be more difficult and expensive than from large point sources. The possibility of CO_2 capture from ambient air (Lackner, 2003) is still at an early stage of research because the CO_2 concentration in ambient air is around 400 ppm, a factor of hundreds lower than those in flue gases. There are four basic systems for capturing CO_2 from the use of fossil fuels and/or biomass:

- Post-combustion capture

- Pre-combustion capture
- Oxy-fuel combustion capture
- Capture from industrial process streams

These systems are shown in schematic form in Figure 1.5.

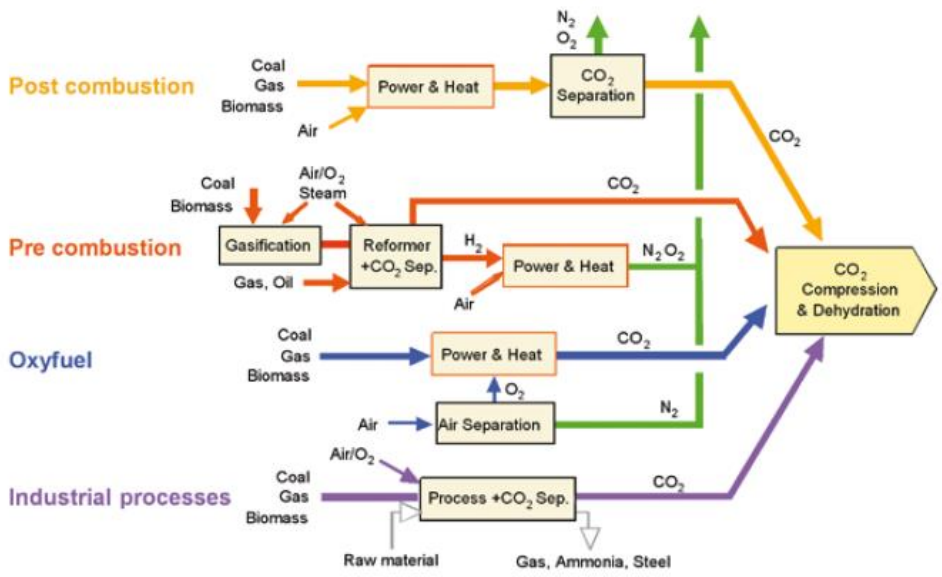

Figure 1.5: Overview of carbon capture systems (IPCC, 2005)

1.3.1 Post-combustion carbon capture

The capture of CO_2 from flue gases produced by combustion of carbonaceous fuels, such as fossil fuels and biomass with air, is referred to as post-combustion capture. Instead of being discharged directly to the atmosphere, a flue gas is passed through a post-combustion capture unit, which separates most of the CO_2 out of the flue gas usually by means of its contact with chemical solvents represented primarily by monoethanolamine (MEA). Other techniques are also being considered but these are not at such an advanced stage of development. The CO_2 captured is compressed for its subsequent use in Enhanced Oil Recovery (EOR) or CO_2 storage, and the remaining flue gas is discharged to the atmosphere. Several modifications to the amine capture process have been proposed over the years. Ahn and co-workers recently evaluated various amine process configurations reported in papers and

patents and quantified how much energy it could save in comparison to the conventional scheme (Ahn et al., 2013).

1.3.2 Pre-combustion carbon capture

Pre-combustion capture involves reacting fuel with oxygen or air and steam to produce ‘synthesis gas (syngas)’ or ‘fuel gas’ composed mainly of carbon monoxide and hydrogen. The carbon monoxide reacts with steam in a catalytic reactor, a so-called shift reactor, to give CO_2 and more hydrogen. CO_2 is then separated by a physical or chemical absorption process, resulting in a hydrogen-rich fuel that can be used in many applications, such as boilers, furnaces, gas turbines, engines and fuel cells. These systems are considered to be strategically important despite the fact that integrated gasification combined cycle (IGCC) power plants represent only 0.1% of the total installed capacity worldwide (WEO, 2004). These systems in fact have higher net plant efficiency (38–41% HHV) than PC-boiler power plant (37–39% HHV) and this difference increases by up to 5–7 % when integrated with carbon capture units (DOE, 2007). Moreover, compared to PC power plants, IGCCs also produce smaller volumes of solid wastes (Shilling and Lee, 2003), use 30–60% less water and provide greater fuel flexibility (Ratafia-Brown et al., 2002).

1.3.3 Oxy-fuel combustion carbon capture

In oxy-fuel combustion, nearly pure oxygen is used for combustion instead of air, resulting in a flue gas that is composed of mainly CO_2 and H_2O. If the fuel is burnt in pure oxygen, the flame temperature is excessively high, but CO_2 and/or H_2O-rich flue gas can be recycled through the combustor to moderate this effect (Takami et al., 2009). Oxygen is usually produced conventionally by low temperature (cryogenic) air separation unit and several novel techniques to supply oxygen to the fuel are being developed, such as ion transport membranes (ITM), chemical looping combustion (CLC) and chemical looping oxygen uncoupling (CLOU). For a new-build pulverised coal fired power boiler using a supercritical steam cycle, Dillon et al. (2005) estimated that the overall thermal efficiency on a lower heating value basis is reduced from 44.2% to 35.4% and the net power output

is reduced from 677 MW_e to 532 MW_e. Prior to the CO_2 compression train, the flue gas leaving the boiler is passed through a gas cooler and separator for water removal.

1.3.4 Capture from industrial process streams

Carbon dioxide has been captured from industrial process streams for 80 years (Kohl and Nielsen, 1997), although most of the CO_2 that is captured is vented to the atmosphere because there is no incentive or requirement to store it. Current examples of CO_2 capture from process streams are purification of natural gas and production of hydrogen-containing synthesis gas for the manufacture of ammonia, alcohols and synthetic liquid fuels. Most of the techniques being employed for CO_2 capture in the above-mentioned examples are similar to those used in pre-combustion capture. On the other hand, significant amounts of CO_2 are being produced by operating refining and petrochemical plants, cement plants, iron and steel plants, and fermentation processes for food and drink production. The CO_2 generated from these sources could be captured using techniques that are common to post-combustion capture or oxy-fuel combustion capture.

1.4 Carbon capture technologies

Carbon capture systems use many of the known technologies for gas separation, which are integrated into the basic systems for CO_2 capture. A summary of these separation methods is given in Figure 1.6. The CO_2 capture systems shown in Figure 1.5 can be cross-referenced with the different separation technologies of Figure 1.6, resulting in a capture toolbox. Table 1.1 gives an overview of both current and emerging technologies in this toolbox. In the following sections, a more detailed description of all these technological options will be given, with more emphasis on the most developed technologies for which the CO_2 capture cost can be estimated more reliably. These leading commercial options are shown in bold in Table 1.1. All the diverse range of emerging options are aimed at more efficient and lower-cost CO_2 capture systems compared with the leading options.

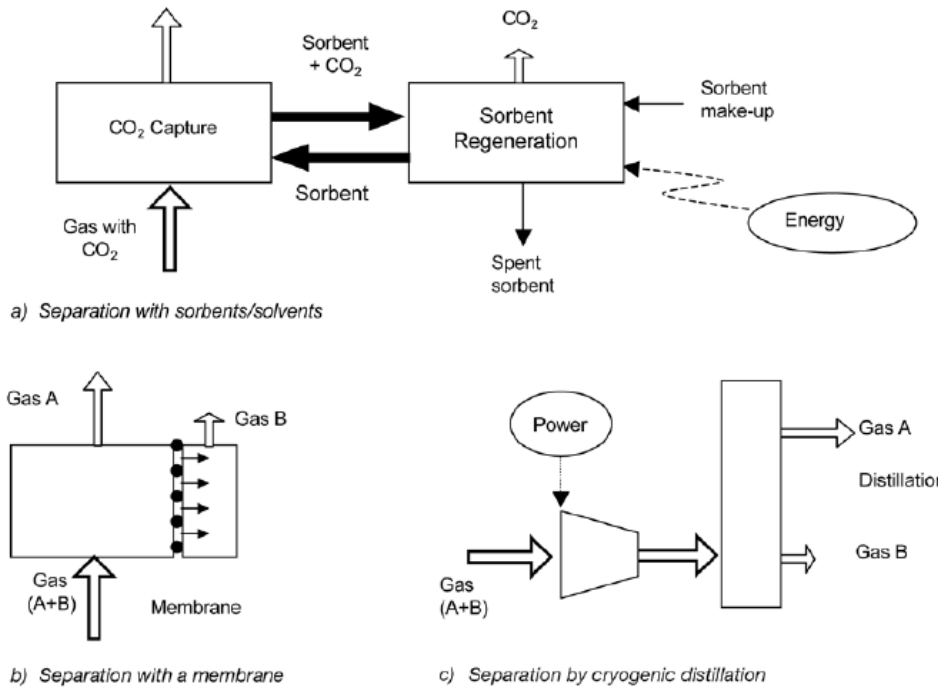

Figure 1.6: General schemes of the main processes relevant for CO_2 capture (IPCC, 2005)

Table 1.1: Carbon capture cross-referenced toolbox between systems and technologies (IPCC, 2005)

Separation task	Process streams*		Post-combustion capture		Oxy-fuel combustion capture		Pre-combustion capture	
	CO_2/CH_4		CO_2/N_2		O_2/N_2		CO_2/H_2	
Capture Technologies	**Current**	**Emerging**	**Current**	**Emerging**	**Current**	**Emerging**	**Current**	**Emerging**
Solvents (Absorption)	**Physical solvents** **Chemical solvents**	Improved solvents Novel contacting equipment Improved design of processes	**Chemical solvents**	Improved solvents Novel contacting equipment Improved design of processes	n. a.	Biomimetic solvents, e.g. hemoglobine-derivatives	**Physical solvent** **Chemical solvents**	Improved chemical solvents Novel contacting equipment Improved design of processes
Membranes	**Polymeric**	Ceramic Facilitated transport Carbon Contactors	Polymeric	Ceramic Facilitated transport Carbon Contactors	Polymeric	Ion transport membranes Facilitated transport	Polymeric	Ceramic Palladium Reactors Contactors
Solid sorbents	Zeolites Activated carbon		Zeolites Activated carbon	Carbonates Carbon based sorbents	Zeolites Activated carbon	Adsorbents for O_2/N_2 separation, Perovskites Oxygen chemical looping	Zeolites Activated carbon Alumina	Carbonates Hydrotalcites Silicates
Cryogenic	Ryan-Holmes process		Liquefaction	Hybrid processes	**Distillation**	Improved distillation	Liquefaction	Hybrid processes

1.4.1 Chemical absorption

Absorption processes based on chemical solvents are currently the preferred option for post-combustion CO_2 capture (Hendriks, 1994; Riemer and Ormerod, 1995) because of their high capture efficiency and selectivity as well as their mature commercial stage of operation. Absorption processes in post-combustion capture make use of the reversible nature of the chemical reaction of an aqueous alkaline

solvent, usually an amine, with an acid or sour gas. The process flow diagram of a commercial absorption system is presented in Figure 1.7.

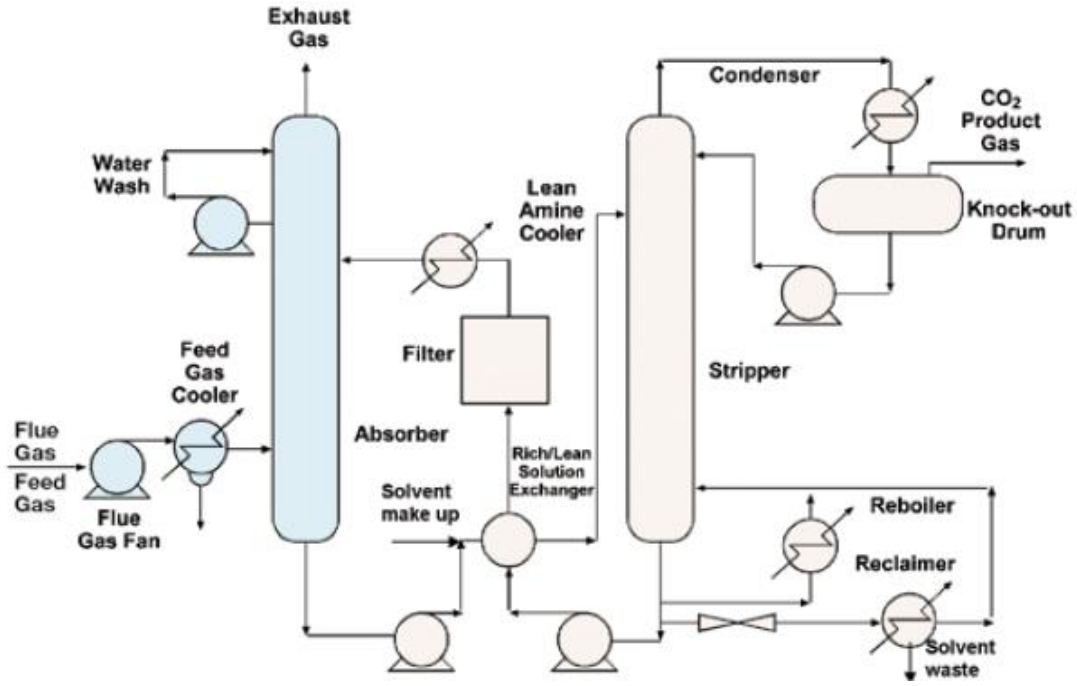

Figure 1.7: Process flow diagram for CO_2 recovery from flue gas by chemical absorption (IPCC, 2005)

After cooling the flue gas, it is brought into contact with the solvent in the absorber. A blower is required to overcome the pressure drop through the absorber. At absorber temperatures typically between 40 and 60 ºC, CO_2 is bound by the chemical solvent in the absorber. The flue gas then undergoes a water wash to balance water in the system and to remove any solvent droplets or solvent vapour carried over, and then it leaves the absorber. It is possible to reduce the CO_2 concentration in the exit gas down to very low values as a result of the chemical reaction in the solvent, but lowering exit concentrations tends to increase the height of the absorption vessel. The 'rich' solvent, which contains the chemically bound CO_2, is then pumped to the top of a stripper (or regeneration vessel) via a heat exchanger. The regeneration of the chemical solvent is carried out in the stripper at elevated temperatures (100–130 ºC) and pressures ranging between 1.1–1.5 bar (IPCC, 2005). Heat is supplied to the reboiler to maintain the regeneration conditions. This leads to a thermal energy penalty as a result of heating up the

solvent, providing the required desorption heat for removing the chemically bound CO_2 and for steam production, which acts as a stripping gas. Steam is recovered in the condenser and fed back to the stripper, whereas the CO_2 product gas leaves the stripper. The 'lean' solvent, containing far less CO_2, is then pumped back to the absorber via the lean-rich heat exchanger and a cooler to bring it down to the absorber temperature level.

The key parameters determining the technical and economic operation of a CO_2 absorption system are the flue gas flow rate, CO_2 content in flue gas, CO_2 removal target, solvent flow rate, energy requirement and cooling requirement. The main energy consumption of the process is due to the reboiler duty of the stripper that, at a carbon capture rate of 90%, is around 3.5 MJ_{th}/kg of captured CO_2 (DOE, 2007). There are absorption processes involving different solvents that are commercially available for CO_2 capture in post-combustion systems (Barchas and Davis, 1992; Sander and Mariz, 1992; Chapel et al., 1999; Mimura et al., 1999). Integration of the absorption process with an existing power plant will require modifications of the low-pressure part of the steam cycle as a sizeable fraction of the steam will be extracted for the reboiler duty and hence will not be available to produce power (Nsakala et al., 2001; Mimura et al., 1997).

Among the emerging technologies for chemical absorption, various novel solvents are being investigated with the objective of achieving reduced energy consumption for solvent regeneration (Chakma, 1995; Mimura et al., 1999; Zheng et al., 2003; Cullinane and Rochelle, 2003). Besides novel solvents, research is also being carried out to improve upon the existing practices and packing types (Aroonwilas et al., 2003). Novel process designs are also becoming available (Leites et al., 2003; Cousins et al., 2001; Ahn et al., 2013). Ahn et al. (2013) also pointed out that simultaneous application of more than one process improvement strategy to the amine process configuration could achieve further reduction in reboiler duty.

Chemical solvents are also used to remove CO_2 from syngas at partial pressures below about 1.5 MPa (Astarita et al., 1983), which are similar to those used for post-combustion capture. The solvent removes CO_2 from the shifted syngas by means of a chemical reaction, which can be reversed by pressure reduction and heating. The tertiary amine methyldiethanolamine (MDEA) is widely used in modern

industrial processes due to the high CO_2 loading possible and the low regenerator heating load relative to other solvents. Hot potassium carbonate, of which the most common commercial version is known as Benfield, had been used for CO_2 removal in most hydrogen plants until about 15 years ago. Table 1.2 lists the common solvents used for the removal of CO_2 from natural gas or shifted syngas in pre-combustion capture processes.

Table 1.2: Common solvents used in pre-combustion capture processes (IPCC, 2005)

Solvent name	Type	Chemical name	Vendors
Rectisol	Physical	Methanol	Lurgi and Linde, Germany Lotepro Corporation, USA
Purisol	Physical	N-methyl-2-pyrolidone (NMP)	Lurgi, Germany
Selexol	Physical	Dimethyl ethers of polyethylene glycol (DMPEG)	Union Carbide, USA
Benfield	Chemical	Potassium carbonate	UOP
MEA	Chemical	Monoethanolamine	Various
MDEA	Chemical	Methyldiethylamine	BASF and others
Sulfinol	Chemical	Tetrahydrothiophene 1,1-dioxide (Sulfolane), an alkaloamine and water	Shell

1.4.2 Physical absorption

There are over 30 acid gas removal processes based on physical absorption in common commercial use throughout the oil, chemical and natural gas industries (Kohl and Nielsen, 1997; DOE, 2007). Physical solvent (or absorption) processes are mostly applicable to gas streams that have a high CO_2 partial pressure and/or a high total pressure. They are often used to remove the CO_2 from the mixed gas stream of CO_2 and H_2 that is usually produced by partial oxidation of coal and heavy hydrocarbons followed by shift reaction. The leading physical solvent processes are also shown in Table 1.2. The regeneration of solvent is carried out by a release of pressure at which CO_2 evolves from the solvent in one or more stages. If a deeper regeneration is required, the solvent would be regenerated by heat. The process has low energy consumption as only the energy for pressurising the solvent (liquid pumping) is required. From Case 6 of the DOE report (2007), for example, the specific energy consumption associated with the CO_2 capture and compression process of a pre-combustion IGCC is evaluated at 0.35 MJ_e/kg against a typical value of 1.38 MJ_e/kg related to a post-combustion process using MEA (Ahn et al., 2013).

The use of high-sulfur fossil fuels in a pre-combustion capture process results in syngas with H_2S. Acid gas components must be removed. If transport and storage of mixed CO_2 and H_2S are possible then both components can be removed together. Sulfinol was developed to achieve significantly higher solubilities of acidic components compared to amine solvents, without added problems of excessive corrosion, foaming or solution degradation (IPCC, 2005). Sulfinol is a mixture of diisopropanolamine (30–45%) or methyl diethanolamine (MDEA), sulfolane (tetrahydrothiophene dioxide) (40–60%) and water (5–15%). If pure CO_2 is required, then a selective process is necessary using physical solvents – often Rectisol or Selexol. The H_2S must be separated at a sufficiently high concentration (generally >30%) to be treated in a sulfur recovery plant.

1.4.3 Adsorption

In the adsorption process for flue gas CO_2 recovery, molecular sieves or activated carbons are used for adsorbing CO_2. Desorbing CO_2 is then done by decreasing the pressure in a pressure swing adsorption operation (PSA) or increasing the temperature in a temperature swing adsorption operation (TSA). Most applications are associated with PSA (Ishibashi et al., 1999; Yokoyama, 2003). Much less attention has been paid to CO_2 removal via temperature swing adsorption because this technique would require longer cycle times than a PSA. For bulk separations at large scales, it is also essential to limit the length of the unused bed and therefore opt for faster cycle times.

Although several authors have tried to apply the PSA technology in the field of carbon capture, especially for post-combustion (Kikkinides et al., 1993; Liu et al., 2011; Wang et al., 2012, Ko et al., 2003), it has not yet reached a commercial stage for CO_2 recovery from flue gases. In these works, different process conditions as well as the use of multi-column systems were analysed with the intention of reducing the energy consumption in order to accomplish the typical carbon capture targets of 90% CO_2 recovery and >95% CO_2 purity. Specific energy consumptions are in the range of 0.7–1.5 MJ_e/kg of captured CO_2 making this separation process a good potential alternative to the amine process. The development of a new generation of

materials that would efficiently adsorb CO_2 will undoubtedly enhance the competitiveness of adsorptive separation in a flue gas application.

PSA cycles may also be applied to pre-combustion capture: PSA is the system of choice for the purification of syngas, where high purity H_2 is required. However, in one single stage of separation, it does not selectively separate CO_2 from the other waste gases so that for an SMR application the CO_2 concentration in the waste gas would be 40–50% and require further upgrading to produce pure CO_2 for storage. Simultaneous H_2 and CO_2 separation is possible by using a particular multibed PSA system capable to co-produce high purity H_2 and CO_2, such as the Air Products Gemini-9 Process (Sircar, 1979).

1.4.4 Membranes

Membrane processes are used commercially for CO_2 removal from natural gas at high pressure and at high CO_2 concentration. In flue gases, the low CO_2 partial pressure difference provides a low driving force for gas separation. The removal of carbon dioxide using commercially available polymeric gas separation membranes results in higher energy penalties on the power generation efficiency compared to a standard chemical absorption process (Herzog et al., 1991; Van der Sluijs et al., 1992; Feron, 1994). Improvements can be made if more selective membranes become available, such as facilitated membranes, described below. The membrane option currently receiving the most attention is a hybrid membrane–absorbent (or solvent) system. These systems are being developed for flue gas CO_2 recovery (Feron, 1994). Membrane/solvent systems employ membranes to provide a very high surface area to volume ratio for mass exchange between a gas stream and a solvent resulting in a very compact system. This results in a membrane contactor system in which the membrane forms a gas-permeable barrier between a liquid and a gaseous phase. In general, the membrane is not involved in the separation process. In the case of porous membranes, gaseous components diffuse through the pores and are absorbed by the liquid; with non-porous membranes, they dissolve in the membrane and diffuse through the membrane.

Several membranes can be configured in a multi-stage system with a different flow pattern in order to meet the carbon capture targets and minimise the energy

consumption. It is reported in the literature that the associated energy consumption would be around 2.1 MJ_e/kg of captured CO_2 (Bocciardo et al., 2013).

1.4.5 Chemical looping

The chemical looping technology is based on the splitting of the combustion of a hydrocarbon or carbonaceous fuel into separate oxidation and reduction reactions by introducing a suitable metal oxide as an oxygen carrier to circulate between two reactors. Unlike the oxy-fuel process technology, there is no need for air separation. The reaction between fuel and oxygen occurs in a second reactor by the release of oxygen from the metal oxide in a reducing atmosphere caused by the presence of a hydrocarbon or carbonaceous fuel. The recycle rate of the solid material between the two reactors and the average solid residence time in each reactor control the heat balance and the temperature levels in each reactor. The fact that the combustion takes place in two reactors compared to conventional combustion in a single stage indicates that the CO_2 is not being diluted with nitrogen gas, but being almost pure after separation from water, without requiring any extra energy demand and costly external equipment for CO_2 separation (IPCC, 2007). Pioneering works in this field have been reported by Richter and Knoche (1983) and Ishida and Jin (1994).

The oxides of some transition state metals, such as Fe, Ni, Cu and Mn, can be used as oxidising agents (Zafar et al., 2005). The temperature in the reactor may be in the range of 800 °C–1200 °C; NO_x formation at these temperatures is low and the fuel conversion in the reduction reactor may not be complete (Cho et al., 2002). Brandvoll and Bolland (2004) studied the use of natural gas as a fuel in a chemical looping configuration incorporated in a combined cycle plant and estimated the fuel-to-electricity conversion efficiency to be in the range of 45–50%.

1.4.6 Cryogenic distillation

Cryogenic separation is another method that can be used to separate CO_2 from other components of a gas stream. While cryogenic separation has long been applied to commercial air separation, it has also been considered as an option to achieve CO_2 capture. The gas stream is transformed into liquid after a series of compressions and expansions, and the components of interest are separated by distillation. This system

remains the preferred technology in the food and beverage industries where a very high CO_2 purity (>99.9%) is required (ISBT, 2006).

1.5 Carbon dioxide capture costs

Published estimates for CO_2 capture costs vary widely, mainly as a result of different assumptions regarding technical factors related to plant design and operation (e.g., plant size, net efficiency, fuel properties and load factor), as well as key economic and financial factors, such as fuel cost, interest rates and plant lifetime. A number of recent papers have addressed this issue and identified the principal sources of cost differences and variability (Herzog, 1999; Simbeck, 1999; Rubin and Rao, 2003).

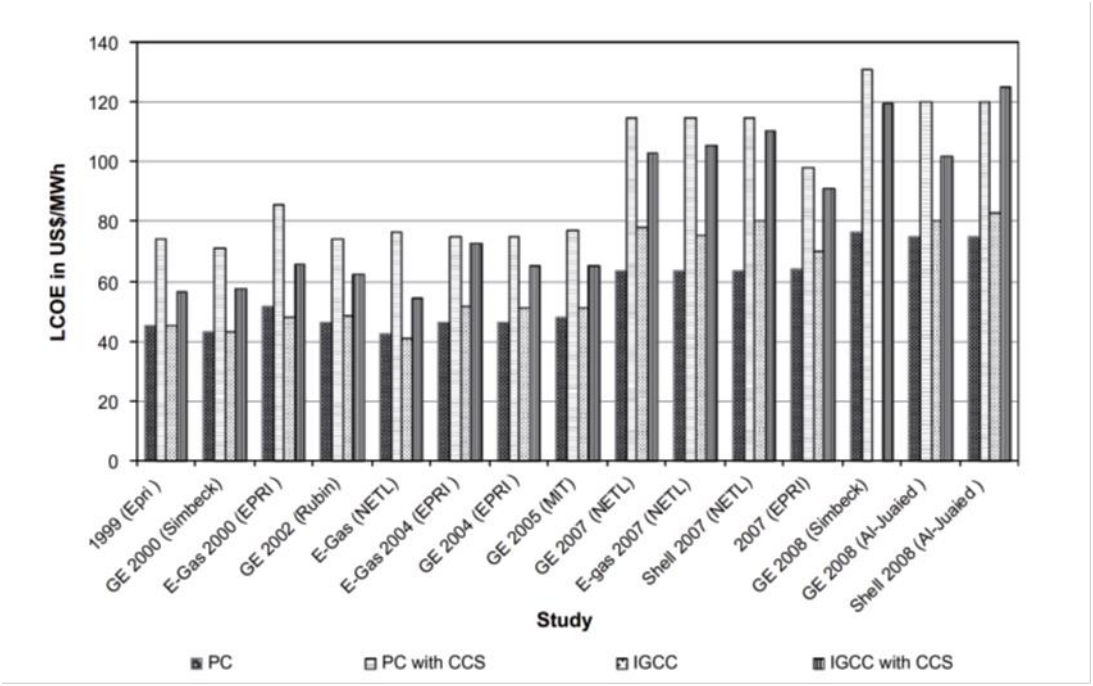

Figure 1.8: Levelised cost of electricity (LCOE) of PC and IGCC power plants (Hoffmann and Szlo, 2011)

For example, Hoffman and Szklo (2011) reviewed the studies performed for PC boiler and IGCC power plants in terms of the costs associated with them. They reported two criteria to evaluate the plants studied: the levelised cost of electricity (LCOE) and the cost of CO_2 avoided. It is obvious that, as shown in Figures 1.8 and 1.9, most studies have demonstrated that IGCC power plants, regardless of the years

performed and the assumptions that the studies were based on, would be more economical than the PC boiler power plants when CO_2 capture units are integrated.

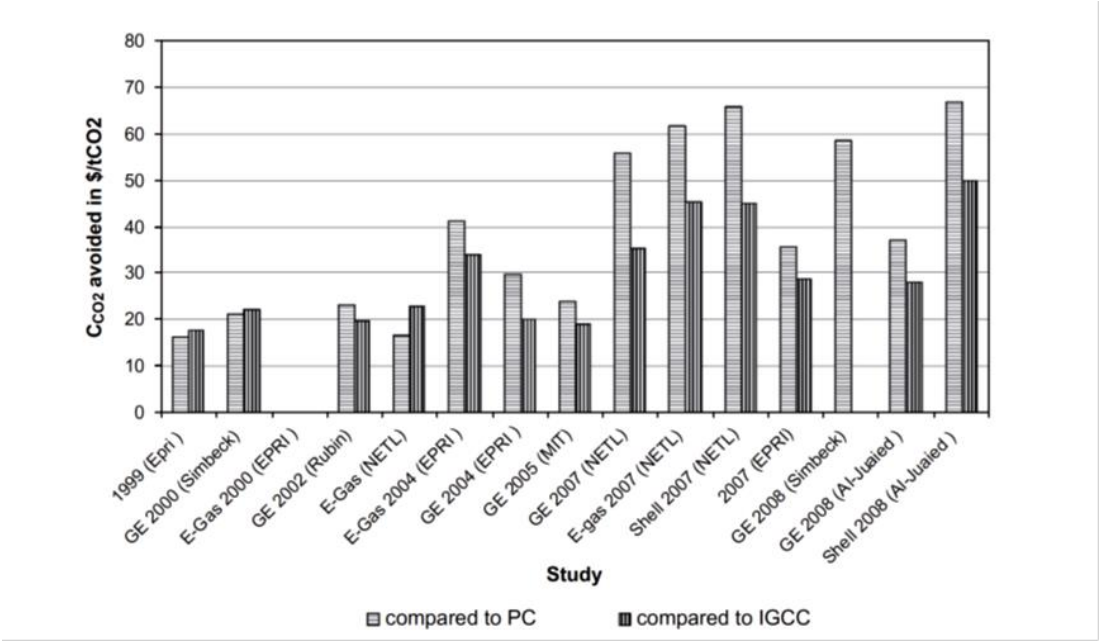

Figure 1.9: Cost of CO_2 avoided of PC and IGCC power plants (Hoffmann and Szlo, 2011)

1.6 Global hydrogen demand

Hydrogen is the most abundant element in the universe. It cannot be destroyed, unlike hydrocarbons, and it simply changes state from water to hydrogen and back to water during consumption. When released, it quickly rises to the upper atmosphere and dissipates, leaving virtually no hydrogen gas on the Earth's surface. Because hydrogen gas must be manufactured from feedstocks that contain hydrogen compounds, it is considered to be an energy carrier, like electricity, rather than a primary energy resource (DOE, 2008). Approximately 10–11 million metric tonnes of hydrogen are produced in the US each year (DOE, 2008). For reference, this is enough to power 20–30 million cars or about 5–8 million homes. Globally, around 50 million tonnes (equal to about 475 billion cubic meters) of hydrogen are produced each year and the production is expected to grow 3.5% annually through to 2018 (Freedonia Group, Inc., 2014). Over the years, hydrogen demand has regularly increased in every part of the world, as reported in Table 1.3.

Table 1.3: World hydrogen demand over years expressed in billion cubic meters (Freedonia Group, Inc., 2014)

Item	2003	2008	2013	% Annual Growth 2003-2008	% Annual Growth 2008-2013
World Hydrogen Demand	307.0	402.3	475.0	5.6	3.4
North America	96.0	122.9	132.0	5.1	1.4
Western Europe	61.0	73.3	78.0	3.7	1.3
Asia/Pacific	87.2	119.6	157.0	6.5	5.6
Other Regions	62.8	86.5	108.0	6.6	4.5

The majority of hydrogen is produced using fossil fuel feedstocks, as extensively depicted in Figure 1.10. Around half is used to produce ammonia and around a quarter is used for hydroprocessing in petroleum refining, with the balance used to make methanol and other industrial applications, including coal-to-liquids (Figure 1.10).

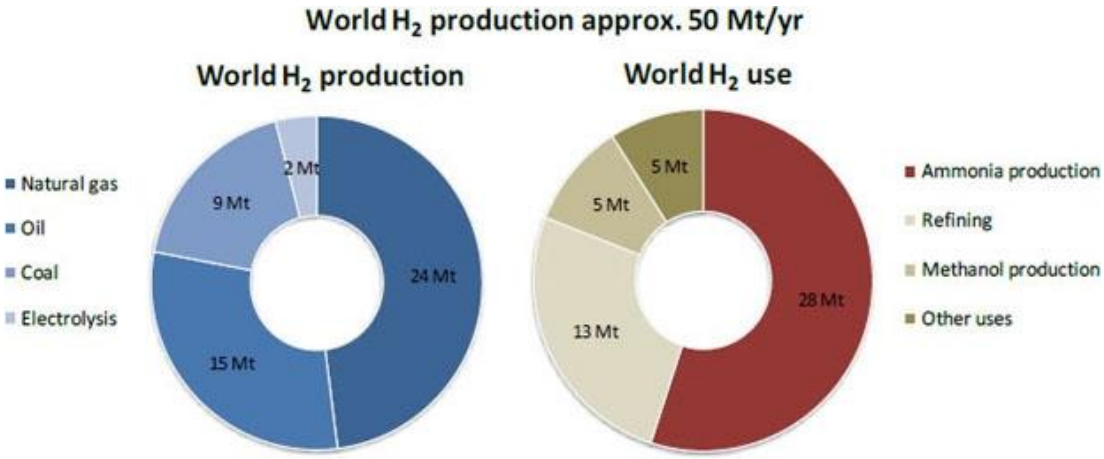

Figure 1.10: World hydrogen production and use (Evers, 2008)

A growing use of hydrogen is supporting emerging applications based on fuel cell technology along with other ways to use hydrogen for electricity production or energy storage. More than 50 types and sizes of commercial fuel cells are being sold and the value of fuel cell shipments reached $500 million in 2009 (DOE, 2010).

1.7 Methods for producing hydrogen

Hydrogen can be produced from a variety of feedstocks. These include fossil resources, such as natural gas and coal, as well as renewable resources, such as biomass and water with input from renewable energy sources (e.g., sunlight, wind, wave or hydro power). A variety of process technologies can be used, including chemical, biological, electrolytic, photolytic and thermochemical. Each technology is in a different stage of development and each offers unique opportunities, benefits and challenges. Local availability of feedstock, the maturity of the technology, market applications and demand, policy issues and costs will all influence the choice and timing of the various options for hydrogen production (EIA, 2006). Several technologies are already available in the marketplace for the industrial production of hydrogen. The first commercial technology, dating from the late 1920s, was the electrolysis of water to produce pure hydrogen. In the 1960s, the industrial production of hydrogen shifted slowly towards a fossil-based feedstock, which is the main source for hydrogen production today. An overview of the various feedstocks and process technologies is presented in Figure 1.11. A detailed review of all the hydrogen production methods can be found in the EIA's report (2006).

The natural gas or steam reforming process involves pre-heating, purifying and reacting the gas with steam in the presence of an active nickel catalyst to produce hydrogen and carbon monoxide. The carbon monoxide is then reacted further with water in the 'shift' reaction to produce additional hydrogen. The heat is often supplied from the combustion of some of the methane feed gas. The process typically occurs at temperatures of 700 to 850 °C and pressures of 3 to 25 bar. Process efficiencies range typically between 65–75%. Other ways of producing hydrogen from natural gas are the partial oxidation and autothermal reforming processes.

Hydrogen can be produced from coal through a variety of gasification processes (e.g. fixed bed, fluidised bed or entrained flow). In practice, high-temperature entrained flow processes are favoured to maximise carbon conversion to gas, thus avoiding the formation of significant amounts of char, tars and phenols. A coal gasifier converts pulverised coal into hydrogen and carbon monoxide when steam and oxygen are added in a cycle known as the IGCC. Partial oxidisers produce

hydrogen from heavy hydrocarbons (e.g., oil), typically at process efficiencies of about 50%.

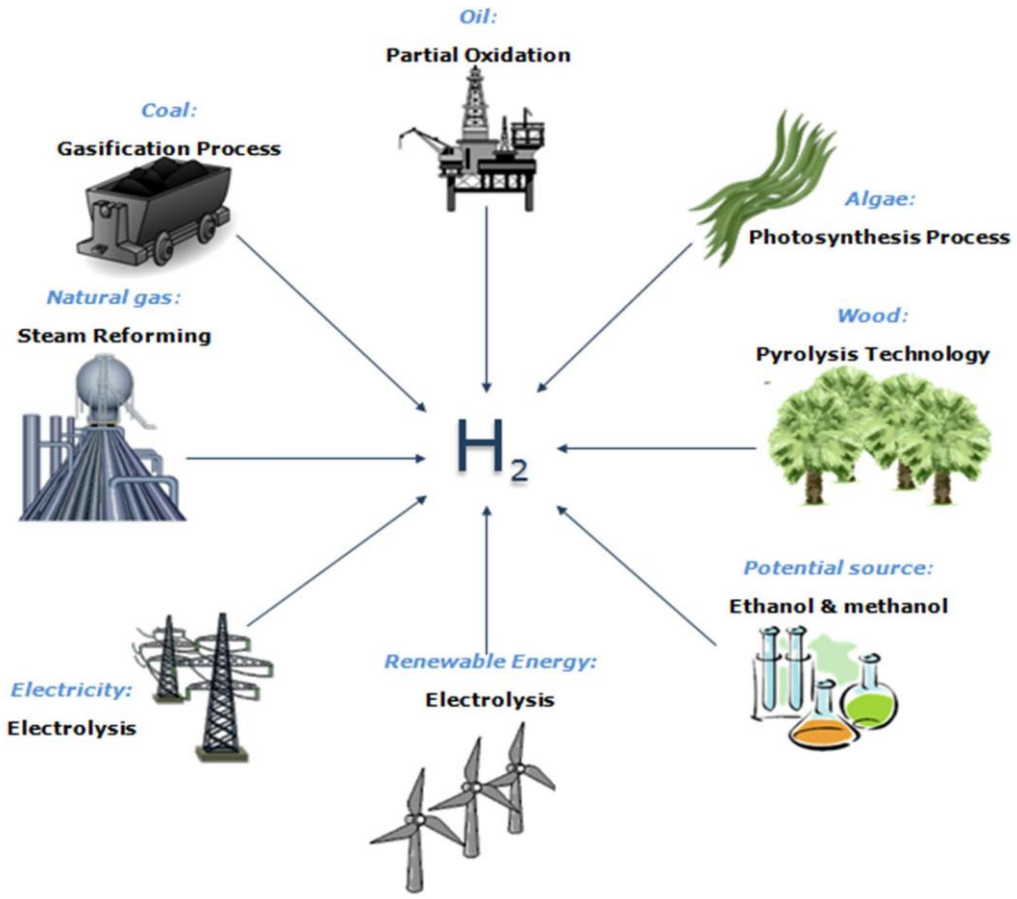

Figure 1.11: Hydrogen sources and production processes (IGEM, 2012)

Water electrolysis is the process whereby water is split into hydrogen and oxygen through the application of electrical energy. The total energy that is needed for water electrolysis increases slightly with temperature, while the required electrical energy decreases. Ideally, 39 kWh of electricity and 8.9 litres of water are required to produce 1 kg of hydrogen at 25 °C and 1 atm. Typical commercial electrolyser system efficiencies are between 56–73%, which corresponds to 53.4–70.1 kWh/kg (some new technologies have been shown to achieve up to 80% efficiency on a gross calorific value [GCV] basis).

Pyrolysis, photo-biological and thermo-chemical processes are the less well-known hydrogen production routes. Gasification and pyrolysis are considered the most promising medium-term technologies for the commercialisation of H_2

production from biomass. Biomass pyrolysis, similar to the gasification process, produces a variety of gases at temperatures in excess of 800 °C including hydrogen, methane, carbon monoxide and carbon dioxide.

Photo-biological production of hydrogen is the process whereby photosynthetic microbes undergo metabolic activities using light energy to produce hydrogen from water. Examples of microbes with such metabolic capabilities include green algae and cyanobacteria. Long-term basic and applied research is needed in this area, but if successful, a long-term solution for renewable hydrogen production will result.

1.8 Carbon capture from hydrogen plants: Research perspective

A lot of research has been carried out both by academia and companies in order to investigate the feasibility and challenges associated with the CO_2 capture process applied to H_2 plants. The following Table 1.4 summarises all these works, focusing on type of hydrogen production plant, type of carbon capture unit and comments related to key research points.

Table 1.4: Summary of research works on carbon capture processes from hydrogen plants

Reference	Organisation	H_2 production method	CO_2 capture method	Comments
Soltani et al., 2014	Academia	SMR	N/A	Detailed investigation and comparison were carried out on the effect of steam-to-carbon ratio on CO_2 capture criteria from various locations in the SMR process, such as the syngas stream, the PSA tail gas and the furnace flue gas.
Muradov and Veziroglu, 2005	Academia	Methane pyrolysis	Not required	Technological, environmental and economic aspects of large-scale production of hydrogen and carbon by the catalytic dissociation of natural gas were discussed in detail with focus on a new "hydrogen-carbon"-based scenario.

Ogden, 2002	Academia	SMR	MEA	A techno-economic model of a large-scale fossil H_2 system with CO_2 capture demonstrated that H_2 production, distribution and refuelling are the major costs contributing to the delivered cost of H_2, while CO_2 capture added only ~10%.
Dufour et al., 2009	Academia	Methane pyrolysis	Not required	Autocatalytic decomposition of methane was found to be the most environmentally friendly process for hydrogen production (lowest impact and CO_2 emission) compared with the SMR with and without CO_2 capture and storage.
Tarun et al., 2007	Academia	SMR	MEA, Membrane	Best operating conditions that minimise the energy penalty for CO_2 capture while maximising H_2 production were determined. Both membrane and MEA capture process were found comparable in terms of energy penalty.
Cormos, 2014	Academia	Bioethanol reforming	MDEA, Syngas chemical loop, Bioethanol chemical loop	Assessment of H_2 production from bioethanol at industrial scale was performed comparing three carbon capture designs: the results for chemical looping processes showed higher energy efficiencies than MDEA (59–63% vs. 53–58%).
Mueller-Langer et al., 2007	Academia	SMR, Coal gasif., Biomass gasif., Electrolysis	MEA, Selexol, Not required, Not required	Different H_2 production processes involving different CO_2 capture methods were investigated economically. Coal gasification will be more competitive while biomass gasification and electrolysis could become relevant if technological barriers are overcome.
Terrien et al., 2014	Company	SMR	Cryogenic distillation, Membrane	The new Air Liquid solution for capturing CO_2 from an SMR H_2 plant based on cryogenics was described in detail. This could be a viable option for EOR application and for massive adoption of CCS as a CO_2 mitigation technique.
Lindsay et al., 2009	Company	SMR, ATR	MDEA, Econamine	Several process designs for production of H_2 and simultaneous

			FG plus	capture of CO_2 were examined. The ATR/MDEA plant showed better performances compared with SMR/MDEA both in terms of emissions cuts (81% vs. 74%) and costs ($35/ton vs. $71/ton).
Molburg and Doctor, 2003	Company	SMR	MDEA	Detailed simulations were carried out on the SMR process with heat integration and MDEA capture technology using Aspen Plus. Sensitivity studies were addressed to operating pressure, S/C ratio and combustion air pre-heat.
Rostrup-Nielsen and Rostrup-Nielsen, 2002	Company	SMR	N/A	Steam methane reforming process was described accurately in relation to novel options such as the membrane reforming and the autothermal reforming: the latter could become competitive at very large-scale conversion.
Wu and Kuo, 2015	Academia	SMR	Oxy-combustion	Traditional SMR process with oxy-combustion capture was compared with a novel design involving a CO_2 reforming reactor between SMR and WGS: this process was more efficient from an energy utilisation viewpoint.
Montazer-Rahmati and Binaee, 2010	Academia	SMR	DGA	An existing hydrogen plant with CO_2 capture and a methanator was simulated and optimised in terms of maximisation of H_2 product and export steam flowrate. Sets of Pareto-optimal operating conditions were obtained.
Martinez et al., 2014	Academia	SMR	Ca/Cu Chemical looping	It was demonstrated that the use of more reactive reforming catalysts and higher oxidation temperatures for Cu improved the equivalent H_2 efficiency of the Ca/Cu looping process, resulting in 1.6 MJ/kg of CO_2 captured.
Ryden and Lyngfelt, 2006	Academia	SMR	Chemical looping	A new reactor was designed to capture CO_2 by chemical-looping combustion from SMR H_2 plant while operating below 900 ºC. In addition, this new process has potential to achieve higher selectivity

				towards H_2 than conventional plant.
Chiesa et al., 2008	Academia	SMR	Chemical looping	Intrinsic capture of CO_2 from SMR H_2 plant was made possible by a system consisting of three CL reactors equipped with Fe oxides. This process showed better environmental results due to the virtually complete CO_2 removal.

1.9 Carbon capture from hydrogen plants: Industrial perspective

In June 2010, the US Department of Energy (DOE) selected gas-specialty company Air Products to receive American Recovery and Reinvestment Act (ARRA) funding to design, construct and operate a system to capture CO_2 from two steam methane reformers located within the Valero refinery in Port Arthur, Texas. The CO_2 removal technology was retrofitted to the SMRs, which produce hydrogen to assist in the manufacture of petrochemicals and the production of cleaner burning transportation fuels by refinery customers on the Gulf Coast hydrogen pipeline network. The DOE is providing a total of $284 million or approximately 66% of the over $400 million project (Baade et al., 2012). The main objective of this CO_2 capture project is to demonstrate an advanced technology that captures and sequesters carbon dioxide emissions from large-scale industrial sources into underground formations.

Figure 1.12 is a block flow diagram for the project that illustrates how the CO_2 capture facility is integrated within the existing SMRs. The facility utilises a proprietary design CO_2 vacuum swing adsorption (VSA) system that is retrofitted to each of the two existing SMR trains (PA-1 and PA-2). Each VSA unit is designed to remove more than 90% of the CO_2 contained in the reformer PSA feed gas with a purity of >97%. Sweet syngas (CO_2 removed) is returned from the CO_2 VSA system to feed the existing SMR hydrogen PSAs. CO_2 produced from the VSA units is compressed and dried in a single train located at PA-2. The CO_2 is then delivered, via a 12-mile connector pipeline, to Denbury's Green Pipeline, Texas. The CO_2 will be piped 100–150 km before injection for EOR in Denbury's onshore operations. The

CO_2 will aid in recovering 1.6–3.1 million additional barrels of domestic oil annually. In June 2014, Air Products announced that it had successfully captured more than one million metric tons of CO_2 at Port Arthur.

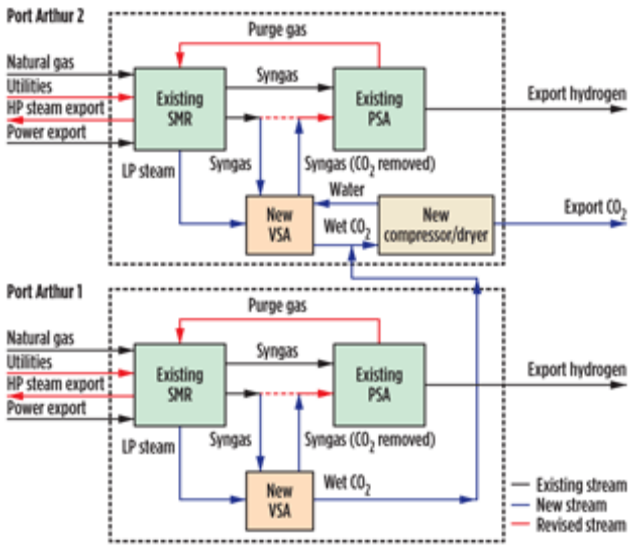

Figure 1.12: Block flow diagram of Port Arthur SMRs and integrated CO_2 capture facility (Baade et al., 2012)

1.10 The role of hydrogen in the future energy matrix

As discussed in the previous sub-sections, the production of hydrogen is both a sought after target and an appropriate environmental solution. Ultrapure hydrogen is commonly utilised as a feedstock in refineries as well as an energy carrier in fuel cells (Mormilan and Veziroglu, 2005).

It is very likely that most refining complexes will face a significant deficiency of their existing hydrogen production capacity. Hydrogen is needed for operating their hydrotreating desulfurisation process, which removes mainly sulfur and other impurities from raw petroleum products and hydrocracking units for upgrading low-grade heavy residues to more valuable diesel and lube base oil. The need for H_2 is bound to increase due to the trends of: 1) more stringent sulfur and nitrogen specifications in fuel oils; 2) increasing crack spread; and 3) the rapid change of crude oil properties from ‘light and sweet’ to ‘heavy and sour’. Due to the requirement of very high operational severity in both units for deep desulfurisation and improved product quality, ultrapure hydrogen with a purity of >99.99 mol%

should be utilised for the hydroprocessing. Accordingly, most refineries are forced to increase their hydrogen production capacities rapidly to cope with the increased H_2 demand, but it is doubtful that, given the upcoming carbon emission regulation, conventional steam methane reforming (SMR) H_2 processes would still be the best option to meet this demand.

A valid alternative to produce hydrogen is through coal gasification with CO_2 capture. Relative to coal gasification with CO_2 capture for power generation (IGCC), there are few studies in the public domain on those for H_2 production (NRC, 2004; Parsons, 2002; Gray and Tomlinson, 2003; Chiesa et al., 2005; Kreutz et al., 2005). With commercial technology, H_2 can be produced via coal gasification and CO_2 capture in a system similar to a coal IGCC plant with CO_2 capture. While synthesis gas can be produced by various routes, it is well-known that PSA is the only economically feasible, commercialised separation process to produce ultrapure hydrogen (99.99+ mol%) from a synthetic gas.

Recently, a novel process for cogenerating electricity and pure hydrogen from coal gasification where a Polybed PSA unit was integrated with an IGCC was investigated in detail (Luberti et al., 2014). Polybed PSA systems involve large number of columns undergoing different cycle steps and complex process schedules in order to exploit all the columns at the same time and to achieve crucial targets, such as the maximisation of product recovery and bed productivity.

1.11 Objectives of the thesis

Since climate change is a grave challenge that the world is facing today and coal is playing and will continue to play an important role in energy production globally, the development of efficient CO_2 capture technologies is urgently required in order to effectively meet the targets set for the CO_2 emission reduction. For decarbonised power production, IGCC power plants can be an attractive option for achieving this goal, since they have been reported to be more efficient and economical than PC-fired boiler power plants. Physical absorption has been attracting research interest for many decades as an effective technology, initially for acid gas removal but also for the recovery of CO_2 at a high purity for subsequent CO_2 storage or EOR. However, installing and running CO_2 capture processes gives

rise to significant energy loss to the power plants. Therefore, it is necessary to develop new and more efficient carbon capture process configurations to minimise the energy penalty involved. The development of automated tools that realistically represent the operation of an IGCC power plant in its entirety is essential to evaluate quickly and accurately the performance of the power plant. At the same time, the production of ultrapure hydrogen is an important and sought-after target to be utilised in either refineries or as an energy carrier in fuel cells. IGCC power plants can offer a clean and efficient way to cogenerate both hydrogen and electricity.

The aim of the thesis is to design a novel hydrogen PSA system integrated with a pre-combustion IGCC plant and to evaluate its integrated efficiency. The main objectives are:

- Detailed simulation of a dry coal-fed IGCC process with pre-combustion capture using a commercial steady-state simulator
- Development of a numerical simulator for a dynamic hydrogen PSA unit for process optimisation and scale-up
- Process design of an advanced IGCC plant integrated with a H_2 PSA unit for co-producing electricity and hydrogen where more than 90% of carbon from raw syngas can be captured using physical absorption
- Optimisation of the cogenerating IGCC plant through process flow modifications

Since there is the need to retrofit an H_2 PSA unit to the IGCC plant, this work will firstly investigate the overall IGCC process in order to rigorously obtain the info on the pressure, temperature and composition of the stream that will become the feed for the novel PSA system. This is due to the fact that H_2 PSA performance is highly affected by the CO conversion rate in the water gas shift reactors and the carbon capture rate in the Selexol unit. Compared to a conventional H_2 PSA unit applied to the SMR process, better purification performances are expected in this novel PSA because of the higher hydrogen partial pressure in the feed and the relatively lower amount of impurities. In the retrofitted advanced IGCC plant, the H_2-rich fuel gas coming from the CO_2 capture unit is split into two streams, one of which is fed to the

H_2 PSA unit. The H_2 PSA tail gas needs to be compressed up to the pressure of the H_2 fuel gas for feeding it to a high-pressure gas cycle for additional power generation.

Numerical simulations will be carried out using multi-column systems in order to meet the following specifications for hydrogen product:

- H_2 purity of 99.99+ mol%
- Maximisation of H_2 recovery so that H_2 recovery is at least higher than that in the Universal Oil Products (UOP) Polybed system applied to SMR (89%)
- Minimisation of energy consumption for the operation of the H_2 PSA tail gas compressor

The last two objectives are intrinsically related because the higher the hydrogen recovery is, the lower the off-gas flowrate to be recompressed will be. Through the integration of the IGCC with H_2 PSA it will be possible to optimise the whole process. A detailed economic analysis of the H_2 PSA unit will also be presented and discussed.

Given such a cogenerating plant where several units are fully integrated, another task of the present thesis relies on the improvement of the overall advanced IGCC performance. By investigating modified process flow schemes having in particular CO_2 capture and H_2 PSA units, it will be shown that it is possible to increase the H_2 yield and reduce the auxiliary power consumption at the carbon capture unit, allowing a higher net plant efficiency within the IGCC.

In order to carry out these simulations a considerable number of commercial and in-house software packages had to be employed. UniSim Design R400 steady state simulator (Honeywell, 2011) was used for the simulation of the whole IGCC plant including all the units with exception of the Claus plant. ProMax software (BR&E, 2011) was considered for this particular unit because UniSim does not allow to differentiate the various sulfur species. The dynamic simulations concerning the lab-scale H_2 PSA unit were performed with CySim in-house simulator (Friedrich et al., 2013) developed within the carbon capture group at The University of Edinburgh. Since CySim becomes unstable for high velocity regimes in the adsorption column, the industrial H_2 PSA unit simulations were carried out using a code in gPROMS

environment (PSE, 2010). Eventually, Origin 8.5 software (OriginLab, 2010) was employed for the fitting of experimental isotherms while column and adsorbent parameters were calculated utilising MATLAB (Mathworks, 2008).

1.12 Outline of the thesis

The present thesis is organised in six chapters, each with their own introduction and bibliography. Chapter 1 represents a general introduction to the thesis concerned with fossil fuels, global warming, CO_2 emissions, and carbon capture options and technologies, as well as the importance of ultrapure hydrogen in the future low-decarbonised energy matrix. The motive and the aim of the whole thesis are also revealed in detail.

Chapter 2 focuses on the modelling of integrated gasification combine cycles (IGCCs) with pre-combustion carbon capture. Each section of the plant is thoroughly described together with the simulation approach used for them. These sections include: Shell gasifier, water gas shift reactors (WGSRs), air separation unit (ASU), dual-stage Selexol unit, CO_2 compression train, Claus plant, gas turbine (GT) and heat recovery steam generation (HRSG). Simulation results are compared with the DOE report (2007) data while energy penalties associated with auxiliary units as well as plant efficiency are explained in detail.

Chapter 3 reports the fundamentals of adsorption and pressure swing adsorption processes. All the equilibrium and kinetic mechanisms are explained in depth as well as the mass, energy and momentum balances that govern the dynamic behaviour of an adsorption column. Industrial applications using PSA technology are also examined with particular emphasis on hydrogen purification applications.

Chapter 4 exhibits the design basis of a novel H_2 PSA integrated with an IGCC power plant. Numerical simulations are carried out in order to evaluate steady-state performances of various PSA designs with different numbers of adsorption beds and their associated step configurations. All these configurations are compared to each other in terms of hydrogen recovery and bed productivity at the same ultrapure hydrogen purity condition.

Chapter 5 describes how to integrate the H_2 PSA with the IGCC plant for cogenerating power and hydrogen from coal. A detailed economic analysis of the

entire cogenerating plant is reported with particular emphasis on the H_2 PSA unit. Innovative process configurations based on a recent patent application are also presented in order to improve the overall plant performance.

Chapter 6 summarises the results and conclusions of the previous chapters and proposes guidelines for future work.

References

Ahn H, Luberti M, Liu Z, Brandani S. Process configuration studies of the amine capture process for coal-fired power plants. Int. J. Greenh. Gas. Con. 2013; 16: 29-40.

Aroonwilas A, Chakma A, Tontiwachwuthikul P, Veawab A. Mathematical modelling of mass-transfer and hydrodynamics in CO_2 absorbers packed with structured packings, Chemical Engineering Science 2003; 58: 4037-4053.

Astarita G, Savage DW, Bisio A. Gas treating with chemical solvents. Chapter 9: Removal of carbon dioxide. 1983; New York, USA.

Audus H, Kaarstad O, Kowal M. Decarbonisation of fossil fuels: Hydrogen as an energy carrier. Proceedings of the 11th World Hydrogen Energy Conference 1996; Frankfurt, Germany.

Baade W, Farnand S, Hutchinson R, Welch K. CO_2 capture from SMRs: A demonstration project. Hydrocarbon Processing 2012; Special report: 63-68.

Barchas R, Davis R. The Kerr-McGee / ABB Lummus crest technology for the recovery of CO_2 from stack gases. Energy Conversion and Management 1992; 33: 333-340.

Bocciardo D, Ferrrari MC, Brandani S. Modelling and multi-stage design of membrane processes applied to carbon capture in coal-fired power plants. Energy Procedia 2013; 37: 932-940.

Bottoms RR. Organic bases for gas purification. Ind. Eng. Chem. 1931; 23: 501-504.

BR&E. ProMax, 2011.

Brandvoll O, Bolland O. Inherent CO_2 capture using chemical looping combustion in a natural gas fired power cycle. ASME Paper No. GT-2002-30129, ASME Journal of Engineering for Gas Turbines and Power 2004; 126: 316-321.

Chakma A. An energy efficient mixed solvent for the separation of CO_2. Energy Conversion and Management 1995; 36: 427-430.

Chapel DG, Mariz CL, Ernest J. Recovery of CO_2 from flue gases: commercial trends, paper No. 340 at the Annual Meeting of the Canadian Society of Chemical Engineering 1999; Saskatoon, Canada.

Chiesa P, Consonni S, Kreutz T, Williams R. Co-production of hydrogen, electricity and CO_2 from coal with commercially ready technology. Part A: Performance and emissions. Hydrogen energy 2005; 30: 747-767.

Chiesa P, Lozza G, Malandrino A, Romano M, Piccolo V. Three-reactors chemical looping process for hydrogen production. Int. J. of Hydrogen Energy 2008; 33: 2233–2245.

Cho P, Mattisson T, Lyngfelt A. Reactivity of iron oxide with methane in a laboratory fluidised bed – application of chemical-looping combustion. 7th International Conference on Circulating Fluidised Beds 2002; 599-606.

Central Intelligence Agency. The World Factbook; 2010.

Coates JF. Energy needs, choices, and possibilities scenarios to 2050: The global business environment. Technological Forecasting and Social Change 2002; 69: 527-531.

Committee on Climate Change, Chapter 5: Reducing emissions from buildings and industry through the 2020s; 2011.

Cormos CC. Renewable hydrogen production concepts from bioethanol reforming with carbon capture. Int. J. of Hydrogen Energy 2014; 39: 5597-5606.

Cousins A, Wardhaugh LT, Feron PHM. A survey of process flow modifications for energy efficient CO_2 capture from flue gases using chemical absorption. Int. J. Greenh. Gas. Con. 2011; 5: 605-619.

Cullinane JT, Rochelle GT. Carbon dioxide absorption with aqueous potassium carbonate promoted by piperazine, Greenhouse Gas Control Technologies 2003; Vol. II: 1603-1606.

Deb–Mondol J, Mcllven–Wright D, Rezvani S, Huang Y, Hewitt N. Techno-economic evaluation of advanced IGCC lignite coal fuelled power plants with CO_2 capture. Fuel 2009; 88: 2495-2506.

DECC. Final emissions estimates by fuel type and end-user sector; 2009.

Dillon, D J, Panesar R S, Wall A, Allam R J, White V, Gibbins J, Haines M R. Oxy-combustion processes for CO_2 capture from advanced supercritical PF and NGCC power plant. Proceedings of 7th International Conference on Greenhouse Gas Control Technologies. 2005; Volume I: 211-220.

DOE NETL. Cost and performance baseline for fossil energy plants; 2007.

DOE NETL. The impact of increased use of hydrogen on petroleum consumption and carbon dioxide emissions; 2008.

DOE NETL. An integrated strategic plan for the research, development, and demonstration of hydrogen and fuel cell technologies; 2010.

Dufour J, Serrano DP, Galvez JL, Moreno J, Garcia C. Life cycle assessment of processes for hydrogen production. Environmental feasibility and reduction of greenhouse gases emissions. Int. J. of Hydrogen Energy 2009; 34: 1370-1376.

EIA. Hydrogen production and storage – R&D priorities and gaps; 2006.

Emun F, Gadalla M, Majozi T, Boer D. Integrated gasification combined cycle (IGCC) process simulation and optimization. Computers and Chemical Engineering 2010; 34: 331-338.

Encyclopedia of Energy. 2004; Volumes 1-6.

EPA. Technical support document for the petroleum refining sector: proposed rule for mandatory reporting of greenhouse gases; 2008.

Evers AA. Actual worldwide hydrogen production. Hannover FAIR Presentation; 2008.

Feron PHM. Membranes for carbon dioxide recovery from power plants. In Carbon Dioxide Chemistry: Environmental Issues 1994; 236-249.

Friedrich D, Ferrari MC, Brandani S. Efficient simulation and acceleration of convergence for a dual piston pressure swing adsorption system. Ind. Eng. Chem. Res. 2013; 52: 8897-8905.

Freedonia Group, Inc. World hydrogen; 2014.

Gray D, Tomlinson G. Hydrogen from coal. Mitretek Technical Paper MTR-2003-13, prepared for the National Energy Technology Laboratory, US DOE; 2003.

Hendriks CS. Carbon dioxide removal from coal-fired power plants, Dissertation, Utrecht University 1994; Utrecht, The Netherlands.

Hendriks CS, Blok K, Turkenburg WC. The recovery of carbon dioxide from power plants. Proceedings of the Symposium on Climate Change 1989; Utrecht, The Netherlands.

Herzog H, Golomb D, Zemba S. Feasibility, modeling and economics of sequestering power plant CO_2 emissions in the deep ocean. Environmental Progress 1991; 10: 64-74.

Herzog HJ. The economics of CO_2 capture. Proceedings of the 4th International Conference on Greenhouse Gas Control Technologies 1999; 101-106.

Hoffmann BS, Szklo A. Integrated gasification combined cycle and carbon capture: A risky option to mitigate CO_2 emissions of coal-fired power plants. Applied Energy 2011; 88: 3917-3929.

Honeywell. UniSim Design R400, 2011.

Horn FL, Steinberg M. Control of carbon dioxide emissions from a power plant (and use in enhanced oil recovery). Fuel 1982; 61: 415-422.

Institution of Gas Engineers and Managers. Hydrogen – Untapped energy ?; 2012.

IPCC. Annex B: Glossary of terms. 2008.

IPCC. Couplings between changes in the climate system and biogeochemistry. 2007.

IPCC. Special report on carbon dioxide capture and storage. 2005.

International Society of Beverage Technologists (ISBT). Carbon dioxide quality guidelines and analytical procedure bibliography; U.S. 2006.

Ishibashi M, Otake K, Kanamori S, Yasutake A. Study on CO_2 removal technology from flue gas of thermal power plant by physical adsorption method. Greenhouse Gas Control Technologies 1999; 95-100.

Ishida M, Jin H. A New advanced power-generation system using chemical-looping. Combustion Energy 1994; 19: 415-422.

Jacob D. Introduction to atmospheric chemistry. Princeton University Press 1999; Princeton, USA.

Kikkinides ES, Yang RT, Cho SH. Concentration and recovery of CO_2 from flue gas by pressure swing adsorption. Ind. Eng. Chem. Res. 1993; 32: 2714-2720.

Ko D, Siriwardane R, Biegler LT. Optimization of a pressure swing adsorption process using zeolite 13X for CO_2 sequestration. Ind. Eng. Chem. Res. 2003; 42: 339-348.

Kohl AO, Nielsen RB. Gas purification, Gulf Publishing Co., 1997; Houston, USA.

Kreutz T, Williams R, Chiesa P, Consonni S. Coproduction of hydrogen, electricity and CO_2 from coal with commercially ready technology. Part B: Economic analysis. Hydrogen Energy 2005; 30: 769-784.

Lackner KS. Climate change: a guide to CO_2 sequestration. Science 2003; 300: 1677-1678.

Leites IL, Sama DA, Lior N. The theory and practice of energy saving in the chemical industry: some methods for reducing thermodynamic irreversibility in chemical technology processes. Energy 2003; 28: 55-97.

Linsday I, Lowe C, Reddy S, Bhakta M, Balkenende S. Designing a climate friendly hydrogen plant. Energy Procedia 2009; 1: 4095-4102.

Liu Z, Grande C, Li P, Yu J, Rodrigues AE. Multi-bed vacuum pressure swing adsorption for carbon dioxide capture from flue gas. Sep. Purif. Technol. 2011; 81: 307-317.

Luberti M, Friedrich D, Brandani S, Ahn H. Design of H_2 PSA for cogeneration of ultrapure hydrogen and power at an advanced integrated gasification combined cycle with pre-combustion capture. Adsorption 2014; 20: 511-524.

Martizez I, Romano MC, Fernandez JR, Chiesa P, Murillo L, Abanades JC. Process design of a hydrogen production plant from natural gas with CO_2 capture based on a novel Ca/Cu chemical loop. Applied Energy 2014; 114: 192-208.

Mastandrea MD, Schneider SH. Probabilistic assessment of "dangerous" climate change and emissions scenarios. International Symposium on Stabilisation of Greenhouse Gases 2005; Exeter, UK.

Mathworks. MATLAB, 2008.

Mimura T, Simayoshi H, Suda T, Iijima M, Mitsuoka S. Development of energy saving technology for flue gas carbon dioxide recovery in power plant by chemical absorption method and steam system. Energy Conversion and Management 1997; 38: 57-62.

Mimura T, Satsumi S, Iijima M, Mitsuoka S. Development on energy saving technology for flue gas carbon dioxide recovery by the chemical absorption method and steam system in power plant, Greenhouse Gas Control Technologies 1999: 71-76.

Molburg JC, Doctor RD. Hydrogen from Steam-Methane Reforming with CO_2 Capture. 20th Annual International Pittsburgh Coal Conference 2003; Pittsburgh, USA.

Momirlan M, Veziroglu TN. The properties of hydrogen as fuel tomorrow in sustainable energy system for a cleaner planet. Int. J. of Hydrogen Energy 2005; 30: 795-802.

Montazer-Rahmati MM, Binaee R. Multi-objective optimization of an industrial hydrogen plant consisting of a CO_2 absorber using DGA and a methanator. Computers and Chemical Engineering 2010; 34: 1813-1821.

Mora C. The projected timing of climate departure from recent variability. Nature 2013; 502: 183–187.

Mueller-Langer F, Tzimas E, Kaltschmitt M, Peteves S. Techno-economic assessment of hydrogen production processes for the hydrogen economy for the short and medium term. Int. J. of Hydrogen Energy 2007; 32: 3797-3810.

Muradov NZ, Veziroglu TN. Designing a climate friendly hydrogen plant. Int. J. of Hydrogen Energy 2005; 30: 225-237.

Nature 2014. Available at www.natureworldnews.com

NRC. The hydrogen economy: Opportunities, costs, barriers, and R&D needs, Prepared by the Committee on Alternatives and Strategies for Future Hydrogen Production and Use; 2004.

Nsakala YN, Marion J, Bozzuto C, Liljedahl G, Palkes M, Vogel D, Gupta JC, Guha M, Johnson H, Plasynski S. Engineering feasibility of CO_2 capture on an existing US coal-fired power plant, Paper presented at First National Conference on Carbon Sequestration 2001; Washington DC, USA.

Ogden JM. Modelling infrastructure for a fossil hydrogen energy system with CO_2 sequestration. 6th Greenhouse Gas Control Technologies conference 2002; Kyoto, Japan.

OriginLab. Data analysis and graphing software. Origin 8.5, 2010.

Parsons Infrastructure and Technology Group, Inc. Hydrogen production facilities: Plant performance and cost comparisons. Final report, prepared for the National Energy Technology Laboratory, US DOE; 2002.

PSE Ltd. 2010; available at http://www.psenterprise.com.

Ratafia-Brown JA, Manfredo LM, Hoffmann JW, Ramezan M, Stiegel GJ. An environmental assessment of IGCC power systems. Proceedings of the 19th annual Pittsburgh Coal Conference; 2002.

Richter HJ, Knoche K. Reversibility of combustion processes, efficiency and costing - second law analysis of processes, ACS Symposium series 1983; 235: 71-85.

Riemer PWF, Ormerod WG. International perspectives and the results of carbon dioxide capture disposal and utilisation studies. Energy Conversion and Management 1995; 36: 813-818.

Rostrup-Nielsen JR, Rostrup-Nielsen T. Large-scale hydrogen production. 6th World Congress of Chemical Engineering 2001; Melbourne, Australia.

Rubin ES, Rao AB. Uncertainties in CO_2 capture and sequestration costs. Greenhouse Gas Control Technologies, Proceedings of the 6th International Conference on Greenhouse Gas Control Technologies 2003.

Ryden M, Lyngfelt A. Using steam reforming to produce hydrogen with carbon dioxide capture by chemical-looping combustion. Int. J. of Hydrogen Energy 2006; 31: 1271–1283.

Sander MT, Mariz CL. The Fluor Daniel® Econamine™ FG process: Past experience and present day focus. Energy Conversion Management 1992; 33: 341-348.

Schiffer HW. WEC energy policy scenarios to 2050. Energy Policy 2008; 36: 2464-2470.

SEPA. National air quality report; 2008.

Shilling N, Lee D. IGCC-Clean power generation alternative for solid fuels. Proceedings of the PowerGen Asia 2003 Conference 2003; Ho Chi Minh City, Vietnam.

Simbeck DR. A portfolio selection approach for power plant CO_2 capture, separation and R&D options. Proceedings of the 4th International Conference on Greenhouse Gas Control Technologies 1999.

Sircar S. Separation of multi-component gas mixtures 2009; US Patent No. 4171206.

Soltani R, Rosen MA, Dincer I. Assessment of CO_2 capture options from various points in steam methane reforming for hydrogen production. Int. J. of Hydrogen Energy 2014; 39: 20266–20275.

Takami KM, Mahmoudi J, Time RW. A simulated H_2O/CO_2 condenser design for oxy-fuel CO_2 capture process. Energy Procedia 2009; 1: 1443-1450.

Tarun CB, Croiset E, Douglas PL, Gupta M, Choudhury MHM. Techno-economic study of CO_2 capture from natural gas based hydrogen plants. Int. J. of Hydrogen Energy 2007; 1: 55-61.

Terrien P, Lockwood F, Granados L, Morel T. CO_2 capture from H_2 plants: implementation for EOR. Energy Procedia 2014; 63: 7861-7866.

Van der Sluijs JP, Hendriks CA, Blok K. Feasibility of polymer membranes for carbon dioxide recovery from flue gases. Energy Conversion Management 1992; 33: 429-436.

Wang L, Yang Y, Shen W, Kong X, Li P, Yu J, Rodrigues AE. CO_2 capture from flue gas in an existing coal-fired power plant by two successive pilot-scale VPSA units. Ind. Eng. Chem. Res. 2012.; 52: 7947-7955.

World Energy Outlook. International Energy Agency. 2004.

World Energy Outlook. International Energy Agency. 2013.

Wu W, Kuo PC. Conceptual designs of hydrogen production, purification, compression and carbon dioxide capture. Energy Conversion and Management 2015; 103: 73-81.

Yokoyama T. Japanese R&D on CO_2 capture. Greenhouse Gas Control Technologies, Proc. of the 6th International Conference on Greenhouse Gas Control Technologies 2003; 13-18.

Zafar Q, Mattisson T, Gevert B. Integrated hydrogen and power production with CO_2 Capture using chemical-looping reforming-redox reactivity of particles of CuO, Mn_2O_3, NiO, and Fe_2O_3 using SiO_2 as a support. Ind. Eng. Chem. Res. 2005; 44: 3485-3496.

Zheng XY, Diao YF, He BS, Chen CH, Xu XC, Feng W. Carbon dioxide recovery from Flue gases by ammonia scrubbing. Greenhouse Gas Control Technologies, Proc. of the 6th International Conference on Greenhouse Gas Control Technologies 2003; Kyoto, Japan.

Chapter 2: IGCC power plant design and simulation

There are 160 gasification plants operating already, with about 35 in planning (Minchener, 2005), producing electricity, ammonia, methanol and hydrogen. For power generation, initial projects were mainly based on coal feed but recently refinery waste has also been considered as an alternative feed (Wall, 2007). Since the technology was initially demonstrated in the 1980s, approximately 4 GW_e of IGCC power plants have been built globally. Most of them are fuelled by oil or petcoke and only less than 1 GW_e of the total was designed for coal (IEA CCC, 2005). Among the IGCC projects, all coal-based IGCCs have been subsidised, while the only Italian oil-based IGCC has been subsidised. Other polygeneration projects in Canada, the Netherlands and the United States, as well as an oil-based IGCC in Japan, have not been subsidised (Simbeck, 2001). IGCC has not yet been deployed more widely because of strong competition with the natural gas combined cycle (NGCC) wherever natural gas is readily available at low prices, because coal-based IGCC plants are more costly than pulverised coal fired steam-electric plants and because of their limited available number. IGCC availability has improved in recent years in commercial-scale demonstration units (Wabash River Energy, 2000; McDaniel and Hornick, 2002). Furthermore, the economics have become more favourable in the case of its application to industrial polygeneration or oil refineries and chemical plants where personnel are experienced with the chemical processes involved. The recent rise in natural gas prices in the USA has also triggered general interest in IGCCs (IPCC, 2005).

Gasification technologies can be classified into entrained flow, fluidised bed and moving bed gasifiers with respect to solid fluid dynamics, oxygen and air blown with respect to its oxidants, and dry or wet slurry fed with respect to the phase of the coal feed (Collot, 2002). The gasifier is the “heart” of the IGCC power plant. It is the part of the plant where coal is converted at high temperature and pressure into synthesis gas (syngas).

2.1 IGCC power plants in the literature

Recent literature is inundated of works related to IGCC power plants. Doctor et al. (1996) reported the evaluation of several commercially available CO_2 capture technologies that were incorporated into IGCC power plants for 90% carbon capture.

Chiesa and Consonni (1999) studied a Selexol process to recover 90% CO_2 in the shifted syngas and concluded that addition of the Selexol process would result in a 5–7% reduction in the LHV-based power efficiency and around 40% increase in the cost of electricity.

Haslbeck (2002) investigated the energy penalty involved in implementing CO_2 capture at two IGCC cases driven by Destec and Shell gasifiers, both of which have a net power output of 400 MW_e in the non-capture case. Selexol process was selected for CO_2 capture with an overall capture efficiency of 87%. In the Destec IGCC case, the net power output was reduced by 42 MW_e, which is equivalent to the decrease of plant thermal efficiency by 6.6%. In the Shell IGCC case, the net power output was reduced by 61 MW_e resulting in a 7.3% decrease of the plant thermal efficiency.

O'Keefe et al. (2002) studied a 960 MW_e (gross) IGCC power plant driven by a Texaco quench gasifier integrated with a Selexol unit for recovering 75% of the carbon that the coal feed contains.

In a study by Foster Wheeler (2003), various pre-combustion capture absorption processes were assessed for decarbonising a coal-based 750 MW_e (gross) IGCC. Several chemical solvents and physical solvents for H_2S removal and CO_2 capture were investigated to select the most suitable acid gas removal process and the best arrangement of the shift reactors. The carbon capture target in this study was 85%.

Cormos and Agachi (2012) compared key performance indicators of two coal-based power plants with and without carbon capture. The case studies evaluated the process performance of IGCCs of a scale of around 400–500 MW net power and those of PC boilers of a scale of 900–1000 MW net power at 90% overall carbon capture rate.

Padurean et al. (2012) proposed an optimised IGCC plant design integrated with CO_2 capture absorption processes using different solvents. By carrying out process simulations in Aspen Plus, they showed the performance results of the various cases in terms of overall energy consumption, CO_2-specific emissions, and net electric power output and plant efficiency. The paper presented IGCC designs with CO_2 capture at three different CO_2 capture efficiencies, 70%, 80% and 90%.

Maurstad et al. (2009) investigated the effect of coal quality on the performance of an IGCC power plant, such as net power efficiency and CO_2 emission factor based on net electricity production.

An IGCC power plant simulation with CO_2 capture was conducted by Ng et al. (2010) considering the different available gasification technologies. They showed that the cost of electricity (COE) from the heat-integrated decarbonised IGCC sites is significantly lower compared to IGCC sites without heat integration, making application of CCS in IGCC sites economically competitive.

Robinson and Luyben (2010) carried out process simulations of a GEE gasifier IGCC power plant with carbon capture and a hybrid IGCC/methanol plant in both steady-state and dynamic modes using Aspen Plus.

Bhattacharyya et al. (2010) carried out the most complete steady-state simulation in terms of units simulated in the plant for an GE gasifier-based IGCC power plant with carbon capture.

Jones et al. (2011) focused their study on various process configurations of air separation units (ASUs) in an IGCC power plant. They investigated the effect of ASU process configurations on its power consumption.

Zheng and Furinsky (2005) compared different types of gasifiers, including coal slurry and dry coal gasifiers for IGCC power plants. Among eight cases simulated, they demonstrated that the overall thermal efficiency varies within less than 0.5% but BGL gasifiers have better environmental performance.

Emun et al. (2010) optimised an IGCC power plant using Aspen Plus. The optimum design was obtained by a pinch analysis in order to reveal opportunities of heat integration among the units.

Huang et al. (2008) conducted a detailed techno-economic study on IGCC power plants integrated with CO_2 capture, including CO_2 transport and storage costs.

They found that the specific CO_2 transportation and storage cost depend strongly on the internal and external parameters, such as onshore and offshore pipelines.

Several papers investigated the cogeneration of power and ultrapure hydrogen using coal gasification, as discussed below.

Damen et al. (2006) performed a consistent comparison of state-of-the-art and advanced electricity and hydrogen production technologies with CO_2 capture using coal and natural gas. This study is useful in the sense that it gives a complete overview of electricity and hydrogen production technologies with CO_2 capture and standardised ranges in energetic and economic performance both in the short and longer term.

Chiesa et al. (2005) and Kreutz et al. (2005) published a two-part paper investigating performances, costs and prospects of using technologies ready for commercialisation to convert coal to hydrogen and electricity with CO_2 capture and storage.

Cormos et al. (2008) investigated a number of H_2 production plant configurations based on standard entrained-flow gasification processes producing hydrogen at pipeline pressure. The paper showed that the production of very pure hydrogen can be achieved in the least penalty in plant efficiency by the use of a raw syngas compressor between gasifier and shift reactors and by the use of CO_2 as a transport gas rather than N_2 in a dry feed gasifier.

Cormos (2010) focused on the evaluation of energy integration aspects for hydrogen and electricity co-production scheme based on coal gasification process with CCS. A system optimisation has been carried out, including heat and power integration among the main plant units and sensitivity analysis relating to ambient conditions.

IGCC power plants would experience different energy penalties involved in CO_2 capture depending on gasifier types. Conventional IGCC power plants with slurry coal-fed GE gasifiers typically have net plant efficiency on the HHV basis of around 38%. In the case of IGCC with carbon capture, this efficiency decreases approximately by 6%. An IGCC process with a Shell gasifier fed by dry coal has 41% net plant efficiency (HHV) without carbon capture but it ends up with 32% net plant efficiency when integrated with a dual-stage Selexol process for carbon capture

(DOE, 2007). Figure 2.1 shows the block flow diagram of the Shell IGCC with carbon capture.

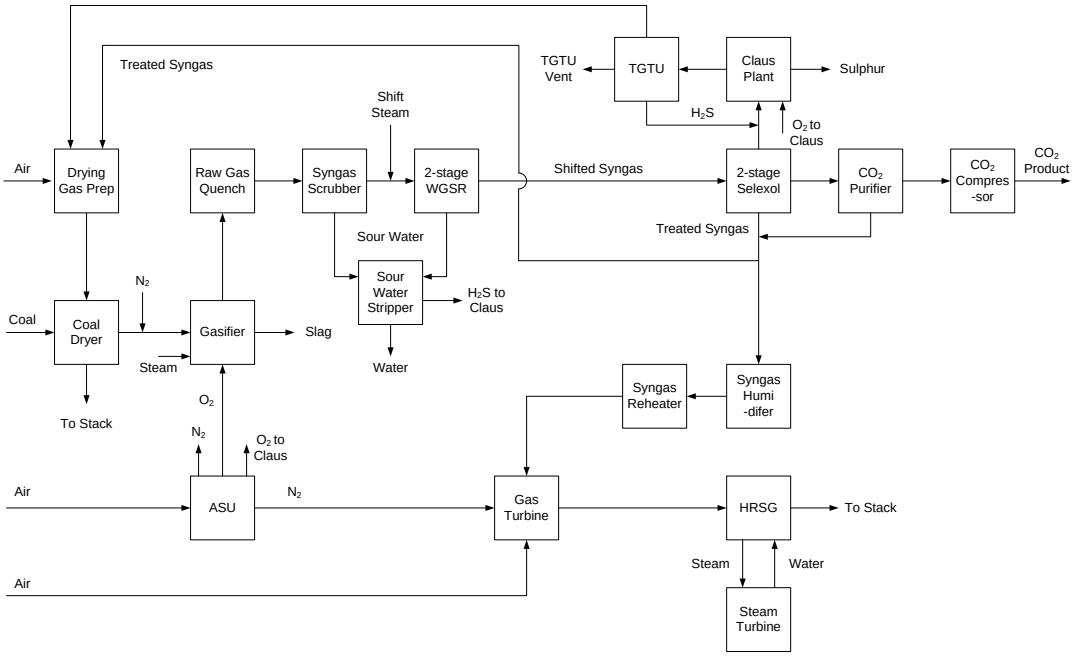

Figure 2.1: Block flow diagram of the Shell IGCC with carbon capture

2.2 Gasification process

Gasification is a chemical process of converting low-value solid feedstocks such as coal, oil refining residues or biomass, to synthesis gas with oxidants and moderators, aiming to produce high-value products (chemicals, electricity, clean synthetic fuels) (Figure 2.2). Gasification is partial oxidation, although steam is also supplied to the reactor in most processes. Fixed bed, fluidised bed or entrained flow gasifiers can be used. These can have very different characteristics with respect to oxidant (air or O_2), operating temperature (up to 1350 ºC), operating pressure (0.1–7 MPa), feed system (dry or water slurry), syngas cooling method (water quench or via radiative and convective heat exchangers) and gas clean-up systems. These alternative design options determine the fraction of feedstock converted to syngas, the syngas composition and the cost. The gasifier output contains CO, H_2, CO_2, H_2O and impurities (e.g., N_2, COS, H_2S, HCN, HCl, NH_3, CH_4, C_2+, volatile trace minerals and Hg) that must be managed appropriately.

As with any technology, widespread market penetration of gasification relies on economic conditions and enabling infrastructures that allow it to be competitive with other alternatives. For gasification, the largest potential market is electricity generation from coal, where IGCC power plants are being proposed with increasing frequency (Puigjaner, 2011).

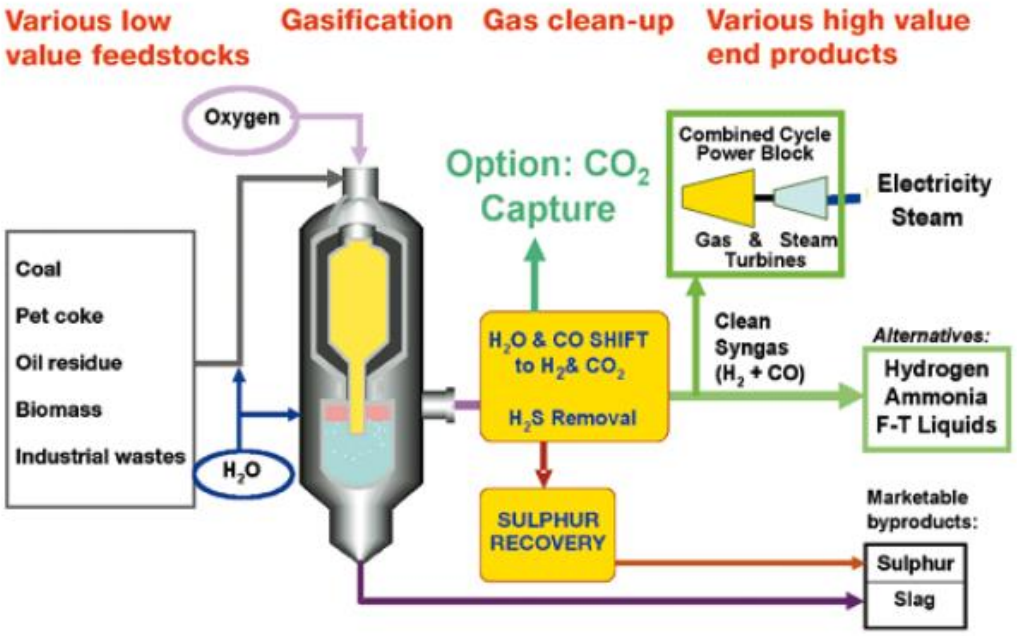

Figure 2.2: Simplified schematic of a gasification process showing options with CO_2 capture and electricity, hydrogen or chemical production (IPCC, 2005)

The gasification process takes place at temperatures in the range of 800 °C to 1800 °C. The reactor temperature depends on the characteristics of the feed, such as the softening and melting temperatures of the ash. Pyrolysis or devolatilisation followed by char gasification are the predominant reactions occurring in the gasifier, and are common for any type of gasifier feed. Over the whole temperature range described above, the reaction rates are high enough to make it possible to assume that modelling on the basis of the thermodynamic equilibrium of chemical reactions can generate results that approximate the performances actually observed in most commercial gasification reactors (Higman and van der Burgt, 2003).

The principal chemical reactions occurring during the gasification process are listed as follows. The combustion of carbon, CO and H_2 to form CO_2 and H_2O are described in eqns (2-1, 2-2 and 2-3). Carbon is also reacting with CO_2 to form CO by

reverse Boudouard reaction described by eq. (2-4). The carbon gasification reaction with steam is reported in eq. (2-5). Hydrogasification reaction (eq. (2-6)), water gas shift reaction (eq. (2-7)) and steam methane reforming reaction (eq. (2-8)) also occur.

$$C + \frac{1}{2}O_2 \Leftrightarrow CO \qquad \Delta H = -111 \text{ kJ/mol} \qquad (2\text{-}1)$$

$$CO + \frac{1}{2}O_2 \Leftrightarrow CO_2 \qquad \Delta H = -283 \text{ kJ/mol} \qquad (2\text{-}2)$$

$$H_2 + \frac{1}{2}O_2 \Leftrightarrow H_2O \qquad \Delta H = -242 \text{ kJ/mol} \qquad (2\text{-}3)$$

$$C + CO_2 \Leftrightarrow 2CO \qquad \Delta H = +172 \text{ kJ/mol} \qquad (2\text{-}4)$$

$$C + H_2O \Leftrightarrow CO + H_2 \qquad \Delta H = +131 \text{ kJ/mol} \qquad (2\text{-}5)$$

$$C + 2H_2 \Leftrightarrow CH_4 \qquad \Delta H = -75 \text{ kJ/mol} \qquad (2\text{-}6)$$

$$CO + H_2O \Leftrightarrow CO_2 + H_2 \qquad \Delta H = -41 \text{ kJ/mol} \qquad (2\text{-}7)$$

$$CH_4 + H_2O \Leftrightarrow CO + 3H_2 \qquad \Delta H = +206 \text{ kJ/mol} \qquad (2\text{-}8)$$

The operation temperatures of coal gasifiers are generally so high that the formation of C_2+ hydrocarbons, including tar, can be suppressed (Higman and van der Burgt, 2003).

2.3 Gasification technologies

For the gasification process, several types of reactors have been used. These reactors can be generally classified into one of the following three categories: moving bed, fluidised bed and entrained flow. Some characteristics of the aforementioned gasifiers are summarised in Table 2.1.

Moving-bed gasifiers utilise lump coal as the feed: coal feed moves slowly down the bed under the effect of gravity and gasification occurs with the oxidant flowing counter-currently. Heat and mass transfer is promoted in fluidised bed gasifiers due to good mixing between the coal and the oxidant inside the reactor. The size of the particles in the feed is a significant factor affecting the operation of the fluidised bed gasifiers. In the entrained-flow gasifiers, the feed and the oxidant flow

concurrently along the reactor. Entrained-flow gasifiers operate at high temperatures to ensure good carbon conversion. Entrained-flow gasifiers have fundamental environmental advantages over fluidised bed and moving-bed gasifiers. They produce no hydrocarbon liquids, and the only solid waste is an inert slag. The dry feed entrained-flow gasifiers also have minor environmental advantages over the slurry feed entrained-flow gasifiers. They produce a higher H_2S/CO_2 ratio acid gas, which improves sulfur recovery and lessens some of the gray water processing and the fixed salts blowdown problems associated with slurry feeding. Gasification technology examined herein is the dry coal entrained flow technology developed by Shell.

Table 2.1: Categories of gasification processes (Simbeck et al., 1993)

	Moving-bed	**Fluidised-bed**	**Entrained-flow**
Typical process	Lurgi, BGL	Winkler, HTW, CFB, KRW, U-Gas	Shell, GE, E-Gas, GSP, KT
Feed rank	Any/High	Low/Any	Any
Outlet gas temperature	425–650 °C	900–1050 °C	1200–1600 °C
Oxidant demand	Low	Moderate	High
Steam demand	High/Low	Moderate	Low

2.4 Shell gasifier description and modelling

Development of the Shell gasification process for partial oxidation of oil began in the early 1950s. More than 75 commercial Shell partial oxidation plants have been built worldwide to convert a variety of hydrocarbons to carbon monoxide and hydrogen. However, it was not until 1972 that coal started to be used as a gasifier feed by Shell Internationale Petroleum Maatschappij B.V. Several pilot plants have been built and demonstration projects have led to useful experience and conclusions with regards to the quality of the coal used for the gasification as well as extensive environmental monitoring and side stream testing of different acid gas removal (AGR) technologies. Currently, Nuon IGCC power plant at Buggenum, in the

Netherlands, uses Shell technology for coal gasification (DOE, 2007). A schematic of the Shell gasifier is shown in Figure 2.3.

The key advantage of the Shell coal gasification technology is its lack of feed coal limitations. One of the major achievements of the Shell development program has been the successful gasification of a wide variety of coals ranging from anthracite to brown coal. The dry pulverised feed system developed by Shell uses all coal types with essentially no operating and design modifications. The dry-fed Shell gasifier also has the advantage of lower oxygen requirements than comparable slurry-fed entrained flow gasifiers.

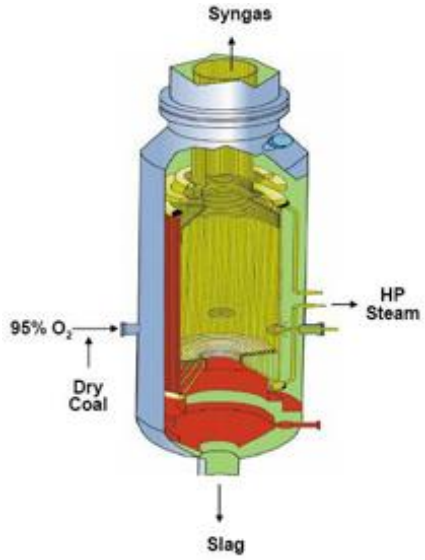

Figure 2.3: Shell gasifier schematic (DOE, 2007)

Characteristics desirable for coal considered for use in the Shell gasifier include moderate ash fusion temperature and relatively low ash content. High ash fusion temperature coals may require flux addition for optimal gasifier operation. The ash content, fusion temperature and composition affect the required gasifier operating temperature level, oxygen requirements, heat removal, slag management and maintenance. However, dry feeding reduces the negative effects of high ash content relative to slurry feed gasifiers.

Shell gasifier is simulated referring to Case 6 of the DOE report (DOE, 2007) and using the commercial software Honeywell UniSim Design R400 (Honeywell, 2011). A detailed flow scheme of the process, including mass and energy balances around the units, can be found in Appendix 1 of this thesis. After crushing, milling

and drying processes, Illinois No. 6 bituminous coal is fed to the gasifier with the properties shown in Table 2.2. The oxygen required for the gasification consists of 95% oxygen, 1.4% nitrogen and 3.6% argon, and is provided by the Elevated Pressure Air Separation Unit (EP ASU).

Table 2.2: Illinois No. 6 proximate and ultimate analysis (DOE, 2007)

Proximate Analysis	**w/w (%) As received**	**w/w (%) Dry**
Moisture	11.12	0.00
Ash	9.70	10.91
Volatile matter	34.99	39.37
Fixed carbon	44.19	49.72
Total	100	100
HHV, kJ/kg	27,113	30,506
LHV, kJ/kg	26,151	29,544
Ultimate Analysis	**w/w (%) As received**	**w/w (%) Dry**
Moisture	11.12	0.00
Carbon	63.75	71.72
Hydrogen	4.50	5.06
Nitrogen	1.25	1.41
Chlorine	0.29	0.33
Sulfur	2.51	2.82
Ash	9.70	10.91
Oxygen	6.88	7.75
Total	100	100

It is generally considered advantageous for gasification to occur under pressure. The reasons for this are potential savings in compression energy and reduction of equipment size (Higman and van der Burgt, 2003). It is therefore sensible to select the gasification pressure according to the requirements of the process and equipment upstream or downstream of the gasifier. Since the selected gas turbine (GE 7FA) for the case investigated requires a pressure of approximately 32 bar, the gasifier pressure should be chosen to be sufficiently higher than 32 bar

taking into account pressure losses at the units located between the gasifier and the gas turbine. The minimum operating temperature is generally set on the basis of the ash properties. Since the gasification process is assumed to operate at approximately 42 bar and 1,427 °C, the syngas produced contains a low methane concentration, as also demonstrated by Figure 2.4.

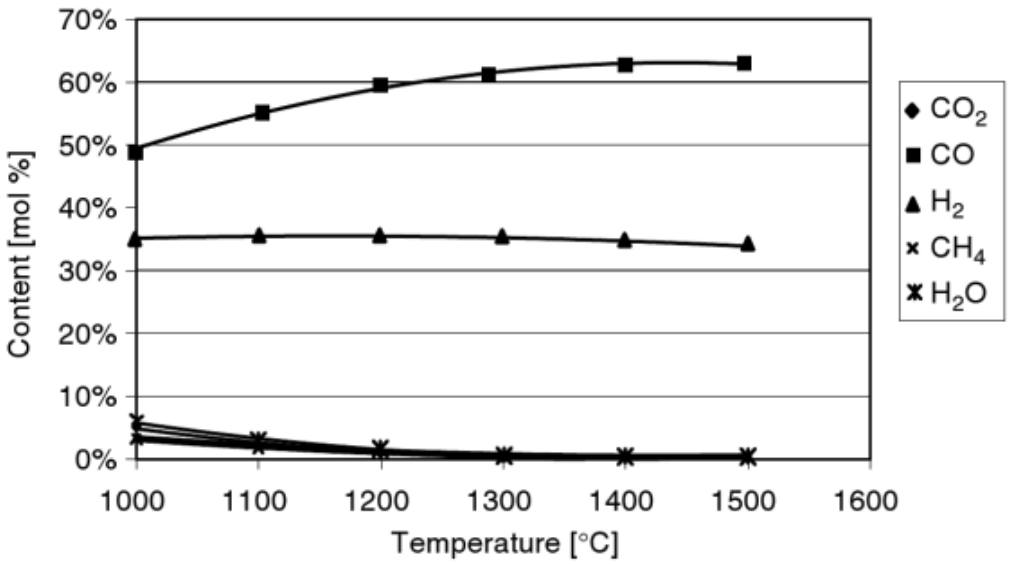

Figure 2.4: Variation of syngas composition with temperature at 40 bar (Higman and van der Burgt, 2003)

The gasifier was modelled as a "Conversion" reactor in UniSim Design R400 with Peng–Robinson EOS to account for non-ideality resulting from the high pressure of the gasifier (Kapetaki et al., 2013). It was assumed that the following reactions additionally take place in the gasifiers as well as eqns (2.1)-(2.8):

$$2C + 2S + O_2 \Leftrightarrow 2COS \quad (2\text{-}9)$$

$$S + H_2 \Leftrightarrow H_2S \quad (2\text{-}10)$$

$$Cl_2 + H_2 \Leftrightarrow 2HCl \quad (2\text{-}11)$$

$$N_2 + 3H_2 \Leftrightarrow 2NH_3 \quad (2\text{-}12)$$

The conversion rate of each reaction was carefully estimated to reproduce the composition of the syngas at the outlet of the gasifier, as detailed in the DOE report (2007).

Based on this model, the syngas composition estimated for the gasifier is reported in Table 2.3. The simulated values perfectly match with the DOE report results.

The carbon conversion is defined as:

$$\text{Carbon conversion (\%)} = \left[1 - \left(\frac{\text{Carbon in slag}}{\text{Carbon in feed}}\right)\right] \text{x}100 \qquad (2\text{-}13)$$

With an O_2/Coal ratio of 0.827 $kg_{O2}/kg_{drycoal}$, the total carbon conversion is evaluated at 99.5%, resulting in a H_2/CO fraction of 0.51.

Table 2.3: Validation of the simulation approach with DOE (2007) data for Shell gasifier

	Simulation	**DOE**
Ar	0.0097	0.0097
CH_4	0.0004	0.0004
CO	0.5720	0.5716
CO_2	0.0211	0.0211
COS	0.0007	0.0007
H_2	0.2900	0.2901
H_2O	0.0364	0.0364
H_2S	0.0081	0.0081
N_2	0.0574	0.0585
NH_3	0.0033	0.0033
O_2	0.0000	0.0000
SO_2	0.0000	0.0000
F (lb/h)	865,655	865,967
T (°F)	2,595	2,595
P (psia)	604.7	604.7

2.5 Gasifier and surroundings modification for carbon capture

The Shell gasifier and its ancillary units designed for non-capture mode are shown in Figure 2.5 and correspond to Case 5 of the DOE report (2007). High-temperature heat recovery is accomplished in three steps, including the gasifier jacket, which cools the syngas by maintaining the reaction temperature at 1427 °C. The product gas from the gasifier is cooled to 885 °C by adding cooled recycled fuel

gas to lower the temperature below the ash melting point. Gas then goes through a raw gas cooler, which lowers the gas temperature from 885 °C to 315 °C, and produces high-pressure steam for use in the steam cycle. The syngas is further cooled to 204 °C by heating water that is used to humidify the sweet syngas prior to the combustion turbine.

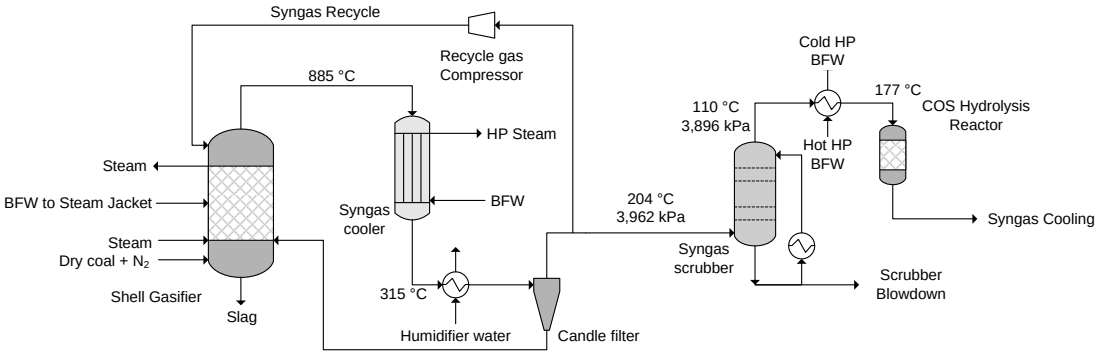

Figure 2.5: Shell Gasifier, syngas scrubber and COS hydrolysis reactor for non-capture mode (Kapetaki et al., 2013)

After passing through the raw gas cooler, the syngas passes through a cyclone and a raw gas candle filter where the majority of the fine particles are removed and returned to the gasifier with the coal fuel. About 45% of the raw gas from the filter is recycled back to the gasifier as quench gas. A single-stage compressor is utilised to boost the pressure of a cooled fuel gas stream from 40 bar to 42 bar to provide quench gas to cool the gas stream from the gasifier. The raw synthesis gas exiting the particulate filter then enters the scrubber for removal of chlorides and remaining particulate. The sour water stripper removes NH_3, SO_2, and other impurities from the waste stream of the scrubber. After the water scrubber, the gas is reheated to 177 °C and fed to the COS hydrolysis reactor. The COS in the sour gas is hydrolysed with steam over a catalyst bed to H_2S, which is more easily removed by the following AGR unit. If retrofitting a pre-combustion capture unit to an IGCC power plant, it can be expected that additional fuel would be fed to the gasifier in order to operate the same gas turbine. This is because the heating value of the fuel gas will be reduced due to the exothermic shift reaction so more coal should be fed to the gasifier to compensate the heat loss. The additional thermal input is almost equivalent to the difference of heat generated in the shift reaction. Moreover, the different H_2 and CO recovery in the AGR units between the non-capture and capture cases would also

affect the coal input increment. Some modifications are therefore essential for the Shell IGCC equipped for carbon capture, as reported in Figure 2.6.

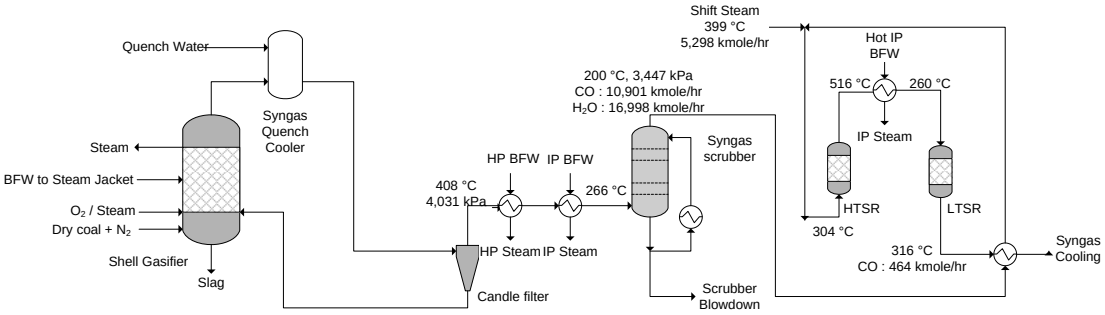

Figure 2.6: Shell Gasifier, syngas scrubber and water gas shift reactors for carbon capture mode (Kapetaki et al., 2013)

The first change is due to the requirement to cool down the raw syngas, making use of quench water instead of using the syngas recycle in the non-capture Shell IGCC. In non-capture Shell IGCC, the syngas recycle reduces the syngas temperature to 885 °C, which facilitates the operation of the syngas cooler at a lower temperature. In carbon capture Shell IGCC, however, the syngas is cooled by water quench, which sacrifices most high pressure (HP) steam generation but enriches the syngas with water for subsequent shift reaction. This change is beneficial in that the amount of shift steam injection can be drastically reduced. The amount of water quench and its temperature is determined so that the syngas at the syngas scrubber outlet is saturated with water at 200 °C. In this case, heat recovery is obtained beyond the gasifier jacket by means of two heat exchangers located between the particulate filter and the syngas scrubber producing HP and IP steam. After the scrubber, the syngas is ready to be shifted in a two-stage WGS reactor.

2.6 Water gas shift reactors

While in the conventional IGCC power plants without CO_2 capture WGSRs are not required, this is not the case when the IGCC power plants operate in a carbon capture mode. The objective is to convert the CO of the syngas to H_2 and CO_2 by reacting it with water over a bed of catalyst, as already described by eq. (2-7):

$$CO + H_2O \Leftrightarrow CO_2 + H_2 \qquad \Delta H = -41 \text{ kJ/mol} \qquad (2\text{-}7)$$

Currently, there are two main classes of materials being used in industry as CO-shift catalysts: Fe-based and Cu-based. However, further developments of catalysts have been introduced and materials such as Co, Au and Pt can also be used, along with Pd-based membrane reactors (Mendes et al., 2010). The molar ratio of H_2O to CO was set approximately 2 to 1 (DOE, 2007). This adjustment is achieved by utilising intermediate pressure (IP) steam extracted from the steam cycle of the power plant.

As seen in Figure 2.6, the CO-shift sections consist of two fixed-bed reactors arranged in series: a high temperature shift reactor (HTSR) operating at 516 °C and a low temperature shift reactor (LTSR) operating at 260 °C. The syngas after the scrubber is reheated to 285 °C and then steam is added. The two-stage WGSR results in 95.7% overall conversion of the CO to CO_2. In the simulation, adiabatic equilibrium reactors (Gibbs reactors) were used in UniSim Design R400, considering methane as an inert gas (Salazar et al., 2011) and allowing the simulator to calculate the conversion rates at the given conditions.

The HTSR product is cooled before entering the LTSR to recover the exothermic heat by generating steam. The heat exchanger is located after the HTSR to produce IP steam from the BFW. The IP steam is subsequently injected into the syngas for the shift reaction. The warm syngas from the second stage of the WGS is cooled to 241 °C by preheating the syngas prior to the first stage of WGS. The WGS catalyst also serves to hydrolyse COS, thus eliminating the need for a separate COS hydrolysis reactor. Following the second stage of WGS, the syngas is further cooled to 35 °C prior to the AGR unit.

2.7 Air separation unit

The very large quantities of oxygen required for CO_2 capture using the techniques of oxy-fuel combustion and pre-combustion de-carbonisation can only be economically produced, at present, by using the established process of oxygen separation from air by distillation at cryogenic temperatures (Latimer, 1967). This is a technology that has been used for over 100 years since the first air separation plant was built by Carl von Linde in 1902. Currently, there are three commercially available technologies for air separation, including pressure swing adsorption systems and membrane modules. Although cryogenic distillation is a mature

technology, there has been an average of twenty patents in the 1990s regarding this process (Thorogood, 1991). It is still indispensable in terms of high product purities and capacities, as shown in Figure 2.7 for nitrogen systems.

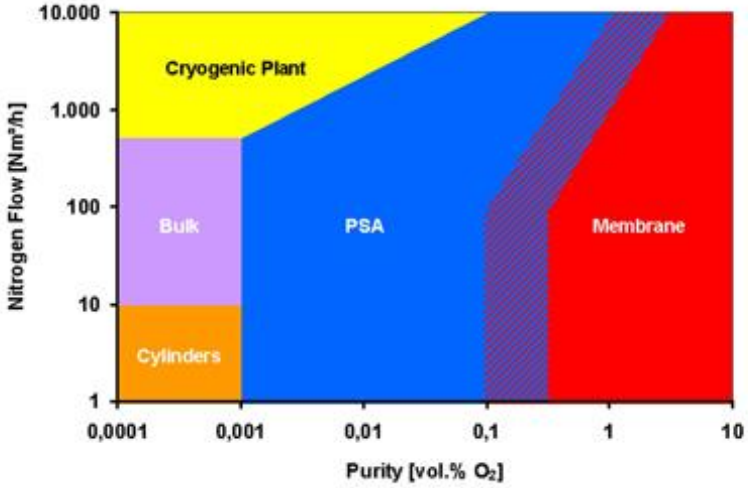

Figure 2.7: Technology comparison for nitrogen production systems

In a typical cryogenic air separation plant (Castle, 1991; Figure 2.8), air is compressed to a pressure of 5 to 6 bar and purified to remove water, CO_2, N_2O and trace hydrocarbons, which could accumulate to dangerous levels in oxygen-rich parts of the plant, such as the reboiler-condenser. Two or more switching fixed-bed adsorbers are used, which can be regenerated by either temperature or pressure swing, using in each case, a low-pressure waste nitrogen stream. The air is cooled against returning products (oxygen and nitrogen) in a battery of aluminium plate-fin heat exchangers and separated into pure oxygen and nitrogen fractions in a double distillation column, which uses aluminium packing.

Oxygen can be pumped as liquid and delivered as a high-pressure gas at up to 100 bar. Pumped oxygen plants have largely replaced the oxygen gas compression systems. They have virtually identical power consumptions but in a pumped cycle, a high-pressure air booster compressor provides a means of efficiently vaporising and heating the liquid oxygen stream to ambient temperature. Current plant sizes range up to 3500 t_{O2} d^{-1} and larger single train plants are being designed. Typical power consumption for the delivery of 95% O_2 at low pressure (1.7 bar, a typical pressure for an oxy-fuel application) is 200 to 240 kWh/t_{O2}. There are numerous process cycle

variations particularly for the production of oxygen at less than 97.5% purity, which have been developed to reduce power and capital cost. Note that adsorption and polymeric membrane methods of air separation are only economic for small oxygen production rates.

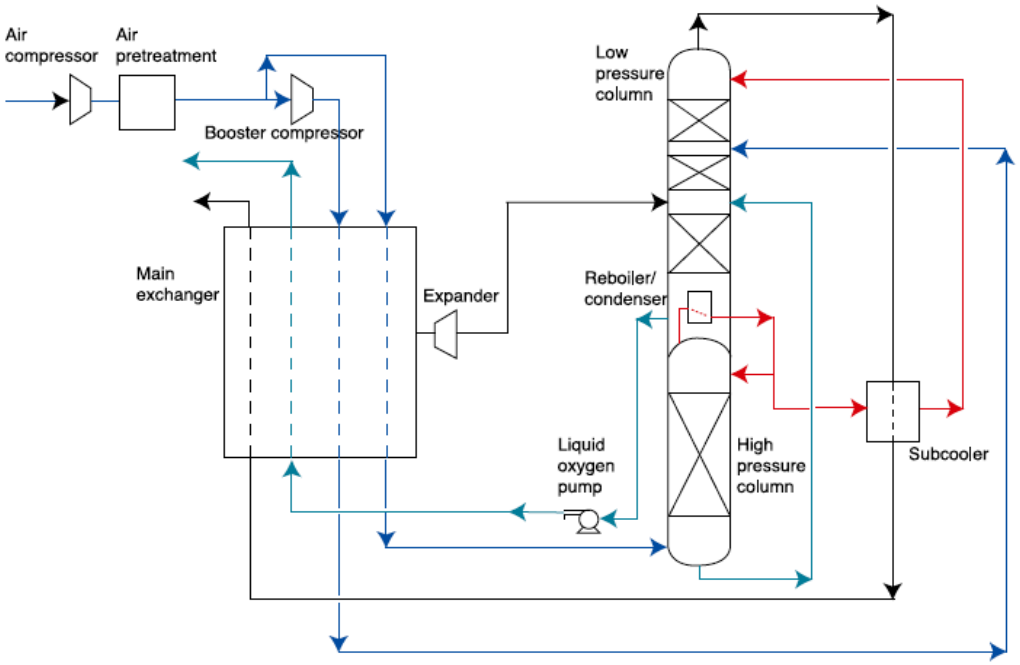

Figure 2.8: Cryogenic process for oxygen production by distillation of liquid air (Castle, 1991)

Cornelissen and Hirs (1998) conducted an exergy analysis on cryogenic air separation including an argon separation column. They showed that more than half of the exergy loss takes place in the liquefaction unit and almost one-third in the air compression unit. Fu and Gundersen (2012) studied ways to reduce power consumption in air separation units for oxy-combustion processes. They concluded that a significant improvement cannot be expected unless the flowsheet structures are improved considering, for example, the heat integration with a dual reboiler.

The air separation unit plays a key role in improving the efficiency, availability and operability of an IGCC power plant. An optimal integration between the ASU and the balance of the plant, especially the gasifier and the gas turbine, has significant potential for enhancing the overall plant efficiency. Considering the higher pressure of the gas turbine, an elevated-pressure air separation unit operating at 13.1 and 4.2 bar is usually favoured instead of the conventional low-pressure air

separation unit operating at 6.0 and 1.5 bar. Three product streams from the ASU are of interest for an IGCC plant: the oxygen stream with a purity of 95% is mainly used in the gasifier while a small portion of it goes to the Claus unit for combusting hydrogen sulfide. Nitrogen is produced in the ASU at two pressure levels. The majority of the low-pressure nitrogen is compressed and fed to the gas turbine as a fuel diluent for NO_X reduction and power augmentation in the gas turbine. A small fraction is used as a coal carrier for the Shell gasifier. The high-purity nitrogen at high pressure is also produced from the ASU and it is further compressed and directed to the gas turbine. Even though the power consumption in the oxygen and nitrogen compressors decrease in an elevated-pressure ASU, the power consumption in the main air compressor (MAC) increases to compensate. In addition, the higher operating pressure also decreases the relative volatility of oxygen and nitrogen, causing separation challenges.

The general scheme of the EP ASU adopted herein is based on Configuration 2 proposed by Jones et al. (2011) and is modified according to the simulation requirements. The simulation schematic of the process is shown in Figure 2.9.

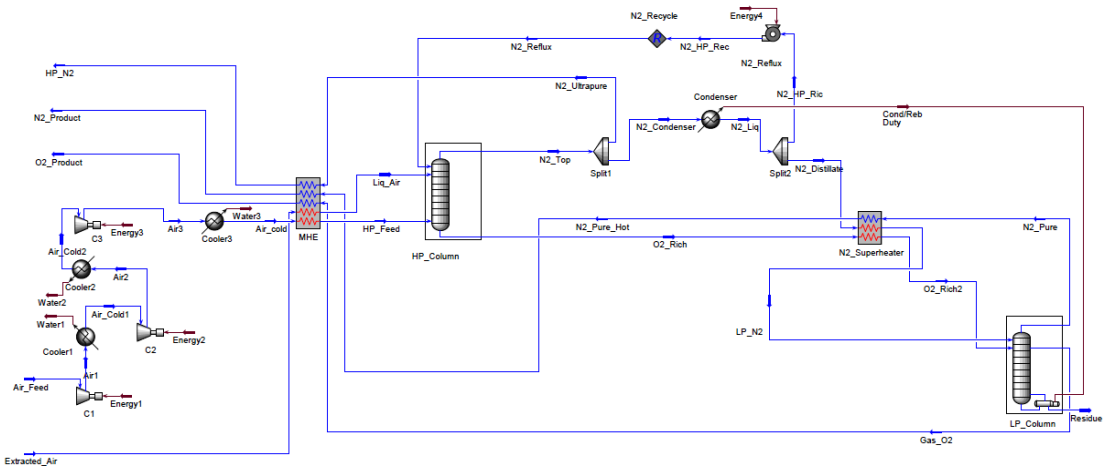

Figure 2.9: Simulation flowsheet of cryogenic air separation unit

The ASU consists of a multi-stream heat exchanger (main heat exchanger or MHE) that recovers refrigeration from the product streams and cools the incoming streams. Products leave the main heat exchanger at near ambient temperatures after refrigerating one air stream and, if applicable, liquefying another air stream and the

nitrogen reflux. Refrigerated air leaving the main heat exchanger is superheated by approximately 10 °C. The liquefied air stream, approximately 1% of total airflow, leaves the main heat exchanger as a saturated liquid. The refrigerated air stream is then sent to the bottom of the high-pressure column. The refrigerated air stream provides the boil-up for the HP column and the LP column via the coupled reboiler/condenser. The liquefied air stream is split with a portion being sent to the nitrogen superheater for subcooling with the remainder being sent to an intermediate stage of the HP column. The HP column, for this case, operates at a pressure of 13.1 bar. The HP column consists of 50 equilibrium stages. The HP column yields a crude liquid oxygen product (~34 mol% O_2) from the bottom and an ultra-pure, high-pressure gaseous nitrogen product from the top. The crude oxygen from the bottom and liquid nitrogen from the top of the HP column are subcooled in a multi-stream heat exchanger (nitrogen superheater) against the nitrogen vapour from the top of the LP column. The subcooled streams are sent to the LP column. The LP column operates at 4.2 bar and consists of 25 equilibrium stages. Both oxygen and nitrogen products are sent to the compressors for the related IGCC applications.

All simulation parameters and product specifications for the ASU are given in Table 2.4. It should be noted that the low-pressure nitrogen purity requirement is dependent on the fuel and combustor types used in the gas turbine. The EP-ASU process model was simulated using UniSim Design R400 and the Peng–Robinson equation of state. The oxygen and nitrogen produced are sufficient to accommodate the requirements of oxygen and nitrogen for the units within the IGCC. A detailed diagram including coal gasification and air separation unit is provided in Figure 2.10.

Table 2.4: Simulation parameters and product specifications for ASU simulation

Simulation parameter/product specification	Value
Compressors isentropic efficiency (%)	85
Air feed flowrate (kmol/h)	25,500
Liquefied air flowrate (kmol/h)	300
HP column pressure (bar)	13.1
LP column pressure (bar)	4.2
Condenser/reboiler duty (MW)	30.4
Compression energy (MW)	59.0
HP column reboiler temperature (°C)	-160.7
LP column reboiler temperature (°C)	-167.2
N_2 amount in the bleed stream (mol)	0.999
O_2 amount in oxygen product stream (mol)	0.950
N_2 amount in nitrogen product stream (mol)	0.981

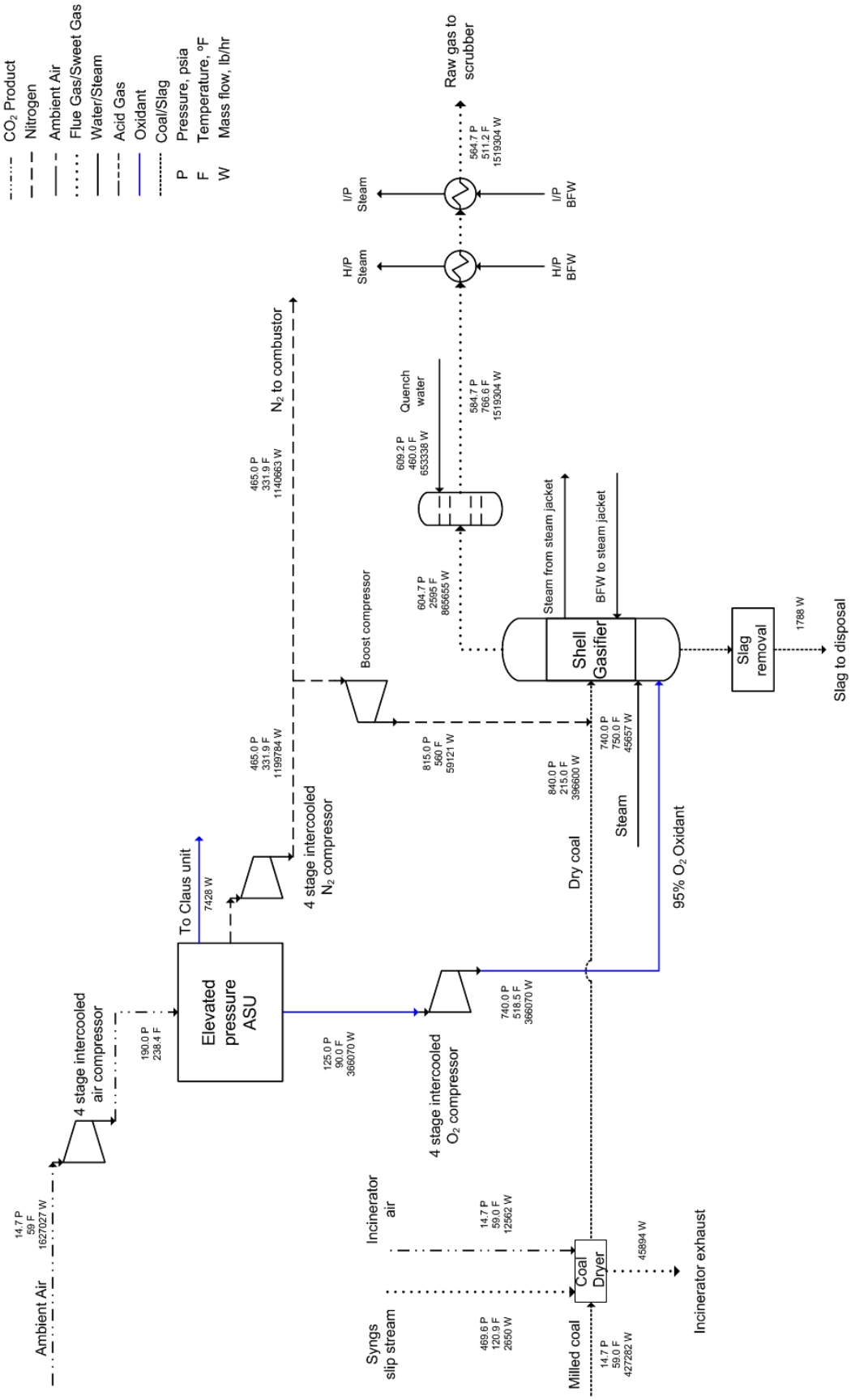

Figure 2.10: Coal gasification and air separation unit schematic (Kapetaki, 2015)

2.8 Dual-stage Selexol™

Since the partial pressure of acid gas in the syngas is generally high in IGCC power plants, physical solvents appear to be favourable as a CO_2 capture option. Like all physical solvents, dimethyl ether of polyethylene glycol (DEPG) or Selexol™ can be used for the absorption of the acid gases taking advantage of their high solubility into the solvent. Padurean et al. (2012) proposed a detailed study and optimisation of plant design (column height and packed dimensions) with the CO_2 capture process using different solvents of: aqueous solutions of alkanolamine, dimethyl ethers of polyethylene glycol, chilled methanol and *N*-methyl-2-pyrolidone. Simulation results show that for the solvents evaluated for CO_2 capture, the physical solvent, DEPG, is more energy efficient that the other physical and chemical solvents investigated. Robinson and Luyben (2010) proposed a scheme with the H_2S removal unit prior to WGSRs (sweet shift), while the CO_2 capture part is located downstream. Bhattacharyya et al. (2011) optimised the entire IGCC plant with CO_2 capture focusing on modelling assumptions, such as equilibrium tray calculations, in the Selexol absorbers.

DEPG is a mixture of dimethyl ethers of polyethylene glycol of the following chemical formula:

$CH_3O(C_2H_4O)_nCH_3$, with n being between 2 and 9

Compared to other solvents, DEPG has a higher viscosity, which reduces mass transfer rates and tray efficiencies and increases packing or tray requirements, especially at reduced temperatures. Since it is sometimes necessary to reduce the temperature to increase acid gas solubility and reduce the solvent circulation rate, this could be a disadvantage (Burr and Lyddon, 2008). Some physical properties of DEPG and other solvents are listed in Table 2.5.

Table 2.5: Properties of physical solvents (Ranke and Mohr, 1985)

Solvent	DEPG	PC	NMP	MeOH
Process name	Selexol or Coastal	Fluor Solvent	Purisol	Rectisol
Viscosity at 25 ºC (cP)	5.8	3.0	1.65	0.6
Density at 25 ºC (kg/m^3)	1,030	1,195	1,027	785
Molecular weight (g/mol)	280	102	99	32
Vapour pressure at 25 ºC (Pa)	0.097	11.3	53	16,700
Freezing point (ºC)	-28	-48	-24	-92
Boiling point at 1 atm (ºC)	275	240	202	65
Thermal conductivity (W/m/K)	0.19	0.21	0.16	0.21
Maximum operating temperature (ºC)	175	65	-	-
Specific heat at 25 ºC (kJ/kg/K)	2.05	1.4	1.68	2.37
CO_2 solubility at 25 ºC (m^3_{CO2}/m^3_{sol})	3.63	3.40	3.57	3.18

Typically, the Selexol process consists of two stages, where H_2S is removed prior to CO_2 and the regeneration of the solvent is achieved in two sections:

- In the stripper, by imposing a pressure drop along the column and steam extracted from the low pressure (LP) section of the power plant's steam cycle.
- By a series of pressure vessels downstream the CO_2 removal stage.

Probably one of the first detailed schemes for the dual-stage Selexol process was the one presented by Padurean et al. (2012), as shown in Figure 2.11.

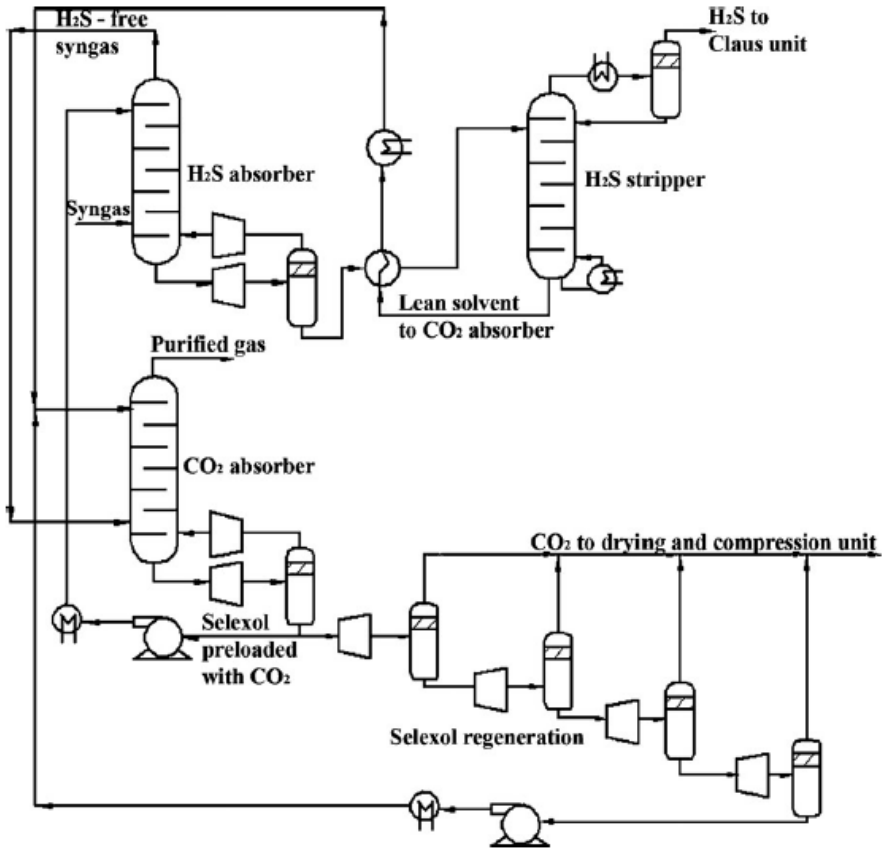

Figure 2.11: Selexol process flow diagram for acid gas removal (Padurean et al., 2012)

2.8.1 Thermodynamics of the process

Fluid phase equilibria are at the heart of unit operation calculations in Chemical Engineering and this also applies to the dual-stage Selexol process. In this case, we face a gas–liquid equilibrium that has to be solved by applying the iso-fugacity condition (Smith et al., 2005; Sandler, 1999). In IGCC power plants, since the operating pressures are elevated, non-idealities in the gas phase must be taken into account: this results in the evaluation of fugacity coefficients φ_i from a specific equation of state. By contrast, the solubility behaviour of the solute gas in physical solvents for the IGCC case conditions will closely approach Henry's law, with the acid gas loading in the solvent being proportional to the acid gas partial pressure (Sciamanna and Lynn, 1988; Xu et al., 1992; Henni et al., 2005). Therefore, the gas–liquid equilibrium can be expressed by:

$$f_i^G = f_i^L \tag{2-14}$$

$$Py_i\varphi_i^G = K_{i,s}x_i \quad (2\text{-}15)$$

where $K_{i,s}$ is the Henry's law constant for the gas i in the Selexol solvent.

The temperature dependency of the Henry's law constant for H_2S and CO_2 in Selexol has been reported in the literature (Xu et al., 1992) and it is illustrated in Table 2.6.

Table 2.6: Henry's law constants for H_2S and CO_2 in Selexol (Xu et al., 1992)

Temperature (°C)	Henry's law constant (MPa)	
	H_2S	CO_2
25	0.440	3.570
30	0.506	3.950
40	0.641	4.670
50	0.787	5.620
60	1.010	6.550

The enthalpy change from vapour to dissolved solute represents the heat of solution (or heat of absorption) and can be evaluated by the variation of the Henry's law constants with temperature. The correlation between the Henry's law constants and the heat of absorption can be represented by eq. (2-16) (Clausius–Clapeyron equation for gas–liquid equilibrium).

$$\frac{d\ln K}{dT} = \frac{\Delta H}{RT^2} \quad (2\text{-}16)$$

The enthalpy of absorption can be therefore calculated by the slope of a linear equation obtained by integrating eq. (2-16) with an assumption of constant heat of absorption, given the Henry constants at different temperatures. For H_2S and CO_2, the corresponding values are presented in Table 2.7.

Table 2.7: Standard heats of absorption for H_2S and CO_2 in Selexol (Xu et al., 1992)

Standard state heats of absorption (kJ/mol)	
H_2S	CO_2
19.1	14.3

Equilibrium solubility data for H_2S and CO_2 in various representative solvents have been reported in the DOE report (2007), as shown in Figure 2.12. This figure exhibits an order of magnitude higher solubility of H_2S over CO_2 at a given temperature, which enables the selective absorption of H_2S over CO_2 with physical solvents. It also illustrates that the acid gas solubility in physical solvents increases with lower solvent temperatures. Moreover, Table 2.8 shows the gas solubilities of some physical solvents relative to CO_2.

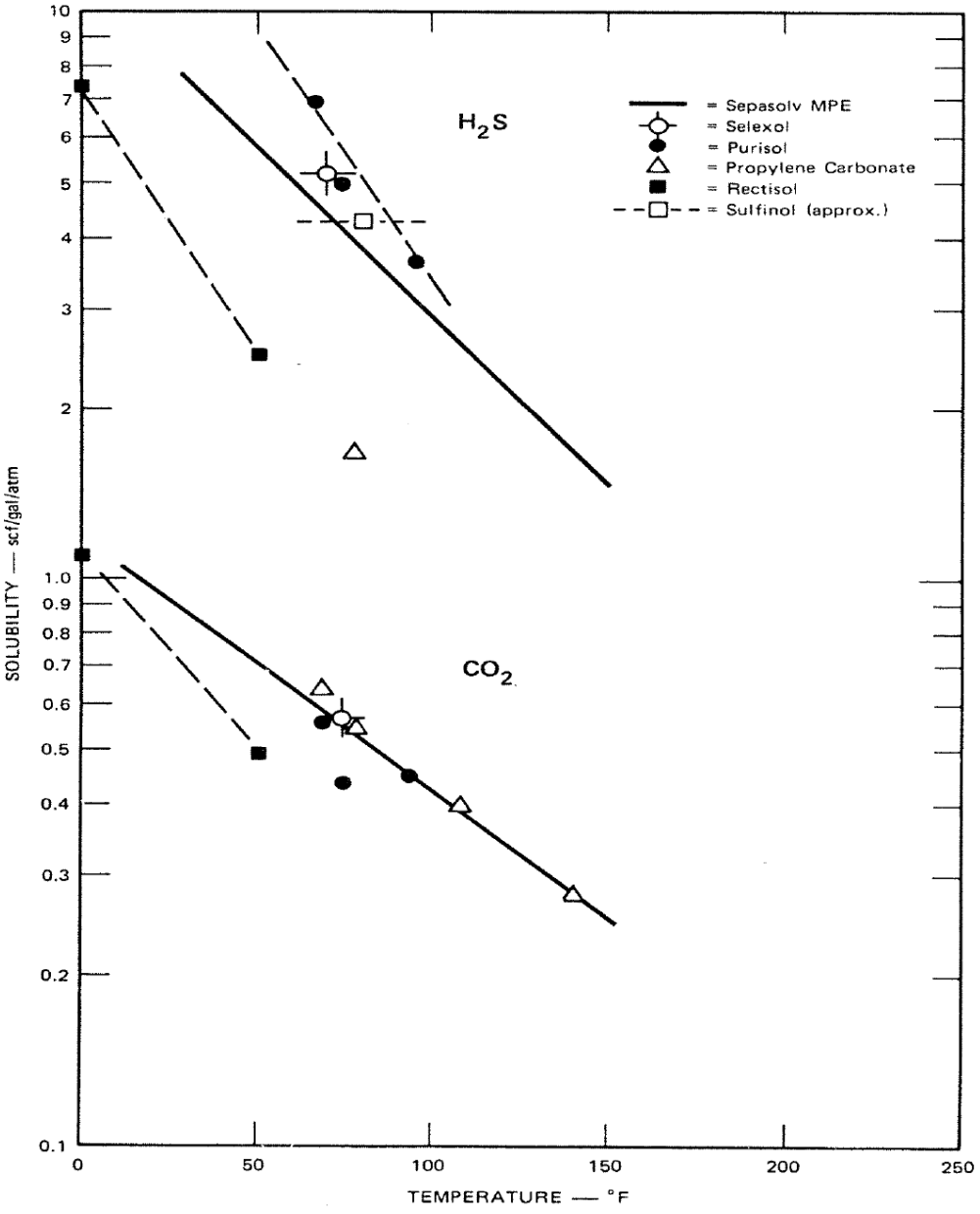

Figure 2.12: Gas solubilities of H_2S and CO_2 in physical solvents (DOE, 2007)

Table 2.8: Gas solubilities of some physical solvents relative to CO_2 (Burr and Lyddon, 2008)

Component	DEPG at 25 ºC	PC at 25 ºC	NMP at 25 ºC	MeOH at -25 ºC
CO_2	1.000	1.000	1.000	1.000
H_2	0.013	0.008	0.006	0.005
N_2	0.020	0.0084	-	0.012
O_2	-	0.026	0.035	0.020
CO	0.028	0.021	0.021	0.020
CH_4	0.420	0.038	0.072	0.051
NH_3	4.800	-	-	23.200
H_2S	8.820	3.290	10.200	7.060
H_2O	730.000	300.000	4,000.000	-
HCN	1,200.000	-	-	-

Some additional advantages for the application of DEPG in the Selexol process to gasification plants are listed below (Chen, 2005):

- A very low vapour pressure that limits its losses to the treated gas
- High chemical and thermal stability (no reclaiming or purge) because the solvent is a true physical solvent and does not react chemically with the absorbed gases
- Non-toxic for environmental compatibility and worker safety
- Non-corrosive for mainly carbon steel construction
- Non-foaming for operational stability
- Compatibility with gasifier feed gas contaminants
- High solubility for HCN and NH_3 allows removal without solvent degradation
- Low heat requirements for regeneration because the solvent can be regenerated by a simple pressure let down

2.8.2 Gas–liquid equilibrium in UniSim Design

The simulation of the two-stage Selexol process was conducted using UniSim Design R400. Although the software is sufficient to represent the unit operations involved in the process, particular effort was made to build a simulation tool that

would accurately represent the thermodynamic regime described previously and in particular the gas–liquid equilibrium of the shifted syngas components entering the Selexol process into the solvent. Despite the fact that the software allows for the simulation of chemical absorption using amines with a customised package (Amine package), there is no such facility when physical solvents are to be used. Therefore, the software database has to be calibrated accordingly to obtain an accurate prediction of the gas solubilities.

Initially, flash calculations were performed using the software to examine the predicted behaviour of the gas system in the DEPG solvent. Since the equilibrium calculations were far away from the experimental data reported in Table 2.6, calibration of the software was essential in order to produce a model capable of accurately representing the gas–liquid equilibrium of the acid gases in the DEPG solvent. For the gas phase, the Peng–Robinson equation of state was used, but since there is no option of imposing Henry's law explicitly, it was implemented indirectly by adjusting the software's database. In UniSim Design R400 the Henry's law constant can be described by eq. (2-17):

$$\ln K = A + \frac{B}{T} + C \cdot \ln T + D \cdot T^{E} \tag{2-17}$$

where T is the temperature in K.

The parameters A, B, C, D and E should be regressed so that the temperature dependency of the Henry's law is described correctly. Nevertheless, by integrating eq. (2-16), we obtain:

$$\ln K = -\frac{\Delta H}{RT} + const \tag{2-18}$$

Hence, the only parameters having a physical meaning are A, being the logarithm of the Henry's law constant at the reference temperature, and B, being the heat of absorption divided by the universal gas constant. Therefore, the parameters C, D and E are not required and were set as zero in the regression. Table 2.9 shows the original parameters in the UniSim database and the new regressed parameters. Figure 2.13 illustrates that after parameter regression, the simulation results were in good agreement with the experimental data reported in the literature. Once the gas–liquid equilibrium was described well, it was possible to move to the overall simulation of the dual stage Selexol process.

Table 2.9: Original and regressed parameters of Henry's law equation for acid gases in Selexol

	A	B	C	D	E
Original UniSim parameters					
CO_2	69.68	-3,892	-8.408	$1.07 \cdot 10^{-3}$	1
H_2S	37.84	-2,972	-3.395	$-3.15 \cdot 10^{-3}$	1
Regressed UniSim parameters					
CO_2	13.828	-1,719.99	0	0	0
H_2S	13.678	-2,297.20	0	0	0

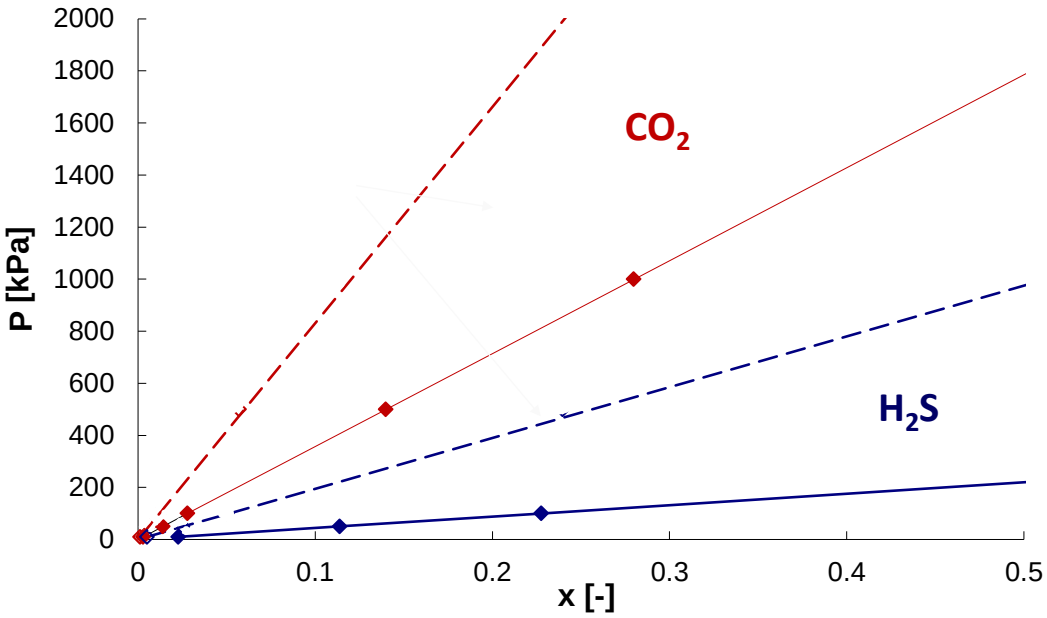

Figure 2.13: Solubilities of CO_2 and H_2S in Selexol solvent at 25 °C. The Y-axis reports the gas partial pressure while the X-axis reports the component mole fraction in the liquid phase. Dotted lines represent UniSim original curves, continuous lines represent UniSim regressed curves, dots represent experimental obtained values by Xu et al. (1992)

2.8.3 Proposed configuration

Several configurations have been proposed for the capture of CO_2 using DEPG in the Selexol process. In this section, the key point was to set the target for carbon capture rate to be achieved in the two-stage Selexol process. Additionally, very few

studies have presented a detailed scheme of the two-stage Selexol process incorporated for carbon capture.

EPRI and DOE reports (EPRI, 1987; DOE, 2007) suggested an integrated scheme for the two-stage Selexol process, which is shown in Figure 2.14. Both schemes operate in two solvent loops, which perform both the H_2S removal and the CO_2 capture stages. In the configuration described here, the gas product of the WGSRs enters the first absorber where H_2S is preferentially removed using solvent from the CO_2 absorber. The gas exiting the H_2S absorber passes through the second absorber where CO_2 is removed using regenerated solvent from the flash drums, combined with the thermally regenerated solvent from the bottoms of the stripping column. The clean gas exits the absorber and is sent either directly to the combustion turbine or is partially humidified prior to entering the combustion turbine depending on the gasification technology incorporated.

The CO_2-loaded solvent exits the CO_2 absorber and some of it is sent to the H_2S absorber, while the rest of the solvent is sent to a series of flash drums for regeneration. The gas from the first flash drum is recycled to the CO_2 absorber while the CO_2 product stream is obtained from the other two flash drums. After flash regeneration, the solvent is chilled and returned to the CO_2 absorber.

The rich solvent exiting the H_2S absorber enters the H_2S concentrator and partially flashes. The solvent exiting the H_2S concentrator is sent to a flash drum and while the gas stream is recycled to the H_2S absorber, the liquid product is sent to the stripper. The acid gas from the stripper is sent to the Claus plant for further processing. The lean solvent exiting the stripper is then cooled and recycled to the top of the CO_2 absorber.

This scheme is capable of capturing 90% of the carbon contained in the coal feed of the power plant. The H_2S recovery target of this configuration is set to 99.5% and at the same time the CO_2 product should have less than 10 ppm H_2S. The amount of hydrogen recovered from the syngas stream is dependent on the Selexol process design conditions. Herein, the hydrogen recovery is set at 99%. The degree of dilution is a parameter that has been investigated for the integrated two-stage Selexol process: the fresh solvent composition is 45% H_2O and 55% DEPG by mole.

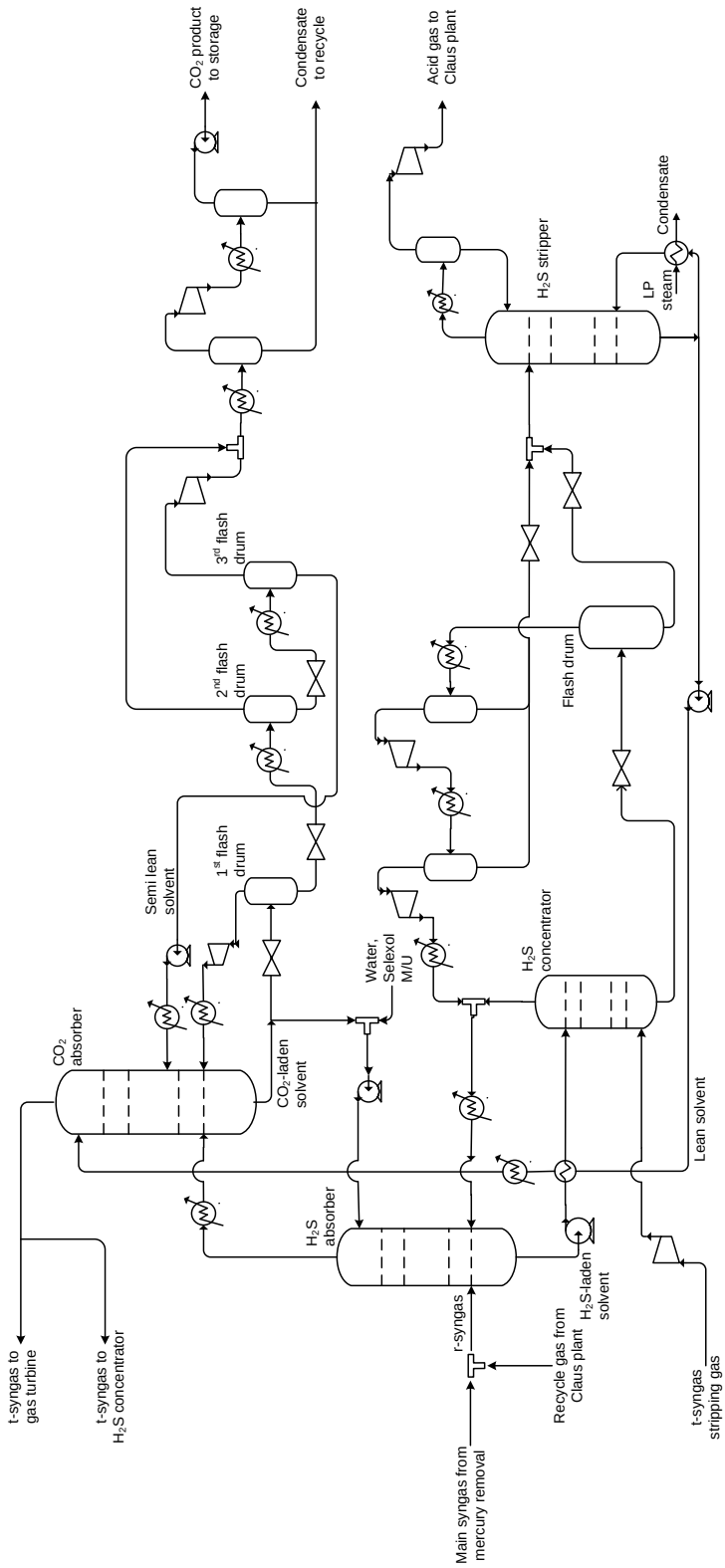

Figure 2.14: Simplified schematic of the integrated Selexol process (Kapetaki, 2015)

Table 2.10 shows the major components contributing to the energy consumption of the two-stage Selexol unit.

Table 2.10: Energy requirements for two-stage Selexol process

Simulation parameter	Value
H_2S stripper duty [MW_{th}]	14.60
CO_2 compression power [MW_e]	32.09
Auxiliary power consumption in dual-stage Selexol unit	
Total auxiliary power consumption [MW_e]	20.01
H_2S concentrator stripping gas compressor	0.14
1st flashed gas compressor	0.68
2nd flashed gas compressor	0.32
Gas compressor for recycle gas from 1st flash drum	0.74
H_2S-laden solvent pump	0.10
CO_2-laden solvent pump	0.04
Lean solvent pump	2.24
Semi-lean solvent pump	15.57
Sour gas compressor	0.20

2.9 CO_2 compression and dehydration

The CO_2-laden solvent leaving the CO_2 absorber is depressurised in stages in three flash drums in series operating at three pressure levels. Since the CO_2-laden solvent also contains a significant amount of hydrogen as well as CO_2, the vapour stream at the first HP flash drum is recycled to the CO_2 absorber to minimise H_2 losses to the CO_2 product pipeline. The HP CO_2 stream is flashed at 1.2 MPa, compressed and recycled back to the CO_2 absorber. The MP CO_2 stream is flashed at 0.35 MPa. The LP CO_2 stream is flashed at 0.11 MPa, compressed to 0.35 MPa and combined with the MP CO_2 stream. The combined stream is compressed from 0.35 MPa to a supercritical condition at 15.3 MPa using a multiple-stage, intercooled compressor. During compression, the CO_2 stream is cooled to 25 ºC. The final CO_2 product is dehydrated to a dew point of -40 ºC with triethylene glycol and reaches around 99% CO_2 purity. A detailed schematic of the syngas clean-up is reported in Figure 2.15.

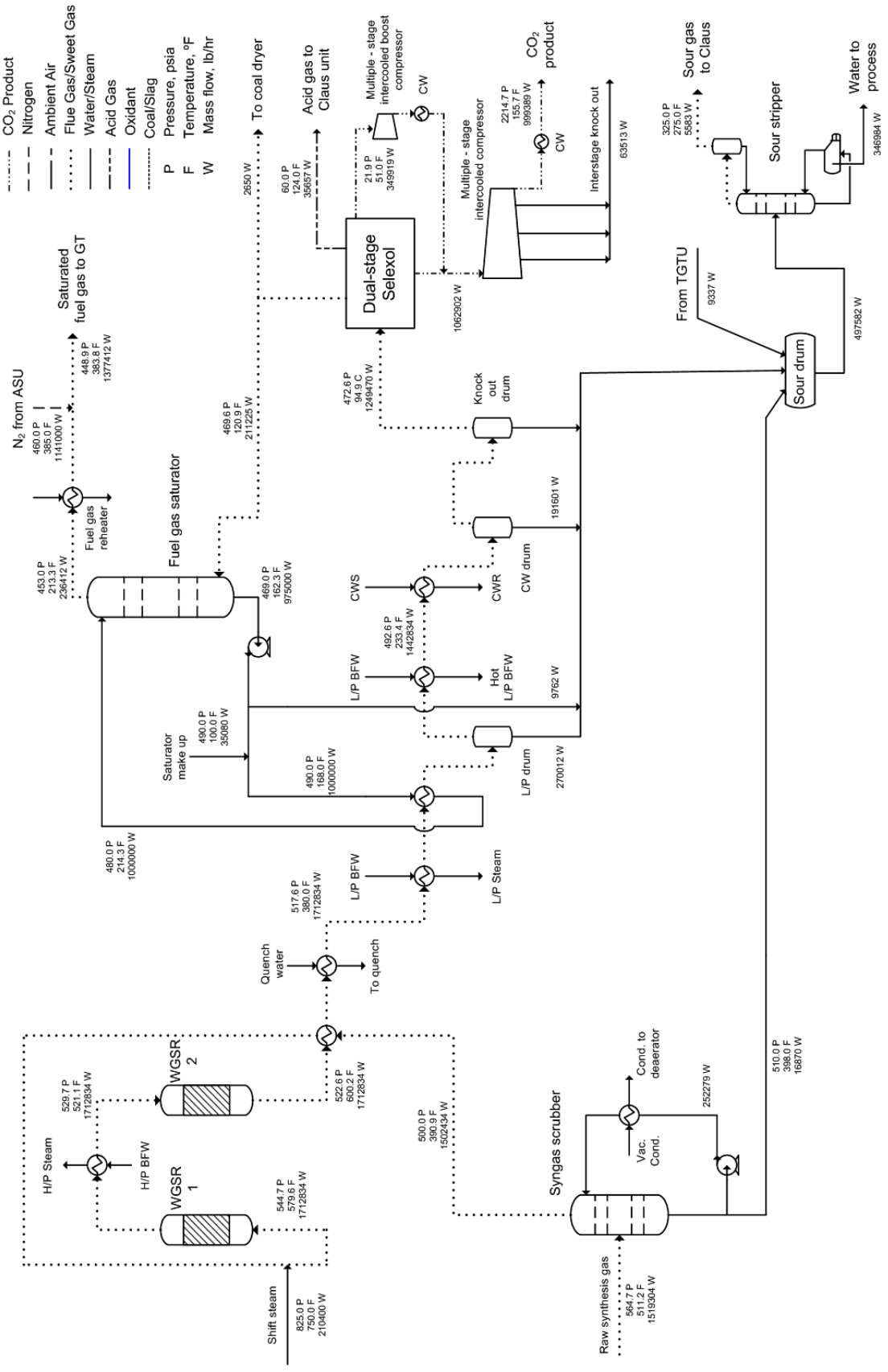

Figure 2.15: Syngas clean-up schematic (Kapetaki, 2015)

2.10 Claus plant

The sulfur recovery plant is a Claus process where H_2S is converted to elemental sulfur. The original Claus process was developed by C. F. Claus in 1883. Several process implementations have been developed to increase the sulfur recovery. However, all these processes are based on the same principles, which are primarily the oxidation of hydrogen sulfide at high temperatures and the formation of sulfur at low temperatures (Wozny and Hady, 2011). The Claus process principal objective is the recovery of sulfur more commonly from acid gas streams containing hydrogen sulfide in high concentrations. These streams typically result from acid gases stripped off sour liquids, such as processes utilising physical solvents for the purification of sour gases, i.e., the Selexol process. The effluent gases from the Claus plant are not valuable and are either vented to the atmosphere or directed to a tail gas treatment unit (Kohl and Nielsen, 1997). Established regulations worldwide strictly prohibit sulfur compounds to be vented to the atmosphere. Therefore, the Claus process is of considerable significance within the general scope of IGCC power plant technology. Furthermore, the Claus process yields elementary sulfur products that are of extremely good quality (Kohl and Nielsen, 1997).

Complete conversion of hydrogen sulfide to elemental sulfur under Claus plant operating conditions is precluded by the equilibrium relationships of the chemical reactions upon which the process is based. As a result of this limitation, the basic Claus process has to be supplemented with another process specifically designed to remove residual sulfur compounds from the Claus plant tail gas (Kohl and Nielsen, 1997). These processes are usually referred to as “tail gas clean-up” or “tail gas treating” processes.

Since the disclosure of the process by Claus in 1883, it has undergone several modifications. The most significant modification was that made by Farbenindustrie A.G. in 1936, which introduced the process concept currently in use, which consists of a thermal conversion step followed by one or more catalytic conversion steps (Kohl and Nielsen, 1997). A schematic of this configuration is shown in Figure 2.16 where two converters are considered.

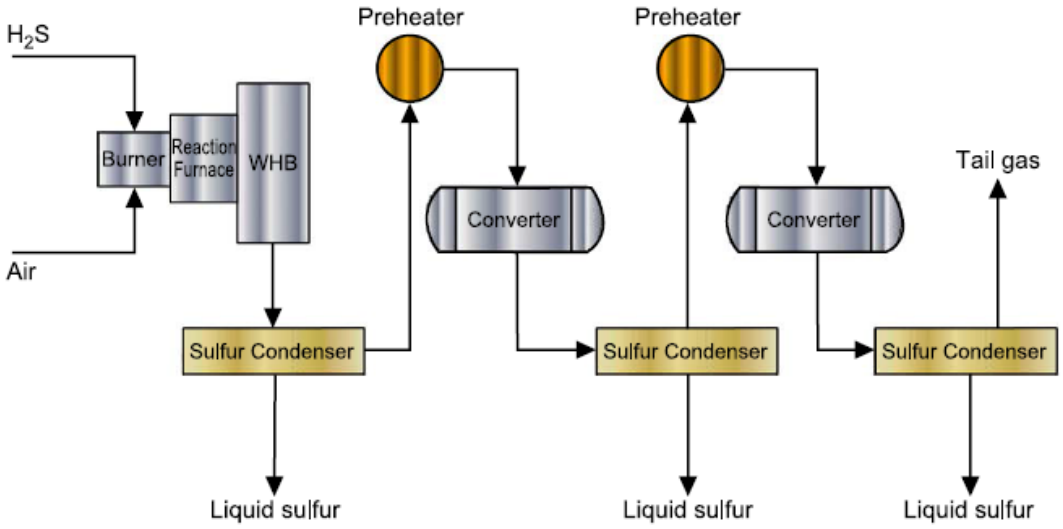

Figure 2.16: Schematic of the Claus process with two converters (El-Bishtawi and Haimour, 2004)

A detailed model of the modified Claus process reaction furnace and the implications on plant design and recovery were presented by Monnery et al. (1993). El-Bishtawi and Haimour (2004) developed a new modification on conventional Claus process to increase the overall sulfur recovery as well as to decrease the costs. The modification combined both oxygen enrichment and recycling. McIntyre and Lyddon (1997) investigated different sulfur recovery options, classifying acid gas into three different categories based on composition and discussing different types of Claus process modifications that may be used to lower sulfur emissions to an acceptable level. Monnery et al. (2000) performed an experimental campaign and published a new kinetic rate expression for the Claus reaction.

In the conventional Claus process, one-third of the acid gas is oxidised to SO_2 in the reaction furnace using air:

$$H_2S + \frac{3}{2}O_2 \Leftrightarrow SO_2 + H_2O \qquad (2\text{-}19)$$

This combustion generates a large amount of heat. Further, the combustion products undergo Claus reaction between H_2S and SO_2 in the converters.

$$2H_2S + SO_2 \Leftrightarrow \frac{3}{2}S_2 + 2H_2O \qquad (2\text{-}20)$$

Reaction (2-20) is a reversible exothermic reaction. Thus, processing under adiabatic conditions greatly increases temperature, which lowers equilibrium conversion to

about 75%. Effluent gas from the reaction furnace passes through a waste heat boiler to recover heat and produce high-pressure steam. The sulfur in the vapour phase exists as S_2, S_6, and S_8 molecular species mainly, with S_2 being predominant at higher temperatures and S_8 predominant at lower temperatures (Kohl and Nielsen, 1997). The sulfur species S_2 in the effluent gas undergoes the following changes:

$$3S_2 \Leftrightarrow S_6 \quad (2\text{-}21)$$

$$4S_2 \Leftrightarrow S_8 \quad (2\text{-}22)$$

Effluent gas from the WHB is cooled in a condenser to condense sulfur. Condenser effluent gas is preheated and is sent to two or three catalytic reactors where Claus reactions occur at lower temperatures. This leads to a higher equilibrium conversion since the Claus reaction is exothermic. Sulfur is recovered after each catalytic stage by cooling converter effluent gas in a sulfur condenser. The overall sulfur conversion obtained in the conventional Claus process is about 94–97% (Nobles, 1977).

The Claus process examined here refers to the configuration reported by the DOE (2007) and has several modifications:

- Three sulfur catalytic converters
- Oxygen enrichment
- Hydrogenation reactor

Utilising oxygen instead of air in the Claus plant reduces the overall cost of the sulfur recovery plant. The sulfur plant produces approximately 5,364 kg/h of elemental sulfur. Feed for this case consists of acid gas from both the acid gas clean-up unit and a vent stream from the sour water stripper in the gasifier section. Vent gas from the tail gas treatment unit is combined with a slipstream of clean syngas, passed through an incinerator, and then the hot, nearly inert incinerator off-gas is used to dry coal before being vented to the atmosphere. The furnace waste heat boiler produces 14,100 kg/h of 47 bar steam, which provides all of the Claus plant process needs and provides some additional steam to the medium-pressure steam header. The sulfur condensers produce 3.4 bar steam for the low-pressure steam header.

The simulation of the Claus process was conducted using the commercial software ProMax (BR&E, 2011). UniSim Design R400 does not allow differentiation of sulfur species, resulting in different heats of condensation/vaporisation for sulfur

and affecting the amount of steam generated within the process (Kapetaki, 2015). The model developed in ProMax to represent the H_2S conversion with the temperatures occurring in the operation of the Claus plant was validated with data reported in the literature (Paskall, 1979). The model utilised runs in the so-called "Sulfur" environment in the simulator. The Sulfur property package is a Gibbs Excess Energy/Activity Coefficient model that is designed to model the liquid phase properties and compositions of liquid sulfur.

As shown in Figure 2.17, the model is capable of describing the fact that the average molecular weight of sulfur vapour increases with decreasing temperature. At temperatures below 700 °F, sulfur vapour is predominately S_6 and S_8, while at the same partial pressure, but at temperatures above l600 °F, the sulfur is mostly S_2 (Kohl and Nielsen, 1997). The Claus plant can recover sulfur from the fuel gas stream with an efficiency of up to 99.7%.

The detailed process schematic is exhibited in Figure 2.18.

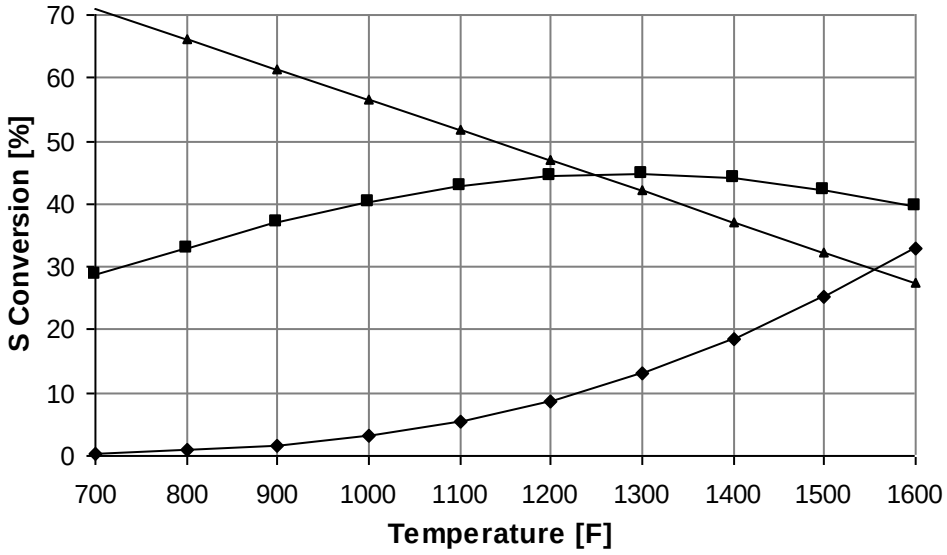

Figure 2.17: Sulfur conversion to species with temperature (♦ S_2, ■ S_6, ▲ S_8)

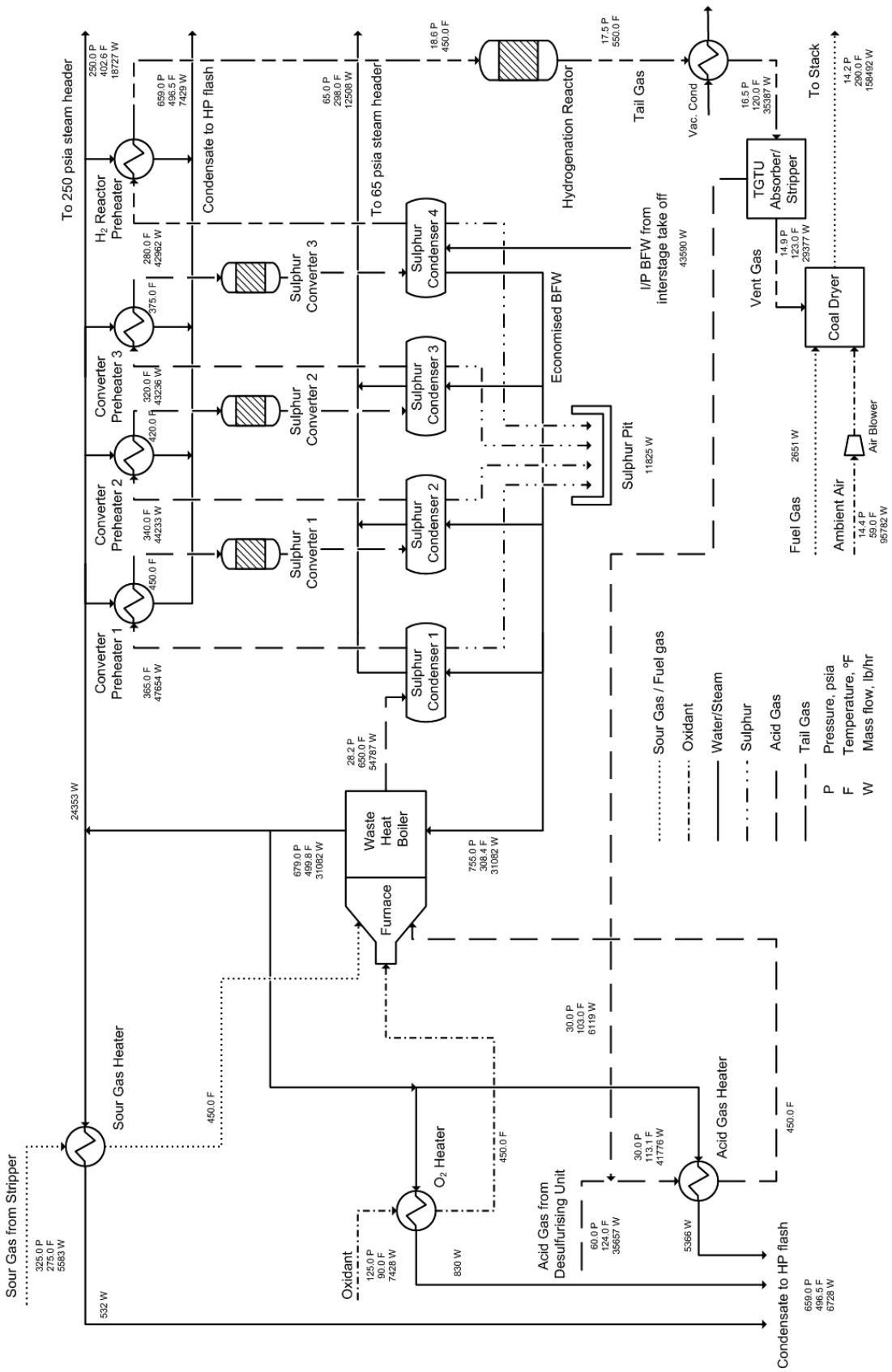

Figure 2.18: Sulfur recovery and tail gas recycle schematic (Kapetaki, 2015)

2.11 Gas turbine

Clean syngas from the AGR plant is combined with a small amount of clean gas from the CO_2 compression process and partially humidified because the nitrogen available from the ASU is insufficient to provide adequate dilution. The moisturised syngas is reheated to 196 °C using HP boiler feedwater, diluted with nitrogen, and then enters the combustion turbine (CT) burner. The advanced F Class turbine produces 464 MW of total electric energy in the IGCC. The oxygen required for the combustion is provided by compressed ambient air. It has been assumed that issues interconnected with high H_2 fuel combustion, such as flame stability, flashback and NO_X formation, would be overcome in the time frame needed to support deployment (DOE, 2007).

A gas turbine when fired on low calorific value syngas has the potential to increase power output due to the increase in flowrate through the turbine. The higher turbine flow and moisture content of the combustion products can contribute to overheating of turbine components, affect rating criteria for the parts lives, and require a reduction in syngas firing temperatures (compared to the natural gas firing) to maintain design metal temperature (Brdar and Jones, 2000). Ong'iro et al. (1995) developed a model in Aspen Plus to study the effects of design and performance parameters on the efficiency and emissions from IGCC and IGHAT (integrated gasification humified air turbine) cycles. Chiesa et al. (2005) discussed the possibility of burning hydrogen in a large, heavy-duty gas turbine designed to run on natural gas as a possible short-term measure to reduce the greenhouse emissions of the power industry. The effects of variations of volume flow rate and of thermophysical properties on the matching between turbine and compressor and on the blade cooling of the hot rows of the gas turbine were analysed in detail. Jones et al. (2011) reported on how the net IGCC power is affected by the choice of fuel diluents in the GT. Nitrogen and steam were considered as fuel diluents and their concentrations were varied while maintaining the NO_X level constant.

The considered firing temperature is 1,318–1,327 °C. The primary diluent used in the combustor is nitrogen produced in the ASU. The advantages of using nitrogen are (DOE, 2007):

- Nitrogen from the ASU is already partially compressed and using it for dilution eliminates wasting the compression energy
- Limiting the water content reduces the need to de-rate firing temperature, particularly in the high-hydrogen CO_2 capture case

However, there are some disadvantages when using nitrogen as the primary diluent, and these are (DOE, 2007):

- There is a significant auxiliary power requirement to further compress the large nitrogen flow from the ASU pressures of 4.2 and 13.1 bar to the CT pressure of 32 bar
- Nitrogen is not as efficient as water in limiting NOx emissions

The combustion products are expanded in the three-stage turbine-expander. The CT exhaust temperature is nominally 566 °C, given the assumed ambient conditions, back-end loss and HRSG pressure drop (DOE, 2007).

The air compressor, combustor and expander block were simulated using UniSim Design R400. The schematic of the process investigated was based on the configuration reported from DOE (2007) and is presented in Figure 2.19. The combustor was modelled as a Gibbs reactor. With this model, the phase and chemical equilibria of the outlet streams can be attained. The Gibbs reactor model does not use a specified reaction stoichiometry to compute the outlet stream composition. The product mixture composition is calculated under the condition that the Gibbs free energy of the reacting system at equilibrium is at its minimum.

The air compressor allows for extraction of cooling air for which no information is available in the report regarding the flow ratio, conditions etc. Although, the turbine cooling air is a crucial issue and has been investigated in detail elsewhere (Kim et al., 2009), in this study, the flow ratio was determined to match the combustor outlet temperature, as reported in the DOE report (2007).

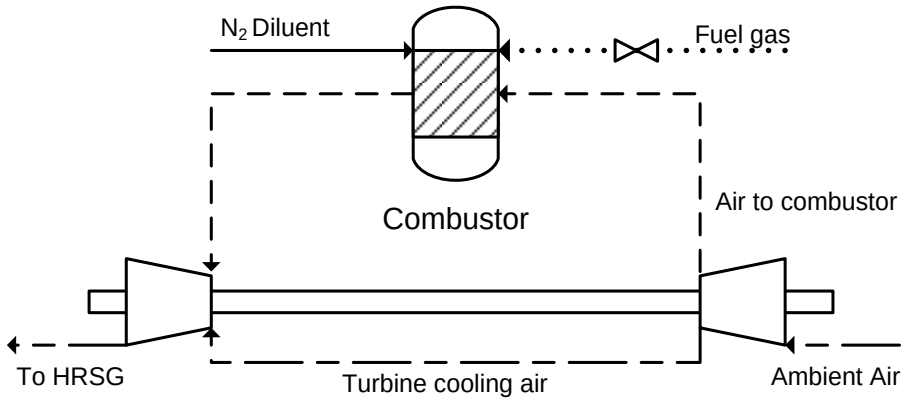

Figure 2.19: Carbon capture Shell IGCC power block schematic

Simulation results involving the combustor outlet stream information are reported in Table 2.11 along with the comparison from the DOE report (2007) data.

Table 2.11: Combustion turbine exhaust gas for carbon capture Shell IGCC compared with DOE report (2007) data

	DOE	**Simulation**
Ar	0.0091	0.0091
CH_4	0.0000	0.0000
CO	0.0000	0.0000
CO_2	0.0063	0.0064
COS	0.0000	0.0000
H_2	0.0000	0.0000
H_2O	0.1258	0.1245
H_2S	0.0000	0.0001
N_2	0.7513	0.7516
NH_3	0.0000	0.0000
O_2	0.1075	0.1084
SO_2	0.0000	0.0000
F (lb/h)	8,438,000	8,447,000
T (°F)	1,051	1,051
P (psia)	15.2	15.2

2.12 Heat recovery steam generation

The heat recovery steam generator (HRSG) is a horizontal gas flow, drum-type, multi-pressure design that is matched to the characteristics of the gas turbine exhaust gas (DOE, 2007). The flue gas exiting the combustor, after passing through the gas turbine is directed to the HRSG to recover the large quantity of thermal energy that it contains. The flue gas passes through the HRSG and exits at approximately 132 °C. In addition to generating and superheating steam, the HRSG provides the heat duties for the cold/hot reheat steams for the steam turbine, condensate and feedwater heating, and deaeration of the condensate. Natural circulation of steam is accomplished in the HRSG by utilising differences in densities due to temperature differences of the steam. The natural circulation HRSG provides the most cost-effective and reliable design (DOE, 2007).

Particular research effort has been given to the HRSG section of the IGCC power plants, as there is big potential of increasing its efficiency and as a consequence improving the overall performance of the power plant. Ganapathy reported several aspects interconnected with HRSG operation in his published works (Ganapathy, 1996; Ganapathy, 1997). Franco and Casarosa (2002) examined different HRSG configurations, such as parallel sections and off-limit subcritical conditions. Franco and Russo (2002) examined the effect of HRSG operating parameters in its performance and they conducted a thermodynamic and thermo-economic optimisation procedure to achieve higher combined cycle efficiencies. Najafi and Najafi (2009) performed a multi-objective optimisation of the HRSG to obtain optimum design parameters that yield the maximum efficiency and the minimum capital cost.

The steam turbine consists of a HP section, an IP section and a LP section, all connected to the generator by a common shaft. Steam from the HRSG is combined with steam from the gasifier island and enters the turbine at 12.4 MPa/538 °C. The steam initially enters the turbine near the middle of the high-pressure span, flows through the turbine, and returns to the HRSG for reheating. The reheat steam enters the IP section at 2.6 to 2.9 MPa and 538 °C. After passing through the IP section, the steam is transported to the LP section. The steam is finally directed into the

condenser. The condensate is sent to the deaerator, through the gland steam condenser, gasifier and low-temperature economiser section in the HRSG. The system consists of one main condenser, condensate pumps and one gland steam condenser. The feedwater from the deaerator is pumped to the various feedwater streams from the HRSG. Feed pumps are provided for each of the three pressure levels, HP, IP and LP.

2.12.1 Main and reheat steam systems

The function of the main steam system is to convey main steam generated in the synthesis gas cooler (SGC) and the HRSG to the HP turbine. The function of the reheat system is to convey steam from the HP turbine exhaust to the HRSG reheater and to the turbine reheat stop valves.

Main steam at approximately 12.4 MPa and 538 °C exits the HRSG superheater and is routed to the HP turbine. Cold reheat steam at approximately 3.1 to 3.4 MPa and 341 °C exits the HP turbine and flows to the HRSG reheater. Hot reheat steam at approximately 2.9 MPa and 538 °C exits the HRSG reheater and is routed to the IP turbines.

2.12.2 Circulating water system

The circulating water system is a closed-cycle cooling water system that supplies cooling water to the condenser to condense the main turbine exhaust steam. The system also supplies cooling water to the AGR plant as required, and to the auxiliary cooling system. The auxiliary cooling system is a closed-loop process that utilises a higher quality water to remove heat from compressor intercoolers, oil coolers and other ancillary equipment, and then transfers that heat to the main circulating cooling water system in plate and frame heat exchangers. The heat transferred to the circulating water in the condenser and other applications is removed by a mechanical draft-cooling tower.

2.12.3 Raw water and cycle makeup water systems

The raw water system supplies cooling tower makeup, cycle makeup, service water and potable water requirements. The water source was assumed to be groundwater (DOE, 2007).

The makeup water system provides high-quality demineralised water for makeup to the HRSG cycle and for steam injection ahead of the water gas shift reactors in CO_2 capture cases.

Compared to a non-capture case, the feedwater requirements for the Shell IGCC equipped with carbon capture unit appear to be higher and this can be justified with the inevitable increase of steam requirements in the WGSRs and in the quench configuration for the gasifier.

The simulation of the HRSG, steam and feedwater systems is part of the overall process flow diagram performed in UniSim Design R400, based on the data reported on the DOE report (2007) and briefly mentioned above. The Peng–Robinson equation of state was used for the flue gas properties and the ASME steam package was used for the water properties calculation. Several assumptions and operating conditions had to be assumed when information required to represent the full operation of the systems was not available from the report. The validation of the simulation results was examined for the IGCC case investigated. The simulation is capable of faithfully replicating the gas path of the combined cycle, as presented in the DOE report (2007). The steam path results were compared with the reported data and the stream properties of the condenser outlet are presented in Table 2.12. The schematics of this part of the IGCC power plant are shown in Figures 2.20 and 2.21.

Table 2.12: Condenser outlet streams validation carbon capture Shell IGCC compared with DOE report (2007) data

	DOE	**Simulation**
H_2O Vapour fraction	0.0	0.0
F (lb/h)	2,059,500	2,059,206
T (°F)	101.1	101.1
P (psia)	1.0	1.0

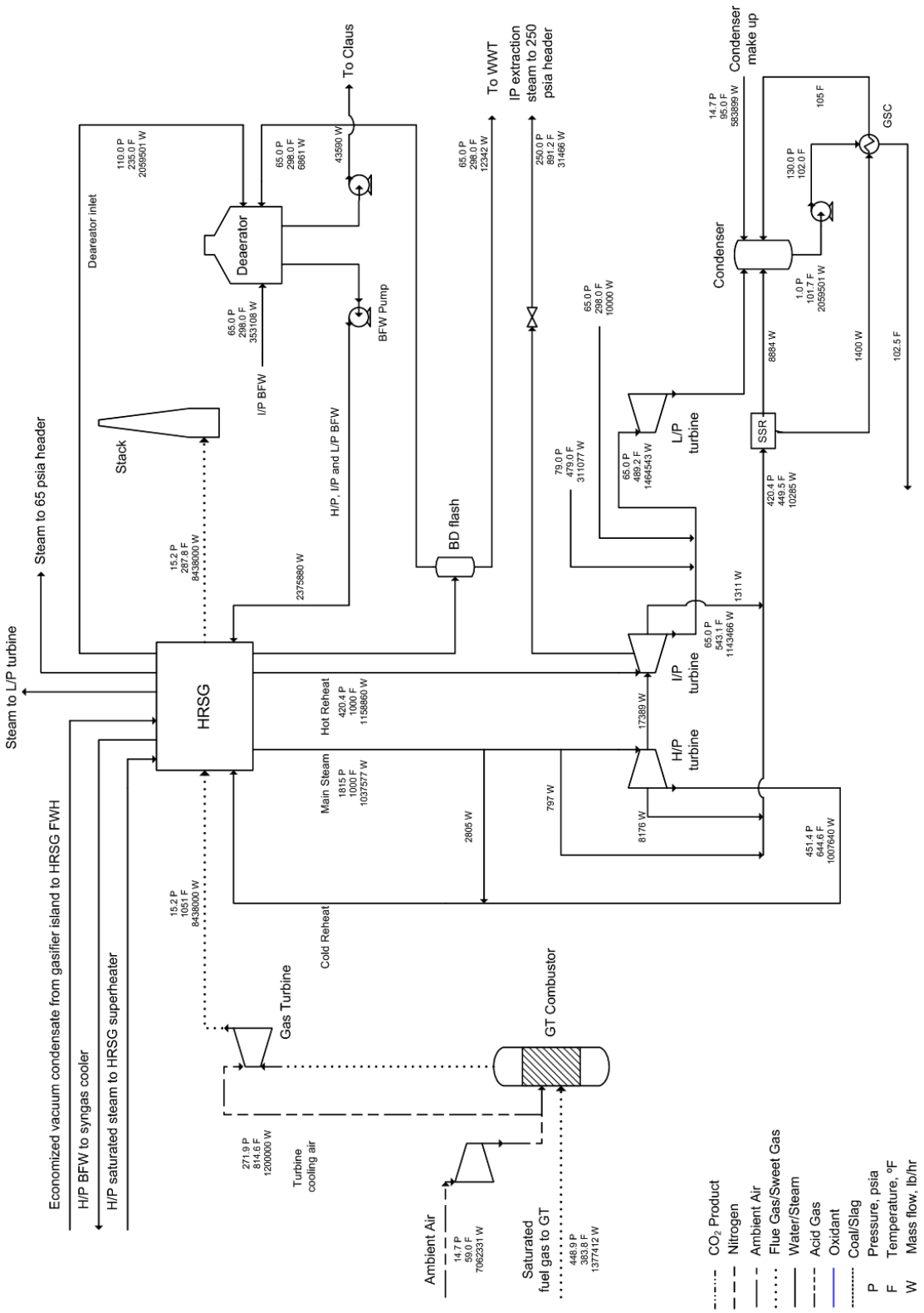

Figure 2.20: Combined cycle power generation schematic (Kapetaki, 2015)

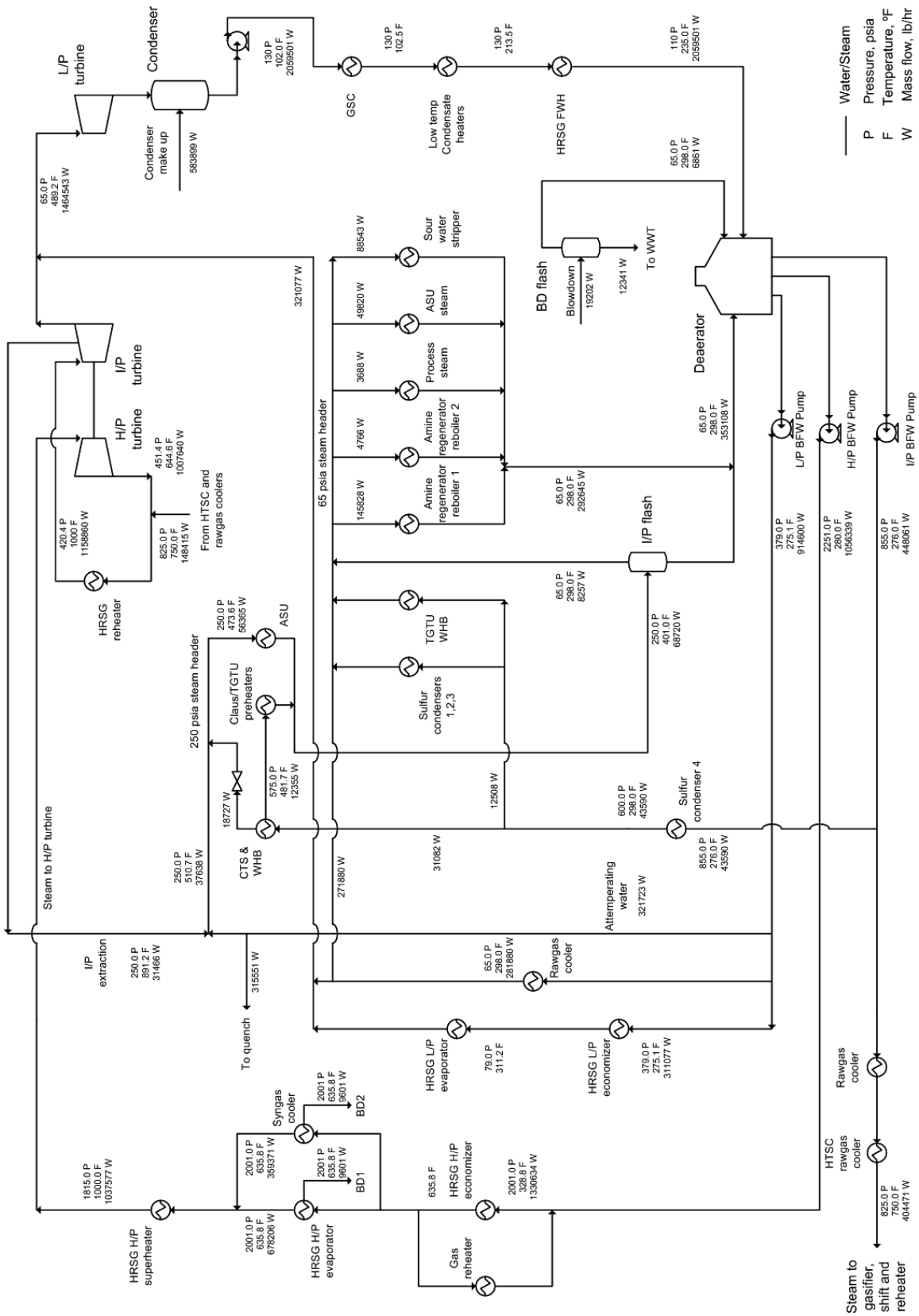

Figure 2.21: Steam and feedwater schematic (Kapetaki, 2015)

2.13 Overall plant performances

Once each section of the IGCC was carefully studied and simulated, it was possible to integrate all the units together in the same flow sheet in order to evaluate the overall plant performances. UniSim Design R400 enables the calculation of mass and energy balances around the units in cascade so that the outputs of a section will be the inputs of the following section. The presence of recycled streams among the units and targeted product specifications makes the calculations iterative until all the tolerances are respected. Figure 2.22 shows the complexity of the fully integrated flow sheet for the Shell IGCC with carbon capture simulation.

IGCC power plants will inevitably be subject to a drop in the overall plant efficiency as a result of the retrofit of the carbon capture process. In case of retrofitting the carbon capture process, it can be expected that additional fuel would be fed to the gasifier in order to operate the same gas turbine. This is because the heating value of the fuel gas will be reduced due to exothermic shift reaction so more coal should be fed to the gasifier to compensate for the heat loss. In addition, the different H_2 and CO recoveries in the AGR units between the non-capture and capture cases would also affect the coal input increment. In non-capture Shell IGCC, the syngas temperature is allowed to decrease below the COS hydrolysis temperature as long as the water content is more than what is required in the reaction. However, in carbon capture Shell IGCC, the syngas temperature should be kept higher than 200 °C until it enters the shift reactor since the amount of water quench was determined as the amount of water needed to saturate the syngas with water at this temperature.

Table 2.13 shows the overall plant performances for the non-capture and capture cases and demonstrates an efficiency drop larger than that reported by the DOE (2007). The overall carbon capture rate defined in eq. (2-23) was set at 90%.

$$Overall\ \ carbon\ \ capture = \left(\frac{Carbon\ \ in\ \ CO_2\ \ product}{Carbon\ \ in\ \ coal - Carbon\ \ in\ \ slag} \right) \times 100 \qquad (2\text{-}23)$$

The overall net plant efficiency was reduced mainly because of the higher power consumption in the AGR unit predicted in this study. The energy penalty relating to carbon capture is summarised in Table 2.14 while all the auxiliary consumptions occurring in each section are presented in Table 2.15.

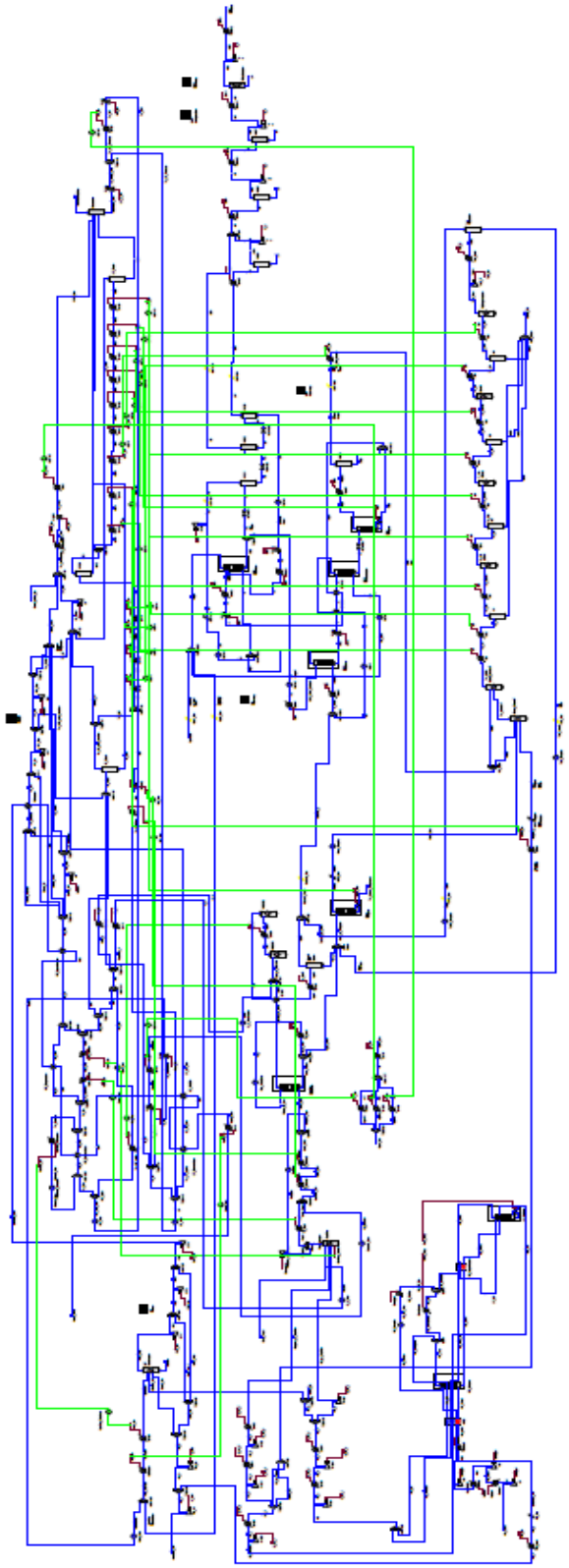

Figure 2.22: Fully integrated IGCC simulation flow sheet in UniSim Design R400 environment

Table 2.13: Comparison of DOE report (2007) data and simulation

Plant Performance (MW_e)	Shell IGCC non-capture		Shell IGCC with capture	
	DOE	This work	DOE	This work
Power summary				
Thermal input (MW_{th})	1,547	1,547	1,618	1,618
Gas turbine power	464.0	464.0	463.6	464.0
Steam turbine power	284.0	284.0	230.0	230.0
Total power generation	748.0	748.0	693.6	694.0
Total Auxiliaries	112.2	111.4	176.4	189.2
Net Power	635.9	636.6	517.1	504.8
Net power plant efficiency (HHV), %	41.1	41.1	32.0	31.2

Table 2.14: Simulated energy penalty in Shell IGCC with capture

Source of energy penalty	Energy change	Energy penalty
Heat input increase, kW_{th}	70,279	–
Gas turbine, kW_e	0	1.30 %
Steam turbine, kW_e	54,046	4.14 %
Gross power generation, kW_e	54,046	5.44 %
Auxiliary total, kW_e	77,783	4.50 %
Total, kW_e	131,829	9.94 %

Table 2.15: Auxiliary consumptions comparison between non-capture and carbon capture IGCCs (DOE, 2007)

	Shell IGCC without capture	Shell IGCC with capture
Coal handling	430	440
Coal milling	2,110	2,210
Slag handling (and dewatering)	540	570
Air separation unit auxiliaries	1,000	1,000
Air separation unit main air compressor	41,630	62,970
Oxygen compressor	10,080	10,540
Nitrogen compressor	37,010	38,670
Syngas recycle compressor	1,650	0
Incinerator air blower	160	160
CO_2 compressor	–	28,050
Boiler feedwater pumps	4,670	3,290
Condensate pump	230	310
Flash bottom pump	200	200
Circulating water pumps	3,150	3,440
Cooling tower fans	1,630	1,780
Scrubber pumps	120	390
Selexol/Sulfinol unit auxiliaries	660	15,500
Gas turbine auxiliaries	1,000	1,000
Steam turbine auxiliaries	100	100
Claus plant auxiliaries	250	250
Miscellaneous balance of plant	3,000	3,000
Transformer loss	2,550	2,550
Total, kW_e	112,170	176,420

2.14 Conclusions

When it comes to retrofitting IGCC power plants with CO_2 capture processes, almost all the parts of the conventional non-capture plant are affected. It is expected that there will be increments in the fuel that is fed to the gasifiers to operate the same

gas turbine. It was found that the energy penalty associated with the capture process reaches approximately 10% for the Shell IGCC.

Water gas shift reactors are an essential addition to the IGCC power plant when it has to be operated with retrofitted carbon capture process. In order to promote the conversion of CO to CO_2, IP steam extracted from the steam cycle has to be added. The conversion occurring is around 95.7%. The dual-stage Selexol process is the state-of-art technology to be used for IGCC in order to not only to remove H_2S, but also to capture CO_2. The CO_2 compression train downstream of the CO_2 capture process is another additional component to the carbon capture IGCCs where the CO_2 product is compressed up to a pressure suitable for CO_2 transport and storage. The EP ASU part of the power plant is not modified as such for carbon capture operation of the power plant. One obvious, yet significant, change in the carbon capture IGCC case is the fact that there is no potential for air integration between the GT compressor and the EP ASU. In the non-capture case about 4% of the GT air is used to supply approximately 19% of the ASU requirements. Conversely, since in the capture case most of CO_2 is removed prior to the combustion, once the syngas is diluted to the target heating value specified by the combustion turbine vendor (around 4.5-4.8 MJ/Nm^3; DOE, 2007), all of the available combustion air is required to maintain mass flow through the turbine and hence maintain power output. The steam cycle has to be redesigned mainly in order to provide steam to the water gas shift reactors.

Most of the discussed modifications necessary for the carbon capture operation of the IGCC power plant are inter-linked with an effect in the performance of the plant and an energy penalty, which is interpreted as the loss in the net plant efficiency.

References

Bhattacharyya D, Turton R, Zitney SE. Steady-state simulation and optimization of an Integrated Gasification Combined Cycle Power Plant with CO_2 capture. Industrial & Engineering Chemistry Research 2010; 50: 1674-1690.

BR&E. ProMax, 2011.

Brdar RD, Jones RM. GE IGCC Technology and experience with advanced gas turbines. Schenectady; GE Power Systems, 2000.

Burr B, Lyddon, L. A comparison of physical solvents for acid gas removal. 87th Annual GPA Convention 2008, Grapevine.

Castle WF. Modern liquid pump oxygen plants: Equipment and performance, Cryogenic Processes and Machinery. Eighth Intersociety Cryogenic Symposium 1991, Houston.

Chen C. A technical and economic assessment of CO_2 capture technology for IGCC power plants. Pittsburgh, 2005. PhD Thesis.

Chiesa P, Consonni S. Shift reactors and physical absorption for low-CO_2 emission IGCCs. Journal of Engineering for Gas Turbines and Power-transactions of The Asme 1999; 121: 295-305.

Chiesa P, Consonni S, Kreutz T, Williams R. Co-production of hydrogen, electricity and CO_2 from coal with commercially ready technology. Part A: Performance and emissions. Hydrogen Energy 2005; 30: 747-767.

Collot AG. Matching gasifiers to coals IEA Clean Coal Centre, IEA 2002.

Cormos CC. Evaluation of energy integration aspects for IGCC-based hydrogen and electricity co-production with carbon capture and storage. Hydrogen Energy 2010; 35: 7485-7497.

Cormos CC, Agachi PS. Integrated assessment of carbon capture and storage technologies in coal-based power generation using CAPE tools. 22 European Symposium on Computer Aided Process Engineering 2012; 30: 56-60, London.

Cormos CC, Starr F, Tzimas E, Peteves S. Innovative concepts for hydrogen production processes based on coal gasification with CO_2 capture. Hydrogen Energy 2008; 33: 1286-1294.

Cornelissen RL, Hirs GG. Exergy analysis of cryogenic air separation. Energy Conversion & Management 1998; 39: 1821-1826.

Damen K, van Troost M, Faaij A, Turkenburg W. A comparison of electricity and hydrogen production systems with CO_2 capture and storage. Part A: Review and selection of promising

conversion and capture technologies. Progress in Energy and Combustion Science 2006; 32: 215-246.

Doctor RD, Molburg JC, Thimmapuram PR. KRW oxygen-blown gasification combined cycle carbon dioxide recovery, transport, and disposal. ANL/ESD-34 1996.

DOE NETL. Cost and performance baseline for fossil energy plants; 2007.

El-Bishtawi R, Haimour N. Claus recycle with double combustion process. Fuel Processing Technology 2004; 86: 245-260.

Emun F, Gadalla M, Majozi T, Boer D. Integrated gasification combined cycle (IGCC) process simulation and optimization. Computers and Chemical Engineering 2010; 34: 331-338.

EPRI. Process screening study of alternative gas treating and sulphur removal systems for IGCC power plant applications. Mountain View, 1987.

Foster Wheeler. Potential for improvement in gasification combined cycle power generation with CO_2 capture. Report No. PH4/19 2003.

Franco A, Casarosa C. On some perspectives for increasing the efficiency of combined cycle power plants. Applied Thermal Engineering 2002; 22: 1501-1518.

Franco A, Russo A. Combined cycle plant efficiency increase based on the optimization of the heat recovery steam generator operating parameters. International Journal of Thermal Sciences 2002; 41: 843-859.

Fu C, Gundersen T. Using exergy analysis to reduce power consumption in air separation units for oxy-combustion processes. Energy 2012; 44: 60-68.

Ganapathy V. Heat-recovery steam generators: understand the basics. Chemical Engineering Progress 1996.

Ganapathy V. Generating steam efficiently from cogeneration plants. Chemical Engineering Progress 1997.

Haslbeck JL. Evaluation of fossil power plants with CO_2 recovery. Parsons Infrastructure & Technology Group Inc. 2002.

Henni A, Tontiwachwuthikul P, Chakma A. Solubility of carbon dioxide, methane and ethane in fourteen promising physical solvents for gas sweetening. Greenhouse Gas Control Technologies 2005; 7: 1887-1889.

Higman C, van der Burgt M. Gasification 2003, Elsevier.

Honeywell. UniSim Design R400, 2011.

Huang Y, Rezvani S, McIlveen-Wright D, Minchener A, Newitt N. Techno-economic study of CO_2 capture and storage in coal fired oxygen fed entrained flow IGCC power plants. Fuel Processing Technology 2008; 89: 916-925.

IEA CCC (Clean Coal Centre). The world coal-fired power plants database 2005.

IPCC. Special report on carbon dioxide capture and storage. 2005.

Jones D, Bhattacharyya D, Turton R, Zitney ES. Optimal design and integration of an air separation unit (ASU) for an integrated gasification combined cycle (IGCC) power plant with CO_2 capture. Fuel Processing Technology 2011; 92: 1685-1695.

Kapetaki Z. Analysis of Integrated Gasification Combined Cycle power plants and process integration with pre-combustion carbon capture. PhD thesis, 2015; The University of Edinburgh.

Kapetaki Z, Ahn H, Brandani S. Detailed process simulation of pre-combustion IGCC plants using coal-slurry and dry coal gasifiers. Energy Procedia 2013; 37: 2196-2203.

Kim YS, Lee JJ, Cha KS, Kim TS, Sohn JL, Joo YJ. Analysis of gas turbine performance in IGCC plants considering compressor operating condition and turbine metal temperature. ASME TURBO EXPO 2009; New York.

Kohl AO, Nielsen RB. Gas purification, Gulf Publishing Co., 1997; Houston.

Kreutz T, Williams R, Consonni S, Chiesa P. Co-production of hydrogen, electricity and CO_2 from coal with commercially ready technology. Part B: Economic analysis. Hydrogen Energy 2005; 7: 769-784.

Latimer RE. Distillation of air. Chem. Eng. Progress 1967; 63: 35-59.

Maurstad O, Herzog H, Bolland O, Beer J. Impact of coal quality and gasifier technology on IGCC performance, 2009.

McDaniel JE, Hornick MJ. Tampa electric polk power station integrated gasification combined cycle project, Final technical report to the National Energy Technology Laboratory 2002.

McIntyre G, Lyddon L. Claus sulphur recovery options. Technical paper; Petroleum Technology Quarterly Spring 1997: 57-61.

Mendes D, Chibante V, Zheng JM, Tosti S, Borgognoni F, Mendes A, Madeira LM. Enhancing the production of hydrogen via water–gas shift reaction using Pd-based membrane reactors. Hydrogen Energy 2010; 35: 12596-12608.

Minchener AJ. Coal gasification for advanced power generation. Fuel 2005; 84: 2222-2235.

Monnery WD, Svrcek WY, Behie LA. Modelling the modified Claus process reaction furnace and the implications on plant design and recovery. The Canadian Journal of Chemical Engineering 1993; 71: 711-724.

Monnery WD, Hawboldt KA, Pollock A, Svrcek WY. New experimental data and kinetic rate expression for the Claus reaction. Chemical Engineering Science 2000; 55: 5141-5148.

Ng KS, Lopez Y, Campbell GM, Sadhukhan J. Heat integration and analysis of decarbonised IGCC sites. Chemical Engineering Research and Design 2010; 88: 170-188.

Najafi H, Najafi B. Multi-objective optimization of a fire-tube heat recovery steam generator system. Electrical Power & Energy Conference (EPEC), 2009.

Nobles JE. Plant performance process. Hydrocarbon Processing 1977; 56: 143-145.

O'Keefe LF, Griffiths J, Weissman RC, De Puy RA, Wainwright JM. A Single IGCC Design for Variable CO_2 Capture. Fifth European Gasification Conference 2002.

Ong'iro AO, Ugursal VI,Al Taweel AM, Blamire DK. Simulation of combined cycle power plants using the Aspen Plus Shell. Heat Recovery System & CHP 1995; 15: 105-113.

Padurean A, Cormos CC, Agachi PS. Pre-combustion carbon dioxide capture by gas–liquid absorption for Integrated Gasification Combined Cycle power plants. International Journal of Greenhouse Gas Control 2012; 7: 1-11.

Paskall HG. Capability of the Modified Claus Process. Alberta/Canada Energy Resources Research Fund, 1979.

Puigjaner L. Syngas from Waste: Emerging Technologies 2011, Springer.

Ranke G, Mohr VH. The Rectisol wash: New developments in acid gas removal from synthesis gas. Acid and Sour Gas Treating Processes 1985; pp. 80-111.

Robinson PJ, Luyben WL. Integrated Gasification Combined Cycle dynamic model: H_2S absorption/stripping, water-gas shift reactors, and CO_2 absorption/stripping. Industrial & Engineering Chemistry Research 2010; 49: 4766-4781.

Salazar JM, Diwekar UM, Zitney SE. Rigorous-simulation pinch-technology refined approach for process synthesis of the water–gas shift reaction system in an IGCC process with carbon capture. Computers and Chemical Engineering 2011; 35: 1863-1875.

Sandler SI. Chemical Engineering Thermodynamics, 3rd Edition 1999.

Sciamanna SF, Lynn S. Solubility of hydrogen sulfide, sulfur dioxide, carbon dioxide, propane, and n-butane in poly(glycol ethers). Industrial & Engineering Chemistry Research 1988; 27: 492-499.

Simbeck DR. World gasification survey: industrial trends and developments. Gasification Technology Conference 2001, San Francisco.

Simbeck DR, Korens DR, Biasca FE, Vejtasa S, Dickenson RL. Coal gasification guidebook: status, applications, and technologies. Electric Power Research Institute (EPRI); 1993.

Smith JM, Van Ness HC, Abbott MM. Introduction to Chemical Engineering Thermodynamics, 7th Edition 2005.

Sweny JW, Valentine JP. Physical solvent stars in gas treatment/purification. Chemical Engineering 1970: 54-56.

Thorogood RM. Developments in air separation. Gas Separation & Purification 1991; 5: 83-94.

Wabash River Energy Ltd. Wabash river coal gasification repowering project, Final technical report to the National Energy Technology Laboratory 2000.

Wall TF. Combustion processes for carbon capture. Proceedings of the Combustion Institute 2007; 31: 31-47.

Wozny G, Hady L. Process Engineering and Chemical Plant Design. Berlin, Universitatsverlag der TU Berlin, 2011.

Xu Y, Schutte RP, Hepler LG. Solubilities of carbon dioxide, hydrogen sulfide and sulfur dioxide in physical solvents. The Canadian Journal of Chemical Engineering 1992; 70: 569-573.

Zheng L, Furinsky E. Comparison of Shell, Texaco, BGL and KRW gasifiers as part of IGCC plant computer simulations. Energy Conversion and Management 2005; 46: 1767-1779.

Chapter 3: Fundamentals of adsorption and pressure swing adsorption processes

The separation and purification of gas mixtures using adsorption systems is widely used in the chemical, petrochemical, environmental, medical and electronic gas industries (Keller et al., 1987; Sircar, 2000). According to the operating conditions, the commercial adsorbents may allow different mass transfer mechanisms between the gas and solid phases (Ruthven, 1984; Yang 1987; Suzuki, 1990), leading to different sets of partial differential equations (PDEs) to model the adsorption dynamics. In formulating mathematical models for pressure swing adsorption (PSA) processes, several assumptions can be made to simplify the problem without losing the accuracy of the solution (Sircar and Hufton, 2000). The overall performance of a PSA process depends on both equilibrium and kinetic factors, but the relative importance of these factors varies greatly depending on the system it is being applied to. The majority of PSA processes are equilibrium-driven in a sense that the selectivity depends on differences in the equilibrium affinities (Ruthven et al., 1994).

Fundamentals of adsorption phenomena and industrial PSA cycles for hydrogen purification will be discussed in this chapter.

3.1 Adsorbents

The use of adsorption as a separation unit operation is based on the selective retention of the gas molecules in the pores of the adsorbent (Ruthven, 1984); this selective retention may be caused by differences in the adsorption equilibrium or in the adsorption rate. The molecules of a gas mixture in the neighbourhood of a solid experience a reduction in their potential energy due to the interaction forces between the atoms of the solid and the gaseous molecules; consequently, the gas molecules will tend to concentrate in this region leading to larger density in comparison with the free gas phase zone. The nature of the surface forces will depend on the adsorbent and the sorbates. If the interactions between the adsorbent and the sorbates are Van der Waals forces or dipole fields, the phenomena can be classified as

physisorption; in the case that a transfer of electrons between the gas and the solid phase takes place, a chemisorption phenomenon will occur (Ruthven, 1984).

The role of the adsorbents is to provide the surface area for the selective sorption to take place: the specific selectivity and the adsorption capacity are important factors that must be taken into account when choosing the sorbent as well as the operating conditions for gas separation. The selectivity may be a consequence of the "chemical similarity" (equilibrium-driven sorbents) between the surface of the solid and the sorbate or else caused by steric restriction (kinetically driven sorbents).

According to the IUPAC classification, pores are divided into three categories:

- Micropores: < 20 Å
- Mesopores: 20–500 Å
- Macropores > 500 Å

In a micropore, the guest molecule never escapes from the field of the solid surface, even at the centre of the pore. It is therefore reasonable to consider all the molecules within a micropore to be in the adsorbed phase. By contrast, in mesopores and macropores, the molecules in the central region of the pore are essentially free from the force field of the surface; therefore, it becomes physically reasonable to consider the pore as a two-phase system containing both adsorbed molecules at the surface and free gaseous molecules in the central region. Of course, the IUPAC classification is arbitrary but PSA processes deal generally with relatively small molecules up to 20 Å. Commercial adsorbents can be classified into hydrophilic or hydrophobic, amorphous or crystalline, as summarised in Table 3.1.

Table 3.1: Classification of commercial adsorbents

Equilibrium selective		Kinetically selective	
Hydrophilic	Hydrophobic	Amorphous	Crystalline
Activated alumina Silica gel Al-rich zeolites Polymeric resins	Activated carbon Silicalite™ Other polymeric resins	Carbon molecular sieves (CMS)	Small-pore zeolites

In the case of the equilibrium-driven sorbents, the gas separation is based on the chemical similarity between the solid surface and the sorbate. The hydrophilic adsorbents tend to retain polar molecules such as water or other polar gases/liquids; on the contrary, activated carbon (hydrophobic) will be highly selective for the non-polar species.

The most important characteristic of a sorbent is its high porosity. Thus, physical characterisation is equally important as chemical characterisation. The microporous structure of the sorbent can be characterised by standard techniques. The most important physical characteristics include pore volume, pore size distribution and surface area. Also of practical importance are bulk density, crush strength and abrasion resistance. Many commercial adsorbents consist of composite particle crystals (or char particles) aggregated together and formed into a macroporous pellet, often with the aid of a binder. Such particles have a well-defined bimodal pore size distribution in which the first peak represents the micropores and the second peak represents the large intraparticle pores resulting from the pelletisation process, as shown for 5A zeolite in Figure 3.1.

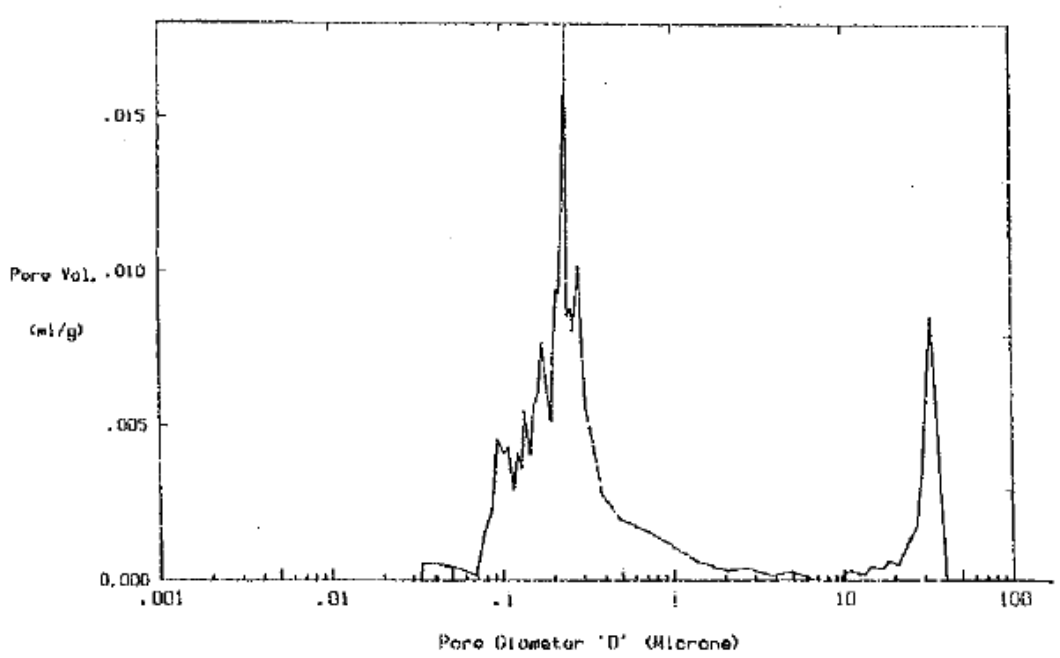

Figure 3.1: Pore size distribution for pelleted 5A zeolite (Ruthven et al., 1994)

Table 3.2 reports the physical properties of some common adsorbents and their major uses for gas sorption. The following subsections are devoted to a brief summary of the most important commercial adsorbents.

Table 3.2: Physical properties of some common adsorbents and their industrial application (Yang, 1987; Ruthven et al., 1994)

Adsorbent	Specific pore volume (cm^3/g)	Average pore diameter (Å)	Pore size distribution	Specific area (m^2/g)	Particle density (g/cm^3)	Major applications
Silica gel	0.43	22	Unimodal	800	1.09	Drying Gas chromatog.
Activated alumina	0.50	30–3000	Unimodal	320	1.28	Drying Gas chromatog.
Activated carbon	0.15–0.5	Wide range	Bimodal	200–2000	0.6–0.9	Removal of VOCs H_2 purification
Carbon molecular sieve	0.25	-	Bimodal	400	0.98	Air separation Landfill gas separation
Zeolites	0.26	< 10	Bimodal	430	1.12	Drying H_2 purification Air separation Aromatics separation Iso-paraffins separation Gas chromatog. Carbon capture

3.1.1 Silica gel

Silica gel is a partially dehydrated form of polymeric colloidal silicic acid. The chemical composition can be expressed as $SiO_2 \cdot nH_2O$. A variety of methods for the manufacture of silica gel have been described, including the hydrolysis of soluble alkali metal silicates with acid and the direct removal of sodium from sodium silicate solutions by ion exchange (Ruthven, 1984). The presence of hydroxyl groups imparts a degree of polarity to the surface so that polar molecules, such as water, alcohols, phenols and amines and unsaturated hydrocarbons, are adsorbed in preference to non-polar molecules, such as saturated hydrocarbons. Although water is adsorbed more strongly on molecular sieves than on alumina or silica gel, the ultimate capacity of silica gel, at least at low temperatures, is generally higher. Silica gel is therefore a

useful desiccant where high capacity is required at low temperature and moderate vapour pressures.

3.1.2 Activated alumina

Activated alumina is a porous high-surface-area form of aluminium oxide, prepared either from bauxite ($Al_2O_3 \cdot 3H_2O$) or from the monohydrate by dehydration and recrystallisation at elevated temperature. The surface is more strongly polar than that of silica gel and has both acid and basic character, reflecting the amphoteric nature of the metal. At elevated temperature, the capacity of activated alumina is higher than that of silica gel and it is therefore commonly used as a desiccant for drying warm air or gas streams. However, for this application it has been largely replaced by molecular sieve adsorbents, which exhibit both a higher capacity and a lower equilibrium vapour pressure under most conditions of practical importance (Ruthven, 1984).

3.1.3 Activated carbon

Activated carbon is normally made by thermal decomposition of carbonaceous material followed by activation with steam or carbon dioxide at an elevated temperature (700–1100 °C). The activation process essentially involves the removal of tarry carbonisation products formed during the pyrolysis, thereby opening the pores. The structure of activated carbon consists of elementary microcrystallites of graphite, but these microcrystallites are stacked together in random orientation and it is the spaces between the crystals that form the micropores. The surface of carbon is essentially non-polar, although a slight polarity may arise from surface oxidation. As a result, carbon adsorbents tend to be hydrophobic and organophilic. They are therefore widely used for the adsorption of organics in decolourising sugar and oil, water purification and solvent recovery systems, as well as for the adsorption of gasoline vapours in automobiles and as a general-purpose adsorbent in air purification systems (Ruthven, 1984).

3.1.4 Carbon molecular sieves

Activated carbon adsorbents generally show very little selectivity in the adsorption of molecules of different sizes. However, by applying special activation procedures it is possible to prepare carbon adsorbents with a very narrow distribution of micropore size and which therefore behave as molecular sieves. Most commercial carbon sieves are prepared from anthracite or hard coal by controlled oxidation and subsequent thermal treatment. By these means, it is possible to prepare carbon molecular sieves with effective micropores diameters ranging from about 4 to 9 Å (Ruthven, 1984). The micropore size distribution of such sieves is much narrower than in a typical activated carbon and both porosity and adsorptive capacity are generally much smaller. Nevertheless, the kinetic selectivities that may be attained with a well-prepared carbon sieve are remarkably high. At present, the most important large-scale application is air separation. Another potential area of application includes the clean-up of the off-gases from nuclear facilities.

3.1.5 Polymeric resins

The use of synthetic adsorbent polymers, particularly in drinking water treatment, arose from the development in polymer science technology, allowing the production of highly porous polymers of 800-1500 m^2/g, which is similar to the surface of activated carbons. Polymeric resins are characterized by lower energy demand and, consequently, lower costs of regeneration or renewal of the adsorbents in comparison with carbonaceous materials. Their main application consists in the removal of various organic compounds including phenols, pharmaceuticals and pesticides from aqueous solutions (Lin and Juang, 2009). Resins (synthetic or natural) have also become popular and been used more and more frequently in high performance liquid chromatography (HPLC) practice for the separation and quantitative determination of commercial pesticides (Kyriakopoulos and Doulia, 2006).

3.1.6 Mesoporous silica

Silicate mesoporous materials possess well-defined pore sizes of about 2.0-10.0 nm and surpass the pore-size constraint (<2.0 nm) of microporous zeolites. They also have extremely high surface areas (>700 m^2/g) and narrow pore size distributions. Instead of using small organic molecules as templating compounds, as in the case of zeolites, long chain surfactant molecules are employed as the structure-directing agent during the synthesis of these highly ordered materials. The structure, composition, and pore size of these materials can be tailored during synthesis by variation of the reactant stoichiometry, the nature of the surfactant molecule, the auxiliary chemicals, the reaction conditions, or by post-synthesis functionalisation techniques (ALOthman, 2012). Mesoporous silica have generally received interest because of their potential applications as supports for catalysis, gas separation, selective adsorption and novel functional materials. Recently, it has been reported that mesoporous silica nanoparticles as drug delivery systems show significant advantages over traditional drug nano-carriers (Tang et al., 2012).

3.1.7 Zeolites

Zeolites are alumino-silicate crystallines containing alkali or alkali-earth elements, such as sodium, potassium and calcium. The cations are necessary to balance the electrical charge of the aluminium atoms, each having a net charge of -1. The water molecules can be removed with ease upon heat and evacuation, leaving an almost unaltered alumino-silicate skeleton with a void fraction between 0.2 and 0.5 (Yang, 1987). The skeleton has a regular structure of cages, which are usually interconnected by six windows in each cage. The cages can imbibe or occlude large amounts of guest molecules in place of water. The size of the window apertures, which can be controlled by fixing the type and number of cations, ranges from 3 to 10 Å (Yang, 1987). The sorption may occur with great selectivity because of the size of the aperture, hence the name molecular sieve.

The primary structural units of zeolites are the tetrahedra of silicon and aluminium, SiO_4 and AlO_4. These units are assembled into secondary polyhedral building units, such as cubes, hexagonal prisms, octahedra and truncated octahedra. The silicon and aluminium atoms, located at the corners of the polyhedral, are joined

by a shared oxygen atom. The final zeolite structure consists of assemblages of the secondary units in a regular three-dimensional crystalline framework. The ratio of Si/Al is commonly one to five. The aluminium atom can be removed and replaced by silicon in some zeolites, thereby reducing the number of cations, and the cations can also be exchanged. The inner atoms in the windows are oxygen. The size of the windows depends on the number of oxygen atoms in the ring, four, five, six, eight, ten or 12. The aperture size, as well as the adsorptive properties, can be further modified by the number and type of exchanged cations. The structural unit in type A zeolite, as well as in types X and Y, is the truncated octahedron, as shown in Figure 3.2a. This unit is also called a sodalite cage, as sodalite is formed by directly fusing the four-member rings of the unit. The sodalite units can also be linked through four-member prisms or six-member prisms, generating type A zeolite and types X and Y zeolites, respectively (Figure 3.2b). Commercial zeolites are used in a wide range of applications, as seen in Table 3.2.

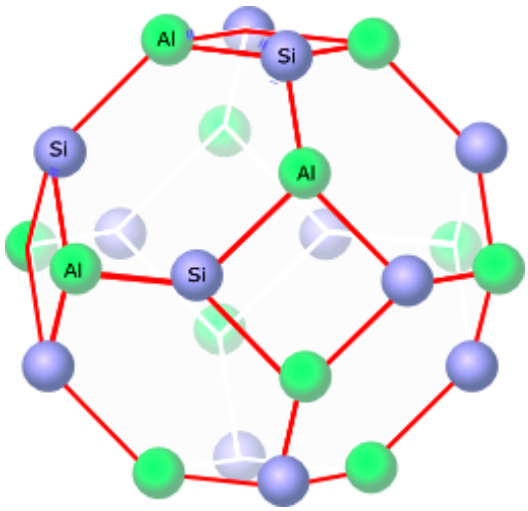

Figure 3.2a: Representation of a sodalite cage or truncated octahedron (Manske, 2009)

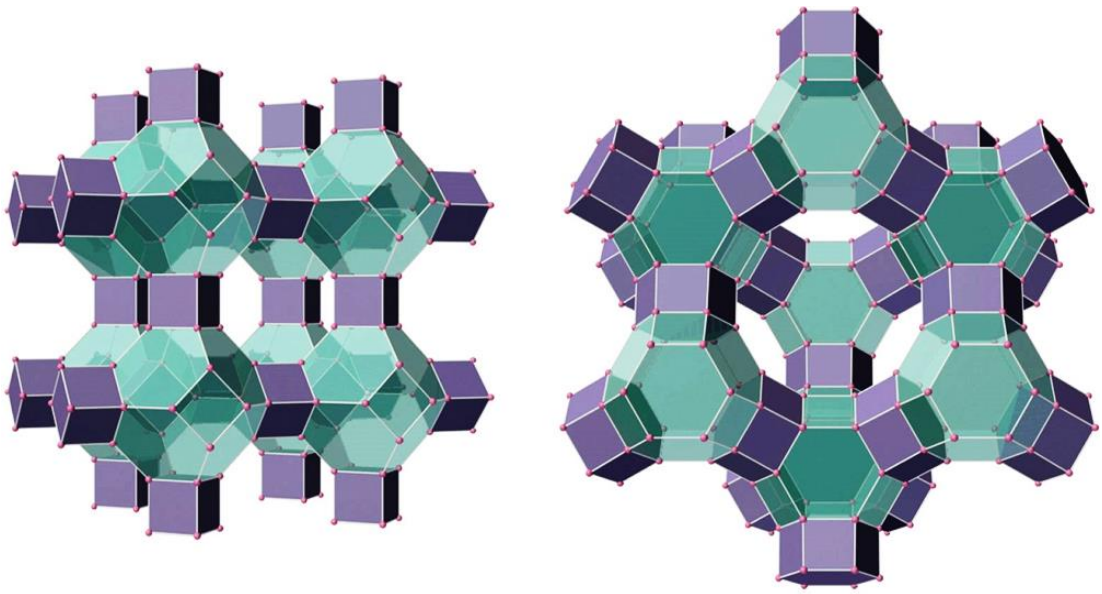

Figure 3.2b: Representation of type A zeolite unit cell (left) and unit cell of types X and Y, or faujasite (right) (Averill and Eldredge, 2007)

3.1.8 Metal organic frameworks (MOFs)

MOFs are comprised of transition metal ions linked by organic ligand bridges and assembled principally through strong coordination bonds. MOFs have geometrically and crystallographically well-defined framework structures and in most cases, these structures are robust enough to allow the removal of the included guest species resulting in permanent porosity. The crystallinity of MOFs also allows precise structural characterization by diffraction methods, thus facilitating their rational design and the formulation of structure–function relationships. MOFs can be conceptually designed and synthesized based on how building blocks come together to form a net (an example is shown in Figure 3.3). MOFs can be made with exceptionally high porosity and are typically synthesized by a self-assembly reaction between various metal ions and organic linkers under mild conditions. MOFs hold several records in porous materials including highest surface areas, hydrogen uptake based on physical adsorption, methane and CO_2 storage (Li et al., 2011). As porous material, MOFs are therefore ideal adsorbents or membrane materials for gas storage and separation, including CO_2 capture due to their large surface areas, adjustable pore sizes, and controllable pore surface properties.

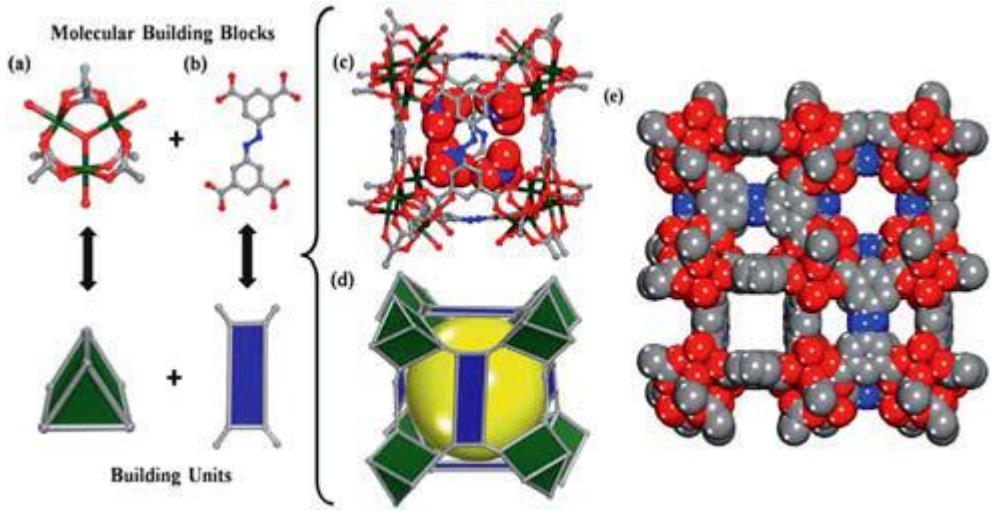

Figure 3.3: X-ray crystal structure of indium soc-MOF, in which (a) is a cluster of metal ions, (b) is an organic linker, (c) and (d) are representations of a cuboidal cage of indium soc-MOF and (e) is a space filling representation of the framework viewed along the y-direction (Wang et al., 2011)

3.2 Adsorption equilibrium

The adsorbed layer at the surface of a solid may be regarded as a distinct phase in the thermodynamic sense. Equilibrium with the surrounding gas is governed by the ordinary laws of thermodynamics. Physical adsorption from the gas phase is an exothermic process, so equilibrium favours adsorption at lower temperatures and desorption at higher temperatures. At sufficiently low concentrations, the equilibrium relationship generally approaches a linear form (Henry's law):

$$q = K' \cdot P \quad \text{or} \quad q = K \cdot C \tag{3-1}$$

and the constant of proportionality (K' or K) is referred to as the Henry's law constant. It is evident that the Henry constant is simply the adsorption equilibrium constant, and the temperature dependence can be described by the van't Hoff relations:

$$K' = K'_0 \, e^{-\Delta H / RT} \quad \text{or} \quad K = K_0 e^{-\Delta U / RT} \tag{3-2}$$

where $\Delta H = \Delta U + RT$ is the enthalpy change on adsorption. Since for an exothermic process ΔH and ΔU are negative, the Henry's law constant decreases with increasing temperature. At higher concentrations, the equilibrium relationship becomes curved.

The first systematic attempt to interpret adsorption isotherms for gas–solid equilibria was introduced by Brunauer et al. (1938), who classified isotherms for physical adsorption into five types. This classification has become the core of the modern IUPAC classification (1985) together with an additional isotherm introduced much later by Sing. The IUPAC classification is illustrated in Figure 3.4.

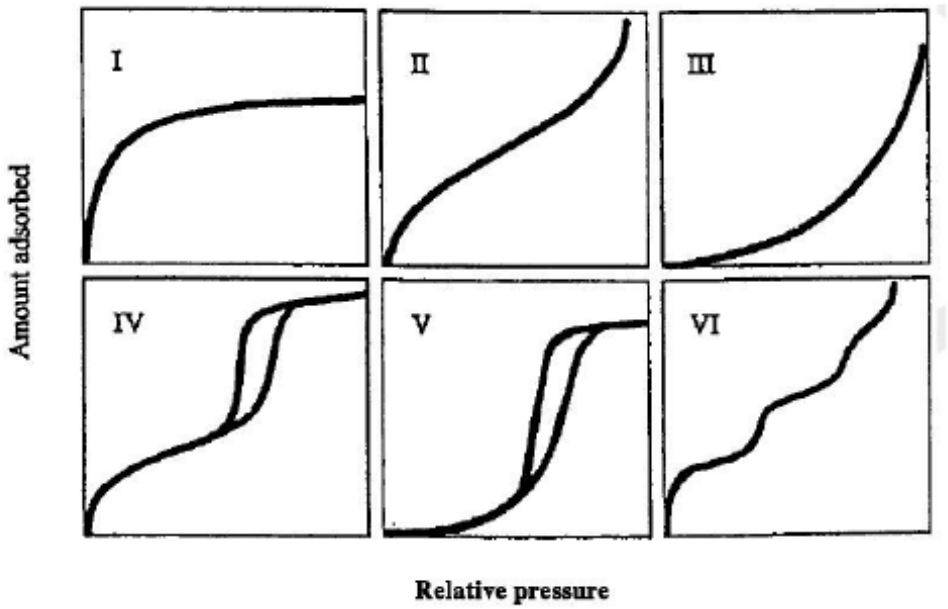

Figure 3.4: The IUPAC classification for adsorption isotherms (IUPAC, 1985)

The type I isotherm function corresponds to true microporous adsorbents for which the pore size is not very much greater than the molecular diameter; for those adsorbents, there is a definite saturation limit that is associated with complete filling of the micropores. The type V isotherm can be observed if there is a strong molecular interaction. An isotherm of type IV suggests the formation of two surface layers, either on a plane surface or on the wall of a pore very much wider than the molecular diameter of the sorbate. Types IV and V show adsorption hysteresis. The types II and III isotherms are generally observed only in those adsorbents for which there is a wide range of pore sizes (mesoporous and macroporous); in such systems there is a continuous progression with increasing loading from monolayer to multilayer adsorption and then to capillarity condensation taking place in the pores, which enables a drastic increase of capacity when the pressure of the gas mixture is raised (Ruthven, 1984). Finally, the new type VI isotherm has steps that are typical of multi-layering.

When the dynamics of adsorption systems is under study, it is useful to define the concept of a favourable and linear as well as a non-favourable adsorption isotherm. This concept is based on the plot (x, y) shown in Figure 3.5. The definitions for x and y are presented in the axis of the plot. As can be seen from the plot, in the case of favourable adsorbents, the dimensionless adsorbed concentration (x) is always larger than the dimensionless concentration (y) in the gas phase. Since for desorption the initial and final states are reversed, an isotherm that is favourable for adsorption will be unfavourable for desorption and vice versa.

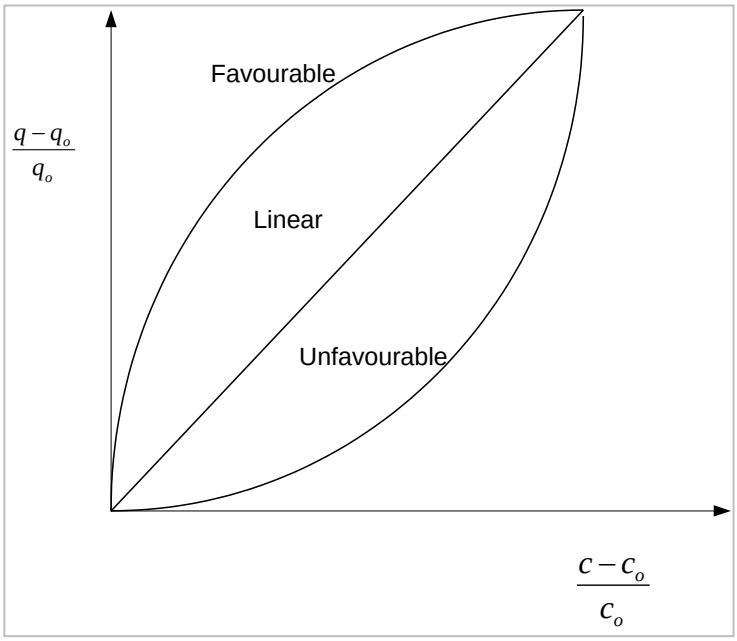

Figure 3.5: Dimensionless equilibrium isotherms

The simplest theoretical model for monolayer adsorption was formulated by Langmuir (1918). The Langmuir model was originally developed to represent chemisorption on a set of distinct localised adsorption sites. The basic assumptions on which the model is based are:

- Molecules are adsorbed at a fixed number of well-defined localised sites
- Each site can hold one adsorbate molecule
- All sites are energetically equivalent
- There is no interaction between molecules adsorbed on neighbouring sites

The model can be described by:

$$q = \frac{q_s \cdot b \cdot P}{1 + b \cdot P} \tag{3-3}$$

This expression shows the correct asymptotic behaviour for monolayer adsorption since at saturation P → ∞, q → q_s while at low sorbate concentration it becomes the Henry's law constant:

$$\lim_{P \to 0}\left(\frac{q}{P}\right) = b \cdot q_s = K' \tag{3-4}$$

q_s is supposed to represent a fixed number of surface sites and therefore it should be constant regardless of temperature while the temperature dependence of the equilibrium constant should follow a van't Hoff equation:

$$b = b_0 \exp\left(\frac{-\Delta H}{R \cdot T}\right) \tag{3-5}$$

Since adsorption is exothermic, b should decrease with increasing temperature. The assumption of identical sites with no interaction between adsorbed molecules implies that the heat of adsorption is independent of coverage. The isosteric heat of adsorption is therefore given by:

$$\left(\frac{\partial \ln P}{\partial T}\right)_q = \frac{\Delta H}{R \cdot T^2} \tag{3-6}$$

Although there are relatively few systems that conform accurately to the Langmuir model, there are a great number of systems that show approximate conformity and this model has the further advantage that it reduces to Henry's law at the low-concentration limit, which is a requirement for thermodynamic consistency in any physical adsorption system. For these reasons, the Langmuir model has become widely accepted as a reliable equilibrium model in analysing PSA systems.

The Langmuir model yields a simple extension to binary and multicomponent systems, reflecting the competitive adsorption of different adsorbates on the adsorption sites:

$$q_i = \frac{q_s \cdot b_i \cdot P_i}{1 + \sum_i b_i \cdot P_i} \tag{3-7}$$

This equation is known as the extended Langmuir model and for thermodynamic consistency it requires that q_s has to be the same for all the components. It is clear that at a given temperature (which determines the value of b) and at a given partial

pressure, the adsorption amount of a component will be lower than for a single component system at the same condition. This model is widely used in the modelling of PSA systems because of its simplicity but also because when the loading is relatively low the extended Langmuir model is generally accurate. The separation factor or selectivity for a system described by eq. (3-7) is given simply by the ratio of the adsorption equilibrium constants for the two components and it is independent of concentration:

$$\alpha_{12} = \frac{x_1 / x_2}{y_1 / y_2} = \frac{b_1}{b_2} \tag{3-8}$$

When the Langmuir model fails, more complicated isotherm models involving more than two parameters are used, such as dual-site Langmuir, Langmuir–Freundlich, Toth, Nitta, Unilan and O'Brien & Myers. Other adsorption theories can be found in Dubinin–Polanyi theory, Ideal Adsorbed Solution Theory (IAST), vacancy solution theory and potential theory.

3.3 Adsorption kinetics

The rate of physical adsorption can be controlled by diffusional limitations rather than by the actual rate of equilibration at a surface, which, for physical adsorption, is normally very rapid. From the perspective of sorption kinetics, adsorbents may be divided into two broad classes: homogeneous and composite. In the homogeneous adsorbents, the pore structure persists on the same scale through the entire particle. By contrast, the composite adsorbent particles are formed by aggregation of small microporous microparticles, sometimes with the aid of a binder. In a composite adsorbent, there are three distinct resistances to mass transfer, as illustrated in Figure 3.6. In homogeneous adsorbents, external film resistance also exists.

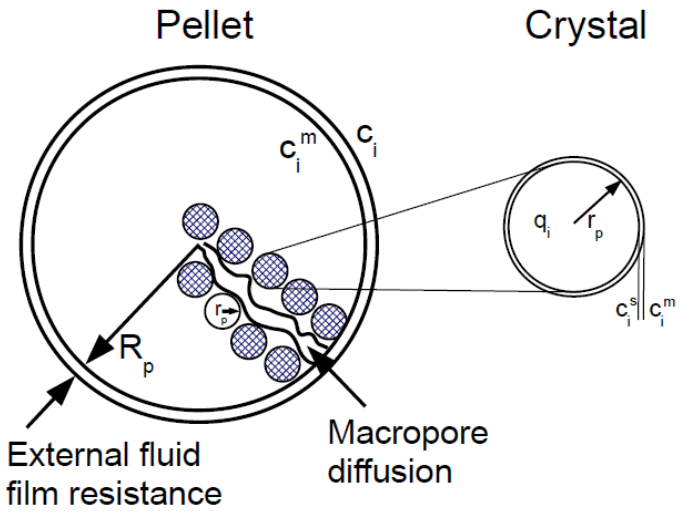

Figure 3.6: The resistances to mass transfer in a composite adsorbent pellet

Under practical conditions of operation, the external film resistance is seldom rate limiting, so the sorption/desorption rate is generally controlled by either macropore or micropore diffusion or by the combined effects of these resistances (Ruthven et al., 1994).

3.3.1 Diffusion in mesopores and macropores

There are four distinguishable mechanisms that contribute to the mass transfer in the case of the mesopores and the macropores (pores where diameter is larger than the diameter of the diffusing species). These mechanisms are:

- Bulk or molecular diffusion
- Knudsen diffusion
- Poiseuille diffusion
- Surface diffusion

Bulk or molecular diffusion becomes dominant when the pore diameter is larger than the mean free path of the molecules (the distance that a molecule can travel without having collisions with other molecules or with the wall of the pores). Eq. (3-9) is the Chapman–Enskog equation, which shows the influence of pressure and temperature on the binary molecular diffusivity (Poling et al., 2001):

$$D_{ij} = \frac{1.88 \cdot 10^{-7} \cdot \sqrt{T^3 \cdot \left(\frac{1}{M_i} + \frac{1}{M_j} \right)}}{P \cdot \sigma_{ij}^2 \cdot \Omega_{ij}} \tag{3-9}$$

where P is in bar, D_{ij} is in m^2/s while σ_{ij} and Ω_{ij} are related to the characteristic Lennard–Jones length and energy of pure components i and j. The molecular diffusivity of the gas relating to component i is calculated as follows:

$$D_{m,i} = \frac{1 - y_i}{\sum_{j=1, j \neq i}^{n} \frac{y_i}{D_{ij}}} \tag{3-10}$$

The Knudsen diffusivity becomes relevant at low pressure or in those adsorbents in which the pore diameters are lower than the molecular mean free path since this mass transfer mechanism is a consequence of the collisions between the diffusing molecules and the pore wall (Ruthven, 1984). The Knudsen diffusivity can be estimated by the Kauzmann correlation (Yang, 1987):

$$D_{k,i} = 9700 \cdot r_p \cdot \sqrt{\frac{T}{M_i}} \tag{3-11}$$

where r_p is in cm and $D_{k,i}$ is in cm^2/s.

In the transition region between the two mechanisms, it is valid to say that the two diffusivities can be summed up as two resistances in parallel, also taking into account the tortuosity, as described by the Bonsanquet equation (Yang, 1987):

$$D_{p,i} = \frac{1}{\tau_p} \cdot \left(\frac{1}{D_{m,i}} + \frac{1}{D_{k,i}} \right)^{-1} \tag{3-12}$$

It is clear that at higher pressures, D_p tends to D_m, while at lower pressure and small pore radius, D_p tends to D_k. Since the actual diffusion path does not equal the distance in the radial direction, the tortuosity factor (τ_p) defines the ratio between the actual diffusion path length and the radial distance.

There may be also a contribution related to the flux from forced flow (Poiseuille flow). The equivalent Pouiseuille diffusivity is given by eq. (3-13) where r_p refers to the pore radius and μ_i to the viscosity of component i in the gas mixture (Ruthven, 1984).

$$D_{v,i} = \frac{P \cdot r_p^2}{8 \cdot \mu_i} \tag{3-13}$$

The Pouiseuille diffusivity becomes relevant only in relatively large pores and high pressures; its effect is generally negligible in a packed bed since the pressure drop over an individual particle is very small. The contribution of the Pouiseuille diffusivity is directly additive to the one arising from the combination of the Knudsen and molecular mechanisms (Ruthven et al., 1994).

When the adsorbed phase is sufficiently mobile and the concentration sufficiently high, there may be an additional contribution from surface diffusion (Kapoor et al., 1989) through the adsorbed layer on the pore wall:

$$D_{s,i} = \frac{1-\varepsilon_p}{\varepsilon_p} \cdot K \cdot D_{s0,i} \cdot \exp\left(\frac{-E}{R \cdot T}\right) \tag{3-14}$$

Surface diffusion is an activation process and is in many ways similar to micropore diffusion.

An overall macropore diffusivity can be obtained by combining all the four mechanisms previously described (Ruthven et al., 1994):

$$D_{p,i} = \frac{1}{\tau_p} \cdot \left[\left(\frac{1}{D_{m,i}} + \frac{1}{D_{k,i}} \right)^{-1} + D_{v,i} + D_{s,i} \right] \tag{3-15}$$

3.3.2 Diffusion in micropores

Micropore diffusion is diffusion in pores of dimensions comparable with the diameters of the diffusing molecules. In this situation, the diffusing molecule never escapes from the force field of the pore wall. In such small pores, it no longer makes sense to distinguish between adsorbed molecules on the pore wall and molecules in the central region of the pore, and it is preferable to regard all sorbate molecules within the micropores as the adsorbed phase. A strong concentration dependence of the micropore diffusivity is commonly observed. The true driving force for any diffusive process is the gradient of chemical potential, as assumed in the Fickian formulation:

$$J = -B \cdot q \cdot \frac{\partial \mu}{\partial z} \tag{3-16}$$

where B is the mobility of a molecule. Considering equilibrium with an ideal vapour phase:

$$\mu = \mu^0 + R \cdot T \cdot \ln a = \mu^0 + R \cdot T \cdot \ln P \tag{3-17}$$

Therefore:

$$J = -B \cdot R \cdot T \cdot \frac{d \ln P}{d \ln q} \cdot \frac{\partial q}{\partial z} \tag{3-18}$$

The Fickian diffusivity is given by:

$$D = D_0 \cdot \frac{d \ln P}{d \ln q} \quad \text{with} \quad D_0 = B \cdot R \cdot T \tag{3-19}$$

Eq. (3-19) is referred to as Darken's relation and D_0 is the corrected diffusivity. In the vapour phase at low concentration, Henry's law is obeyed; the system is linear and dlnP/dlnq → 1, so the Fickian diffusivity becomes independent of concentration. For most microporous adsorbents, however, the isotherm is of type I form; therefore, eq. (3-19) predicts an increasing trend of diffusivity with concentration. In particular for the Langmuir isotherm:

$$\frac{d \ln P}{d \ln q} = \frac{1}{1 - q / q_s} \tag{3-20}$$

for which it may be seen that, in the saturation region, the concentration dependence is very strong. Micropore diffusion is an activation process; so, in contrast to molecular or Knudsen diffusivities, the temperature dependence is strong and generally follows the Arrhenius form:

$$D_\mu = D_\infty \cdot \exp\left(\frac{-E}{R \cdot T} \right) \tag{3-21}$$

where E is the adsorption activation energy. In small-pore zeolites and carbon molecular sieves, the major energy barrier is simply the repulsive interactions associated with the molecule passing through constrictions in the pore. As a result, there is a well-defined correlation between activation energy and molecular diameter.

3.4 Adsorption column model

The model hierarchy for the adsorption column is derived from the mass, energy and momentum balances. This model hierarchy, which is shown in Figure

3.7, contains models of varying complexity that are valid for different parameters regimes.

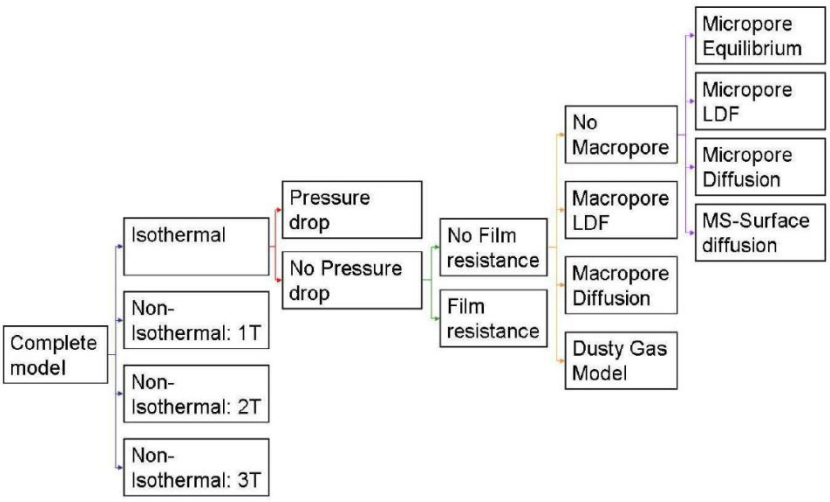

Figure 3.7: Model hierarchy for the adsorption column: in each stage the different options are only shown for one option of the previous stage but apply to all options of the previous stage

The model hierarchy is traversed from left to right and in each stage one model is chosen. For example, the choice of non-isothermal 1T, pressure drop, no film resistance, no macropore and micropore diffusion will generate a unique set of governing equations.

3.4.1 Column dimensions

A schematic of the adsorption column is shown in Figure 3.8. The flow through a packed bed is described by the axial dispersed plug flow model. More details, including radial dispersion, are generally not necessary (Ruthven, 1984), while the ideal plug flow can be approximated by letting the dispersion coefficient go to zero.

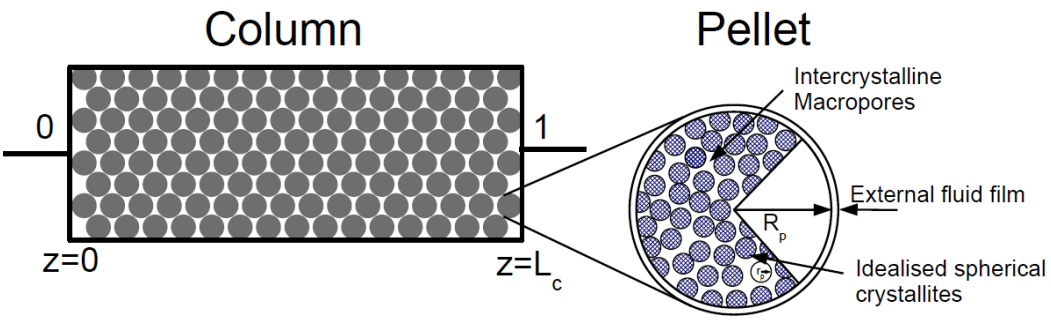

Figure 3.8: Schematic of an adsorption column showing the two inlets and the adsorbent pellets: the inset shows a schematic of an idealised adsorbent pellet including the spherical crystallites

Table 3.3 summarises the column and pellet dimensions as well as the densities and void fractions, which will be used in following sub-sections. A list of the abbreviations and the corresponding variables displayed in the table as well as in the equations can be found in the list of symbols at the beginning of this thesis.

Table 3.3: Summary of column and pellet dimensions, densities and void fractions

Symbol	Explanation	Formula
$A_{c,a}$	Column axial surface area	$A_{c,a} = \pi R_c^2$
$A_{c,l}$	Column lateral surface area	$A_{c,l} = 2\pi R_c L_c$
A_c	Column area	$A_c = 2A_{c,a} + A_{c,l}$
V_c	Column Volume	$V_c = \pi R_c^2 L_c$
A_p	Pellet surface area	$A_p = \frac{4\pi R_p^2}{\varphi}$
V_p	Pellet volume	$V_p = \frac{4}{3}\pi R_p^3$
ρ_{bulk}	Bulk density	$\rho_{bulk} = \frac{\mathrm{m_p}}{V_c}$
ρ_p	Pellet density	$\rho_p = \frac{\mathrm{m_p}}{V_p}$
ρ_{cry}	Crystal density	$\rho_{cry} = \frac{\mathrm{m}_p}{V_{cry}}$
ρ_{skel}	Skeletal density	$\rho_{skel} = \frac{\mathrm{m}_p}{V_{skel}}$
ε	Inter-particle void fraction	$\varepsilon = 1 - \frac{\rho_{bulk}}{\rho_p}$
ε_p	Pellet void fraction	$\varepsilon_p = 1 - \frac{\rho_p}{\rho_{cry}}$
ε_{cry}	Crystal void fraction	$\varepsilon_{cry} = 1 - \frac{\rho_{cry}}{\rho_{skel}}$

where φ represents the non-spherically coefficient of the particle.

3.4.2 Mass balance

The mass balance for the gas phase is described by the axial dispersed plug flow model with an adsorption term as shown in eq. (3-22). From a numerical point of view, it can be classified as a non-linear parabolic dispersive advection equation with a "reaction term".

$$\frac{\partial c_i}{\partial t} + \frac{(1-\varepsilon)}{\varepsilon} \cdot \frac{\partial \overline{Q}_i}{\partial t} + \frac{\partial (c_i \cdot v)}{\partial z} + \frac{\partial J_i}{\partial z} = 0 \tag{3-22}$$

$$\overline{Q}_i = \varepsilon_p \cdot c_i^m + \rho_p \cdot \overline{q}_i \tag{3-23}$$

$$\overline{Q}_i = \frac{3}{r_p^3} \cdot \int_0^{R_p} Q_i r^2 dr \tag{3-24}$$

$$\overline{q}_i = \frac{3}{r_c^3} \cdot \int_0^{r_p} q_i r^2 dr \tag{3-25}$$

$$J_i = -D_z \cdot c_T \cdot \frac{\partial y_i}{\partial z} \tag{3-26}$$

The overall mass balance is given by:

$$\frac{\partial c_T}{\partial t} + \frac{(1-\varepsilon)}{\varepsilon} \cdot \sum_i^n \frac{\partial \overline{Q}_i}{\partial t} + \frac{\partial (c_T \cdot v)}{\partial z} = 0 \tag{3-27}$$

Here, c_i is the gas phase concentration of component i, c^m_i is the macropore concentration of component i, Q_i is the concentration of component i in the adsorbent pellet and q_i is the sorbate concentration of component i. The bar at the top of Q_i and q_i indicates the average concentration over the pellet and the micropore, respectively. Eqs. (3-24) and (3-25) show the definition of $\overline{Q}_i$ and $\overline{q}_i$ in the pellet and in the micropore but these equations are not used in the mass balance calculations. D_z is the mass axial dispersion coefficient. The boundary conditions for the gas phase concentrations are given by the Danckwerts boundary conditions (1953) for flow into the column and the no diffusive flux for flow out of the column. With the conventions that the positive flow directions are from 0 to L, these can be written in a combined form as:

$$J_i\big|_{z=0} = \frac{v+|v|}{2}\cdot\left(c_{i,0-} - c_{i,0}\right) \tag{3-28}$$

$$J_i\big|_{z=L_c} = \frac{v-|v|}{2}\cdot\left(c_{i,L_c+} - c_{i,L_c}\right) \tag{3-29}$$

where the superscripts − and + indicate the concentrations values to the left and right of the boundary, respectively.

The material balance in the adsorbent pellet can also be described by a hierarchy of models of varying complexity. The concentration c^m_i in the macropores is governed by the diffusion equation with an effective diffusion coefficient $D_{p,i}$:

$$\varepsilon_p \cdot \frac{\partial c_i^m}{\partial t} + \rho_p \cdot \frac{\partial \overline{q}_i}{\partial t} + \frac{1}{r^2}\cdot\frac{\partial}{\partial r}\left(-D_{p,i}\cdot r^2 \cdot \frac{\partial c_i^m}{\partial r}\right) = 0 \tag{3-30}$$

The adsorbed concentration q_i in the micropores is governed by the diffusion equation with an effective diffusion coefficient $D_{\mu,i}$:

$$\frac{\partial q_i}{\partial t} + \frac{1}{r^2}\cdot\frac{\partial}{\partial r}\left(-D_{\mu,i}\cdot r^2 \cdot \frac{\partial q_i}{\partial r}\right) = 0 \tag{3-31}$$

Eqns (3-30) and (3-31) describe the mass balance in the adsorbent pellet in the most general case, i.e., external film resistance, macropore diffusion and micropore diffusion with film resistance or barrier resistance. In many cases, the behaviour of the adsorption column can be adequately described by simpler models: the LDF approximation is one of those (Glueckauf, 1949). The variables of interest will change only with time and this change will be proportional (k_{LDF}) to the difference between the current values for it in the pore and the associated values for the closest external gas phase. If the LDF model is assumed for the macropores, the parabolic PDE defined by eq. (3-30) transforms into the ODE described by eq. (3-32):

$$\varepsilon_p \cdot \frac{dc_i^m}{dt} + \rho_p \cdot \frac{d\overline{q}_i}{dt} = k_i^p \frac{A_p}{V_p}\cdot\left(c_i - c_i^m\right) \tag{3-32}$$

where k_i^p refers to the combined macropore LDF coefficient that can be obtained based on the correlation published by Nakao and Suzuki (1983):

$$k_i^p \frac{A_p}{V_p} = \frac{15\cdot\varepsilon_p\cdot D_{p,i}}{r_P^2} \tag{3-33}$$

In the case of applying the LDF model to the micropores, it is possible to state that the temporal evolution of the concentration in the adsorbed phase is proportional to

the difference between the one predicted using the equilibrium isotherm for the concentration of the adsorbing species in the macropores (q_i^*) and the current value of the concentration of the adsorbed phase, as shown in Eq. (3-34). Eq. (3-34) therefore replaces eq. (3-31):

$$\frac{d\bar{q}_i}{dt} = k_i^{cr} \frac{3}{r_p} \cdot \left(q_i^* - \bar{q}_i\right) \tag{3-34}$$

where k_i^{cr} is the combined micropore LDF coefficient and can be estimated by using eq. (3-35):

$$k_i^{cr} \frac{3}{r_c} = \frac{15 \cdot \varepsilon_{cry} \cdot D_{\mu,i}}{r_c^2} \tag{3-35}$$

The LDF approximation reduces the complexity of the computational implementation of the problem and it has had great success in modelling PSA cycles, as reported by Sircar and Hufton (2000).

3.4.3 Energy balance

Assuming that thermal equilibrium is instantaneous between the gas phase and the pellet ($T_f = T_p$) and considering a constant wall temperature, the energy balance can be expressed as:

$$\varepsilon \cdot \frac{\partial U_f}{\partial t} + (1-\varepsilon) \cdot \frac{\partial U_P}{\partial t} + \varepsilon \cdot \frac{\partial \left(H_f \cdot v\right)}{\partial z} + \frac{\partial J_T}{\partial z} + \sum_{i=1}^{n} \frac{\partial \left(J_i \tilde{H}_i\right)}{\partial z} + h_w \cdot \frac{A_c}{V_c} \cdot \left(T_f - T_w\right) = 0 \tag{3-36}$$

$$\frac{dU_P}{dt} = \varepsilon_P \cdot \frac{dU_{P,f}}{dt} + \left(1-\varepsilon_P\right) \cdot \frac{dU_{P,s}}{dt} \tag{3-37}$$

$$J_T = -k_z \cdot \varepsilon \cdot \frac{\partial T_f}{\partial z} \tag{3-38}$$

Here v is the interstitial flow velocity, U_f is the internal energy in the fluid phase per unit volume, U_p is the internal energy in the pellet per unit volume, H_f is the enthalpy in the fluid phase per unit volume, $U_{p,f}$ is the internal energy in the macropore per unit volume and $U_{p,s}$ is the internal energy in the solid and sorbate phase per unit volume. The heat transfer coefficient between the bed fluid and the column wall is given by h_w. The thermal axial dispersion is represented by k_z. The boundary conditions for the gas phase concentrations and the enthalpy are given by the Danckwerts boundary conditions for flow into the column and the no diffusive flux

for flow out of the column. With the conventions that the positive flow direction is from 0 to L, these can be written in a combined form as:

$$J_T\big|_{z=0} = \frac{v+|v|}{2}\left(H_{f,0-} - H_{f,0}\right) \tag{3-39}$$

$$J_T\big|_{z=L_c} = \frac{v-|v|}{2}\left(H_{f,L_c+} - H_{f,L_c}\right) \tag{3-40}$$

where the superscripts − and + indicate the concentration values to the left and right of the boundary, respectively. The constitutive equations for the energy terms are given by:

$$U_f = U_{ref} + \int_{T_{ref}}^{T} c_T c_V dT' \tag{3-41}$$

$$H_f = H_{ref} + \int_{T_{ref}}^{T} c_T c_P dT' \tag{3-42}$$

$$U_p = \varepsilon_p U_{p,f} + \left(1-\varepsilon_p\right) U_{p,s} \tag{3-43}$$

$$U_{p,f} = U_{p,ref} + \int_{T_{ref}}^{T} c_T^m c_V dT' \tag{3-44}$$

$$U_{p,s} = U_{sol} + U_{ads} \tag{3-45}$$

$$U_{sol} = U_{sol,ref} + \int_{T_{ref}}^{T_P} \rho_s c_{P,s} dT' \tag{3-46}$$

$$U_{ads} = H_{ads} = H_{ads,ref} + \int_{T_{ref}}^{T_P} q_T c_{P,ads} dT' - \left(-\Delta H_{ads}\right)_{T_p} \tag{3-47}$$

$$\left(-\Delta H_{ads}\right)_{T_p} = \sum_{i=1}^{N_C} \int_0^{q_i} \left(-\Delta H_i\right)_{T_p, q_{j\neq i}} dq_i' \tag{3-48}$$

$$\tilde{H}_i = \tilde{H}_{i,ref} + \int_{T_{ref}}^{T} c_{P,i} dT' \tag{3-49}$$

U_{sol} and U_{ads} are the internal energy per unit volume in the adsorbent and the adsorbed phase, respectively. The total concentration in the fluid phase and in the macropore is given by c_T and c_T^m, respectively. q_T is the total adsorbed concentration in the micropore and $c_{p,sol}$ is the specific heat capacity at constant pressure in the solid phase. The total heat of adsorption per unit volume ($-\Delta H_{ads}$) is calculated from the component heat of adsorptions ($-\Delta H_i$).

The molar heat capacities at constant volume c_v in the fluid phase and at constant pressure in the fluid c_p and in the adsorbed phase $c_{p,ads}$ are calculated from the respective component heat capacities in the following way:

$$c_v = \sum_i^n y_i \cdot c_{v,i} \;;\; c_p = \sum_i^n y_i \cdot c_{p,i} \;;\; c_{p,ads} = \sum_i^n \frac{q_i}{q_T} \cdot c_{p,i} \;;\; c_v^m = \sum_i^n y_i^m \cdot c_{v,i} \tag{3-50}$$

The superscript 'm' indicates the macropore concentrations and heat capacities and y_i are the component mole fractions.

3.4.4 Momentum balance

In most adsorption processes, the adsorbent is contacted by the fluid phase in a packed column. Such variables as the particle size, fluid velocity and bed dimensions determine the pressure drop and have an important impact on the economics of the process since they determine the compression cost as well as the extent of the axial mixing and the heat transfer properties. The pressure drop along the column is estimated using the Ergun equation (Ergun, 1952):

$$-\frac{\partial P}{\partial z}=\frac{150\mu(1-\varepsilon)^2}{d_p^2\varepsilon^2}v+\frac{1.75\rho_g(1-\varepsilon)}{d_p\varepsilon}v|v| \tag{3-51}$$

where μ is the fluid viscosity.

3.4.5 Transport parameters and physical properties of gases

Some transport parameters as well as physical properties of the gas encountered in the previous sections are analysed here in detail. The axial mass dispersion coefficient, D_z, and the axial thermal dispersion coefficient, k_z, are estimated using the correlations by Wakao and Funazkri (1978):

$$\frac{\varepsilon\cdot D_z}{D_m}=20+0.5\cdot Sc\cdot \mathrm{Re} \tag{3-52}$$

$$\frac{k_z}{k_g}=7+0.5\cdot \mathrm{Pr}\cdot \mathrm{Re} \tag{3-53}$$

where k_g is gas thermal conductivity while the other dimensionless parameters are listed in Table 3.4.

Table 3.4: Some dimensionless numbers used in the correlations

Dimensionless number	Definition
Reynolds, Re	$\frac{\rho_g \cdot v \cdot d_p}{\mu}$
Schmidt, Sc	$\frac{\mu}{\rho_g \cdot D_m}$
Prandtl, Pr	$\frac{c_p \cdot \mu}{k_g}$

Heat transfer between packed beds and column wall surroundings has been widely studied. In the one-dimensional model, the overall heat transfer resistance may be represented by the sum of internal, external and wall resistances (Ruthven, 1984):

$$\frac{1}{h_w} = \frac{1}{h_{\text{int}}} + \frac{D_c}{D_{c,ext} \cdot h_{ext}} + \frac{D_c \cdot x}{k_w \cdot D_{lm}} \tag{3-54}$$

where x is the wall thickness ($D_{c,ext} = D_c + 2x$), k_w is the wall thermal conductivity and D_{lm} is the logarithmic mean diameter. Cooling at the external surface is normally by natural convection and hence this term can be generally neglected considering the same temperature between the external surface and the surroundings. For metal-walled vessels, the heat transfer resistance of the wall is usually neglected; but, of course, this term becomes important if the wall is insulated. The heat transfer coefficient at the internal surface may be estimated Wasch and Froment's correlation (1972):

$$h_{\text{int}} = \frac{k_g}{D_c} \cdot \left(140 + 0.013396 \cdot \frac{D_c^2}{d_p \cdot k_g} \cdot \text{Re} \right) \tag{3-55}$$

Gas density was evaluated applying the ideal gas law:

$$\rho_g = \frac{P \cdot \overline{M}}{R \cdot T} \tag{3-56}$$

The heat capacity at constant pressure of component i was calculated using a polynomial function of temperature (Poling et al., 2001):

$$c_{p,i} = A + B \cdot T + C \cdot T^2 + D \cdot T^3 + E \cdot T^4 \tag{3-57}$$

The viscosity of a pure gas was calculated according to the first order Chapman–Enskog equation (Poling et al., 2001):

$$\mu_i = 2.669 \cdot 10^{-6} \cdot \frac{(M_i \cdot T)^{0.5}}{\varepsilon_i \cdot \Omega_\mu} \tag{3-58}$$

where μ_i is in Pa·s and Ω_μ is related to the Lennard–Jones parameters of component i. The viscosity of the gas mixture was calculated using the Wilke method (Poling et al., 2001):

$$\mu = \sum_i^n \frac{y_i \cdot \mu_i}{\sum_j^n y_j \cdot \Phi_{ij}} \tag{3-59}$$

where Φ_{ij} is function of the viscosities and molecular weights of the i,j components.

The thermal conductivity of a pure gas was calculated according to the following equation proposed by Eucken (Poling et al., 2001):

$$k_{g,i} = \left(\hat{c}_{p,i} + 1.25 \cdot \frac{R}{M_i} \right) \cdot \mu_i \tag{3-60}$$

Gas mixture thermal conductivity was evaluated using the Wassiljewa method (Poling et al., 2001):

$$k_g = \sum_i^n \frac{y_i \cdot k_{g,i}}{\sum_j^n y_j \cdot \Phi_{ij}} \tag{3-61}$$

A detailed explanation of the units of measurements for these entities is given in the list of symbols at the beginning of the thesis.

3.5 Industrial use of adsorption for gas separation

Large-scale adsorptive processes may be conveniently divided into two broad classes; cyclic batch systems, in which the adsorbent bed is alternately saturated and regenerated in a cyclic manner, and continuous flow systems, generally involving continuous contact between feed and adsorbent. It is also convenient to distinguish between purification processes, where the aim is to remove an undesirable component or components from a feed stream, and concentration processes, where the valuable component or components are the most strongly adsorbed ones, which need to be recovered. An example of the first case is a H_2 purification process while an example of the latter is a CO_2 enrichment process. The process schemes used in these types of separation are obviously somewhat different although the general

principles of design and operation are similar. Four basic sorbent regeneration methods are in common employed although combinations of two or more methods may also be used with advantage in particular situations (Ruthven, 1984):

- *Thermal swing*: the bed is regenerated by heating, usually with a stream of hot gas, to a temperature at which the adsorbed species are desorbed and removed from the bed into the fluid stream
- *Pressure swing*: desorption is accomplished by reducing the pressure and then purging the bed at the low pressure. The basic difference between the pressure swing and thermal swing operations is shown schematically in Figure 3.9
- *Purge gas stripping*: the bed is regenerated at essentially constant pressure by purging with a non-adsorbing inert gas. This method of regeneration is applicable only when the adsorbed species are weakly held
- *Displacement desorption*: the temperature and pressure are maintained essentially constant but instead of an inert purge the adsorbed species are displaced by a stream containing a competitively adsorbed species

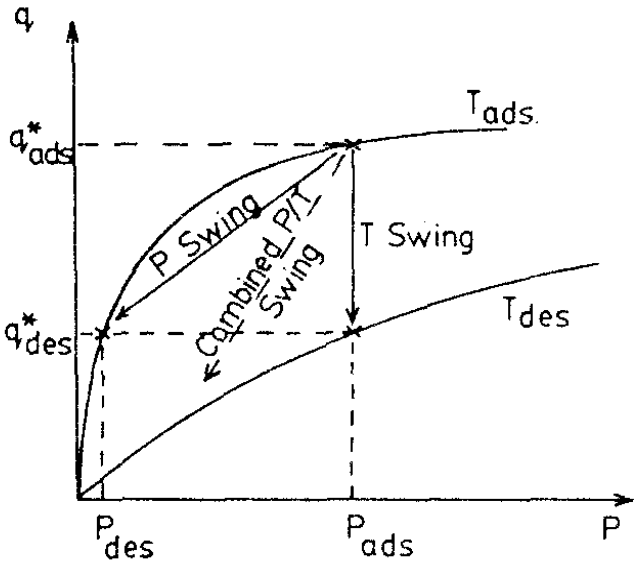

Figure 3.9: Schematic isotherms showing pressure swing, thermal swing and combined pressure–temperature swing operation for an adsorption process (Ruthven et al., 1984)

In case of thermal swing adsorption (TSA), the difference of temperature is the driving force for the separation. TSA cycles are mainly employed in gas purification

processes for which the concentration of the adsorbing specie is relatively low (Sircar, 2001) like the case of gas sweeting systems or processes for air pollution control; only in the case of gas drying TSA is used industrially for bulk gas separation. The simplest configurations for TSA cycles operate with two beds, one in which the adsorption takes place and the second where the desorption is carried out to provide continuity of flow. For the regeneration of the bed, the hot stream is circulated in a reverse way so that any possible residue of the sorbate remaining at the end of the desorption cycle is concentrated at the bed inlet and does not affect the raffinate purity in the subsequent adsorption cycle. The design and optimisation of TSA cycles is extensively reported in the literature (Merel et al., 2006; Davis and Levan, 1989; Ruthven, 1984).

In pressure swing adsorption (PSA) systems the regeneration of the adsorbent during the desorption cycle is achieved simply by reducing the total pressure and by purging the bed at low pressure with a small fraction of the stream that leaves from the column in which the adsorption step is taking place. The most basic PSA configurations consist of two beds, which are alternately pressurised and depressurised according to a pre-programmed sequence. The major advantage of PSA cycles comparing with other separation techniques is based on the fact that the pressure can be changed much more rapidly than the temperature, thus a PSA process can be operated on a much faster cycle and thus an increase of the throughout per unit of adsorbent bed volume will be observed (Ruthven, 1984). The first commercial uses of PSA cycles dated from the late 1960s with the patents by Guerrin de Montgareuil and Domine (US patent No. 3155468, 1964) and Skarstrom (US Patent No. 2944627, 1960); nowadays the PSA systems are widely used for the separation of N_2 and O_2 from air.

Any PSA cycle can be considered as a sequence of elementary steps, the most common of which are:

- Pressurisation, with feed or raffinate product
- High-pressure feed adsorption
- Depressurisation or “blowdown”, cocurrent or countercurrent to the feed

- Desorption at the lower operating pressure; this may be accomplished by evacuation or purging the bed with the raffinate product
- Pressure equalisation, which is used in many cycles, prior to the blowdown step, to conserve energy and for separative work

The processes differ from one another in the sequence of the elementary steps and in the way in which these steps are carried out. In the original Skarstrom cycle, two packed adsorbent beds were used for heatless drying process, as shown schematically in Figure 3.10.

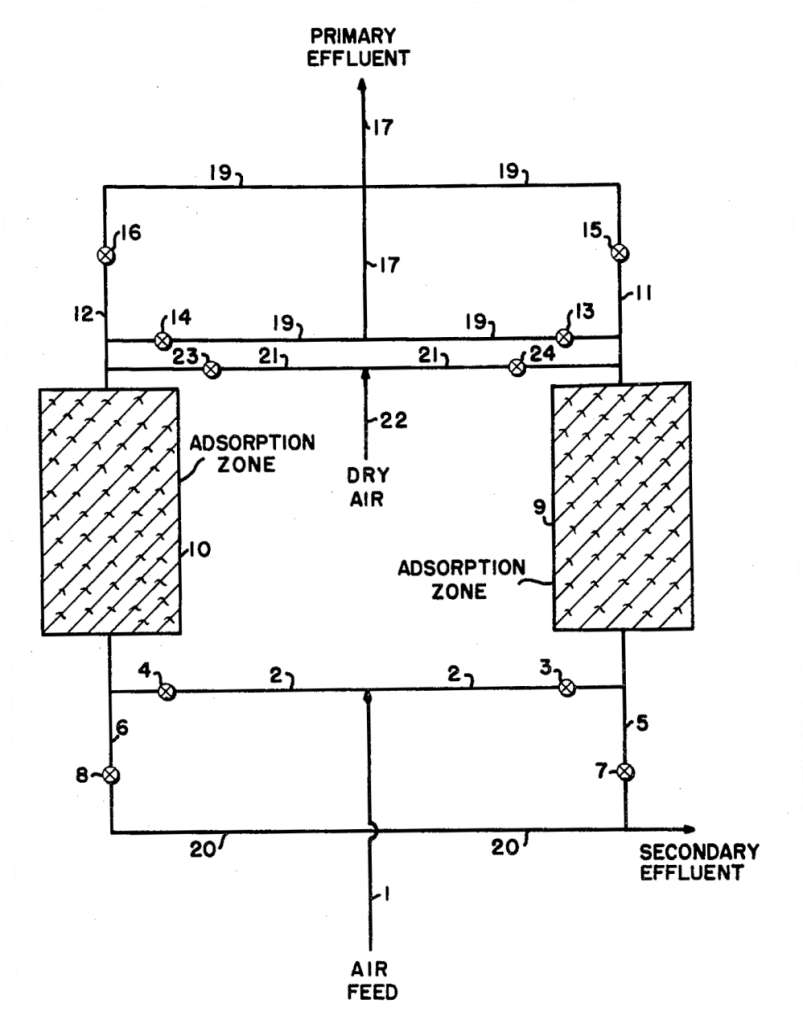

Figure 3.10: The basic two-bed pressure swing adsorption system (Skarstrom, 1960)

The following four steps comprise the cycle: adsorption, countercurent blowdown, countercurrent purge and feed pressurisation. Both beds undergo these four operations and their sequence is shown in Figure 3.11.

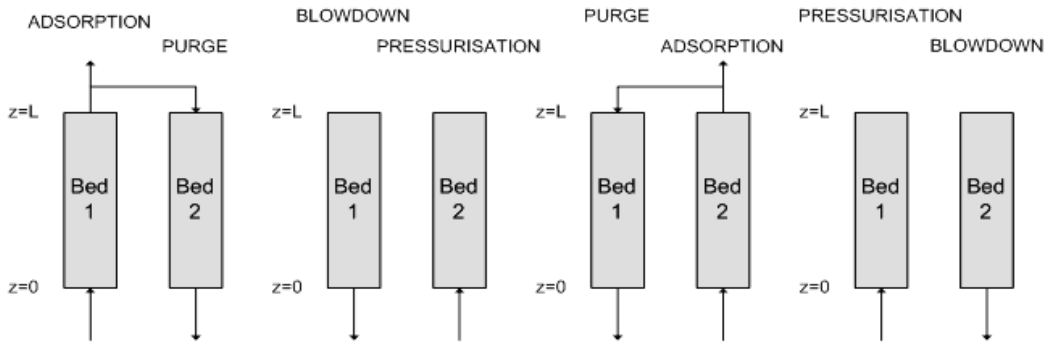

Figure 3.11: The sequence of steps in the basic Skarstrom cycle

Another successful application of the Skarstrom cycle is oxygen production from air using 5A or 13X zeolite.

From a thermodynamic perspective, the essential difference between PSA and TSA is that in the PSA system the energy required to achieve the separation is put into the system as mechanical work rather than heat. Since mechanical energy is generally more expensive than heat, efficient utilisation of energy is essential for an economical PSA system. Such considerations become especially important in the larger-scale units. A pressure swing system is well suited to rapid cycling and generally operates at relatively low adsorbent loadings since selectivity is greatest in the Henry's law region. Low-temperature operation is also desirable to maximise capacity and selectivity but cooling below ambient temperature is generally not economical. The purging step is essential for an efficient separation. Reverse-flow purge ensures that the more strongly adsorbed components are pushed back towards the bed inlet and prevents the raffinate product in the following cycle end from being contaminated by the more strongly adsorbed component. It is essential that sufficient purge flow is used to flush completely the void spaces within the bed as well as to desorb any of the more strongly adsorbed components from the outlet region of the bed. Product purity increases as the purge flow increases, but after a certain point the gain becomes marginal. In practice the volume of the purge flow, measured at low pressure, should generally be between one and two times the volume of the feed stream (Ruthven, 1984). The increase in gas volume by depressurisation means that the actual fraction of the product stream required for purging is quite small and varies with the operating pressures. Thus, high-pressure operation during adsorption

is desirable from the standpoint of minimising purge loss but this gain is to some extent offset by the greater blowdown losses for a high-pressure system.

The first improvement over Skarstrom's original cycle was the introduction of a pressure equalisation step proposed by Berlin (1966). After the first bed is purged and the second bed completes the high-pressure adsorption step, instead of blowing down the second bed, the two beds are connected through their product ends to equalise the pressure. The pressure equalisation step conserves energy since the compressed gas from the high-pressure bed is used to partially pressurise the low-pressure bed and, since this gas is partially depleted of the strongly adsorbed species, separative work is also conserved. Blowdown losses are reduced to about half, with a consequent improvement in the recovery of the raffinate product.

Further improvements in efficiency are generally achievable by using multiple adsorption beds in order to incorporate pressure equalisation steps into the cycle (Davis, 1972; Batta, 1971). In fact, multiple bed systems also enable the blowdown gas to be used for purging other beds. Examples can be found in air separation and hydrogen purification units. Moreover, the idea of product repressurisation was put forward for the first time in a patent by Wagner (1969). Pressurisation with product pushes the residual adsorbed components toward the feed end of the adsorber, thereby enhancing the product purity. In multiple bed systems, greater conservation of energy and separative work are achieved at the cost of a more complex process scheme. In some large-scale hydrogen purification PSA systems up to 12 adsorbent beds have been designed so far (Yang, 1987).

Another modification is a vacuum swing cycle, originally proposed by Guerin and Domine (1964). In comparison to the original Skarstrom cycle, the vacuum swing cycle can be discerned in that the low-pressure countercurrent product purge step is replaced by a vacuum desorption. The product end of the column is kept closed and the vacuum is pulled through the feed end. The gain in raffinate recovery is achieved at the expense of the additional mechanical energy required for the evacuation step. A significant energy saving is possible if the cycle is operated with a high pressure slightly above atmospheric pressure and a very low desorption pressure (Ruthven et al., 1994). A vacuum swing cycle will therefore be advantageous over a Skarstrom cycle if a low-pressure product is valuable.

3.6 PSA process for hydrogen purification

Hydrogen purification is a necessary step in the production of hydrogen, which at present is done by catalytic steam reforming of natural gas, naphtha or refinery gases. It is also of use to recover hydrogen from catalytic reformer effluent gas, ethylene plant effluent gas and ammonia plant purge gas, in addition to a number of other sources (Yang, 1987). Since the first commercial PSA hydrogen purification plant was installed in Toronto in 1966 (Stewart and Heck, 1969), it has become the largest use of PSA in terms of both cumulative capacity and the number of installed units. The compositions of the three major gas mixture sources for PSA hydrogen purification are:

- Steam methane reformer effluent (after water gas shift): 70–75% (by volume) hydrogen. The major impurity is CO_2, with smaller amounts of CO, CH_4 and sometimes N_2
- Catalytic reformer effluent: 65–85% hydrogen. The primary impurity is methane, with lesser amounts of C_2–C_5 hydrocarbons
- Ethylene plant effluent: 70–90% hydrogen, with methane as the main impurity

The success of PSA hydrogen purification is largely due to the high selectivities for the impurity gases over hydrogen. Out of the commercial sorbents applicable for H_2 PSA, a combination of activated carbon and zeolites is used in practice. For example, in the four-bed UOP process each bed is packed with activated carbon near the inlet in the first section, whereas 5A zeolite is packed in the second section (Fuderer and Rudelstorfer, 1976). Presumably, the carbon section acts as a guard bed, mainly adsorbing and desorbing carbon dioxide and methane, while the zeolite layer removes carbon monoxide and nitrogen. For capacities below 15 MMSCF/D, the four-bed configuration based on Batta's patent is employed (1971). For larger sizes, UOP's Polybed process, based on the patent of Fuderer and Rudelstorfer (1976), has proved more economical. The Polybed process has a single-train capacity up to 40 MMSCF/D (Heck and Johansen, 1978; Corr et al., 1979). Cycle performances are evaluated according to the common parameters of H_2 purity, H_2 recovery and H_2 productivities defined as follows:

$$H_2\ Purity = \frac{\int_0^{t_{AD}} C_{H_2} u\big|_{z=L}\, dt}{\sum_i^n \int_0^{t_{AD}} C_i u\big|_{z=L}\, dt} \tag{3-62}$$

$$H_2\ Recovery = \frac{\int_0^{t_{AD}} C_{H_2} u\big|_{z=L}\, dt - \int_0^{t_{PR}} C_{H_2} u\big|_{z=L}\, dt}{\int_0^{t_{AD}} C_{H_2} u\big|_{z=0}\, dt} \tag{3-63}$$

$$H_2\ Productivity = \frac{\left(\int_0^{t_{AD}} C_{H_2} u\big|_{z=L}\, dt - \int_0^{t_{PR}} C_{H_2} u\big|_{z=L}\, dt\right) \cdot A_c}{t_{cycle} \cdot m_{ads}} \tag{3-64}$$

Both processes can yield hydrogen at purities higher than 99.99%. The product recovery for the four-bed process is 70–75%, whereas an improvement to 85–90% is achieved by the Polybed process.

In both processes, the cycle steps are: (1) adsorption, (2) cocurrent depressurisation, (3) countercurrent blowdown, (4) purge and (5) repressurisation. The effluent gas from one bed is used to purge and repressurise other beds, the latter being referred to as pressure equalisation. The difference between these processes lies in the number and sequence of pressure equalisation steps, which yield significant differences in separation results.

The four-bed process is illustrated in Figure 3.12.

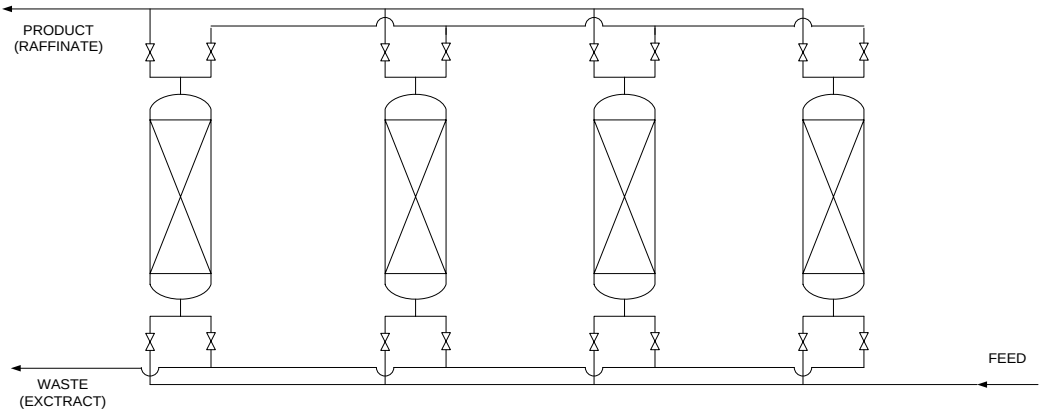

Figure 3.12: UOP four-bed PSA system (Batta, 1971)

During the high-pressure adsorption step, a substantial fraction of the bed is not covered by the deepest-reaching wavefront. Although the wavefronts are sharp, the uncovered portion of the bed is not clean in a cyclic steady state because of the accumulated impurities. With a limited number of beds, as in the four-bed process,

only two pressure equalisation steps can be included in the cycle. The purge step is completed with the discharge gas from another bed undergoing the providing purge step. The final repressurisation is performed by the pure high-pressure product gas from another bed. Because of the limited number of pressure equalisation steps and large amount of product gas required for final repressurisation, the product recovery can reach only 70–75%, at 99.99% to 99.999% purity, in the four-bed process (Yang, 1987).

As the number of beds is further increased, more pressure equalisation steps can be adapted and the beds become cleaner at a cyclic steady state. Consequently, the product gas required for final repressurisation is also reduced. The net result is a higher product recovery at the same product purity. The Polybed process contains seven to twelve beds, with at least three pressure equalisation steps and at least two receiving the feed gas during the entire cycle. Figure 3.13 illustrates the typical UOP nine-bed system. Three of the nine beds are undergoing an adsorption step at any given time.

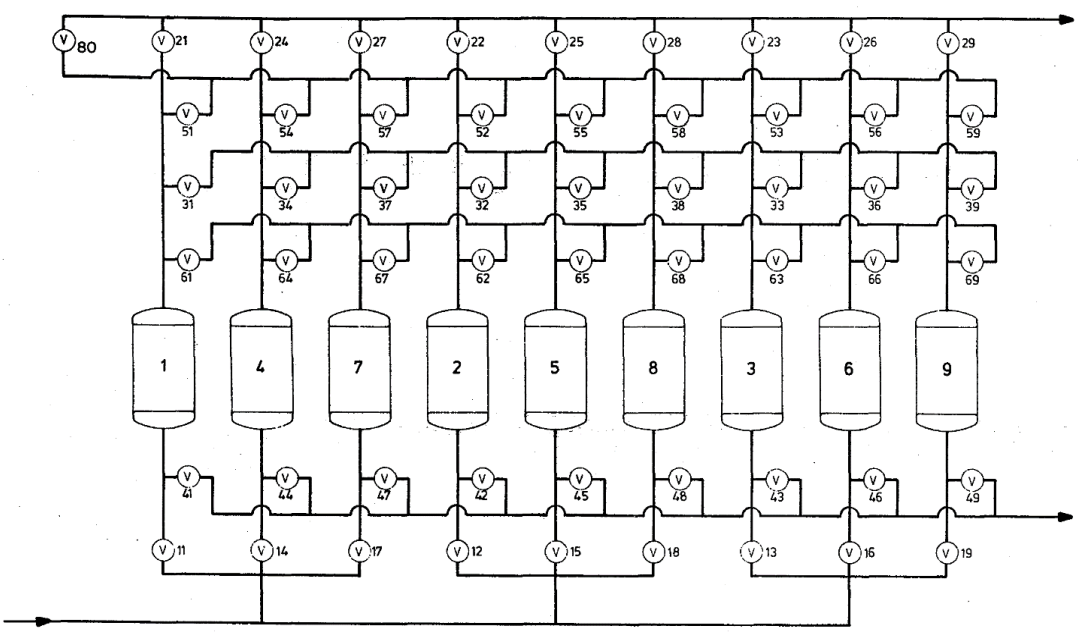

Figure 3.13: UOP Polybed process for hydrogen purification (Fuderer and Rudelstorfer, 1976)

The economics of both the four-bed and Polybed process were well evaluated by Stewart and Heck (1969) and Heck and Johansen (1978). The unit hydrogen product cost for the PSA-based hydrogen plants is 5–7% lower than the conventional

cryogenic and scrubbing (Stewart and Heck, 1969; Heck and Johansen, 1978). For high-purity hydrogen production, 5A zeolite is used as the sorbent. Activated carbon is not used because its selectivity for impurity/hydrogen is not high enough.

The literature contains a large amount of work on hydrogen purification by PSA processes, both from an experimental and a modelling point of view. Table 3.5 summarises all these studies.

Table 3.5: Summary of research works on hydrogen purification by PSA processes

Reference	Type of work	Description
Yang et al., 1997	Modelling/ experimental	The authors studied a two-bed six-step pressure swing adsorption process using zeolite 5A experimentally and theoretically for bulk separation of H_2/CO and H_2/CH_4 systems (70/30 mol%) as major components in coke oven gas. With a cycle pressure between 1 and 11 atm at ambient temperature, 70% H_2 in the feed could be concentrated to 99.99% in the product with a recovery of 75.9% in the H_2/CO mixture and 80.4% in the H_2/CH_4 mixture. The effects of adsorption pressure, P/F ratio, adsorption/purge step time, and pressure equalisation step time were investigated experimentally and all the results were analysed by a mathematical model incorporating heat and momentum balances.
Yang and Lee, 1998	Modelling/ experimental	The authors investigated the adsorption dynamics of a layered bed packed with activated carbon and zeolite 5A. A two-bed PSA process was studied experimentally and theoretically for a coke oven gas purification (56.4% H_2, 26.6% CH_4, 8.4% CO, 5.5% N_2, 3.1% CO_2). The layered bed PSA process was simulated as two single-adsorbent beds linked in series. The dynamic model incorporating mass, energy and momentum balances agreed well with the experimental data.
Ahn et al., 1999	Modelling/ experimental	The authors studied a backfill cycle of a two-bed PSA process using activated carbon beds, zeolite 5A beds and layered beds to recover high-purity hydrogen from coke oven gas. In a layered bed PSA, a comparison was made between two PSA processes with/without a backfill step before the feed pressurisation step. The incorporation of a backfill step

		resulted in an increase in product purity with a decrease in recovery. The highest recovery for an ultrapure hydrogen stream was 68%. The concentration profiles predicted by simulation showed that CO and N_2 played an important role in obtaining high H_2 purity.
Lee et al., 1999	Modelling/ experimental	The authors studied the effects of carbon-to-zeolite ratio on a layered bed H_2 PSA using activated carbon and zeolite 5A from coke oven gas. The PSA system consisted of a seven-step two-bed configuration. The layered bed gave better purity than the single-adsorbent bed at the same operating conditions, except at low purge rate. For a high-purity H_2 product an optimum carbon-to-zeolite ratio was determined to control a leading wavefront of N_2.
Lee et al., 2008	Modelling/ experimental	The authors developed a heat-exchange pressure swing adsorption to design a compact H_2 PSA process for small spatial occupancy in the hydrogen station for fuel cell commercialisation. The adsorption dynamics and performance of the newly designed bed were compared with those of a conventional bed by using a feed mixture obtained from a SMR process. It was found that the HE-PSA performance was higher because the heat effects were reduced by the heat exchange between the adsorption beds.
Ahn et al., 2012	Modelling/ experimental	The authors focused on a PSA process involving layered two- and four-bed systems for H_2 recovery from coal gas with relatively low H_2 concentrations (38% H_2, 50% CO_2, 1% CH_4, 1% CO, 10% N_2). The variations of purity and recovery by operating variables were more significant in the two-bed PSA process than in the four-bed one. It was shown that the four-bed PSA process was able to produce H_2 with a purity of 96–99.5% and a recovery of 71–85% together with N_2 as the major impurity.
You et al., 2012	Modelling/ experimental	The authors developed a two-bed PSA purifier to produce high purity hydrogen for fuel cell applications. Two feeds were considered containing H_2 and CO in the ratios of 99/0.85% and 95/4.55% plus other impurities. Under 6.5 bar and 0.15 P/F ratio the first feed was purified to 1.1 ppm CO with 99.99+% H_2 purity and 80% recovery while the second feed could be reduced to 6.7 ppm with 99.96% H_2 purity and

		78.4% recovery. The PVSA process, which combined vacuum and purge steps, improved recovery by around 10% compared to the PSA process.
Park et al., 2000	Modelling/ experimental	The authors investigated a hydrogen purification process from a typical cracked gas mixture (72.36% H_2, 21.18% CO_2, 2.49% CO, 3.97% CH_4) at 23.6 atm by a layered four-bed PSA process. The roles of the height of the activated carbon layer, the superficial velocity of feed and the heat-transfer resistance on the process were assessed. All the experimental results were well predicted by the theoretical model. There was an optimum carbon-to-zeolite layer, which maximises not only the H_2 recovery, but also the productivity at the given H_2 purity. It was found that for a 99.99% H_2 purity the optimum carbon-to-zeolite ratio is 1.5.
Yang et al., 2008	Modelling/ experimental	The authors evaluated the performance of a four-bed nine-step PSA process for producing high-purity hydrogen from synthesis gas using layered beds of activated carbon and zeolite 5A. The effect of the following PSA variables on separation process were investigated: linear velocity of feed, adsorption time and purge gas quantity. As a result, they recovered 99.999% ultrapure hydrogen with a recovery of 66% when the pressure was cycled between 1 and 8 atm at ambient temperature.
Jang et al., 2011	Modelling/ experimental	The authors optimised the performance of an adsorption layered bed consisting of zeolite 5A and activated carbon for multicomponent gas separation (72.2% H_2, 21.6% CO_2, 2.03% CO, 4.17% CH_4). At a pressure of 8 atm with a 16.67 L/min feed rate it was found that as the carbon ratio increased, the average velocity of CH_4 wavefront became slow, and wavefronts of CO and CO_2 propagated more quickly. To produce ultrapure hydrogen the optimum carbon ratio was evaluated at 0.7.
Ribeiro et al., 2008	Modelling	The authors focused on the separation of hydrogen from a five-component mixture (73.3% H_2, 16.6% CO_2, 3.5% CH_4, 2.9% CO, 3.7% N_2) by PSA. A mathematical model was applied to a four-column PSA process with layered activated carbon/zeolite beds with an eight-step cycle. The predictions of reduced models were evaluated by comparing their results

		with those obtained from the complete model. It was found that the model that merely took into account the micropore resistance and assumed thermal equilibrium between the gas and the solid phases satisfactorily predicted the behaviour of the PSA unit.
Ribeiro et al., 2009	Modelling	The authors studied the purification of hydrogen from synthesis gas at 7 bar saturated in water vapour. Simulation results of a four-bed eight-step PSA process were presented using an activated carbon as the adsorbent. Several operating conditions were considered, such as different flow rates, humid/dry feed and adiabatic/non-adiabatic operation. Simulation results of a single-column PSA and a multi-column system were also shown in detail. At the same hydrogen purity of 99.999%, the recovery was decreased from 71.3% to 62.7%.
Lopes et al., 2011	Modelling/ experimental	The authors performed multicomponent breakthrough experiments up to a five-component mixture of H_2-CO_2-CO-CH_4-N_2 under different operating conditions in activated carbon extrudates to validate the mathematical model. A 10-step one-column VPSA experiment was also carried out. The mathematical model was then employed to assess the effect of operating conditions and the influence of step times and pressure equalisations in the PSA unit. It was verified that high-purity hydrogen (99.99+%) can be obtained at 5 bar feed using this adsorbent with recoveries higher than 75% and unit productivities of 160 $mol_{H2}/kg_{ads}/d$.
Silva et al., 2013	Modelling/ experimental	The authors performed hydrogen purification experiments by PSA using CuBTC (supplied by KRICT) MOF as adsorbent. The PSA system consisted of a four-step cycle and the experiments were performed starting from different feeds (CO_2/H_2, $CO_2/H_2/CH_4$, $CO_2/H_2/CO$ and $CO_2/H_2/N_2$). Although the PSA cycles carried out experimentally were not optimised, the mathematical model was validated successfully and it can be used for the prediction of PSA experiments, saving time, money and number of required experiments.
Kumar et al., 1995	Modelling	The authors proposed a new process concept to utilise low- and high-pressure feed streams efficiently in a single PSA

		process. The low-pressure feed is processed first in the PSA unit to produce low-pressure product. Following this, the high-pressure stream is processed in the same unit. The low pressure generated in the first part of the process is used internally in the process to assist the production of high-pressure product. Considering a 25% CH_4 / 75% H_2 mixture, the simulation showed that both recovery and adsorbent productivity could be enhanced.
Malek and Farooq, 1998	Modelling/ experimental	The authors investigated the performance of a six-bed, dual sorbent PSA operation for hydrogen purification from refinery fuel gas. Major impurities were methane, ethane, propane and butane, and comprised 30–40% of the feed. The dual-sorbent PSA bed consisted of an initial layer of silica gel followed by an activated carbon layer. The simulation model agreed well with the experimental results from a laboratory unit as well as with available H_2-PSA plant data from a refinery.
Jiang et al., 2004	Modelling	The authors developed a general PSA unibed framework model simulating only one bed over a cycle and using storage buffers to mimic the bed interactions. A five-bed 11-step hydrocarbon separation process, which separates H_2 from a mixture of H_2, N_2, CO, CO_2 and CH_4, was used for illustration. By manipulating valve constants, step times, flow rates and bed geometry, the optimiser successfully maximised H_2 recovery, while meeting product purity and pressure specifications.
Huang et al., 2008	Modelling/ experimental	The authors optimised a PSA process for producing enriched hydrogen from plasma reactor gas using gPROMS software. The extensive simulation results involving parametric studies of PSA separation performance were well matched with experimental results using an activated carbon made from coconut shell as an adsorbent. The investigated mixtures were binary systems consisting of 50% H_2, 50% CH_4 and 25% H_2, 75% CH_4, representing exit gas from a plasma reactor.
Majlan et al., 2009	Experimental	The authors designed a compact pressure swing adsorption system to produce purified hydrogen for use in fuel cells with activated carbon as the adsorbent. With a four-bed system,

		the CPSA was capable of reducing the CO concentration in a $H_2/CO/CO_2$ mixture from 4000 to 1.4 ppm and the CO_2 concentration from 5% to 7.0 ppm in 60 cycles and 3600 s. Based on the mixture used in the experimental work, the H_2 purity obtained was 99.999%, suitable for fuel cell applications.
Casas et al., 2013	Modelling	The authors carried out a multi-objective optimisation of a PSA process for pre-combustion capture within an IGCC power plant having the CO_2 purity and recovery as objectives. The results were presented in detail using sets of optimal operating points, the so-called Pareto fronts. The separation performance was found to mainly depend on the operating temperature, on the adsorption pressure at which H_2 is produced and on the desorption pressure at which CO_2 is produced.
Rahimpour et al., 2013	Modelling/ experimental	The authors developed a mathematical model to simulate the industrial four-bed layered PSA unit of a domestic petrochemical plant that operates for purification of hydrogen. The effects of cycle time and feed flow rate on hydrogen recovery and purity were investigated and an optimal value was estimated for cycle time and feed flow rate. It was shown that by applying this optimum configuration, H_2 recovery increased from 75% to 80% with almost the same H_2 purity.
Yavary et al., 2015	Modelling	The authors focused on the performance of a six-bed PSA process for hydrogen purification in terms of cycle sequence and number of pressure equalisation steps employed. Simulation results showed that designs with more pressure equalisation steps resulted in higher product recovery while for higher product purity, loss of product in a PSA process was more significant. In addition, a target function including implicit economic factors for choosing the better PSA design was presented and discussed.

3.7 Conclusions

The use of adsorption as a gas separation unit operation has been discussed in this chapter, starting from the fundamentals of adsorption equilibrium and kinetics

and explaining how they may influence the modelling and the simulation of the mass, energy and momentum balance equations. The linear driving force model was also shown in detail as well as how to calculate all the transport parameters and gas properties.

An extensive literature review regarding the application of adsorption as a gas separation unit operation at the industrial level has been presented, starting from the original Skarstrom cycle and proposing successive modifications, such as the incorporation of pressure equalisation steps, the multibed system and the vacuum pressure swing adsorption process. It was highlighted that for hydrogen purification processes the valuable product is the raffinate, which is produced during the high-pressure adsorption step. PSA cycle performance parameters of purity, recovery and productivity have been introduced and explained for this type of separation.

An extensive literature survey has been conducted on H_2 purification processes by PSA systems.

References

Ahn H, Lee CH, Seo B, Yang J, Baek K. Backfill cycle of a layered bed H_2 PSA process. Adsorption 1999; 5: 419-433.

Ahn S, You YW, Lee DG, Kim KH, Oh M, Lee CH. Layered two- and four-bed PSA processes for H_2 recovery from coal gas. Chemical Engineering Science 2012; 68: 413-423.

ALOthman ZA. A review: fundamental aspects of silicate mesoporous materials. Materials 2012; 5: 2874-2902.

Averill BA, Eldredge P. General Chemistry: principles, patterns and application, 2007.

Batta LB. US Patent No. 3564816, to Union Carbide Corporation, 1971.

Berlin NH. US Patent No. 3280536, to Exxon Research and Engineering, 1966.

Brunauer S, Emmet PH, Teller E. Adsorption of gases in multi-molecular layers. J. Am. Chem. Soc. 1938; 60: 309-319.

Casas N, Schell J, Joss L, Mazzotti M. A parametric study of a PSA process for pre-combustion CO_2 capture. Separation and Purification Technology 2013; 104: 183-192.

Corr F, Dropp F, Rudelstorfer E. Hydrocarbon Processing 1979; 58: 19.

Danckwerts PV. Continuous flow systems. Chemical Engineering Science 1953; 2: 1-13.

Davis MM, Levan DM. Experiments and optimization of thermal swing adsorption. Ind. Chem. Res. 1989; 28: 778-785.

Davis JC. Chemical Engineering 1972; 16: p.88.

Ergun S. Fluid flow through packed columns. Chem. Eng. Prog. 1952; 48: 89-94.

Fuderer A, Rudelstorfer E. US Patent No. 3986849, to Union Carbide Corporation, 1976.

Glueckauf E. Theory of Chromatography VII. The general theory of two solutes following non-linear isotherms. Discuss. Faraday Soc. 1949; 7: 12-25.

Guerin P, Domine D. US Patent No. 3155468, to Société L'Air Liquide, 1964.

Heck JL, Johansen T. Hydrocarbon Processing 1978; 57: 175-177.

Huang Q, Malekian A, Eic M. Optimisation of PSA process for producing enriched hydrogen from plasma reactor gas. Separation&Purification Technology 1998; 62: 22-31.

IUPAC. Recommendations Pure Applied Chemistry 1985; 57: 603.

Jang SC, Yang SI, Oh SG, Choi DK. Adsorption dynamics and effects of carbon to zeolite ratio of layered bed for multicomponent gas adsorption. Korean J. Chem. Eng. 2011; 28: 583-590.

Jiang L, Fox G, Biegler LT. Simulation and optimal design of multiple-bed pressure swing adsorption systems. AIChE Journal 2004; 50: 2904-2917.

Kapoor A, Yang RT, Wong C. Surface diffusion. Catal. Rev. Sci. Eng. 1989; 31: 129-214.

Keller GE, Anderson RA, Yon CM. Handbook of Separation Process Technology, 1987.

Kumar R, Guro DE, Schmidt WP. A new concept to increase recovery from H_2 PSA: processing different pressure feed streams in a single unit. Gas. Sep. Purif. 1995; 9: 271-276.

Kyriakopoulos G, Doulia D. Adsorption of pesticides on carbonaceous and polymeric materials from aqueous solution: a review. Separation & Purification Reviews 2006; 35: 97-191.

Langmuir I. The adsorption of gases on plane surfaces of glass, mica and platinum. J. Chem. Soc. 1918; 40: 1361-1403.

Lee CH, Yang J, Ahn H. Effects of carbon-to-zeolite ratio on layered bed H_2 PSA for coke oven gas. AIChE Journal 1999; 45: 535-545.

Lee JJ, Kim MK, Lee DG, Ahn H, Kim MJ, Lee CH. Heat-exchange pressure swing adsorption process for hydrogen separation. AIChE Journal 2008; 54: 2054-2064.

Li JR, Ma Y, McCarthy MC, Sculley J, Yu J, Jeong HK, Balbuena PB, Zhou HC. Carbon dioxide capture-related gas adsorption and separation in metal-organic frameworks. Coordination Chemistry Reviews 2011; 255: 1791-1823.

Lin SH, Juang RS. Adsorption of phenol and its derivatives from water using synthetic resins and low-cost natural adsorbents: a review. Journal of Environmental Management 2009; 90: 1336-1349.

Lopes FVS, Grande CA, Rodrigues AE. Activated carbon for hydrogen purification by pressure swing adsorption: Multicomponent breakthrough curves and PSA performance. Chemical Engineering Science 2011; 66: 303-317.

Majlan EH, Daud WRW, Iyuke SE, Mohamad AB, Kadhum AAH, Mohammad AW, Takriff MS, Bahaman N. Hydrogen purification using compact pressure swing adsorption system for fuel cell. Hydrogen Energy 2009; 34: 2771-2777.

Malek A, Farooq S. Hydrogen purification from refinery fuel gas by pressure swing adsorption. AIChE Journal 1998; 44: 1985-1992.

Manske M. Sodalite picture (2009) available at https://en.wikipedia.org/wiki/Faujasite

Merel J, Clausse M, Meumier F. Carbon dioxide capture by indirect thermal swing adsorption using 13X zeolite. Environmental Progress. 2006; 25: 327-333.

Nakao S, Suzuki M. Mass transfer coefficient in cyclic adsorption and desorption. J.Chem. Eng. Jpn. 1983; 16: 114-119.

Park JH, Kim JN, Cho SH. Performance analysis of four-bed H_2 PSA process using layered beds. AIChE Journal 2000; 46: 790-802.

Poling BE, Prausnitz JM, O'Connell JP. The properties of gases and liquids, 2001.

Rahimpour MR, Ghaemi M, Jokar SM, Dehghani O, Jafari M, Amiri S, Raeissi S. The enhancement of hydrogen recovery in PSA unit of domestic petrochemical plant. Chemical Engineering Journal 2013; 226: 444-459.

Ribeiro AM, Grande CA, Lopes FVS, Loureiro JM, Rodrigues AE. A parametric study of layered bed PSA for hydrogen purification. Chemical Engineering Science 2008; 63: 5258-5273.

Ribeiro AM, Grande CA, Lopes FVS, Loureiro JM, Rodrigues AE. Four beds pressure swing adsorption for hydrogen purification: case of humid feed and activated carbon beds. AIChE Journal 2009; 55: 2292-2302.

Ruthven DM, Farooq S, Knaebel K. Pressure swing adsorption, 1994.

Ruthven DM. Principles of Adsorption and Adsorption Processes, 1984.

Skarstrom CW. US Patent No. 2944627, to Exxon Research and Engineering company, 1960.

Silva B, Solomon I, Ribeiro AM, Lee UH, Hwang YK, Chang JS, Loureiro JM, Rodrigues AE. H_2 purification by pressure swing adsorption using CuBTC. Separation and Purification Technology 2013; 118: 744-756.

Sircar S. Publications on Adsorption Science and Technology. Adsorption 2000; 6: 359-365.

Sircar S. Applications of Gas Separation by Adsorption for the Future. Adsorpt. Sci. Technol. 2001; 19: 347-366.

Sircar S, Hufton JR. Why Does the Linear Driving Force Model for Adsorption Kinetics Work ? Adsorption 2000; 6: 137-147.

Stewart HA, Heck JL. Pressure swing adsorption. Chem. Eng. Prog. 1969; 65: 78-83.

Suzuki M. Adsorption Engineering, 1990.

Tang F, Li L, Chen D. Mesoporous silica nanoparticles: synthesis, biocompatibility and drug delivery. Advanced Materials 2012; 24: 1504-1534.

Wagner JL. US Patent No. 3430418, to Union Carbide Corporation, 1969.

Wakao N, Funazkri T. Effect of fluid dispersion coefficients on particle-to-fluid mass transfer coefficients in packed beds. Chemical Engineering Science 1978; 33: 1375-1384.

Wang Q, Luo J, Zhong Z, Borgna A. CO_2 capture by solid adsorbents and their applications: current status and new trends. Energy & Environmental Science 2011; 4: 42-55.

Wasch APD, Froment GF. Heat transfer in packed beds. Chemical Engineering Science 1972; 27: 567-576.

Yang RT. Gas separation by adsorption processes, 1987.

Yang J, Lee CH. Adsorption dynamics of a layered bed PSA for H_2 recovery from coke oven gas. AIChE Journal 1998; 44: 1325-1334.

Yang J, Lee CH, Chang JW. Separation of hydrogen mixtures by a two-bed pressure swing adsorption process using zeolite 5A. Ind. Eng. Chem. Res. 1997; 36: 2789-2798.

Yang SI, Choi DY, Jang SC, Kim SH, Choi DK. Hydrogen separation by multi-bed pressure swing adsorption of synthesis gas. Adsorption 2008; 14: 583-590.

Yavary M, Ebrahim HA, Falamaki C. The effect of number of pressure equalisation steps on the performance of pressure swing adsorption process. Chemical Engineering and Processing 2015; 87: 35-44.

You YW, Lee DG, Yoon KY, Moon DK, Kim SM, Lee CH. H_2 PSA purifier for CO removal from hydrogen mixtures. Hydrogen Energy 2012; 37: 18175-18186.

Chapter 4: Design of a H_2 PSA applied to an IGCC with pre-combustion capture

This chapter describes a novel hydrogen pressure swing adsorption system that is applied to an advanced integrated gasification combined cycle plant for cogenerating power and ultrapure hydrogen (99.99+ mol%) with CO_2 capture. In designing the H_2 PSA, it is essential to increase the recovery of ultrapure hydrogen product to its maximum since the power consumption for compressing the H_2 PSA tail gas up to the gas turbine operating pressure should be minimised to save the total auxiliary power consumption of the advanced IGCC plant. This is because a higher hydrogen recovery in the product stream leads to a lower hydrogen flowrate in the tail gas stream, and hence to a lower power consumption at the H_2 PSA tail gas compressor. In this study, it is sought to increase the H_2 recovery by increasing the complexity of the PSA step configuration, which enables the PSA cycle to have a lower feed flow to one column for adsorption and at the same time to include more pressure equalisation steps. As a result, the H_2 recovery reaches a maximum around 93% with a Polybed H_2 PSA system having twelve columns and the step configuration contains simultaneous adsorption on three columns and four-stage pressure equalisation.

4.1 Background of the study

In order to produce power and ultrapure hydrogen, the general approach would consist of employing a PC boiler power plant, for example for power generation, and a conventional steam methane reforming plant for ultrapure hydrogen production. By applying a carbon capture unit to those plants, the effluent gas would be at nearly atmospheric pressure in both cases, resulting in a large energy requirement due to the associated lower CO_2 partial pressure. By contrast, in IGCC power plants carbon dioxide is captured in pre-combustion mode from a stream having a pressure higher than 35 bar. IGCCs run gas turbines using H_2-rich fuel gas (88–91 mol% H_2 purity) in CO_2 capture cases instead of mixtures of CO and H_2 in non-capture cases and it is easy to produce ultrapure hydrogen product by purifying the H_2-rich fuel gas. This

means that by replacing both the existing SMR H_2 plant and the coal-fired power plants with an advanced IGCC plant it would be possible to provide refining complexes with ultrapure H_2 and power simultaneously where CO_2 can be inherently captured, as depicted in Figure 4.1.

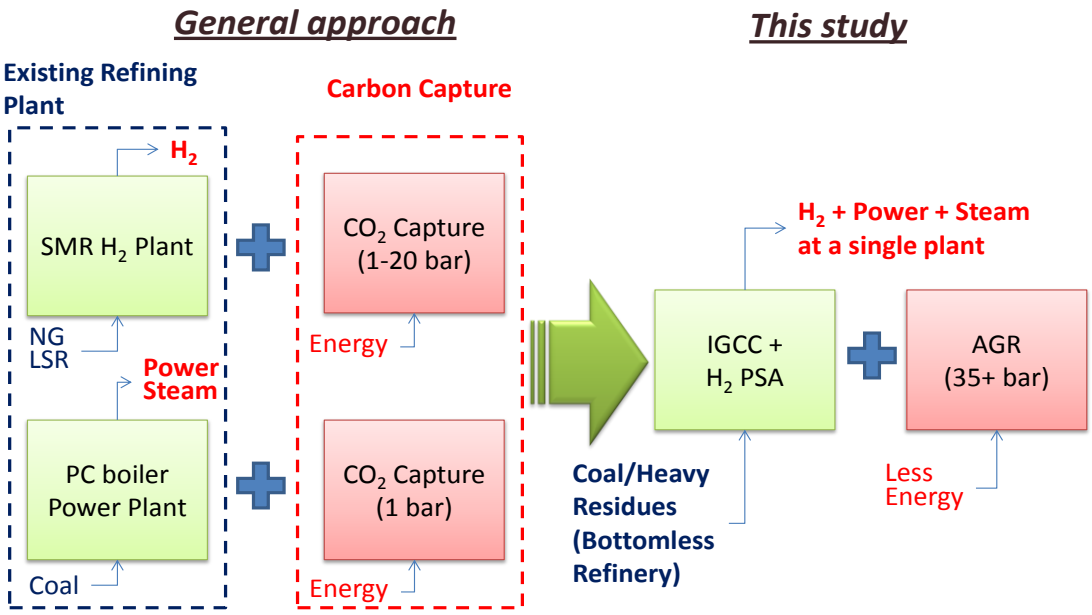

Figure 4.1: A conceptual diagram to compare general approach to capture CO_2 from a SMR H_2 plant and a coal-fired power plant separately to an advanced IGCC process for cogenerating power and ultrapure hydrogen with carbon capture (Luberti et al., 2014a)

In producing ultrapure hydrogen (99.99+ mol%) from such a gas mixture as composed of H_2, CO_2, CO, N_2 and Ar, it is well-known that a PSA is the only economically feasible separation process to be implemented in a commercial scale. The multi-column PSA process, known as UOP Polybed, has been widely applied to SMR H_2 plants to produce ultrapure H_2 from shifted syngas. However, the conventional H_2 PSA has been designed and optimised against a feed stream of around 71% H_2, 19% CO_2, 4% CO and 5% CH_4 at 20 bar found in a SMR H_2 process. This composition and the pressure of the raw H_2 feed in a SMR-based H_2 plant is quite different from the raw H_2 fuel gas in IGCC power plants with carbon capture (88.75% H_2, 2.12% CO_2, 2.66% CO, 5.44% N_2, 1.03% Ar at 34 bar). This composition was obtained from both our previous simulation of the IGCC with

carbon capture and the DOE report (2007). Therefore, there is a need to revisit the design of the H_2 PSA process to estimate the H_2 recovery and productivity obtained at the operating conditions to meet the H_2 product purity as high as 99.99+ mol%.

4.2 Design basis of a H_2 PSA integrated with an IGCC power plant

This study aims to design a H_2 PSA system that is applicable to an advanced IGCC plant for producing both ultrapure H_2 and power. The advanced IGCC plant is a modification of a conventional IGCC power plant with carbon capture to include a new H_2 PSA unit and its block flow diagram is illustrated in Figure 4.2.

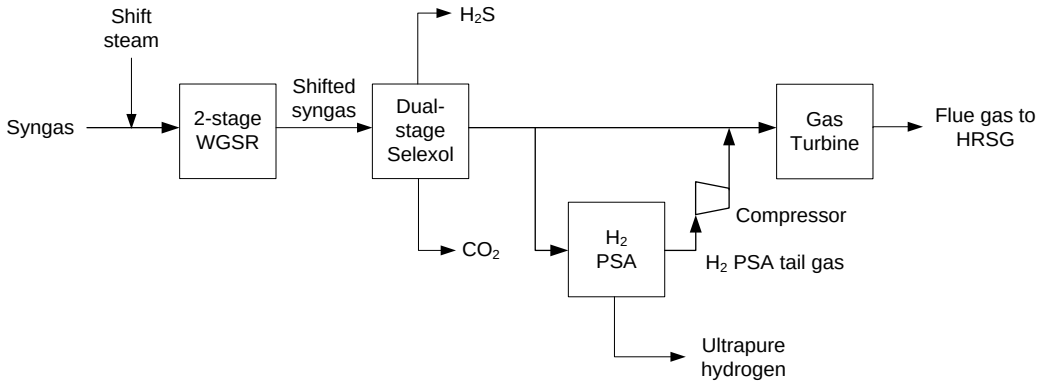

Figure 4.2: Block flow diagram of an advanced IGCC process for cogenerating power and ultrapure hydrogen

The process design of the conventional IGCC power plants with carbon capture is based on an exemplary IGCC power plant using the Shell gasifier that was described in detail in Chapter 2. In the conventional IGCC process, the treated syngas leaving the AGR becomes saturated with water in a fuel gas saturation column and then is fed to the combustion chamber of a gas turbine. In this study, the treated syngas is split into two streams: one stream flows directly to a gas turbine for power generation and the other is sent to a H_2 PSA for ultrapure H_2 production. Given the plant capacity, the split ratio was determined to have a good balance between the two cogenerating outputs in such a way to produce 110 MMSCFD of ultrapure H_2 and still to have the majority of the syngas used for electricity generation in the combined cycle. The gross power generation is, in fact, decreased

by around 31% from 694 MW_e to 479 MW_e. The H_2 PSA tail gas obtained as a by-product needs to be compressed up to the operating pressure of the gas turbine and sent to the combustion chamber along with the H_2-rich fuel gas.

Given the composition and the pressure of raw H_2 feeds that a previous study dealt with (Ahn et al., 2001), it was concluded that H_2 PSA designs that were configured with adsorption columns having two adsorbent layers would exhibit better performance than those having adsorption columns packed with a single adsorbent. This is because it is unlikely to find a versatile adsorbent that has better working capacities than others for all the impurities contained in a raw H_2 feed. Therefore, a layered bed is usually configured such that an activated carbon layer near the feed end plays a role in adsorbing mainly CO_2 and CH_4 while a zeolite layer on top of the activated carbon layer removes CO and N_2. The length ratio of the carbon to zeolite layers is regarded as one of the key parameters that need to be optimised (Ahn et al., 2001, 2012; Ribeiro et al., 2008; Yang and Lee, 1998; Park et al., 1998). Given the composition of the new raw H_2 feed that has relatively small amount of CO_2 and no CH_4, however, it is plausible that an adsorption column packed with zeolite 5A would perform better than those with a layered bed of activated carbon and zeolite 5A.

The production of the H_2 PSA tail gas should be minimised in order to reduce the power consumption relating to its compression before being fed to the gas turbine. In this study, the aim is to maximise H_2 recovery by adding more columns to the H_2 PSA process to enable more complicated step configurations for minimising the H_2 loss and consumption. Knowing the maximum hydrogen recovery that a H_2 PSA could achieve is essential in determining the mass balance around the H_2 PSA, i.e., the flowrate and the composition of both the ultrapure H_2 product and the tail gas. Once the mass balance is determined at the condition of maximum H_2 recovery, it is possible to estimate the auxiliary power consumption in the H_2 PSA tail gas compressor and the power generation in the gas and steam turbines accurately.

4.3 Adsorption equilibria

Adsorption equilibrium of pure hydrogen, carbon dioxide, carbon monoxide and nitrogen on zeolite 5A were reported in the literature by Lopes et al. (2009). Data

were measured gravimetrically at 303, 323 and 343 K in the pressure range between 0 and 7 bar. Adsorption equilibrium isotherms of argon on zeolite 5A were found in Miller et al. (1987) at 297, 233 and 203 K and at pressures up to 4 bar. Given the high non-linearity of carbon dioxide isotherms, the adsorption equilibria were predicted by the following extended dual-site Langmuir model:

$$q_i^* = \frac{q_{s,1} b_{1,i} P y_i}{1 + \sum_{j=1}^{n} b_{1,j} P y_j} + \frac{q_{s,2} b_{2,i} P y_i}{1 + \sum_{j=1}^{N_c} b_{2,j} P y_j} \qquad (4\text{-}1)$$

$$\text{with } b_{n,i} = b_{n,i,0} \exp\left(\frac{-\Delta \tilde{H}_{n,i}}{RT}\right) \quad \text{n = 1,2}$$

Experimental data (Lopes et al., 2009; Miller et al., 1987) were fitted using Origin 8.5 software (OriginLab, 2010). For the fitting purposes, the adsorbent capacities at saturation $q_{s,1}$ and $q_{s,2}$ were determined as those of the most strongly adsorbed component, which in this case is CO_2, at the lowest temperature. Due to thermodynamic consistency (Ruthven, 1984), these capacities were kept fixed for the other temperatures and for all the other components' isotherm fittings. Having three isotherms at different temperatures for each component, it was possible to calculate $b_{i,0}$ and ΔH_i with a linear regression of $\ln(b_i)$ over 1/T. The isotherm parameters of the dual-site Langmuir model with the relative standard errors are given in Table 4.1. Note that these parameters are the optimal values for the fitting of experimental data and do not have a rigorous physical meaning. Adsorption equilibrium data and related dual-site Langmuir model predictions are shown in Figures 4.3 to 4.7.

Table 4.1: Isotherm parameters of dual-site Langmuir model for zeolite 5A

Gas	$q_{s,1}$ (mol/kg)	$q_{s,2}$ (mol/kg)	$b_{1,i,0}$ (bar^{-1})	$b_{2,i,0}$ (bar^{-1})	$(-\Delta H_{1,i})$ (J/mol)	$(-\Delta H_{2,i})$ (J/mol)
H_2	0.7077 ± 0.00%	3.711 ± 0.00%	4.227×10^{-7} ± 4.15%	1.333×10^{-4} ± 0.62%	19,674 ± 8.17%	9,282 ± 1.54%
CO_2	0.7077 ± 0.00%	3.711 ± 0.00%	1.077×10^{-7} ± 2.72%	1.233×10^{-4} ± 7.23%	38,312 ± 3.08%	29,808 ± 5.87%
CO	0.7077 ± 0.00%	3.711 ± 0.00%	2.431×10^{-8} ± 2.06%	2.321×10^{-5} ± 0.03%	47,736 ± 2.05%	20,994 ± 0.05%
N_2	0.7077 ± 0.00%	3.711 ± 0.00%	2.141×10^{-6} ± 5.99%	8.987×10^{-5} ± 3.66%	31,338 ± 6.64%	14,956 ± 6.09%
Ar	0.7077 ± 0.00%	3.711 ± 0.00%	5.952×10^{-8} ± 7.71%	1.424×10^{-4} ± 2.23%	26,828 ± 9.32%	13,193 ± 2.81%

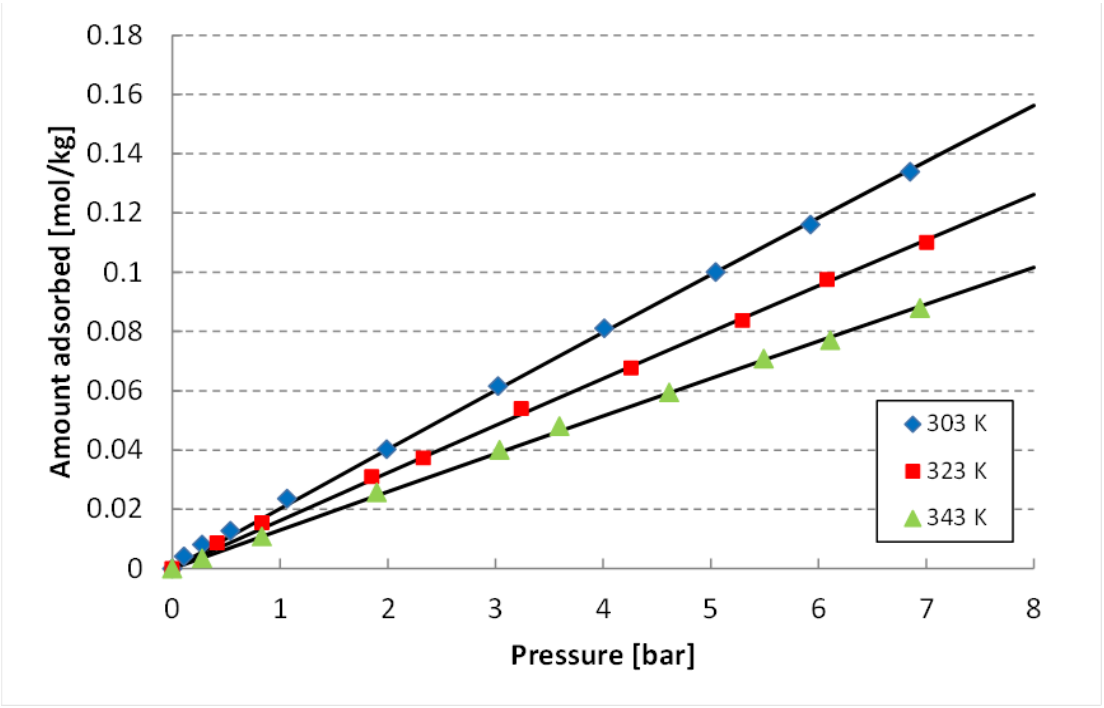

Figure 4.3: Adsorption equilibrium of hydrogen on 5A zeolite. Solid lines: dual-site Langmuir model. Experimental data by Lopes et al. (2009)

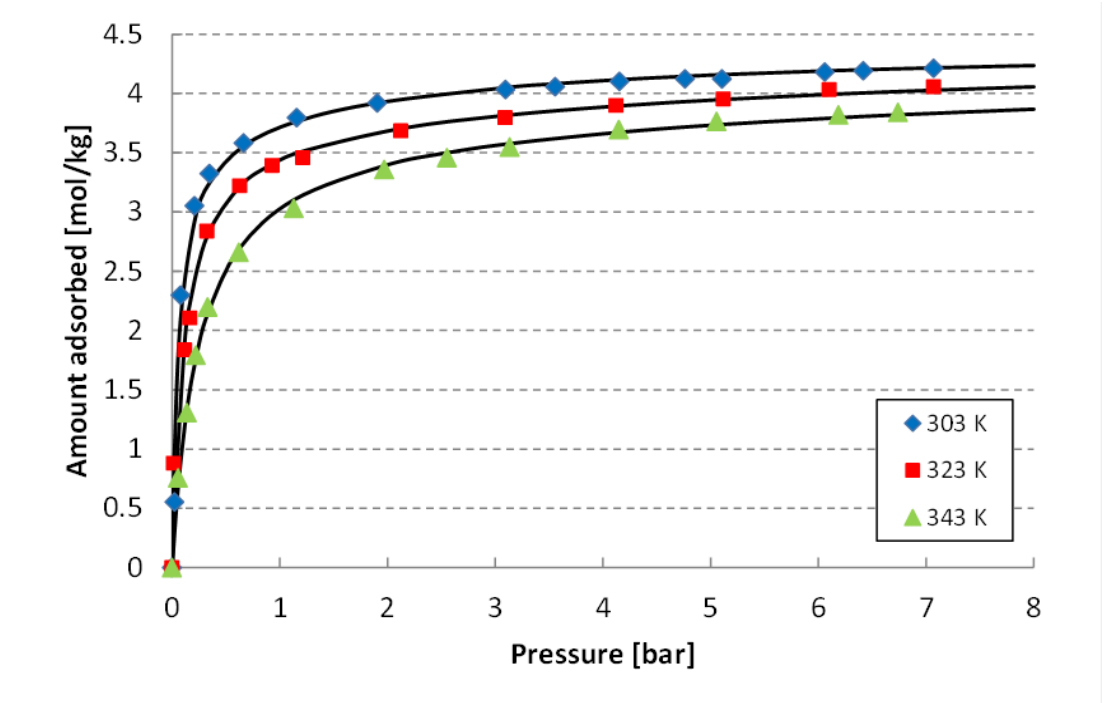

Figure 4.4: Adsorption equilibrium of carbon dioxide on 5A zeolite. Solid lines: dual-site Langmuir model. Experimental data by Lopes et al. (2009)

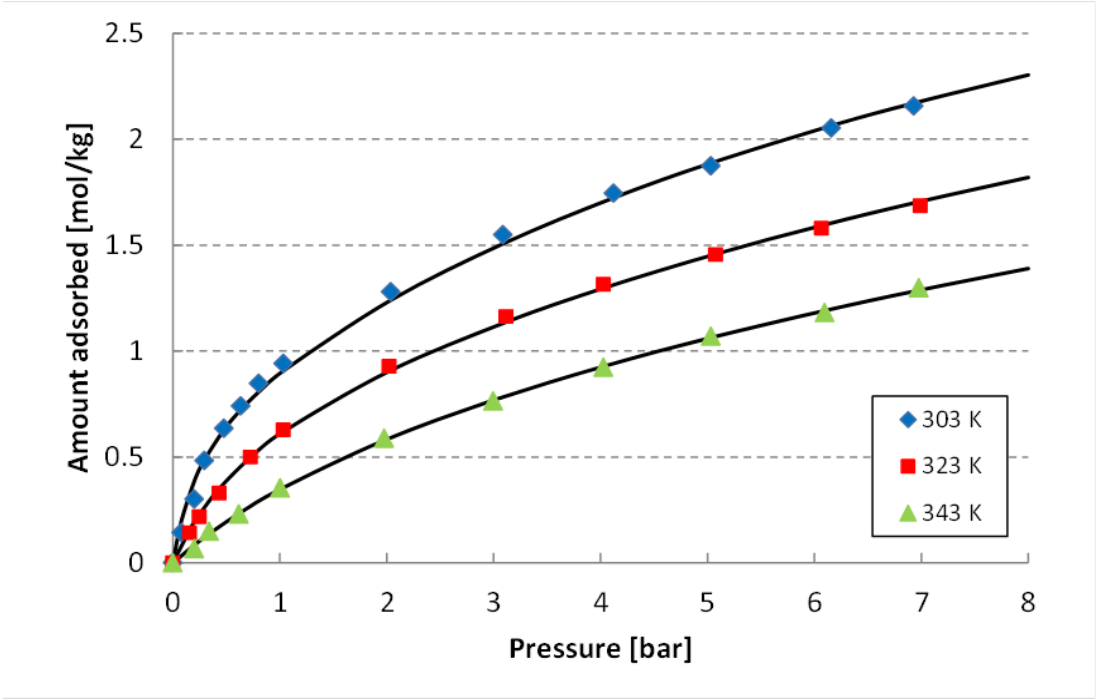

Figure 4.5: Adsorption equilibrium of carbon monoxide on 5A zeolite. Solid lines: dual-site Langmuir model. Experimental data by Lopes et al. (2009)

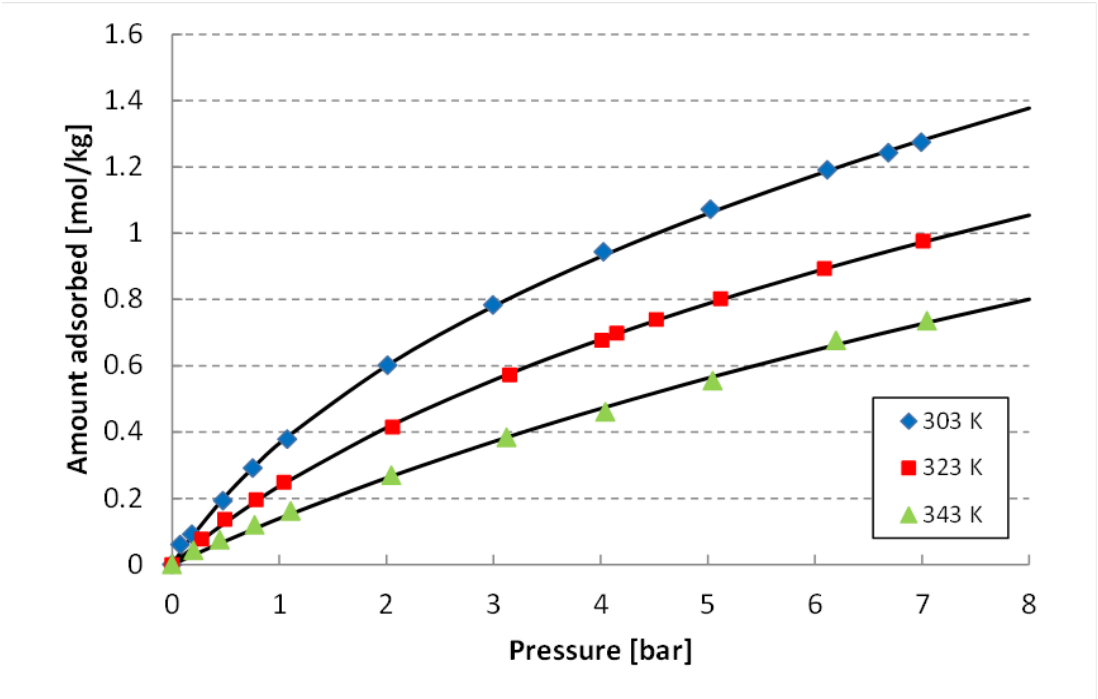

Figure 4.6: Adsorption equilibrium of nitrogen on 5A zeolite. Solid lines: dual-site Langmuir model Experimental data by Lopes et al. (2009)

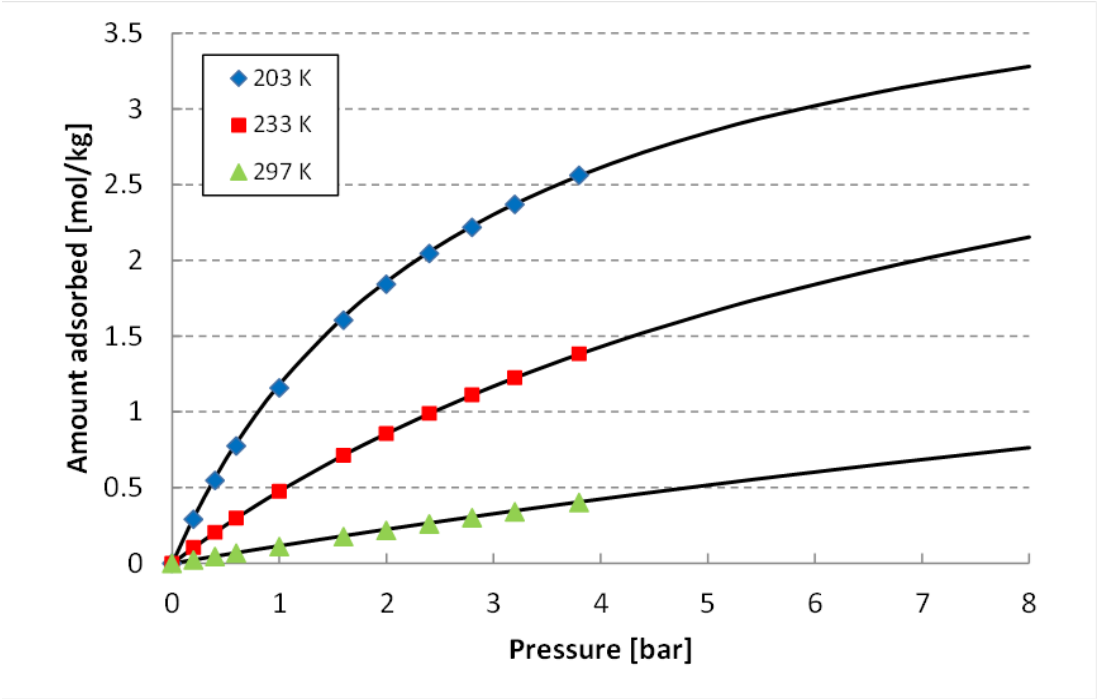

Figure 4.7: Adsorption equilibrium of argon on 5A zeolite. Solid lines: dual-site Langmuir model. Experimental data by Miller et al. (1987)

From the previous figures, it can be seen that the adsorption capacity of the 5A zeolite is: CO_2 > CO > N_2 > Ar > H_2. As expected, carbon dioxide isotherms are much steeper than those of the other gases, with hydrogen isotherms being practically linear in the examined range of temperatures and pressures. From the fitting parameters shown in Table 4.1, it is clear that the heats of adsorption of CO_2 are higher than the other gases: for the different components, it follows the same order as the adsorption capacities. Figure 4.8 compares the equilibrium isotherms of the five components of the IGCC feed stream entering the H_2 PSA unit at 303 K. Since argon isotherms become approximately linear going from 203 K to 297 K they can be safely extended to higher temperatures as 303 K and above.

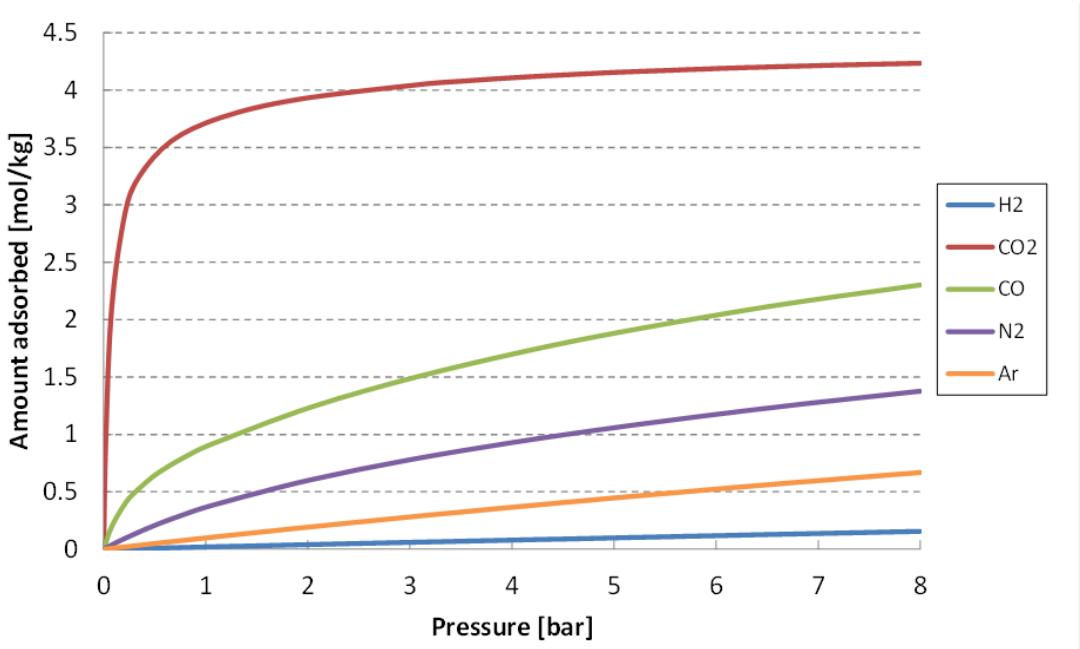

Figure 4.8: Adsorption equilibrium comparison of hydrogen, carbon dioxide, carbon monoxide, nitrogen and argon on 5A zeolite at 303 K

4.4 Simulation of the H_2 PSA unit

Due to its complicated nature and multiple decision parameters, including plant dimensionality and operation conditions, the design of a PSA process is not a trivial task. Some works in the literature focused on general heuristics for a preliminary design of PSA, including the selection of adsorbent, particle size, bed size, bed configuration, pressure equalisations, etc. (Jain et al., 2003). In a H_2 PSA unit, a complex configuration involving a higher number of beds is essential to increase the product recovery at the same product purity. In order to simulate the behaviour of such PSA configurations, two different approaches can be employed: the "unibed" and the "multibed" (Jiang et al., 2004). The unibed approach assumes that all beds undergo identical steps so only one bed is needed to simulate the multibed cycle. Information about the effluent streams is stored in data buffers and linear interpolation is used to obtain information between two time points. The multibed approach considers a multibed process as a sequence of repetitive stages within the cycle. Nikolic et al. (2008) developed a generic modelling framework for multibed PSA flowsheets. The framework is general enough to support an arbitrary number of

beds, a customised complexity of the adsorbent bed model, one or more adsorbent layers, all feasible PSA step configurations and interbed connectivities.

In all the simulations, the set of the partial and ordinary differential equations and the algebraic equations were solved using the in-house CySim simulator (Friedrich et al., 2013; Luberti et al., 2014a). After preliminary simulations using the multibed approach for the four-column system, a unibed approach was developed and validated by comparison with the multibed approach. For more complex cycle configurations, the unibed approach was always utilised to save computational time. The unibed CySim PSA flowsheet is depicted in Figure 4.9.

The complete modelling of a PSA process includes the mathematical model of the different adsorption columns coupled with the individual models of ancillary equipment. As well as the adsorption columns, the entire flowsheet includes:

- Valves: They are considered as delay elements and can result in a significant disturbance to the flow regime. They can be operated as mass flow controllers (MFC) or pressure-driven controllers (PDC). The related equations are:

$$F = F_i \qquad \text{(MFC)} \qquad (4\text{-}2)$$

$$F = cv \cdot c_T \cdot \sqrt{\frac{\Delta P}{\rho_f}} \qquad \text{(PDC)} \qquad (4\text{-}3)$$

  where cv is the valve coefficient. After calculating the flow rate, F, this value is multiplied by the valve stem position. The stem position of the valve indicates if the valve is open or closed. Here 0 indicates a closed valve, 0.5 a half-open valve and 1 a fully open valve. CySim allows the opening and closing of valves at specified times. Pressure, temperature and gas composition are passed through the valve to the neighbouring units. In the model the valves are opened and closed instantaneously without delay times.
- Splitters/mixers: These units consist of a perfectly mixed tank (CSTR) and an arbitrary number of connections. For all other connections, the flow rate of the neighbouring unit is passed into the splitter/mixer. These flow rates define if the unit works as a splitter, a mixer, or a combination of splitter and mixer. A small default dead volume of 10^{-6} m^3 is associated with these units.
- Sources/sinks: These units set the boundary conditions for the simulated system and calculate the number of moles of each component to pass through

the outlet. It establishes the real operating conditions of the connections to the rest of the plant.

- Buffers: They are essential for storing information (pressure, temperature, composition) of streams leaving the column that will be returned in a following step. They are used for purge and pressure equalisation steps.

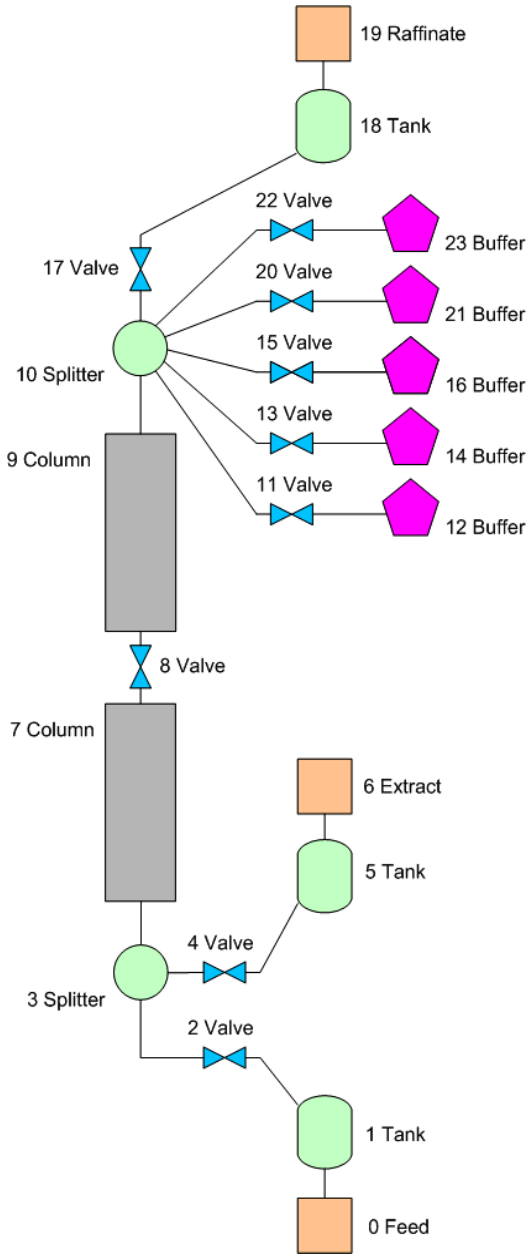

Figure 4.9: Unibed CySim PSA flowsheet

The aim of this study is to design a H_2 PSA process with a capacity of 110 H_2 MMSCFD that is approximately equivalent to 1,609 H_2 mol/s. Given the H_2 mole

fraction in the raw H_2 feed, the required flowrate of a raw H_2 feed flowing to the H_2 PSA would be around 2,015 mol/s, assuming 90% H_2 recovery. According to the design of the IGCC power plant with carbon capture using a Shell dry coal-fed gasifier (DOE Case 6, 2007), the advanced IGCC plant for cogeneration of power and ultrapure hydrogen would be configured such that around 40% of the raw H_2 gas is directed to the H_2 PSA. The remaining 60% of this raw H_2 gas flows to a syngas humidifier and subsequently to a combustion chamber in the gas turbine, just as in the conventional IGCC power plant (Figure 4.2).

Table 4.2: List of column parameters, particle parameters and operating conditions of H_2 PSA simulations (Luberti et al., 2014a)

Column parameters	
Column length, L_c (m)	0.5
Column internal diameter, D_c (m)	0.025
External bed void fraction, ε (-)	0.391
Axial mass dispersion coefficient, D_z (m^2/s)	1.2×10^{-4}
Axial thermal dispersion coefficient, k_z (W/m·K)	1.3
Wall heat transfer coefficient, h_w ($W/m^2\cdot K$)	95.0
Adsorbent parameters	
Pellet density, ρ_p (kg/m^3)	1,126
Pellet void fraction, ε_p (-)	0.503
Adsorbent specific heat capacity, $c_{P,s}$ (J/kg·K)	920
Pellet averaged diameter, d_p (mm)	1.70
Macropore LDF coefficient, $k_i^p\cdot A_p/V_p$ $H_2/CO_2/CO/N_2/Ar$ (s^{-1})	9.22/6.07/7.52/7.90/7.28
Micropore LDF coefficient, $k_i^{cr}\cdot 3/r_c$ $H_2/CO_2/CO/N_2/Ar$ (s^{-1})	0.7467/0.0017/0.0332/0.1697/0.1800 (Lopes et al., 2009)
Operating conditions	
P_{ads} (bar)	34
P_{des} (bar)	1
T_{feed} (K)	303
Q_{feed} (mol/s)	0.002
Feed composition, $y_{H2}/y_{CO2}/y_{CO}/y_{N2}/y_{Ar}$ (molar)	0.8875/0.0212/0.0266/0.0544/0.0103

Planning as a future work an experimental campaign to validate the simulation results subsequent to this study, the dimension of adsorption columns in this study was determined to be the same as those of a lab-scale six-column PSA rig, as shown in Table 4.2. Given the column size and dimensions, the feed flowrate was set at

0.002 mol/s with a scaling factor of approximately 10^{-6}. The values of other parameters used in the simulation are also presented in Table 4.2: most of the column and adsorbent parameters were estimated with the correlations described in detail in Chapter 3 and the data reported by Lopes et al. (2009). The discretisation method for the spatial domain in the column was central finite difference method with 20 grid points along the column. In CySim the system of differential algebraic equations was solved with the DAE solver SUNDIALS (Friedrich et al., 2013).

4.5 Adsorption breakthrough results

First, adsorption breakthroughs of the five-component mixture were simulated using the parameters reported in Table 4.2. Figure 4.10 shows the mole fraction profiles of all components with time at product end in two different scales of mole fraction. It was assumed that the column was initially filled with pure hydrogen.

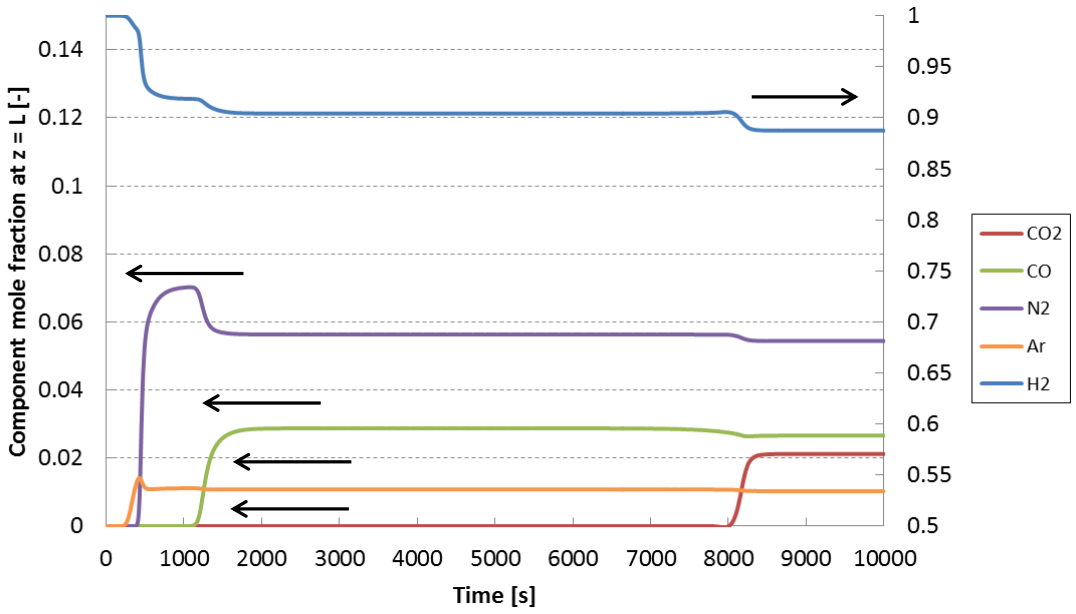

Figure 4.10: Breakthrough simulation results of the shifted syngas stream on zeolite 5A bed at 303 K and 34 bar. Column size and feed condition are reported in Table 4.2

From Figure 4.10 it can be seen that the first contaminant to breakthrough the column is argon, followed by nitrogen, carbon monoxide and carbon dioxide. Since argon breakthroughs at around 420 s, the adsorption step time of any PSA cycle has to be lower than this value in order to meet the required hydrogen purity (99.99+%).

Argon and nitrogen are expected to be the major impurities in the product hydrogen stream since they are the least strongly adsorbed components. Carbon monoxide and carbon dioxide are apparently not problematic because their breakthrough times are much longer at around 1200 s and 8100 s, respectively, following the order dictated by the adsorption capacity. Carbon monoxide content must, however, be monitored because it is the most hazardous impurity for the product specification. For fuel cell application, H_2 should contain less than 10 ppm CO because CO works as a poison on the anode catalyst and dramatically decreases the fuel cell performance (Majilan et al., 2009; You et al., 2012).

4.6 PSA cycle simulation results

Six different H_2 PSA systems were investigated to see the change of H_2 recovery and productivity with different levels of complexity of the step configuration, which is subject to the different number of columns. The H_2 recovery and productivity obtained at different configurations were compared under the operating condition to meet the specification of the H_2 purity (99.99+ mol%). Since the aim is to maximise hydrogen recovery, a simple two-column system where only one pressure equalisation step can be deployed was not investigated.

First, a four-column H_2 PSA system was simulated and the targeted H_2 purity was obtained at a cycle time of 800 seconds. Since all the simulations were carried out at a constant feed flowrate of 0.002 mol/s, the total cycle time became longer as more columns that are identical in size and dimension were added to configure six-, nine-, twelve- and sixteen-column H_2 PSA systems. This is because either more than one column can share the total feed gas for adsorption at the same time or more steps need to be included in one cycle. To evaluate whether or not a simulation reaches its cyclic steady state (CSS), the H_2 purity and recovery from each cycle were compared with those at the previous cycle. It was assumed that a cyclic steady state would be reached if the differences of the H_2 purity and recovery between the new and previous cycles were both less than 10^{-6}.

4.6.1 Four-column H_2 PSA

A four-column H_2 PSA unit is designed such that a providing purge step is located between the two depressurising pressure equalisation (DPE) steps while the two pressurising pressure equalisation (PPE) steps take place in a row after the purge step, as shown in Figure 4.11. The step configuration was reconstructed in reference to the step configuration reported in the literature (Cassidy, 1980).

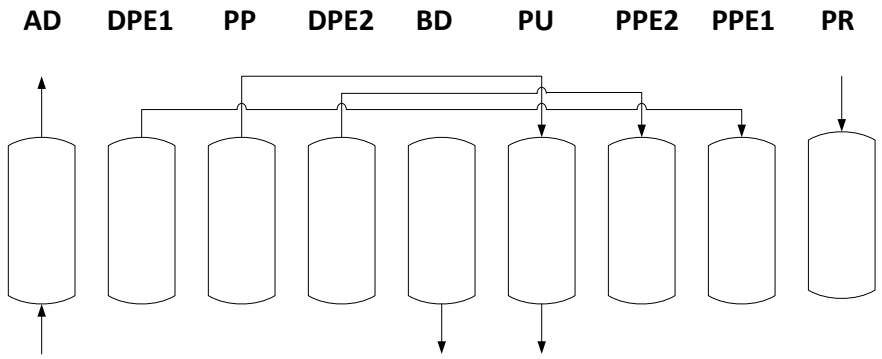

AD			DPE1	PP		DPE2	BD	PU	PPE2	PPE1	PR	
BD	PU	PPE2	PPE1	PR			AD			DPE1	PP	DPE2
DPE1	PP	DPE2	BD	PU		PPE2	PPE1	PR		AD		
PPE1	PR		AD				DPE1	PP	DPE2	BD	PU	PPE2

Figure 4.11: Step configuration of a four-column PSA cycle (AD: adsorption, DPE: depressurising pressure equalisation, PP: providing purge, BD: blowdown, PU: purge, PPE: pressurising pressure equalisation, PR: product pressurisation, $t_{AD} = t_{cycle}/4$; $t_{PR} = 3t_{cycle}/16$; $t_{PP} = t_{PU} = t_{cycle}/8$; $t_{BD} = t_{DPE} = t_{PPE} = t_{cycle}/16$)

In the four-column H_2 PSA simulation, the total cycle time was fixed at 800 seconds with the adsorption step-time equivalent to 1/4 of the cycle time, as shown in Figure 4.11. The purge flow is generated by reducing the column pressure starting from a pressure at the end of the first DPE step to a pressure that can be chosen at the operator's disposal. The equilibrated pressure at the start (or end) of the second DPE step (or the second PPE step) is subject to how much purge flow is generated during the providing purge step. Accordingly, the equilibrated pressure at the end (or start) of the first DPE step (or the first PPE step) is also affected by the amount of purge

flow. The step configuration where the providing purge step is located between the two DPE steps has a clear advantage over a cycle where the providing purge step follows the two DPE steps in that it can increase the purge flowrate to a greater extent since the providing purge step can start at a higher pressure. Therefore, this configuration is capable of controlling the product purity in a wider range without having to change the cycle time. It should be noted that the pressure recovery during the pressure equalisation in this four-column H_2 PSA would decrease with an increasing purge flowrate since the equilibrated pressure at the end of each pressure equalisation stage is affected by the amount of purge flow, as shown in Figure 4.12. By contrast, the pressure recovery can be maintained at a constant level regardless of the change of purge flowrate in the configuration where the providing purge step is located after finishing all the DPE steps.

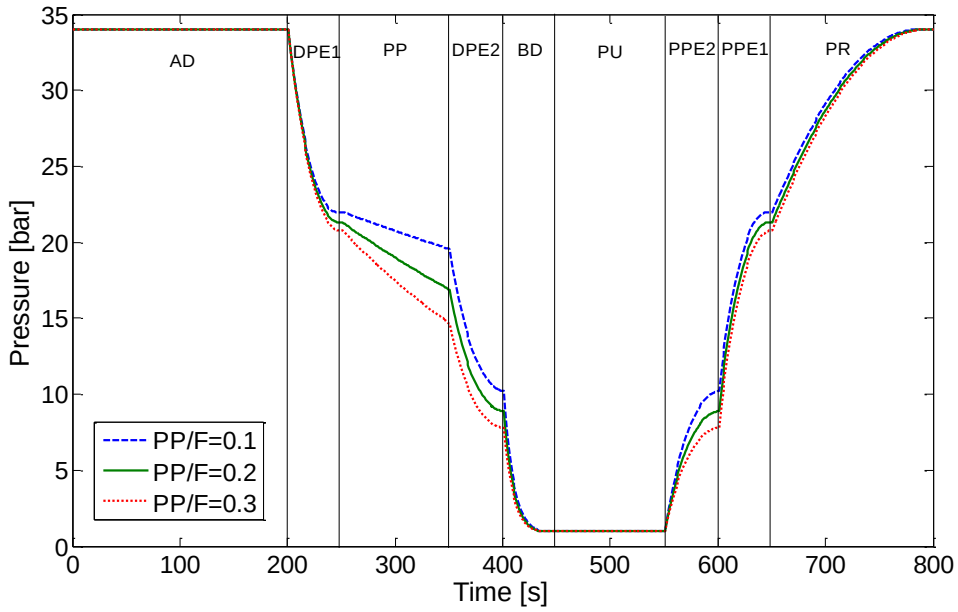

Figure 4.12: Pressure profiles at the product end of a column over a cycle at the cyclic steady state of the four-column H_2 PSA unit: effect of the different amounts of purge flow

As shown in Figure 4.12, the pressure profile of a column over a cycle is varied in response to the use of the different amounts of the purge flow investigated in this section. The actual flowrate of the purge gas flowing between two columns under the providing purge and purge steps must decrease with the step time since the driving

force diminishes with decreasing pressure difference between the columns. Therefore, an index of PP/F to quantify the varying purge flow as an average purge flow is introduced in this context. The PP/F denotes the ratio of an average molar purge flowrate being generated from one column during the providing purge step to a molar feed flowrate to one column for adsorption during one cycle. Note that the amount of the feed flowing to one column is not the same as the total amount of the feed flowing to a PSA system if more than one column shares the total feed flow. The three different numbers of PP/F that were tested in the three runs are shown in Figure 4.12 and Table 4.3. As expected, the start and end pressures during the providing purge step become lower with increasing PP/F.

The targeted H_2 purity of 99.99+ mol% was achieved in Run 2 where during the providing purge step the column pressure changed from 21.5 to 17 bar, which was equivalent to a PP/F of 0.2. At this operating condition, the H_2 recovery and bed productivity were 72.68% and 162.67 mol_{H2}/kg/day, respectively.

Table 4.3: Performances of the four-column H_2 PSA system at different purge flow rates

	Adsorption time [s]	H_2 purity [%]	H_2 recovery [%]	Bed productivity [mol_{H2}/kg_{ads}/day]
Run 1 (PP/F = 0.1)	200	99.976	75.09	168.06
Run 2 (PP/F = 0.2)	**200**	**99.995**	**72.68**	**162.67**
Run 3 (PP/F = 0.3)	200	99.999	70.56	157.93

Figure 4.13 reports the component mole fraction profiles at the feed end over a cycle at the cyclic steady state for Run 2. Hydrogen mole fraction is at feed concentration during the adsorption step and progressively diminishes during the depressurisation equalisation and blowdown steps. It starts to increase again from the purge step because the providing purge stream is H_2-rich, until it reaches a maximum during the final repressurisation step with the ultrapure H_2 product. An opposite trend is observed for all the impurities having a very low mole fraction during adsorption and pressurisation steps, and relatively high during blowdown and purge steps. Since hydrogen is produced ultrapure in the raffinate, the off-gas stream leaving the column during the blowdown and purge steps will be enriched by the impurities

proportionally to their content in the feed. With a H_2 recovery of 72.68%, hydrogen will still be the most abundant component in the off-gas, accounting for around 66%.

At cyclic steady state, the column is relatively saturated with impurities at the end of the adsorption step, as shown in Figures 4.14 and 4.15 for Run 2. It is noticed that within four-fifths of the column length, the hydrogen mole fraction reaches the ultrapure condition target (99.99+ mol%) while all the impurities approach zero, but in different column locations. Carbon dioxide and carbon monoxide, being the most strongly adsorbed components, are adsorbed mainly in the first portion of the column. Nitrogen and argon mole fractions show firstly an almost flat decrease in the first 10 cm of the column and then are lowered more quickly after CO_2 and CO are abated.

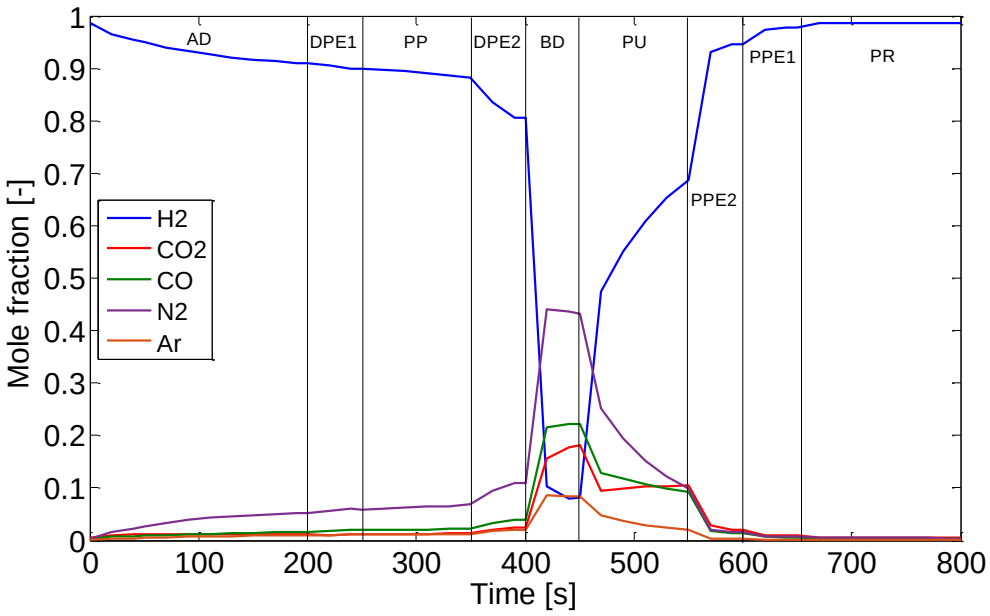

Figure 4.13: Component mole fraction profiles at the feed end of a column over a cycle at the cyclic steady state of the four-column H_2 PSA unit (Run 2)

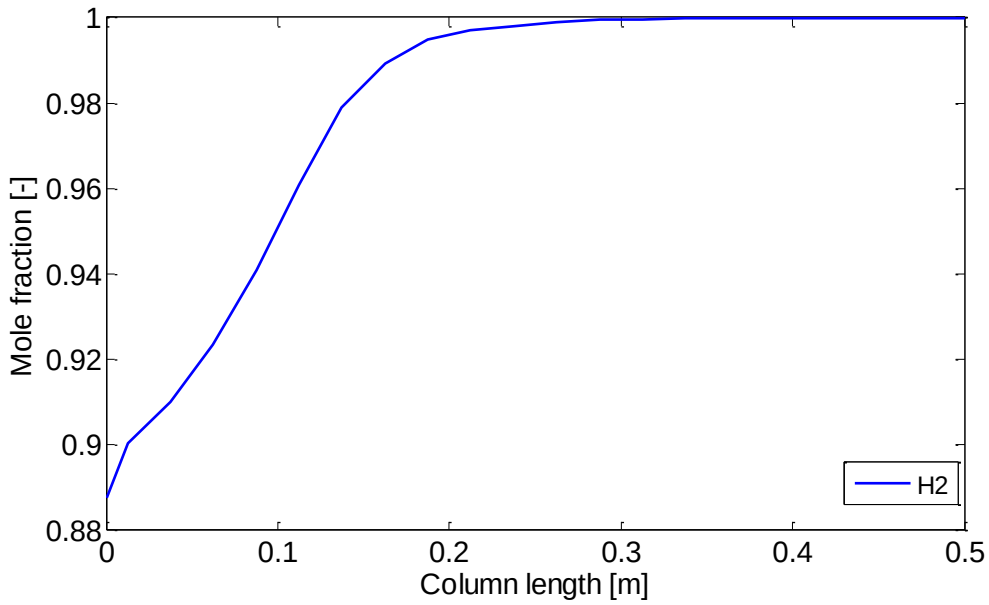

Figure 4.14: Hydrogen mole fraction profile along the column at the end of adsorption step at the cyclic steady state of the four-column H_2 PSA unit (Run 2)

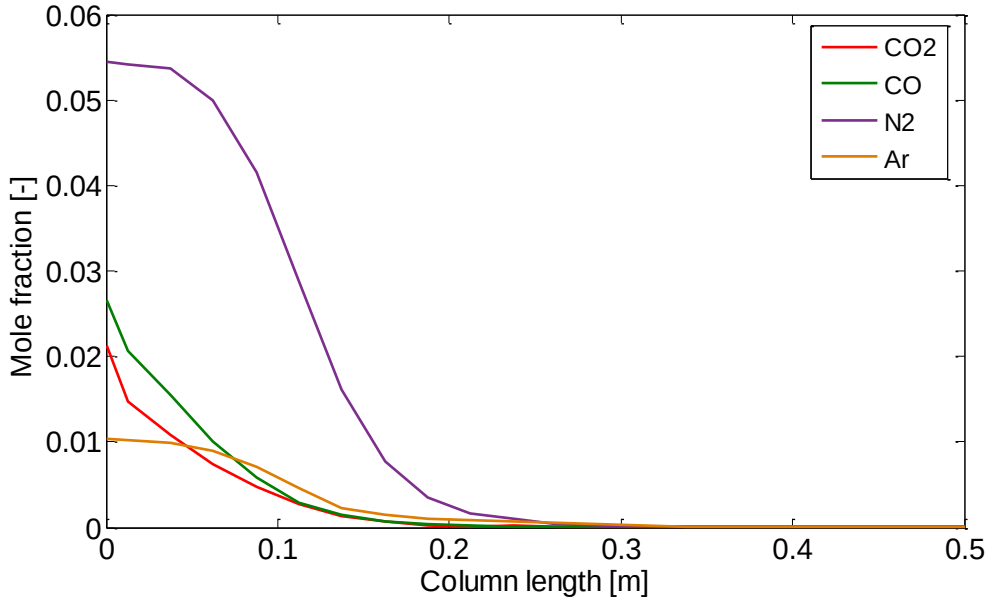

Figure 4.15: Impurities mole fraction profiles along the column at the end of adsorption step at the cyclic steady state of the four-column H_2 PSA unit (Run 2)

Figure 4.16 shows the evolution of the hydrogen purity and recovery with cycle number for Run 2. It can be seen that a cyclic steady state is achieved only after 400 cycles with an increasing recovery and a decreasing purity after each cycle.

The main reason for this delay in achieving CSS is the complexity of the mathematical model associated with the five-component mixture. These trends and results are confirmed by other studies reported in the literature on PSA processes for hydrogen purification (Riberio et al., 2008; Lopes et al., 2011).

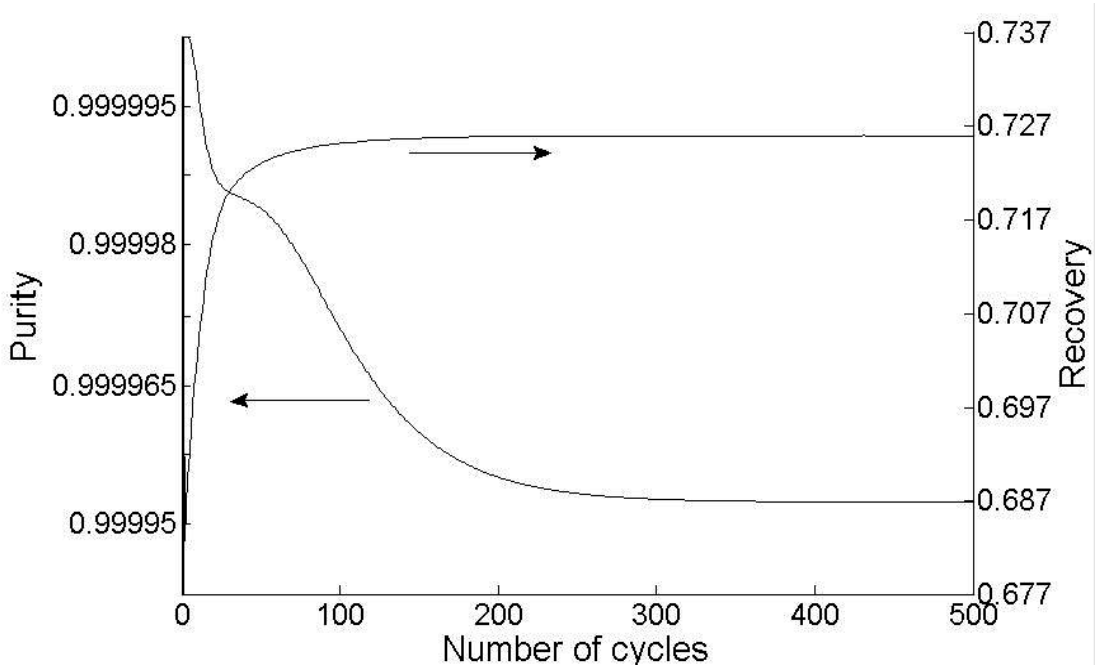

Figure 4.16: Evolution of hydrogen purity and recovery through the cycles (Run 2)

4.6.2 Six-column H_2 PSA

In the case of six-column H_2 PSA systems, two different step configurations were investigated. The first configuration (Figure 4.17) features feeding the raw H_2 to two columns at the same time, that is to say, each of two columns receives half the raw H_2 feed (Malek and Farooq, 1997). Due to two columns being used for adsorption in a cycle, the first configuration cannot accommodate an additional pressure equalisation step but has the two-stage pressure equalisation, which is the same as the above-mentioned four-column PSA system. Contrary to the four-column PSA system, a providing purge step is placed after the two pressure equalisation steps, as shown in Figure 4.17. It is anticipated that the alteration to the step configuration would be capable of improving the H_2 recovery since more pressure can be recovered during the pressure equalisation steps. That is to say, less consumption of pure hydrogen for product pressurisation and the reduced feed

flowrate to one column for adsorption enables more efficient use of the column due to less ingress of impurities into the product end.

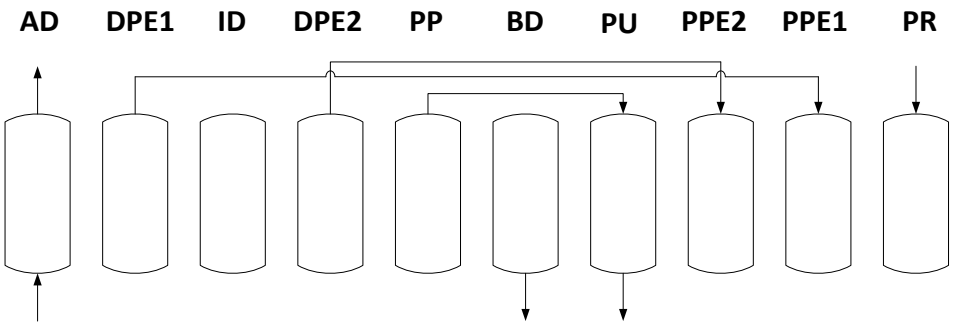

AD								DPE1	ID	DPE2	PP		BD	PU			PPE2	PPE1		PR			
PPE1		PR			AD						DPE1	ID	DPE2	PP		BD	PU			PPE2			
PU			PPE2	PPE1		PR			AD					DPE1	ID	DPE2	PP			BD			
PP			BD	PU			PPE2	PPE1		PR			AD					DPE1	ID	DPE2			
DPE1	ID	DPE2	PP			BD	PU			PPE2	PPE1		PR			AD							
AD				DPE1	ID	DPE2	PP			BD	PU			PPE2	PPE1		PR			AD			

Figure 4.17: Step configurations of a six-column H_2 PSA cycle with two-stage pressure equalisation (AD: adsorption, DPE: depressurising pressure equalisation, ID: idle, PP: providing purge, BD: blowdown, PU: purge, PPE: pressurising pressure equalisation, PR: pressurisation, $t_{AD} = t_{cycle}/3$; $t_{PP} = t_{PU} = t_{PR} = t_{cycle}/9$; $t_{BD} = t_{DPE} = t_{PPE} = t_{cycle}/18$)

In the second configuration (Figure 4.18), however, only one column is taken up for high-pressure adsorption in a cycle, just as in the four-column H_2 PSA. Therefore, it is possible to configure a PSA cycle with three-stage pressure equalisation. The step configuration was reconstructed from a patent found in the literature (Xu et al., 2002). It is generally expected that the more pressure equalisation stages a PSA cycle contains, the higher the hydrogen recovery. This is because less hydrogen product is required during the product pressurisation step since the column can be pressurised to a higher pressure in advance during the PPE steps. It should be noted that while the first six-column configuration has only an idle step between the depressurising equalisation steps, the second configuration should include two idle steps before and after the second pressurising equalisation step.

During an idle step, the column is completely disconnected from the surroundings and this is necessary for the synchronisation of the entire system over a cycle.

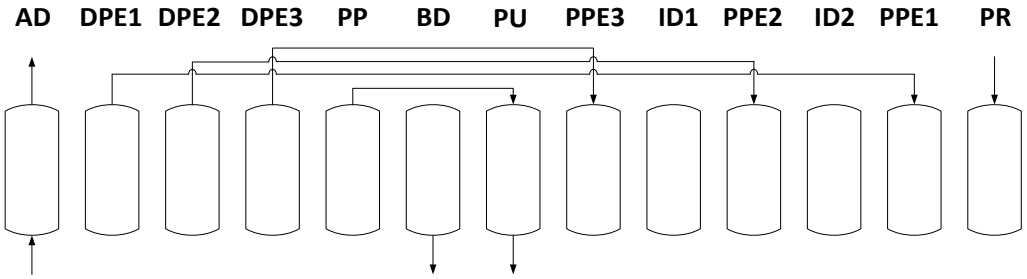

AD				DPE1	DPE2	DPE3	PP		BD	PU		PPE3	ID1	PPE2	ID2	PPE1	PR						
PPE1	PR			AD			DPE1	DPE2	DPE3	PP		BD	PU		PPE3	ID1	PPE2	ID2				
ID1	PPE2	ID2	PPE1	PR			AD			DPE1	DPE2	DPE3	PP		BD	PU		PPE3				
PU		PPE3	ID1	PPE2	ID2		PPE1	PR		AD			DPE1	DPE2	DPE3	PP		BD				
PP		BD	PU		PPE3		ID1	PPE2	ID2	PPE1	PR		AD			DPE1	DPE2	DPE3				
DPE1	DPE2	DPE3	PP		BD		PU		PPE3	ID1	PPE2	ID2	PPE1	PR		AD						

Figure 4.18: Step configurations of a six-column H_2 PSA cycle with three-stage pressure equalisations (AD: adsorption, DPE: depressurising pressure equalisation, PP: providing purge, BD: blowdown, PU: purge, ID: idle, PPE: pressurising pressure equalisation, PR: pressurisation, $t_{AD} = t_{cycle}/6$; $t_{PP} = t_{PU} = t_{PR} = t_{cycle}/9$; $t_{BD} = t_{DPE} = t_{PPE} = t_{ID} = t_{cycle}/18$)

Figures 4.19 and 4.20 clearly exhibit the change of the pressure profile caused by adding one more pressure equalisation steps to a PSA cycle. The first configuration with only two pressure equalisation steps (Figure 4.19) recovers less pressure during the pressure equalisation steps and consumes more hydrogen product during the product pressurisation step than the second configuration with three-stage pressure equalisation (Figure 4.20). In both the configurations, it can be seen that during the idle step the pressure remains constant for its duration.

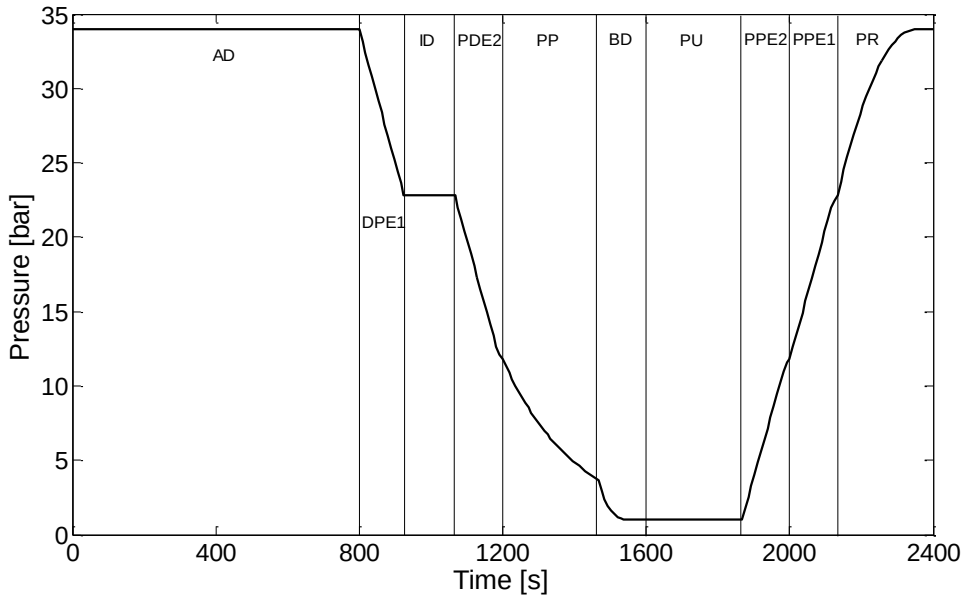

Figure 4.19: Pressure profile at the product end of a column over a cycle at the cyclic steady state of six-column H_2 PSA simulation at PP/F = 0.3 with two-stage pressure equalisation (Run 6)

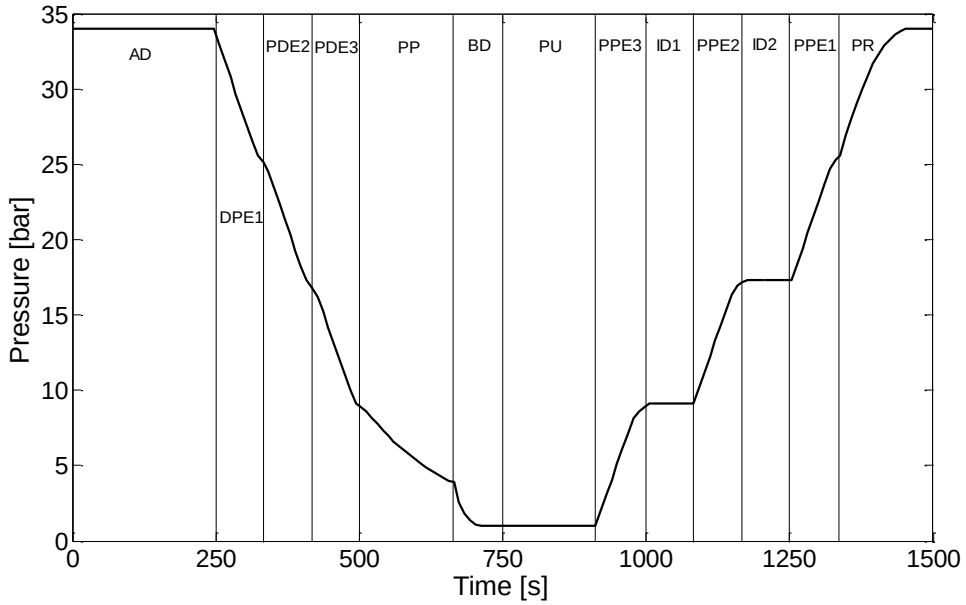

Figure 4.20: Pressure profile at the product end of a column over a cycle at the cyclic steady state of six-column H_2 PSA simulation at PP/F = 0.3 with three-stage pressure equalisation (Run 10)

As observed in Table 4.4, the first and second configurations can achieve the targeted H_2 purity (99.99+ mol%) with cycle times of 2400 and 1500 seconds, respectively (Runs 6 and 10). The adsorption time in Run 6 (800 seconds) is more than three times longer than that in Run 10 (250 seconds) even though the feed gas entering one column for adsorption is just halved in flowrate. This can be explained by two reasons. Firstly, the reduced feed flow to one adsorption column for adsorption prevents the ingress of impurities into the product end so it can allow a cycle to have a longer adsorption time. Secondly, the first configuration with only two-stage pressure equalisation has a better working capacity than the second configuration since its column can be more thoroughly regenerated by a stream having more hydrogen and pressurised by more ultrapure hydrogen during the product pressurisation step. Therefore, it implies that the H_2 recovery would increase with more stages of pressure equalisation in a cycle but the working capacity of the columns would deteriorate due to purging and pressurising the column with more impure gases.

Table 4.4: Performance of six-column H_2 PSA simulations

	Adsorption time [s]	H_2 purity [%]	H_2 recovery [%]	Bed productivity [$mol_{H2}/kg_{ads}/day$]
First configuration (Two-stage pressure equalisation)				
Run 4	600	99.999	78.75	117.51
Run 5	700	99.996	81.98	122.33
Run 6	**800**	**99.994**	**84.41**	**125.95**
Run 7	900	99.975	86.29	128.75
Second configuration (Three-stage pressure equalisation)				
Run 8	150	99.999	76.11	113.57
Run 9	200	99.997	82.47	123.05
Run 10	**250**	**99.994**	**86.26**	**128.71**
Run 11	300	99.969	88.79	132.48

It is noteworthy that the hydrogen recovery is enhanced by around 12% increasing from four columns (Run 2) to six columns (Runs 6) only by changing the step configuration in spite of both having the same number of pressure equalisation

steps. This change is not only caused by less hydrogen consumption during the product pressurisation step but also the longer adsorption time.

At the operating condition of Run 10, the H_2 recovery increases further up to 86.26%, mainly due to enhanced pressure recovery taking place over the three-stage pressure equalisation. The stream leaving the column in the course of reducing the column pressure from 34 bar to 9 bar can be reused for pressurising other columns and a significantly lower amount of hydrogen product is required for product pressurisation.

The bed productivities of both six-column H_2 PSA configurations are similar but lowered in comparison to that of the four-column H_2 PSA performance at the targeted H_2 purity. The change of the bed productivity can be explained with respect to the increasing number of columns (or increasing total amount of adsorbents being utilised) and the increasing H_2 recovery. The reduction of the bed productivity from four- to six-column H_2 PSA is due to the increase of the H_2 recovery being less than the corresponding increase of the amount of adsorbent utilised during the adsorption step.

4.6.3 Polybed H_2 PSA (nine and twelve columns)

As mentioned above, the more columns that are deployed, the higher the anticipated hydrogen recovery in a H_2 PSA system. In this respect, Polybed H_2 PSA processes containing seven to sixteen beds with at least three pressure equalisation steps and at least two columns receiving the feed gas for adsorption have been commercially operated for the purpose of H_2 purification (Yang, 1987). Complex PSA cycle schedules involved in Polybed systems have been studied in detail in the literature. Ebner et al. (2010) developed a graphical approach for obtaining various PSA cycle schedules. This novel PSA scheduling method involves a systematic procedure to fill the entire cycle schedule grid simultaneously, enabling complex, multibed, multi-step, PSA systems. Mehrotra et al. (2011) improved this method by filling only a portion of the schedule grid, called the unit block, making this approach much quicker and easier to implement. Mehrotra et al. (2010) also introduced an arithmetic approach for complex PSA cycle scheduling. This novel approach involved *a priori* specifying the cycle steps, their sequence and any constraints, and

then required solving a set of algebraic equations. The solution identified all the cycle schedules for a given number of beds, the minimum number of beds required to operate the specified cycle step sequence, the minimum number and location of idle steps to ensure alignment of coupled cycle steps, and a simple screening technique to aid in identifying the best performing cycles that deserved further examination.

In this section a nine-column, 11-step system following the step configuration found in the literature is investigated (Fuderer and Rudelstorfer, 1976), as shown in Figure 4.21. Figure 4.22 shows the pressure profile of the nine-column PSA system over a cycle at its cyclic steady state.

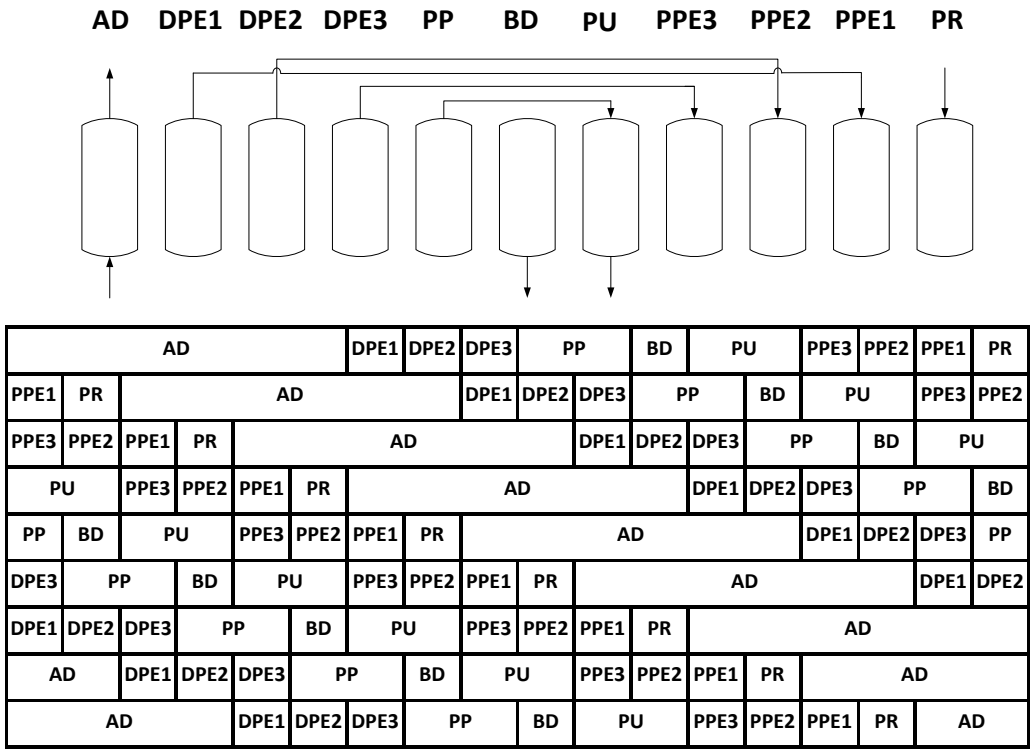

Figure 4.21: Step configurations of a nine-column H_2 PSA cycle (AD: adsorption, DPE: depressurising pressure equalisation, PP: providing purge, BD: blowdown, PU: purge, PPE: pressurising pressure equalisation, PR: pressurisation, $t_{AD} = t_{cycle}/3$; $t_{PP} = t_{PU} = t_{cycle}/9$; $t_{BD} = t_{DPE} = t_{PPE} = t_{PR} = t_{cycle}/18$)

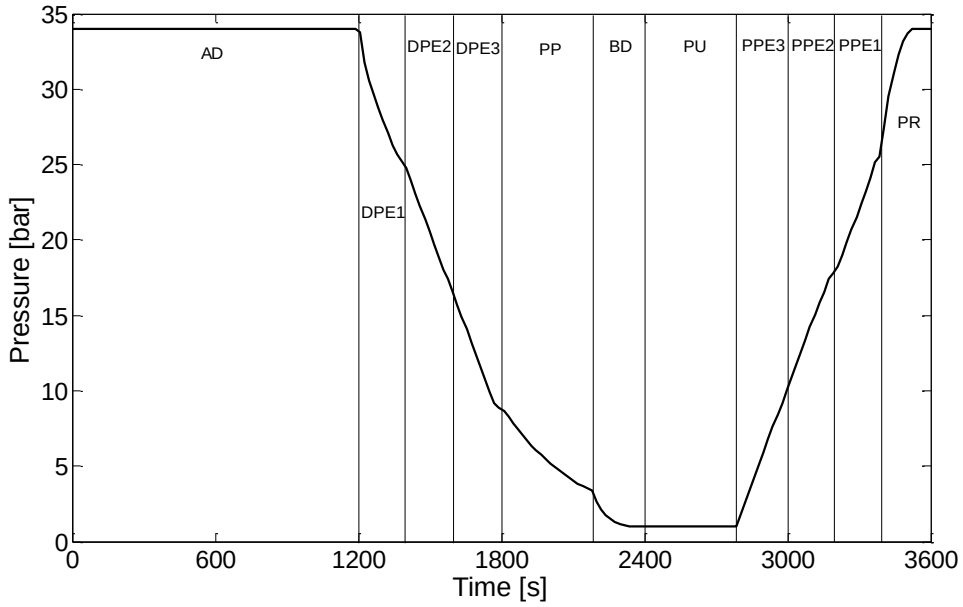

Figure 4.22: Pressure profiles at the product end of a column over a cycle at the cyclic steady state of a nine-column H_2 PSA at PP/F = 0.3 (Run 14)

The nine-column 11-step H_2 PSA system benefits from both reduced feed flowrate to one column and intensified pressure equalisation at each of the two six-column H_2 PSA systems. The feed flowrate fed to one column for adsorption is reduced to one-third of the total feed flowrate since three out of nine columns always work for adsorption at the same time. The product pressurisation step starts at 26 bar and the providing purge step commences at 8.5 bar, both of which are similar to those at the second configuration of six-column H_2 PSA system, as shown in Figures 4.20 and 4.22. This is because both PSA systems contain the same number of stages of pressure equalisation in their cycle.

Furthermore, a twelve-column 13-step H_2 PSA system was investigated in order to increase the H_2 recovery close to its maximum. The step configuration is presented in Figure 4.23 and was originally shown in a patent (Xu et al., 2003). The step configuration features simultaneous adsorption at three columns, simultaneous providing purge and purge at two columns, and four-stage pressure equalisation. Thanks to one additional pressure equalisation step, the product pressurisation step starts at 27 bar and the providing purge step commences at 7.5 bar, as shown in Figure 4.24.

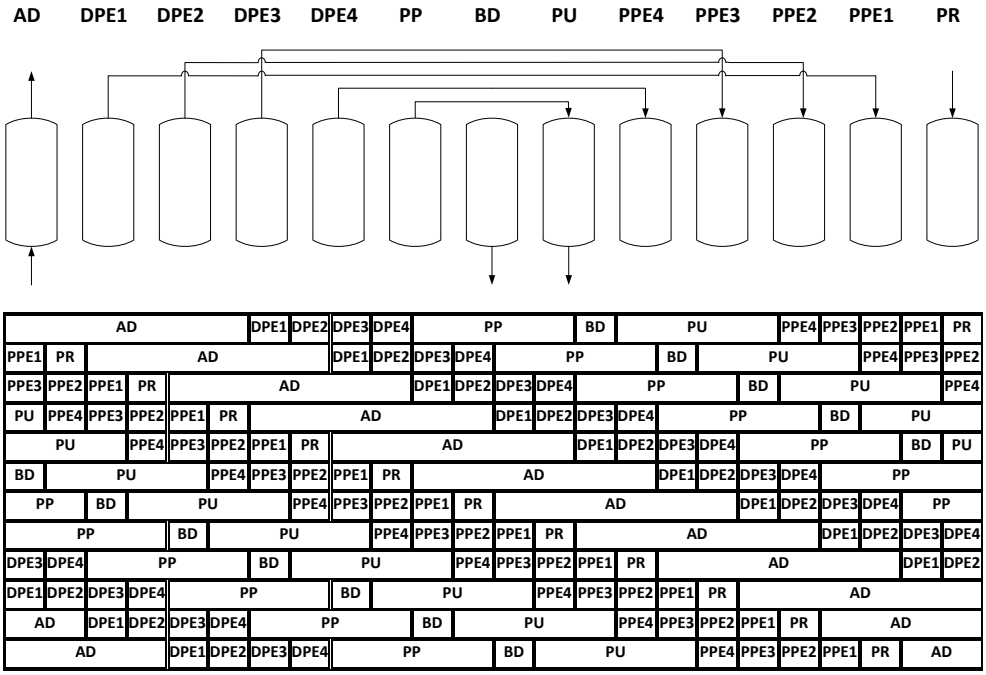

Figure 4.23: Step configurations of a twelve-column H_2 PSA cycle (AD: adsorption, DPE: depressurising pressure equalisation, PP: providing purge, BD: blowdown, PU: purge, PPE: pressurising pressure equalisation, PR: pressurisation, $t_{AD} = t_{cycle}/4$; $t_{PP} = t_{PU} = t_{cycle}/6$; $t_{BD} = t_{DPE} = t_{PPE} = t_{PR} = t_{cycle}/24$)

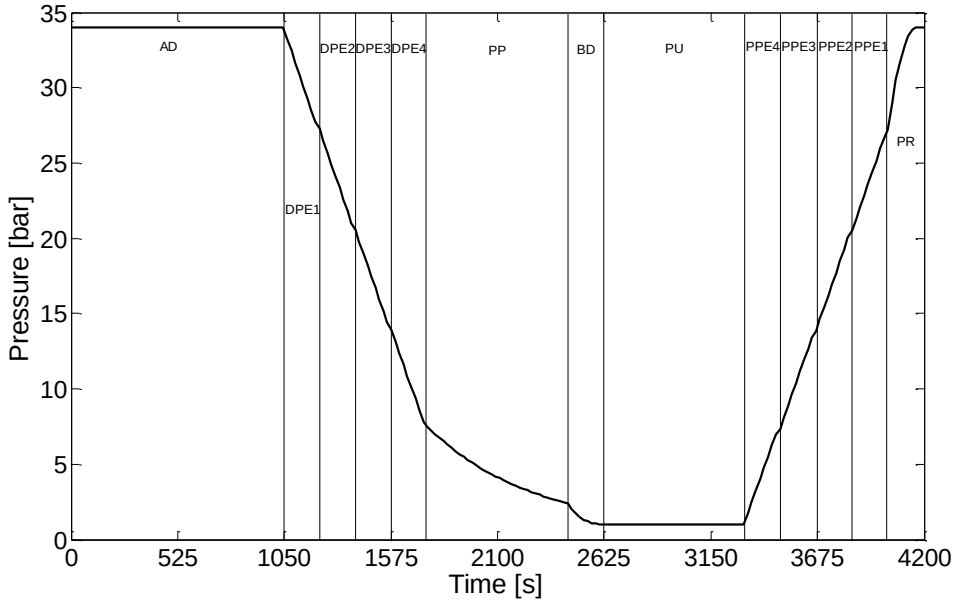

Figure 4.24: Pressure profiles at the product end of a column over a cycle at the cyclic steady state of a twelve-column H_2 PSA at PP/F = 0.3 (Run 18)

Table 4.5 lists the performance of the nine- and twelve-column H_2 PSA systems at their cyclic steady state. The nine-column H_2 PSA system can achieve the targeted H_2 purity at the adsorption step time of 1200 seconds (Run 14). It should be noted that the adsorption step time of the twelve-column H_2 PSA to achieve the targeted H_2 purity (1050 seconds at Run 18) is shorter than that of the nine-column H_2 PSA in spite of the same feed flowrate fed to one column, i.e., one-third of the total feed flowrate. This indicates that the column working capacity starts to deteriorate due to more incomplete regeneration by a purge flow having less hydrogen and by pressurising the column with more impure streams coming from other columns during the PPE steps instead of ultrapure hydrogen during the product pressurisation step. Nevertheless, the H_2 recovery still increases from 91.85% in the nine-column H_2 PSA to 92.74% in the twelve-column H_2 PSA. Since the improvement of the H_2 recovery is minimal, the bed productivity decreases significantly from 91.41 $mol_{H2}/kg_{ads}/day$ in the nine-column H_2 PSA to 69.15 $mol_{H2}/kg_{ads}/day$ with the twelve-column H_2 PSA.

Table 4.5: Performance of nine- and twelve-column PSA simulations

	Adsorption time [s]	H_2 purity [%]	H_2 recovery [%]	Bed productivity [$mol_{H2}/kg_{ads}/day$]
Nine-column H_2 PSA				
Run 12	800	99.998	87.05	86.64
Run 13	1000	99.996	89.94	89.51
Run 14	**1200**	**99.993**	**91.85**	**91.41**
Run 15	1300	99.974	92.58	92.14
Twelve-column H_2 PSA				
Run 16	750	99.999	89.11	66.52
Run 17	900	99.996	91.17	68.06
Run 18	**1050**	**99.993**	**92.74**	**69.15**
Run 19	1200	99.978	93.83	70.04

4.6.4 Sixteen-column H_2 PSA

From the previous section, it was observed that switching from the nine-column to the twelve-column Polybed system could achieve only a marginal hydrogen recovery rise (less than 1%) at the sacrifice of a remarkable increase in the CAPEX of the unit due to the significant reduction in the bed productivity. This situation can be further exacerbated considering a final sixteen-column 15-step H_2 PSA system. The step configuration is presented in Figure 4.25 and was again shown in the patent by Xu et al. (2003). The step configuration features simultaneous adsorption at four columns, simultaneous providing purge and purge at three columns, and five-stage pressure equalisation. The time unit is 1/32 of the total cycle time.

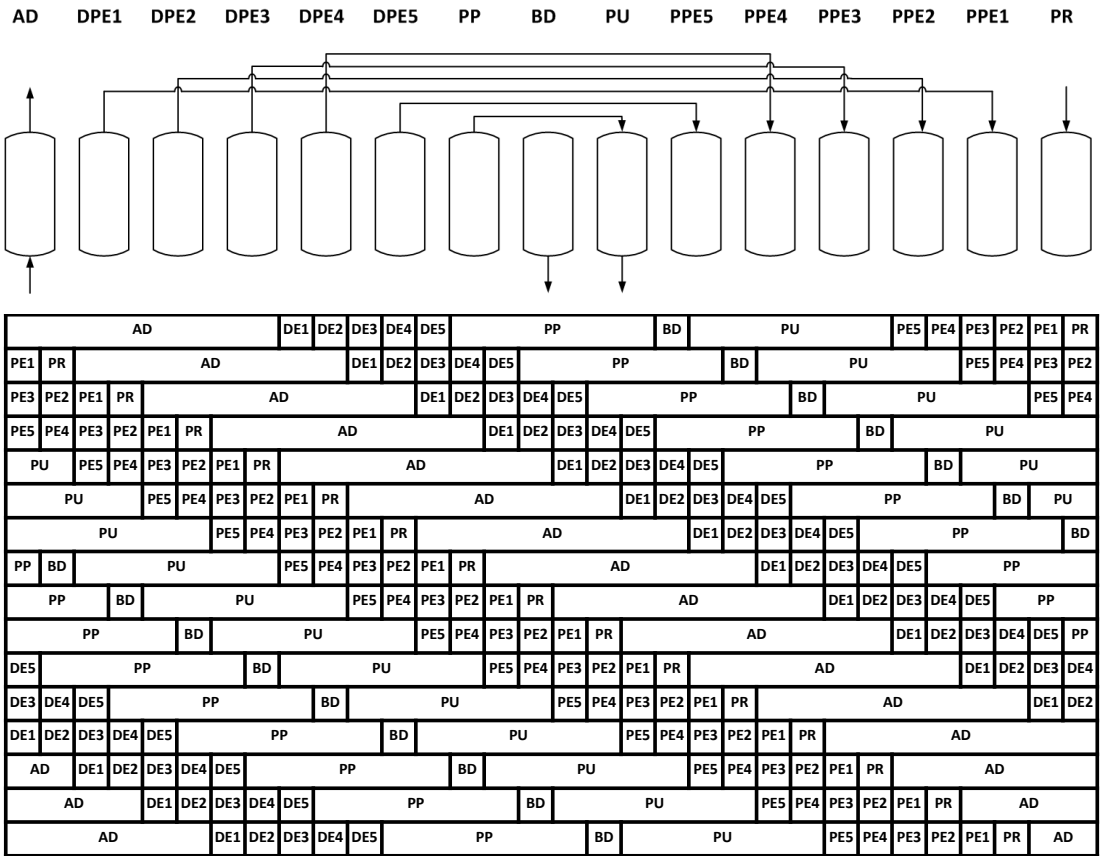

Figure 4.25: Step configurations of a sixteen-column H_2 PSA cycle (AD: adsorption, DPE: depressurising pressure equalisation, PP: providing purge, BD: blowdown, PU: purge, PPE: pressurising pressure equalisation, PR: pressurisation, $t_{AD} = t_{cycle}/4$; tPP = $t_{PU} = 3t_{cycle}/16$; $t_{BD} = t_{DPE} = t_{PPE} = t_{PR} = t_{cycle}/32$)

From Table 4.6, it can be seen that with an additional pressure equalisation step hydrogen recovery increases in Run 22 only by 0.3% compared to the twelve column system while the productivity continues to diminish, mainly due to the reduction to one-fourth of the total flowrate entering one bed. Because of the elevated CAPEX associated with this unit and the extremely marginal H_2 recovery increase, this configuration was not taken into account for the following comparison among the PSA cycles in the next section.

Table 4.6: Performance of sixteen-column PSA simulations

	Adsorption time [s]	H_2 purity [%]	H_2 recovery [%]	Bed productivity [$mol_{H2}/kg_{ads}/day$]
Run 20	900	99.996	90.08	50.40
Run 21	1050	99.994	91.74	51.33
Run 22	**1200**	**99.992**	**93.07**	**52.08**
Run 23	1350	99.976	94.21	52.71

4.6.5 Comparison among various PSA cycles

So far, the hydrogen recovery and bed productivity have been compared at the targeted H_2 purity of around 99.99+ mol% among various H_2 PSA cycles with different numbers of columns and different step configurations. As already mentioned, the bed productivity was reduced with the increasing number of columns while the H_2 recovery improved. The increased number of pressure equalisation steps reduced the total amount of hydrogen lost in the blowdown and purge steps and consumed in the final re-pressurisation step. The twelve-column system combined all the previous benefits leading to a H_2 recovery of around 93%. All the simulation results are plotted on Figure 4.26, indicating a clear relation between hydrogen purity and recovery.

It is expected that a more-than-sixteen-column H_2 PSA configuration may improve the H_2 recovery further to more than 93%, but given the trend of improving H_2 recovery with the number of columns any further improvement of H_2 recovery would be extremely limited. In particular, more than five pressure equalisation steps may not be necessary since the column pressure at the end of the fourth DPE (or

PPE) step in the twelve-column H_2 PSA system is 7.5 bar (or 27 bar) and is close to that at the end of the third DPE (or PPE) step in the nine-column H_2 PSA system, which is 8.5 bar (or 26 bar). Therefore, altering a PSA cycle to have more than five pressure equalisation steps cannot recover a notable pressure nor save the amount of ultrapure hydrogen consumed during the product pressurisation step significantly. In addition, it is likely that the working capacity of the column would be badly affected by incomplete regeneration with purge flow having less hydrogen and re-pressurisation of the column by more impure gas streams than the pure product streams.

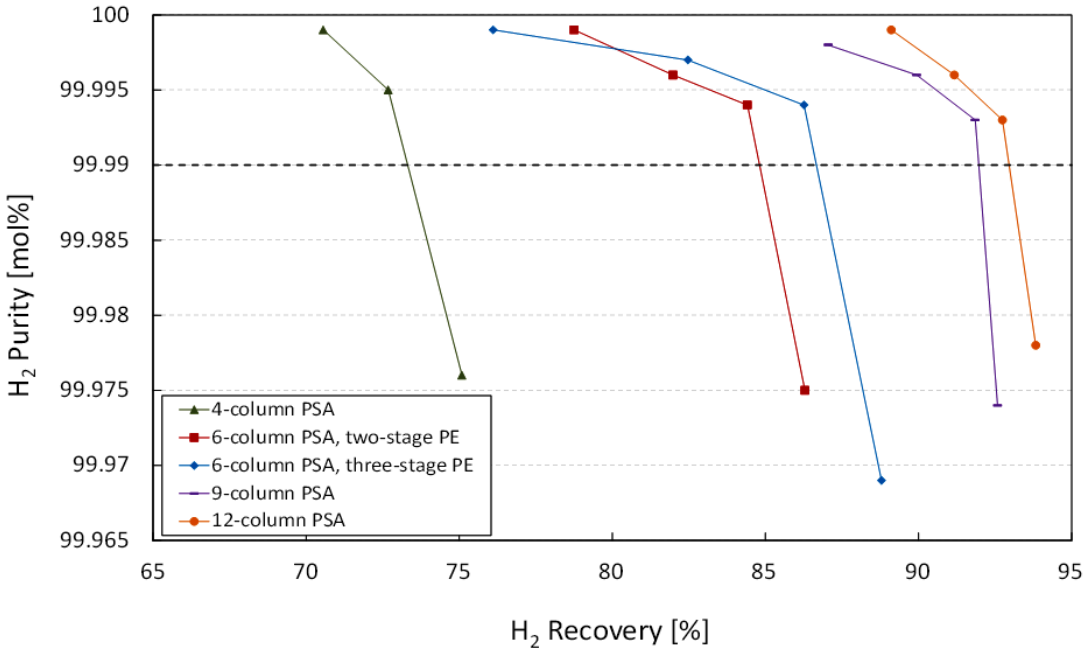

Figure 4.26: Comparison of hydrogen purity and recovery at various H_2 PSA systems with the different number of columns and different step configurations

Figure 4.27 shows the hydrogen mole fraction profile along the column at the end of the adsorption step at the cyclic steady state of all the PSA simulations investigated in this chapter. It clearly shows that with the reduction of the feed flow to one-column for adsorption from four-column to nine-column through six-column with two-stage pressure equalisation the PSA system allows a cycle to have longer adsorption step time so the H_2 mass transfer zone (MTZ) can progress more to the product end at the end of adsorption step. This results in less H_2 remaining in the bed at the end of the adsorption step, leading to higher H_2 recovery. The figure also

shows that the twelve-column PSA has a broader H_2 MTZ than the nine-column PSA does due to the worse regeneration of the column during the purge step and the use of a more impure stream for column pressurisation during the PPE steps. Figure 4.28 shows the hydrogen mole fraction profiles along the column at the end of the blowdown step at the cyclic steady state of all the PSA simulations. Also in this case, the H_2 MTZ is more progressed toward the product end for the Polybed systems but at the feed end the nine- and twelve-column configurations exhibit a higher hydrogen mole fraction compared to the other configurations.

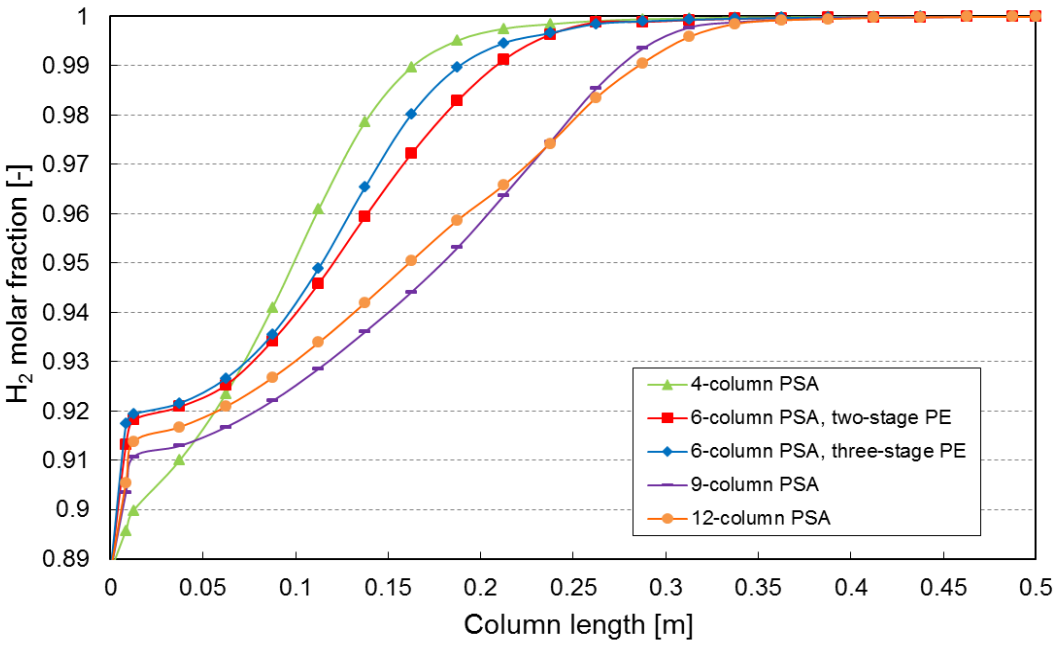

Figure 4.27: Hydrogen molar fraction profiles along the column at the end of the adsorption step in various H_2 PSA cycles at around 99.99% H_2 purity

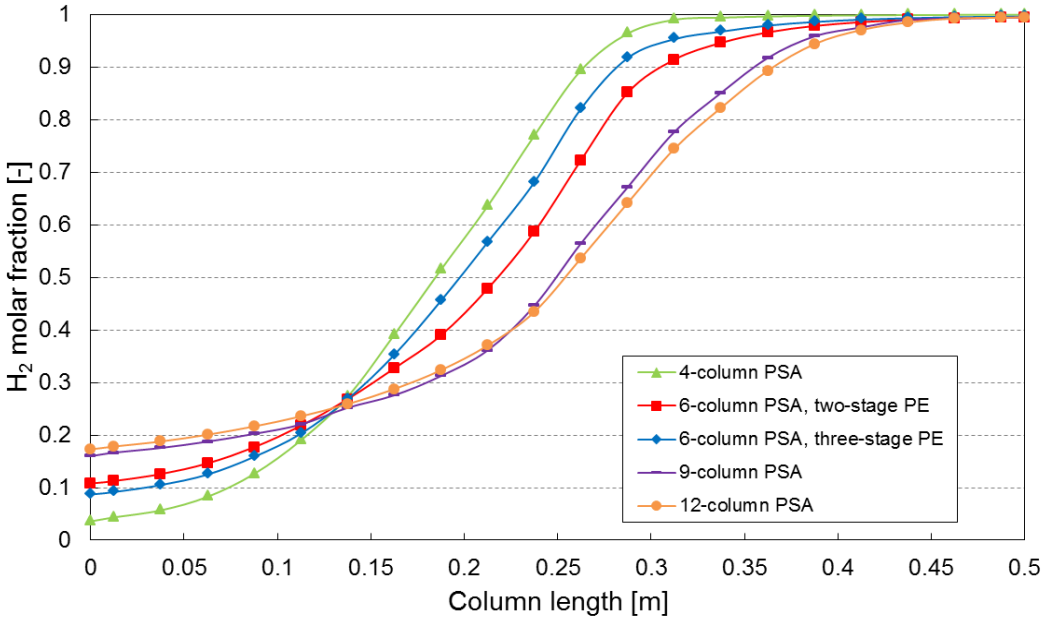

Figure 4.28: Hydrogen molar fraction profiles along the column at the end of the blowdown step in various H_2 PSA cycles at around 99.99% H_2 purity

4.7 H_2 PSA simulation results with fixed total cycle time

In the previous section (Luberti et al., 2014a), the column dimensions were kept constant in all the PSA configurations so the total cycle time increases considerably and the bed productivity decreases with increasing number of columns from four to twelve. This is because more than one column simultaneously undergoes the adsorption step so the feed flowrate to one adsorption column is reduced to half or one-third of the total feed flowrate. In this section, the PSA simulations were performed at a constant total cycle time of 1200 s (20 min) regardless of the various configurations. As a result, the bed productivity can be kept almost constant. Note that with the increasing number of columns, the volume of one column should be reduced to keep the total cycle time constant but the ratio of column length to diameter is kept constant at 20. In simulating the four-, six-, nine- and twelve-column PSA systems, the same step configurations as in the previous section were considered. The six-column configuration selected was the one having two pressure equalisation stages. More details can be found in the reference (Luberti et al., 2014b).

It has been explored at which one-column residence time during the adsorption step ($\tau = V/F$) the H_2 PSA can achieve the target H_2 purity of 99.99+ mol%. Table 4.7 shows the effect of residence time on the performance of each H_2 PSA configuration with respect to hydrogen purity, recovery and productivity. In the four-, six- and nine-column systems, the targeted H_2 purity is obtained with a H_2 PSA run with a column size to give a residence time in the vicinity of 172 s. This is because as the feed flowrate to one column during the adsorption step is reduced from total feed flowrate at the four-column PSA to one-third at the nine-column PSA through to one-half at the six-column PSA, the required volume of one adsorption column is reduced almost at the same ratio. However, the residence time is notably reduced to 154 s with the twelve-column PSA from 172 s with the nine-column PSA since the feed flowrate to one column during the adsorption step does not change but the adsorption step time decreases from one-third to one-fourth of cycle time, i.e., the total amount of feed to be treated by one column during the adsorption step is reduced.

It is clearly demonstrated that given the targeted H_2 purity of 99.99+ mol%, the H_2 recovery increases from 75% to 93% with increasing number of columns, as shown in Table 4.7. In addition, the twelve-column system shows the maximum recovery with a slightly lower productivity compared to the nine-column system due to the different ratio between the adsorption step and total cycle times in the step configuration.

Table 4.7: Effect of the one-column residence time during adsorption step on hydrogen purity, recovery and productivity at different H_2 PSA configurations

One-column residence time [s]	Column length [m]	Column diameter [m]	H_2 purity [%]	H_2 recovery [%]	Bed productivity [mol_{H2}/kg_{ads}/day]
Four-column PSA with two-stage pressure equalisation					
140	0.467	0.0233	99.979	78.25	218.39
172	**0.500**	**0.0250**	**99.992**	**75.28**	**171.51**
210	0.535	0.0267	99.996	71.85	133.69
245	0.563	0.0281	99.998	68.42	109.12
Six-column PSA with two-stage pressure equalisation					
140	0.371	0.0185	99.976	86.38	321.44
172	**0.400**	**0.0200**	**99.993**	**83.43**	**253.44**
210	0.424	0.0212	99.997	80.32	199.26
245	0.447	0.0223	99.999	75.93	161.46
Nine-column PSA with three-stage pressure equalisation					
140	0.324	0.0162	99.971	92.79	345.12
172	**0.346**	**0.0173**	**99.992**	**91.48**	**277.78**
210	0.371	0.0185	99.995	89.71	222.56
245	0.390	0.0195	99.998	86.96	184.39
Twelve-column PSA with four-stage pressure equalisation					
140	0.324	0.0162	99.983	93.41	260.57
154	**0.334**	**0.0167**	**99.992**	**92.94**	**235.92**
172	0.346	0.0173	99.994	92.52	210.71
210	0.371	0.0185	99.997	90.48	168.35

4.8 Conclusions

A novel H_2 PSA system to produce ultrapure hydrogen from a raw H_2 gas generated in an advanced IGCC process has been proposed in this chapter. The advanced IGCC plant where CO_2 is captured by a pre-combustion capture unit is capable of cogenerating both power and ultrapure hydrogen more economically. The advanced IGCC plant can be used in oil refineries experiencing difficulties in sourcing ultrapure hydrogen, which is required to operate hydrotreaters and hydrocrackers, and intending to reduce carbon emissions from their hydrogen and power plants.

It is very important to know the maximum H_2 recovery that a H_2 PSA can produce from the raw H_2 gas in evaluating the performance of an advanced IGCC plant for cogenerating power and ultrapure hydrogen. This is because the flowrate of PSA tail gas, to be determined by the H_2 recovery, should be compressed up to 34 bar from the purge pressure to get the PSA tail gas to be fed to the gas turbine along with the fuel gas. Therefore, it is essential to design a H_2 PSA such that its H_2 recovery can be maximised in order to minimise the power consumption relating to tail gas compression.

H_2 PSAs in commercial SMR hydrogen plants are capable of achieving around 89% H_2 recovery at 99.99+ mol% H_2 purity. Compared to the raw H_2 gas in the SMR hydrogen plant, the raw H_2 gas fed to the H_2 PSA in the advanced IGCC plant has a gas composition of higher hydrogen and lower impurities and the higher total pressure at which conditions the H_2 PSA is expected to perform better than the H_2 PSA in a SMR H_2 plant. As expected, the Polybed H_2 PSA with twelve columns and four-stage pressure equalisation achieves 93% H_2 recovery at 99.99+ mol% H_2 purity. This result was obtained for both the cases of fixed column dimensions and varying cycle time and for fixed cycle time and varying column dimensions, at a given total flowrate.

References

Ahn H, Yang J, Lee CH. Effects of feed composition of coke oven gas on a layered bed H_2 PSA process. Adsorption 2001; 7: 339-356.

Ahn S, You YW, Lee DG, Kim KH, Oh M, Lee CH. Layered two- and four-bed PSA processes for H_2 recovery from coal gas. Chemical Engineering Science 2012; 68: 413-423.

Cassidy RT. Polybed pressure-swing adsorption hydrogen processing. ACS Symposium Series 1980; volume 135 chapter 13: pages 247-259.

DOE NETL. Cost and performance baseline for fossil energy plants; 2007.

Ebner AD, Mehrotra A, Ritter JA. Graphical approach for complex PSA cycle scheduling. Adsorption 2009; 15: 406-421.

Friedrich D, Ferrari MC, Brandani S. Efficient simulation and acceleration of convergence for a dual piston pressure swing adsorption system. Ind. Eng. Chem. Res. 2013; 52: 8897-8905.

Fuderer A, Rudelstorfer E. US Patent 3986849 to Union Carbide Corporation, 1976.

Jain S, Moharir AS, Li P, Wozny G. Heuristic design of pressure swing adsorption: a preliminary study. Separation and Purification Technology 2003; 33: 25-43.

Jiang L, Biegler LT, Fox VG. Simulation and optimal design of multiple-bed pressure swing adsorption systems. AIChE J. 2004; 50: 2904-2917.

Lopes FVS, Grande CA, Ribeiro AM, Loureiro JM, Evaggelos O, Nikolakis V, Rodrigues A E. Adsorption of H_2, CO_2, CH_4, CO, N_2 and H_2O in activated carbon and zeolite for hydrogen production. Separation Science and Technology 2009; 44: 1045-1073.

Lopes FVS, Grande CA, Rodrigues AE. Activated carbon for hydrogen purification by pressure swing adsorption: Multicomponent breakthrough curves and PSA performance. Chemical Engineering Science 2011; 66: 303-317.

Luberti M, Friedrich D, Brandani S, Ahn H. Design of H_2 PSA for cogeneration of ultrapure hydrogen and power at an advanced integrated gasification combined cycle with pre-combustion capture. Adsorption 2014a; 20: 511-524.

Luberti M, Friedrich D, Ozcan DC, Brandani S, Ahn H. A novel strategy to produce ultrapure hydrogen from coal with pre-combustion carbon capture. Energy Procedia 2014b; 63: 2023-2030.

Majlan EH, Daud WRW, Iyuke SE, Mohamad AB, Kadhum AAH, Mohammad AW, Takriff MS, Bahaman N. Hydrogen purification using compact pressure swing adsorption system for fuel cell. Hydrogen Energy 2009; 34: 2771-2777.

Malek A, Farooq S. Study of a six-bed pressure swing adsorption process. AIChE J. 1997; 43: 2509-2523.

Mehrotra A, Ebner AD, Ritter JA. Arithmetic approach for complex PSA cycle scheduling. Adsorption 2010; 16: 113-126.

Mehrotra A, Ebner AD, Ritter JA. Simplified graphical approach for complex PSA cycle scheduling. Adsorption 2011; 17: 337-345.

Miller GW, Knaebel KS, Ikels KG. Equilibria of nitrogen, oxygen, argon, and air in molecular sieve 5A. AIChE J. 1987; 33: 194-201.

Nikolic D, Giovanoglou A, Georgiadis MC, Kikkinides ES. Generic modelling framework for gas separation using multibed pressure swing adsorption processes. Ind. Eng. Chem. Res. 2008; 47: 3156-3169.

OriginLab. Data analysis and graphing software. Origin 8.5, 2010.

Park JH, Kim JD, Yang RT. Adsorber dynamics and optimal design of layered beds for multicomponent gas adsorption. Chemical Engineering Science 1998; 53: 3951-3963.

Ribeiro AM, Grande CA, Lopes FVS, Loureiro JM, Rodrigues AE. A parametric study of layered bed PSA for hydrogen purification. Chemical Engineering Science 2008; 63: 5258-5273.

Ruthven DM. Principles of Adsorption and Adsorption Processes, 1984.

Ruthven DM, Farooq S, Knaebel K. Pressure swing adsorption, 1994.

Xu J, Weist EL. US Patent 6454838 B1 to Air Products and Chemicals Inc., 2002.

Xu J, Rarig DL, Cook TA, Hsu KK, Schoonover M, Agrawal R. US Patent 6565628 B2 to Air Products and Chemicals Inc., 2003.

Yang RT. Gas separation by adsorption processes. Butterworth Publishers, 1987.

Yang J, Lee CH. Adsorption dynamics of a layered bed PSA for H_2 recovery from coke oven gas. AIChE J. 1998; 44: 1325-1334.

You YW, Lee DG, Yoon KY, Moon DK, Kim SM, Lee CH. H_2 PSA purifier for CO removal from hydrogen mixtures. Hydrogen Energy 2012; 37: 18175-18186.

Chapter 5: Process integration of the industrial H_2 PSA unit with the IGCC for cogenerating ultrapure hydrogen and electricity, cost analysis and process improvements

This chapter describes the process integration and optimisation of an industrial H_2 PSA unit with the IGCC described in Chapter 2 for cogenerating ultrapure hydrogen and electricity. As already described in Chapter 4, improving the H_2 recovery at the H_2 PSA unit to its maximum can contribute to reducing the power consumption for compressing the H_2 PSA tail gas by minimising the yield of the H_2 PSA tail gas by-product. Similarly to the results obtained in the previous chapter for a lab-scale unit, it was found that, at the same H_2 purity of 99.99+ mol%, the hydrogen recovery could be enhanced up to 92% by increasing the number of columns. A detailed economic analysis has been carried out to evaluate the capital expenditure (CAPEX) of each PSA configuration analysed. After redesigning the power section of the IGCC to take into account the retrofit of the H_2 PSA unit, the levelised cost of electricity (LCOE) was evaluated for the base, capture and integrated cases. Furthermore, it was demonstrated that the H_2 PSA can also be designed to achieve at least 90% H_2 recovery even when a portion of the tail gas is recycled to the shift reactors or the dual-stage Selexol unit in order to improve the advanced IGCC performances by reducing the auxiliary power consumption of the carbon capture unit and the CO_2 compression train. Additional novel configurations proposed in a recent patent have also been simulated in this chapter to improve the overall net plant efficiency. It was found that the ultimate configuration where a portion of the H_2 PSA tail gas is recycled at the same time to both the coal dryer and the water gas shift reactors resulted in the highest increase of the overall net plant efficiency compared with the base case and other process configurations.

5.1 Retrofit of the H_2 PSA unit to the IGCC with pre-combustion capture

The modified IGCC plant block diagram to simultaneously produce power and ultrapure hydrogen is depicted in Figure 5.1.

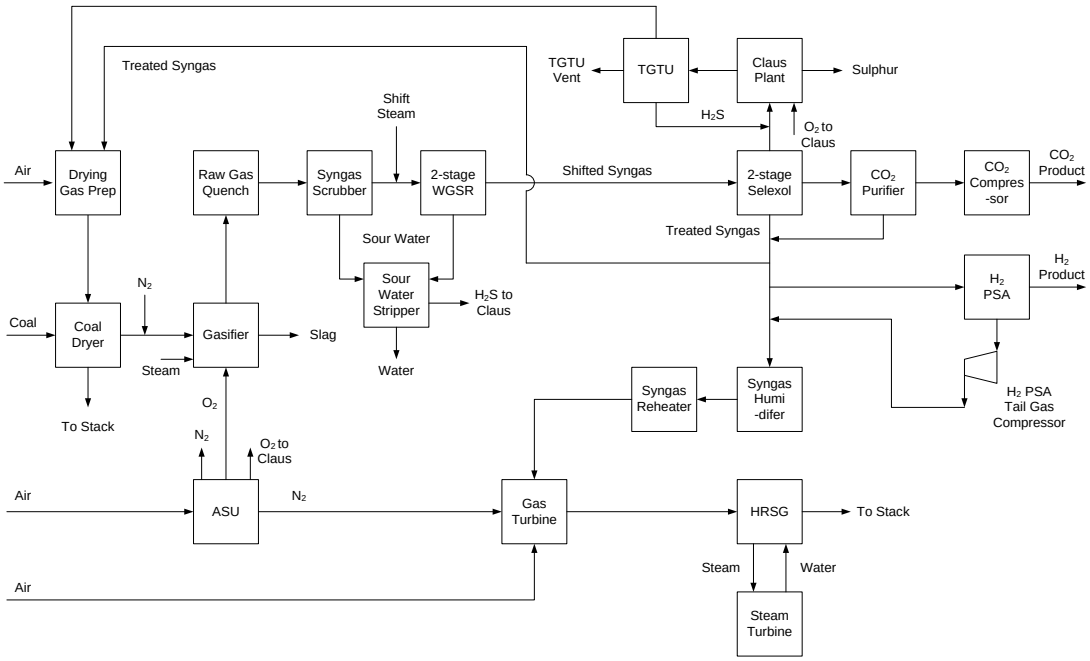

Figure 5.1: Block flow diagram of an advanced IGCC plant for cogenerating power and ultrapure hydrogen with pre-combustion capture

As mentioned in Chapter 4, the starting point of the H_2 PSA retrofit to the IGCC is Case 6 of the DOE report (2007) where all the units and stream specifications remain constant until downstream of the dual-stage Selexol process. In the cogenerating IGCC plant, the H_2-rich fuel gas is split into two streams and one of the two is fed to a H_2 PSA for producing ultrapure hydrogen. The split ratio is determined so as to generate the ultrapure hydrogen at a flowrate of 100 MMSCFD (10,030 kg/h). Figure 5.2 shows the overall mass balance around the industrial H_2 PSA unit with a H_2 recovery of 91.3%.

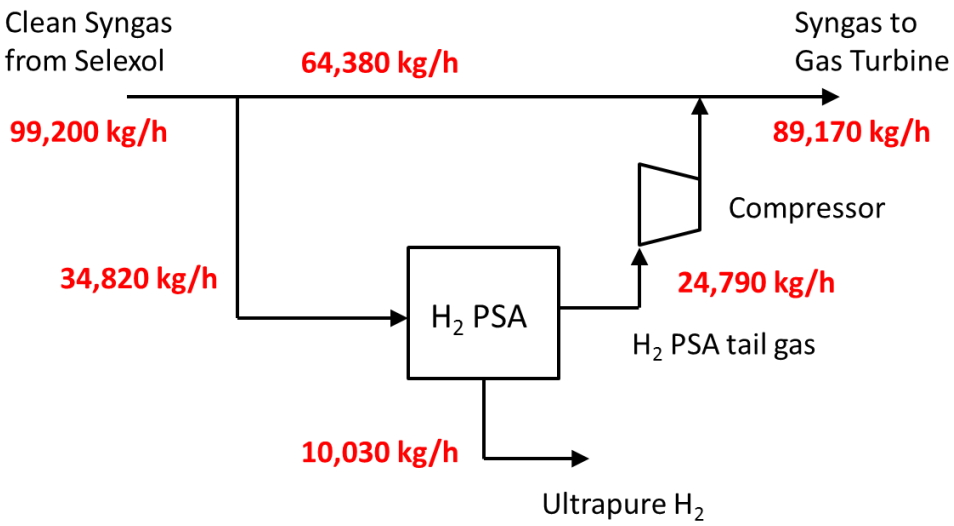

Figure 5.2: Overall mass balance around the industrial H_2 PSA unit of the cogenerating IGCC

The H_2 PSA tail gas needs to be compressed up to the pressure of the H_2 fuel gas for feeding it to a high-pressure gas cycle. This strategy of utilising the H_2 PSA tail gas can augment the power generation at the combined cycle. Therefore, the net power generation from the advanced IGCC should take into account additional power consumption at the H_2 PSA tail gas compressors and power generation at the combined cycle relating to the H_2 PSA tail gas in addition to the H_2 fuel gas.

Since in this configuration a significant part of the syngas is sent to the H_2 PSA and hence it cannot be used for power generation, both gas turbines and steam cycle have to be redesigned in order to take into account this change. With a fixed ultrapure hydrogen production rate of 100 MMSFCD a new configuration for the gas turbine was simulated considering a total power generation of 324 MW_e. Given the GE turbines types and specifications for IGCC syngas applications (GE, 2009) the total power was comprehensive of a 232 MW_e 7F turbine plus a 92 MW_e 6FA turbine (GE, 2009). The HRSG cycle was also redesigned to take into account the reduction of steam generation, capable to produce 155 MW_e of power. Sufficient steam has still to be provided to other units of the plant, such as the WGSRs, as in the non-integrated case.

In this chapter, the industrial H_2 PSA unit has been simulated using gPROMS software (PSE, 2010). The discretisation method for the spatial domain in the column was the second order orthogonal collocation on finite element method with 100

nodes along the column where the absolute and relative numerical accuracies were both set to 10^{-5}.

5.2 Design of an industrial H_2 PSA at the advanced IGCC

In designing an industrial H_2 PSA unit it is essential, as already mentioned, to increase the hydrogen recovery at the H_2 PSA close to its maximum in order to minimise the required H_2 PSA feed flowrate and the tail gas compression work at the same time. This is because the tail gas compression involves significant power consumption, up to a few MWs. Once the mass balance around the H_2 PSA is determined based on the required product flowrate and the maximum H_2 recovery achievable, it is possible to estimate net power generation taking into account the tail gas compression work.

In the previous chapter, an in-depth study on the design of H_2 PSA integrated with an IGCC power plant was carried out to maximise H_2 recovery in the H_2 PSA unit. The results demonstrated that the H_2 recovery could be increased by increasing the complexity of the PSA step configuration, which enables a PSA cycle to have a lower feed flow to one column for adsorption and to accommodate more pressure equalisation steps. In this previous study, the column dimensions were kept constant in all the PSA configurations so that the total cycle time increases considerably and the bed productivity decreases with increasing number of columns from four to twelve. This is because more than one column simultaneously undergoes the adsorption step so the total flowrate is reduced to half or one-third.

In this chapter, similarly to the last paragraph of Chapter 4, the industrial H_2 PSA simulations were performed at a constant total cycle time of 420 s regardless of varying PSA configurations. The total flowrate was evaluated from the IGCC simulation at a value of 1.26 m^3/s (1,745 mol/s) and kept constant for all the configurations. Since this flowrate is huge, six PSA trains in parallel for the four-column H_2 PSA system, three trains for the six-column H_2 PSA and two H_2 PSA trains for the nine- and twelve-column systems were considered in order to have the same flowrate of 0.21 m^3/s entering one single column. As a result, the column dimensions were similar for all the configurations and close to the practical limits for industrial PSA units. Limitations on diameter are generally due to gas distributions

and end-column effects. PSA units rarely exhibit a bed diameter of more than 1.5–2.0 m to ensure even distribution of the gas flow along the column, i.e. axially dispersed plug flow (Mhaskar and Moharir, 2012). Similarly, the limit on height is mainly due to crush strength problems of the adsorbent particles and more elaborated mechanical design related to wind load, seismic load, etc. Normally heights of beds are not more than 10 m (Geankoplis, 1997; Megyesy, 1995).

It has been explored at which one-column residence time during the adsorption step ($\tau = V/F$) the H_2 PSA unit can achieve the targeted H_2 purity of 99.99+ mol%. Table 5.1 shows information about column size as well as the associated mass of adsorbent in one column and pressure drops. The table was constructed considering an adsorption step at the H_2 PSA feed conditions over one packed bed. For all the simulations, the column length to diameter ratio was kept constant at a value of 5, which is common for industrial applications (UOP, 2014) and extensively reported in the literature (Nikolic et al., 2008; Mhaskar and Moharir, 2012). The calculated mass of 5A zeolite sorbent in an industrial column ranges between 11.5 and 18.7 tons.

Table 5.1: List of column parameters and pressure drop evaluation for the industrial H_2 PSA simulations

τ (s)	V (m^3)	D (m)	L (m)	m_{ads} (ton)	ΔP (kPa)	Re_h (-)
130	27.3	1.91	9.55	18.7	3.9	78.6
120	25.2	1.86	9.30	17.3	4.2	82.9
110	23.1	1.80	9.00	15.8	4.5	88.5
100	21.0	1.75	8.75	14.4	4.9	93.7
90	18.9	1.69	8.45	13.0	5.4	100.4
80	16.8	1.62	8.10	11.5	6.0	109.3

Note that for packed beds the equivalent Reynolds number is evaluated as (Bird et al., 2007):

$$\mathrm{Re}_h = \frac{2}{3(1-\varepsilon)} \cdot \frac{\rho u_0 d_p}{\mu} \qquad (5\text{-}1)$$

Even if the superficial velocity of 0.1 m/s is considerably higher than the one from the lab scale, the estimated pressure drops were limited to 0.06 bar in the case of $\tau = 80$ s. Figure 5.3 shows the evolution of the pressure drops with the change of residence time where a fairly linear trend can be observed. Since the Reynolds

number calculated in Table 5.1 is in the vicinity of 100, the fluid flow through the packed column results in the transition region between laminar and turbulent flow (Bird et al., 2007).

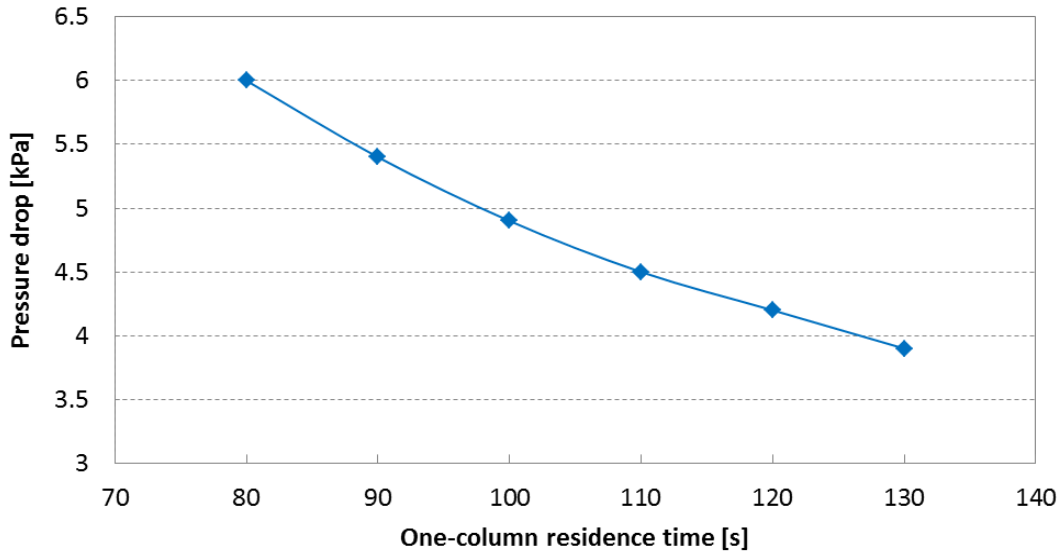

Figure 5.3: Evolution of the pressure drops against one-column residence time for the industrial H_2 PSA simulations

Additional column parameters as well as the particle parameters and operating conditions of the industrial H_2 PSA simulations are reported in Table 5.2. As expected, the transport properties become higher for the industrial process compared to the lab-scale simulations, as shown in Table 5.2 for a one-column residence time of 120 s. Lab-scale transport properties are reported in brackets next to the industrial-scale properties. Figures 5.4–5.7 show the step configurations for the four-, six-, nine- and twelve-bed PSA systems investigated in this chapter. Note that the six-column configuration contains two stages of pressure equalisation. As already mentioned, the total cycle time was maintained constant at 420 s.

Table 5.2: List of additional column parameters, particle parameters and operating conditions of the industrial H_2 PSA simulations for a one-column residence time of 120 s. Numbers in brackets represent transport parameters of lab-scale system

Additional column parameters	
External bed void fraction, ε (-)	0.391
Axial mass dispersion coefficient, D_z (m^2/s)	3.0×10^{-4} (1.2×10^{-4})
Axial thermal dispersion coefficient, k_z (W/m·K)	4.6 (1.3)
Wall heat transfer coefficient, h_w ($W/m^2\cdot K$)	433.4 (95.0)
Adsorbent parameters	
Pellet density, ρ_p (kg/m^3)	1,126
Pellet void fraction, ε_p (-)	0.503
Adsorbent specific heat capacity, $c_{P,s}$ (J/kg·K)	920
Pellet averaged diameter, d_p (mm)	1.70
Micropore LDF coefficient, $k_i^{cr}\cdot 3/r_c$	0.7467/0.0017/0.0332/0.1697/0.1800
$H_2/CO_2/CO/N_2/Ar$ (s^{-1})	(Lopes et al., 2009)
Operating conditions	
P_{ads} (bar)	35
P_{des} (bar)	1
T_{feed} (K)	303
Q_{feed} (mol/s)	291
Feed composition, $y_{H2}/y_{CO2}/y_{CO}/y_{N2}/y_{Ar}$ (molar)	0.8875/0.0212/0.0266/0.0544/0.0103

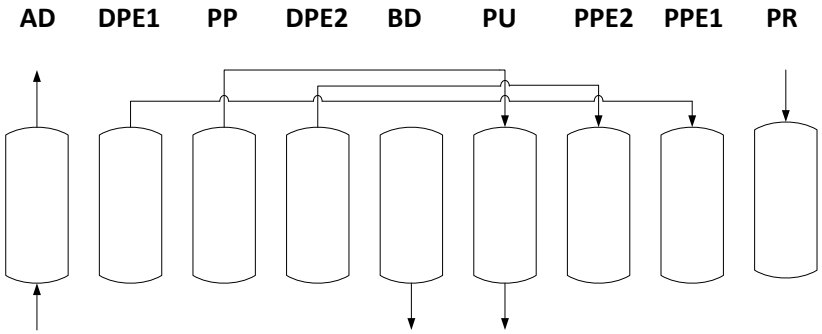

AD			DPE1	PP		DPE2	BD	PU		PPE2	PPE1	PR		
BD	PU		PPE2	PPE1	PR		AD				DPE1	PP		DPE2
DPE1	PP		DPE2	BD	PU		PPE2	PPE1	PR		AD			
PPE1	PR			AD			DPE1	PP		DPE2	BD	PU		PPE2

Figure 5.4: Step configuration of the industrial four-column H_2 PSA cycle at PP/F = 0.2 (See Chapter 4 for configuration details)

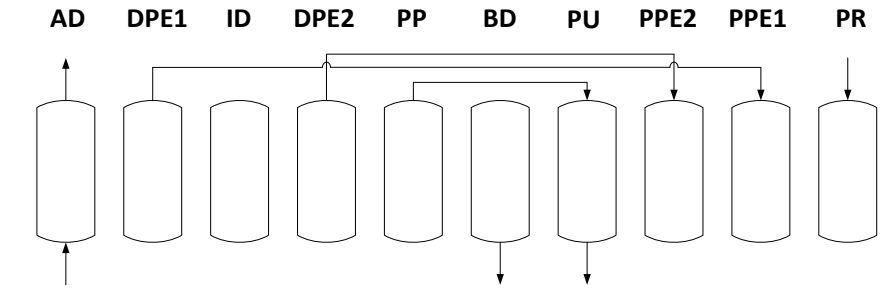

AD			DPE1	ID	DPE2	PP	BD	PU	PPE2	PPE1	PR
PPE1	PR	AD			DPE1	ID	DPE2	PP	BD	PU	PPE2
PU	PPE2	PPE1	PR	AD			DPE1	ID	DPE2	PP	BD
PP	BD	PU	PPE2	PPE1	PR	AD			DPE1	ID	DPE2
DPE1	ID	DPE2	PP	BD	PU	PPE2	PPE1	PR	AD		
AD		DPE1	ID	DPE2	PP	BD	PU	PPE2	PPE1	PR	AD

Figure 5.5: Step configurations of the industrial six-column H_2 PSA cycle with two-stage pressure equalisation at PP/F = 0.3 (See Chapter 4 for configuration details)

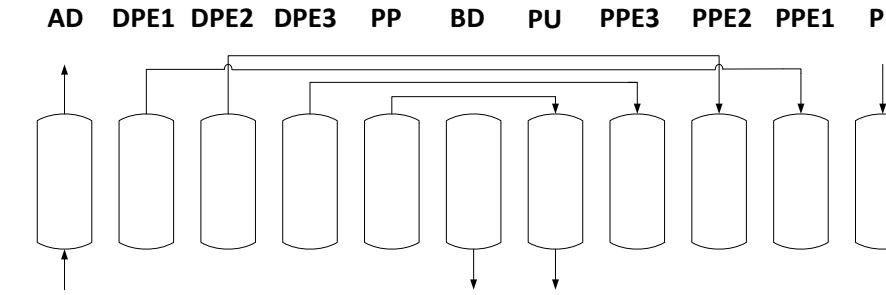

AD			DPE1	DPE2	DPE3	PP	BD	PU	PPE3	PPE2	PPE1	PR
PPE1	PR	AD			DPE1	DPE2	DPE3	PP	BD	PU	PPE3	PPE2
PPE3	PPE2	PPE1	PR	AD			DPE1	DPE2	DPE3	PP	BD	PU
PU		PPE3	PPE2	PPE1	PR	AD			DPE1	DPE2	DPE3	PP	BD
PP	BD	PU		PPE3	PPE2	PPE1	PR	AD			DPE1	DPE2	DPE3	PP
DPE3	PP		BD	PU		PPE3	PPE2	PPE1	PR	AD			DPE1	DPE2
DPE1	DPE2	DPE3	PP		BD	PU		PPE3	PPE2	PPE1	PR	AD		
AD		DPE1	DPE2	DPE3	PP		BD	PU		PPE3	PPE2	PPE1	PR	AD
AD			DPE1	DPE2	DPE3	PP		BD	PU		PPE3	PPE2	PPE1	PR	AD

Figure 5.6: Step configurations of the industrial nine-column H_2 PSA cycle at PP/F = 0.3 (See Chapter 4 for configuration details)

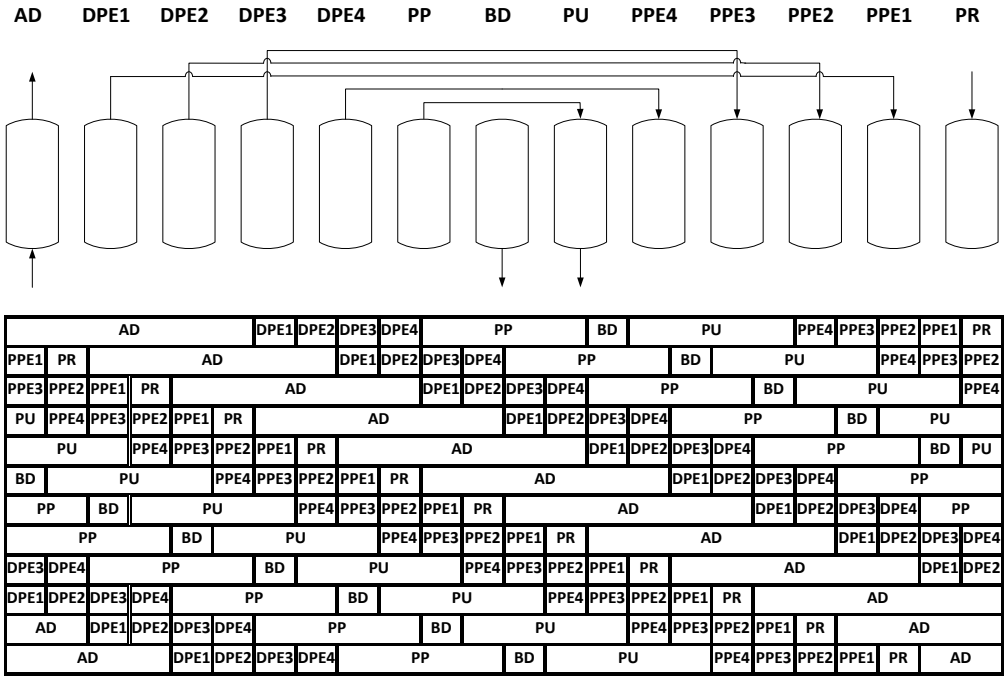

Figure 5.7: Step configurations of the industrial twelve-column H_2 PSA cycle at PP/F = 0.3 (See Chapter 4 for configuration details)

Table 5.3 shows the effect of residence time on the performance of each H_2 PSA configuration with respect to hydrogen purity, recovery and bed productivity. It is expected that with increasing residence time the H_2 purity can be improved as a sacrifice of H_2 recovery and productivity. In the four-, six-, and nine-column systems, the targeted H_2 purity is obtained with a H_2 PSA run having a column size to give a residence time in the vicinity of 120 s. The six- and nine-column systems have identical adsorption step times so this behaviour is expected. In the four-column configuration, the adsorption time is shorter than the previous systems but the beds are not well regenerated during the purge step due to a lower purge-to-feed ratio. As a result, they require the same residence time in order to obtain the desired product purity. However, the residence time is notably reduced to 90 s from the nine-column PSA to the twelve-column PSA system since the feed flowrate to one column during the adsorption step does not change but the adsorption step time decreases from one-third to one-fourth of cycle time, i.e., the total amount of feed to be treated by one column during adsorption step is reduced.

Table 5.3: Effect of the one-column residence time during adsorption step on hydrogen purity, recovery and bed productivity at different industrial H_2 PSA configurations with total cycle time of 420 s

One-column residence time (s)	D (m)	L (m)	H_2 purity (%)	H_2 recovery (%)	Bed productivity ($mol_{H2}/kg_{ads}/day$)
Four-column PSA with two-stage pressure equalisation					
130	1.91	9.55	99.995	75.63	225.4
120	**1.86**	**9.30**	**99.992**	**77.26**	**249.4**
110	1.80	9.00	99.981	80.24	282.6
100	1.75	8.75	99.973	82.30	318.8
Six-column PSA with two-stage pressure equalisation					
130	1.91	9.55	99.996	82.52	327.8
120	**1.86**	**9.30**	**99.993**	**84.22**	**362.5**
110	1.80	9.00	99.986	86.17	404.6
100	1.75	8.75	99.977	87.73	453.1
Nine-column PSA with three-stage pressure equalisation					
130	1.91	9.55	99.995	89.97	357.4
120	**1.86**	**9.30**	**99.992**	**91.26**	**392.8**
110	1.80	9.00	99.983	92.36	433.6
100	1.75	8.75	99.974	93.51	482.9
Twelve-column PSA with four-stage pressure equalisation					
110	1.80	9.00	99.997	89.19	314.1
100	1.75	8.75	99.995	90.36	350.0
90	**1.69**	**8.45**	**99.992**	**91.94**	**395.7**
80	1.62	8.10	99.980	93.24	451.5

All the simulation results are plotted on Figure 5.8, indicating a clear trade-off between H_2 purity and recovery. This figure is similar to the one obtained from the lab scale simulations. Figure 5.9 shows the trends of product purity against bed productivity for the different configurations. Apart from the four-column system where the recoveries are quite low, all the systems exhibit a close productivity for each residence time, with the six-bed system having a productivity relatively lower than the Polybed systems and the nine- and twelve-bed systems having almost

identical productivities. Since the hydrogen feed flowrate per PSA train and the total cycle time are constant for all the configurations, the bed productivity results are directly proportional to the hydrogen recovery and the adsorption step time, and inversely proportional to the adsorbent amount. Table 5.4 lists the relevant variables used to calculate the bed productivity for all the system configurations at 99.99+% H_2 purity. The nine- and twelve-bed curves of Figure 5.9 tend to overlap because the slight increase in hydrogen recovery in the twelve-bed system together with the lower amount of adsorbent in the column (smaller columns volume) perfectly balance the longer adsorption step time of the nine-column system (Table 5.4). This productivity resulted in around 395 $mol_{H2}/kg_{ads}/d$ at the ultrapure hydrogen condition.

Table 5.4: List of variables used to calculate the bed productivity for all the system configurations at 99.99+% H_2 purity

Configuration	F_{H2} (mol/s)	t_{cycle} (s)	H_2 Recovery (%)	t_{ads} (s)	m_{ads} (ton)	Bed productivity ($mol_{H2}/kg_{ads}/day$)
4-column PSA	258.3	420	77.26	105	17.3	249.4
6-column PSA			84.22	140	17.3	362.5
9-column PSA			91.26	140	17.3	392.8
12-column PSA			91.94	105	13.0	395.7

For H_2 PSA the bed productivity is calculated by:

$$\text{Productivity} = \frac{F_{H_2}}{t_{cycle}} \cdot \frac{\text{H}_2\text{Recovery} \cdot t_{ads}}{m_{ads}} \quad (5\text{-}2)$$

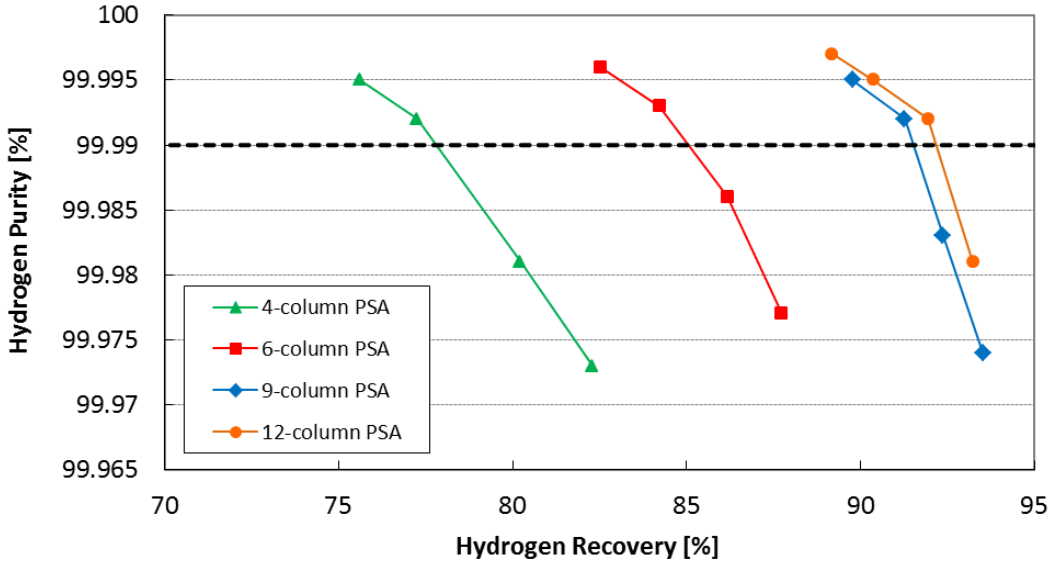

Figure 5.8: Comparison of hydrogen purity against recovery for various industrial H_2 PSA systems with different numbers of columns and different step configurations

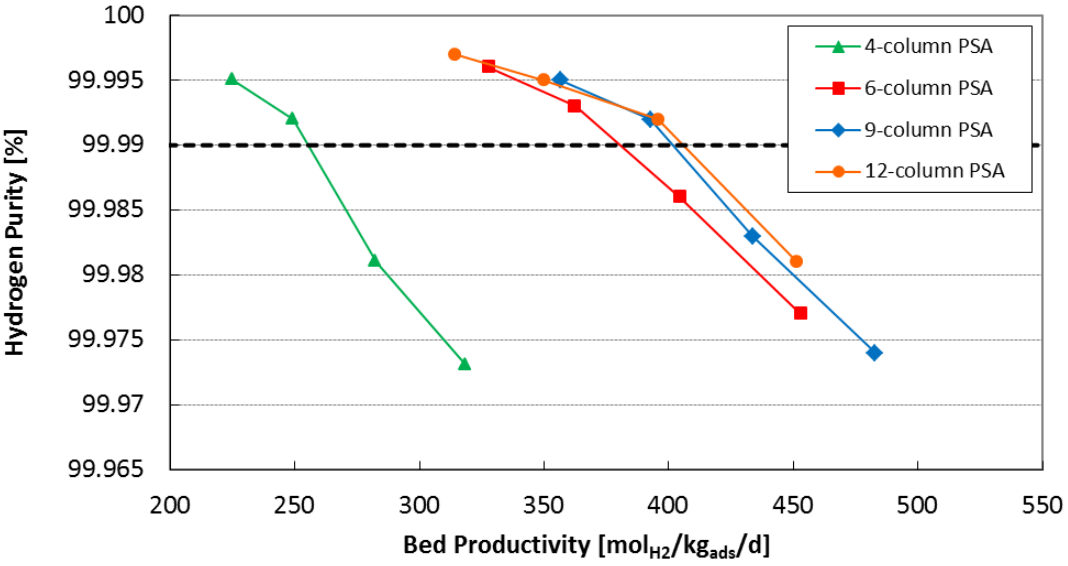

Figure 5.9: Comparison of hydrogen purity against productivity for various industrial H_2 PSA systems with different numbers of columns and different step configurations

The increase in H_2 recovery with the gradually more complex configurations at the same H_2 purity condition can be explained by looking at Figure 5.10, which shows the weakly adsorbed impurities' (nitrogen + argon) molar fraction profiles along the column at the end of the adsorption step and at cyclic steady state for the

different configurations. Here a common dimensionless axial coordinate has been considered for the x-axis to take into account the different one-column residence times, and hence column size, of the various configurations at which the targeted H_2 purity is met. Nitrogen and argon, which are practically the only impurities in the raffinate stream, were grouped into a common weakly adsorbed impurities molar fraction. It can be seen that the concentration front travels towards the end of the column moving from the four-column to the twelve-column system. This means that at the end of adsorption step the bed is more saturated with impurities, and therefore less hydrogen is lost later during the blowdown step, leading to enhanced H_2 recovery. The twelve-column molar fraction profile is very close to that of the nine-column system, confirming the limited increase of H_2 recovery. Unlike the lab-scale simulations, the concentration profiles in the industrial configurations are more affected by dispersion effects due to the higher velocities involved, leading to a maximum H_2 recovery of 91.9%. The maximum H_2 recovery for the lab-scale simulations was 92.7% (see Chapter 4).

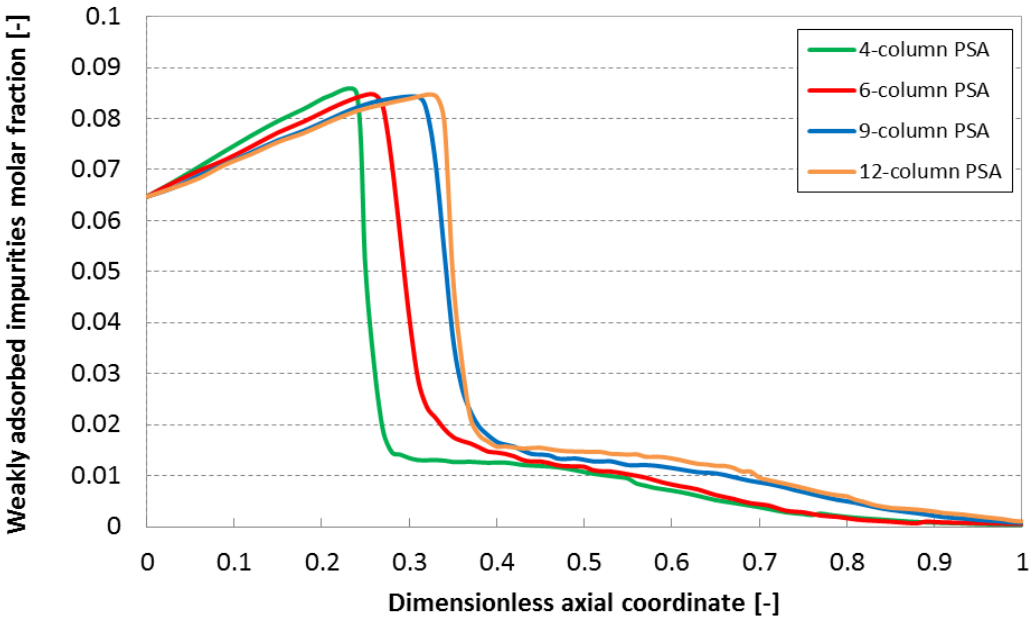

Figure 5.10: Weakly adsorbed impurities (nitrogen + argon) molar fraction profiles along a common dimensionless axial coordinate at the end of adsorption step at CSS and at 99.99+% H_2 purity among various industrial H_2 PSA configurations

It is clearly demonstrated that given the targeted H_2 purity of 99.99+ mol%, the H_2 recovery increases from 77% to 92% with increasing number of columns, as shown in Tables 5.3 and 5.5. Along with the change in the H_2 recovery, the ultrapure hydrogen production rate and the required tail gas compression work are also changed significantly. The hydrogen production rate increases with the increasing H_2 recovery and the tail gas compression work decreases simultaneously (Table 5.5). Moving from the four-column to the twelve-column system, the hydrogen production rate increases by 16.0% while the tail gas compression work decreases by 39.7%. The tail gas compression works were calculated using UniSim Design R400 considering a four-stage intercooling compression train with the adiabatic efficiency set as 85% for all the turbomachinery. In Table 5.5, gross and net power generation is also reported for the different PSA configurations showing a balance between the production of ultrapure hydrogen and electricity. Of course, in order to design the cogeneration plant, there is the need to define specific production rates.

Table 5.5: Ultrapure hydrogen production rate and tail gas compression work at various industrial H_2 PSA configurations at the condition of 99.99+ mol% H_2 purity and total cycle time of 420 s, including IGCC overall plant performances

H_2 PSA configuration	4-column PSA with 2-stage PE	6-column PSA with 2-stage PE	9-column PSA with 3-stage PE	12-column PSA with 4-stage PE
Thermal input (MW_{th})	1,618	1,618	1,618	1,618
H_2 recovery (%)	77.26	84.22	91.26	91.94
H_2 production rate (MMSCFD)	84.6	92.2	100.0	100.7
Tail gas compression work (MW_e)	6.3	5.1	3.9	3.8
Total auxiliaries (MW_e)	187.7	186.5	185.3	185.2
Gross power (MW_e)	528.8	504.0	479.0	476.5
Net power (MW_e)	341.1	317.5	293.7	291.3

5.3 Industrial H_2 PSA economic analysis

A detailed economic analysis has been carried out for the different industrial H_2 PSA configurations simulated in the previous section of this chapter. Omitting the cost associated to the control system, the capital expenditure (CAPEX) of a PSA unit can be divided into four cost items: the cost related to the columns, the adsorbents, the valves and the auxiliaries, which in this case is represented by the four-stage compression train for the PSA tail gas recompression.

Once the residence time has been fixed to meet the hydrogen purity specification, the size of the columns was also determined for all the different configurations (Table 5.1). The column design was completed evaluating the thickness of the cylindrical plating as well as the heads of the columns. The formulae used for the calculations refer to the ASME VIII standards (ASME VIII, 2013) providing the rules for the construction of pressure vessels. It was assumed that the columns were made of carbon steel of which some physical parameters such as the density and the hoop stress are given in Table 5.6. It was also assumed that the column heads were hemispherical, which is in agreement with the range of operating pressure (ASME VIII, 2013). For all the thicknesses, a safety factor of 2 was used once the minimum values were calculated with the ASME formulae. The welding efficiency was set at 85% (ASME VIII, 2013). The resulting thickness was evaluated at 7.9 cm for the column plating and 6.5 cm for the column heads.

Once the all the thicknesses were known, it was possible to evaluate the volume of metal needed and hence the weight of each column. This weight was increased by 1.2 times (column factor in Table 5.6) to take into account extra weight due to the support grid and headspaces (Green and Perry, 2007). With the knowledge of the total column weight, the costing was estimated using *Matches* (Matches, 2014), which provides conceptual process equipment cost estimates for over 275 types of equipment used in the chemical and metallurgical industry.

The mass of adsorbent to be placed in one column was calculated from the column volume and the bulk density. The commercial price for 5A zeolite of 1.7 $/kg was used (XaLvneng, 2014). By referring to the H_2 PSA configurations analysed by Luberti et al. (2014a), it was possible to know the number of valves

needed for each PSA train: this information is reported in Table 5.7. The number of valves is a function of the number of beds in each configuration as well as of the number of pressure equalisation steps employed. Since it is difficult to estimate the price for the single automatic valves associated with the PSA units, it was assumed that their cost accounted for around 6% of the total cost of the unit, whatever the size of the unit. Eventually, the cost of the four-stage compressor for tail gas recompression was again evaluated using *Matches* (Matches, 2014) considering a centrifugal compressor made of carbon steel where the input variable was the compressor power. This power had been previously evaluated using UniSim Design R400 software.

Table 5.6: Design and economic parameters utilised in the economic analysis

Design/economic parameter	Value	Reference
Carbon steel density (kg/m^3)	8,000	Green and Perry, 2007
Stainless steel hoop stress (MPa)	100	Green and Perry, 2007
Welding efficiency (%)	85	ASME VIII, 2013
Column factor (-)	1.2	Green and Perry, 2007
5A zeolite cost ($/kg)	1.7	XaLvneng, 2014
Installation factor (-)	2.1	IEA GHG, 2009
Actualisation factor (CEPCI 2007/CEPCI 2014) (-)	1.09	CEPCI, 2014

Table 5.7: Economic analysis comparison among the different PSA configurations including the comparison with the entire IGCC plant

	4-column PSA	6-column PSA	9-column PSA	12-column PSA
No. trains	6	3	2	2
No. valves per train	17	31	55	85
Total no. columns	24	18	18	24
Column cost ($ × 1,000)	315.4	315.4	315.4	255.1
Column adsorbent cost ($ × 1,000)	29.4	29.4	29.4	22.0
Tail gas compressor cost ($ × 1,000)	906.4	764.3	613.1	597.9
Column valves cost ($ × 1,000)	31.6	32.8	30.8	24.1
Total cost ($ × 1,000)	12,657.2	9,830.9	9,226.1	9,655.0
Total installed cost ($ × 1,000)	27,845.8	21,628.0	20,297.4	21,241.1
IGCC cost fraction (%)	1.85	1.44	1.35	1.41

The economic analysis results related to the different PSA configurations are summarised in Table 5.7. Figure 5.11 exhibits the results expressed in terms of total installed cost in $ millions on a histogram chart. This is the actual PSA unit cost considering an installation equipment factor of 2.1 (IEA GHG, 2009) (Table 5.6). It is possible to see that the previously discussed cost items are represented by different colours and they result in different weights on the overall configuration cost. The cost of the pressure vessels resulted the highest for all the configurations, followed by the tail gas compressor, the valves and the adsorbent.

It can be clearly seen that a minimum cost is registered with the nine-column PSA configuration. This can be explained considering the total number of columns needed against the volume of each column. Although the twelve-column system has smaller columns, less adsorbent and shows slightly higher recovery, it is composed of 24 columns in total against only 18 columns of the nine-bed system because the adsorption time is one-fourth of the total cycle time. After this techno-economic analysis, it can be concluded that for a 100 MMSCFD ultrapure H_2 production rate,

the CAPEX associated with the Polybed system exhibiting nine beds is the lowest and hence this configuration has to be chosen for this separation. The total installed cost of the units is consistent with data reported in the literature (Li et al., 2012), given the hydrogen production rate and the plant capacity factor. The total installed cost results in a fraction of the total IGCC plant cost for the base case (Table 5.7) ranging between 1.85% for the four-column system and 1.35% for the nine-column system. Note that since the overall CAPEX is based on the DOE report (2007), the cost has been actualised using the actualisation factor based on the ratio of CEPCI indices between the two years 2007/2014 (CEPCI 2014) (Table 5.6).

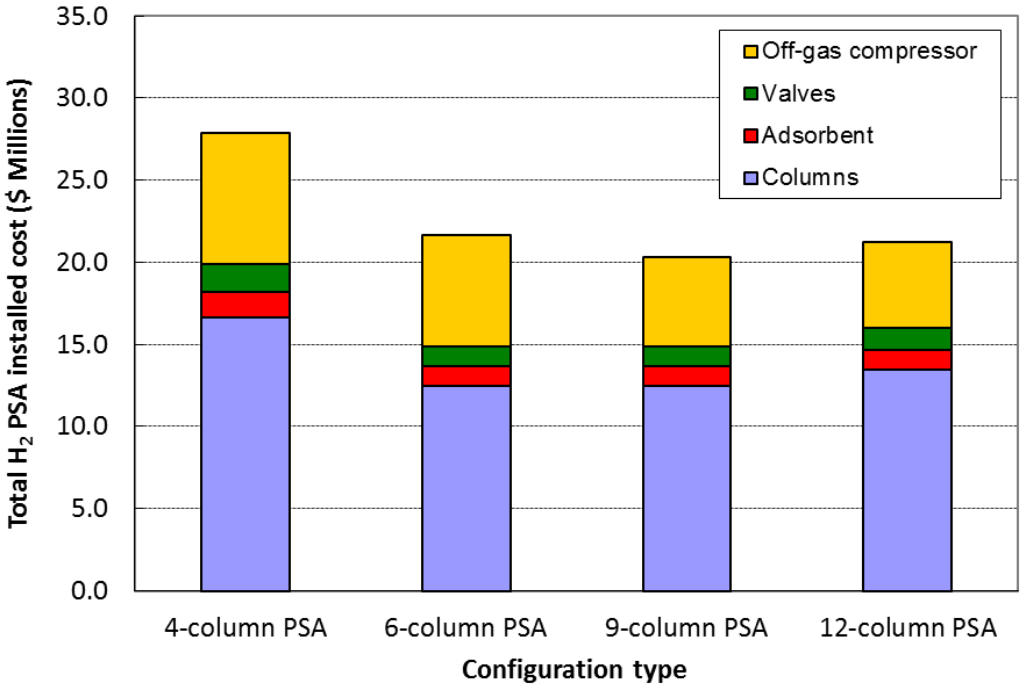

Figure 5.11: Economic analysis summary for the different PSA configurations expressed in total installed cost ($ Millions)

5.4 Integrated IGCC cost analysis

From the first two chapters of this thesis it was shown how IGCC technology could play an important role in the future low-carbonised energy matrix, especially when a carbon capture unit is incorporated in their design. Nevertheless, a lower energy penalty associated with the capture process should be accompanied by a reasonable cost. In the UK Electricity Generation Costs Update report (DECC,

2010), an IGCC is shown to have a significant reduced cost versus an advanced supercritical coal plant when a carbon capture is applied. Furthermore, the Zero Emissions Platform (ZEP, 2011) showed that in terms of costs IGCCs are competitive capture technologies considering the estimates for new power plants with CO_2 capture in Europe, based on new and actualised data. In particular, the current cost of carbon capture and storage is a major factor (and barrier) to its widespread use as a carbon reduction measure and it remains an open debate (IPCC, 2005).

At present, there are significant differences and inconsistences in the way CCS costs are calculated and reported by various authors and organisations. Such inconsistences can result in sizeable differences in the reported cost of otherwise identical systems (Rubin, 2012). In a recent paper, Rubin et al. (2013) put effort into harmonising the methods used to estimate and report the cost of carbon capture and storage systems. This work was co-authored by the main organisations involved in CCS, such as DOE/NETL, EPRI, IEA, ZEP and GCCSI. Any estimate of CCS cost must begin with a clear definition of the scope and the boundaries of the project in terms of greenfield plant/retrofitted plant and CO_2 transport and storage systems. Moreover, cost categories for CCS cost estimates are capital costs, operating and maintenance costs and fuel costs (Rubin et al., 2013). Several cost metrics widely used in CCS studies, including the levelised cost of electricity (LCOE), the cost of CO_2 avoided and the cost of CO_2 captured, have been discussed in many works (IPCC, 2005; Rubin et al., 2007; Rubin, 2012).

The LCOE is a constant unit price ($/MWh) for comparing the costs of power plants that have different technologies, use different fuels, have different capital expenditure paths, different annual costs, different net outputs and different economic lives. It is a characteristic “cost of electricity generation” that incorporates all the expenses for building and operating a power plant over its economic plant life with an expected rate of return on invested capital, normalised over the total net electricity generated. The levelised cost of electricity can be calculated by:

$$LCOE = \sum_t \frac{(CAPEX_t + O\&M_t + Fuel_t)/(1+r)^t}{\sum_t (Electricity Sold)_t /(1+r)^t} \quad (5\text{-}3)$$

The term "levelised" arises from the recognition that the calculations in eq. (5-3) establish a single present value of overall cost that can be transformed into a series of uniform annual values through the use of levelised factors. All the terms of eq. (5-3) are explained in Table 5.8.

Table 5.8: Nomenclature used to define levelised cost of electricity

Parameter	Definition
$CAPEX_t$ ($)	Capital expenditure in year t associated with construction of the plant
$O\&M_t$ ($)	Total non-fuel operating and maintenance costs in year t
$Fuel_t$ ($)	Total fuel costs in year t
Electricity $Sold_t$ (MWh)	Net electricity produced and sold in year t
r (-)	Annual rate used to discount values (interest rate or discount factor)

Another important cost parameter is the cost of CO_2 avoided ($/$t_{CO2}$), defined as:

$$AC = \frac{LCOE_{CCS} - LCOE_{ref}}{SCE_{ref} - SCE_{CCS}} \tag{5-4}$$

This cost measure compares a plant with CCS to a "reference plant" without CCS in order to quantify the average cost of avoiding a unit emission of CO_2 to the air while still providing a unit of useful product. Most commonly, the plants with and without CCS are assumed to be of the same type and approximate size. SCE is the specific carbon dioxide emissions measured in t_{CO2}/MWh.

In this section, three levelised costs of electricity have been evaluated for the cases of IGCC without CCS, IGCC with CCS, and IGCC with CCS and H_2 co-production. The carbon capture rate was fixed at 90% for the latter two cases. The analysis of the IGCC without CSS has been taken into account as the reference case for the cost of CO_2 avoided calculation. All the capital, operating, maintenance and fuel costs were updated to 2014 through CEPCI indices (2014). Table 5.9 reports all the economic and plant parameters for the three cases analysed while Table 5.10 lists the references for all the unit costs.

Table 5.9: Economic and plant parameters used for the cost analysis among the three IGCC cases

Parameter	IGCC without CCS	IGCC with CCS	IGCC with CCS and H_2
Plant life time (yr)	35	35	35
Capacity factor (%)	80	80	80
Discount rate (%)	10	10	10
Net power (MW_e)	636.0	505.0	294.0
Total CAPEX ($10^6 \times$ \$)	1,370.0	1,504.0	1,422.0
Total O&M ($10^6 \times$ \$/yr)	55.1	56.4	56.4
CAPEX division among the first five years (%)	5/20/40/25/10	5/20/40/25/10	5/20/40/25/10
Coal feed flow (ton/h)	182.5	190.8	190.8
Coal cost (\$/ton)	60	60	60
CO_2 flue gas flow (ton/h)	455.2	38.7	38.7
CO_2 captured flow (ton/h)	-	453.3	453.3
CO_2 carbon tax (\$/ton)	-	25	25
CO_2 transport cost (\$/ton)	-	6	6
CO_2 storage cost (\$/ton)	-	9	9
Ultrapure H_2 flow (kg/h)	-	-	10,030
Ultrapure H_2 price (\$/kg)	-	-	2.2
LCOE (\$/MWh)	**86.4**	**107.7**	**105.1**
SCE (ton_{CO2}/MWh)	0.72	0.08	0.13
AC (\$/ton_{CO2})	**-**	**33.4**	**32.1**

Table 5.10: List of references for unit costs

Unit cost	Value	Reference
Plant life time (yr)	35	DECC, 2010; ZEP, 2011
Capacity factor (%)	80	DECC, 2010; Kreutz et al., 2005
Discount rate (%)	10	DECC, 2010; Kreutz et al., 2005
Coal cost (\$/ton)	60	ZEP, 2011
CO_2 carbon tax (\$/ton)	25	DEC, 2010
CO_2 transport cost (\$/ton)	6	Huang et al., 2008
CO_2 storage cost (\$/ton)	9	Huang et al., 2008
Ultrapure H_2 price (\$/kg)	2.2	DOE, 2005

The IGCC plant life time was set at 35 years for all the cases, which is consistent with the cost analysis reports relating to IGCCs (DECC, 2010; ZEP, 2011). In addition, the selected capacity factor and the discount rate were found in the DECC report (2010) and the literature on IGCCs (Kreutz et al., 2005). Net power plant, coal feed flowrate, and CO_2 flowrates in both the flue gas and captured streams were derived from the overall IGCC simulation results (see Chapter 2) based on cases 5 and 6 from the DOE report (2007). For the cogenerating case, the results obtained from the previous sections of this chapter were used considering an ultrapure H_2 production rate of 100 MMSCFD (around 10,030 kg/h) and a nine-column PSA configuration. Total CAPEX as well as total O&M costs were derived from the economic analysis data provided by the DOE report (2007). Meanwhile, for the cogenerating case, it was assumed a suitable CAPEX cost reduction due to the lower energy generation in the power island and the cost of the Polybed PSA system was accounted for, as reported in the previous section of this chapter. Following the instructions issued by the DECC report (2010), the total capital expenditure cost was spread across the first 5 years of plant life, assuming it would take 5 years for construction. The relative year percentages of the construction cost are detailed in Table 5.9. In order to evaluate the coal cost, the low fuel price scenario for hard coals presented in the ZEP report (2011) was considered where, from a value of 2.3 $/GJ, the price of 60 $/ton was obtained by means of coal LHV. The carbon tax of 25 $/ton was chosen according to the minimum carbon cost to make CCS feasible, as reported by DECC (2010). Considering 100 km of offshore pipelines and an offshore storage facility, the CO_2 transport price and CO_2 storage price were evaluated respectively at 6 and 9 $/ton$_{CO2}$ (Huang et al., 2008). Eventually, for the cogenerating case an ultrapure hydrogen delivered price of 2.2 $/kg was assumed, which is in the lower range of the DOE report concerning the hydrogen economy (2005).

Figure 5.12 shows the LCOE calculation results for the examined three cases where the LCOE constituents are classified as capital, O&M, fuel, carbon tax, CO_2 transport and storage costs, and H_2 revenue.

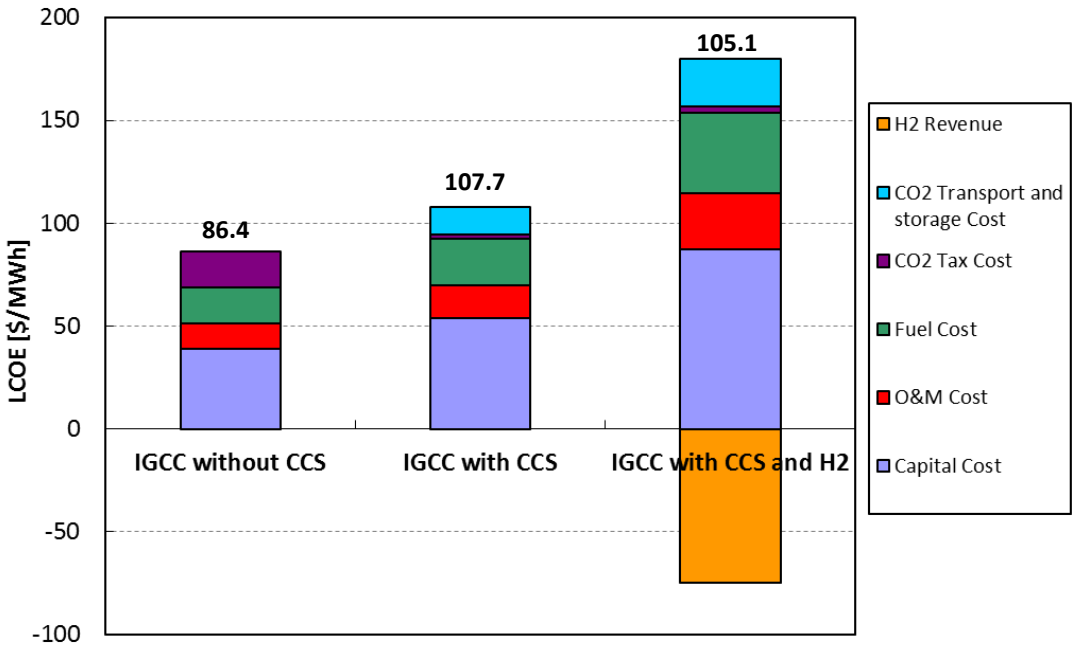

Figure 5.12: LCOE calculation results for the three examined IGCC cases

It can be noticed that in both the cases with CCS the resulting LCOE is relatively higher than that in the first case due to the energy penalty involved in the carbon capture process. In the cogeneration case the capital, O&M and fuel costs are sensibly higher but the overall evaluated LCOE is lower than the second case because of the negative contribution of the hydrogen sale, accounting for -74 $/MWh. For all the three examined cases, the capital cost was the highest, followed by the fuel and O&M costs. The carbon tax is only relevant in the first case where there is no CCS while the CO_2 transport and storage costs remain low in the other two cases. Considering the first case as the reference case, the cost for CO_2 emissions avoided was estimated respectively for the capture case and cogenerating case at 33.4 and 32.1 $/ton$_{CO2}$, following the trend of the LCOE.

Table 5.11 reports some data on IGCC plants with pre-combustion capture both in terms of LCOE and AC. It can be clearly seen that the results obtained in this study are in agreement with the others, particularly with those reported by the DOE (2011) and the GCCSI (2011) calculations, which have been conducted more recently. In fact, differently from the other studies, it should be noted that the results presented in this section were updated to 2014.

Table 5.11: LCOE and AC results of various studies on hard coal IGCC with pre-combustion capture (ZEP, 2011)

	This study	ZEP (2009)	ENCAP (2004)	MIT (2007)	DOE (2011)	EPRI (2009)	Rubin (2012)	GCCSI (2011)
LCOE ($/MWh)	107.7	102.3	94.5	100.7	105.5	116.4	100.3	108.2
AC ($/ton$_{CO2}$)	33.4	28.1	31.5	19.2	35.2	35.2	20.7	36.9

5.5 Recycle of the H_2 PSA tail gas to shift reactors

It has been reported that the ultrapure hydrogen yield could be improved by recycling the H_2 PSA tail gas to shift reactors upstream of the H_2 PSA (UOP, 2002), as shown in Figure 5.13. This is because the CO contained in the tail gas could be converted to CO_2 and H_2 in a reaction with steam by its recycle to the shift reactors. This modification can also reduce the energy penalty involved in the carbon capture unit. The power plant performances are affected by this modification and they will be discussed in detail in the last sections of this chapter.

However, the more tail gas that is recycled to shift reactors, the lower the hydrogen mole fraction of the raw H_2 feed due to the impurities build-up in the recycle loop, as depicted in Figure 5.14. Therefore, this process configuration would be possible only when a substantial amount of impurities is removed out of the recycle loop in order to maintain impurities levels low enough to enable the downstream H_2 PSA unit to achieve satisfactory H_2 purity and recovery at the same time. This implies that it is essential to bleed a portion of the tail gas out of the recycle loop by sending it to the gas turbine, as shown in Figure 5.13.

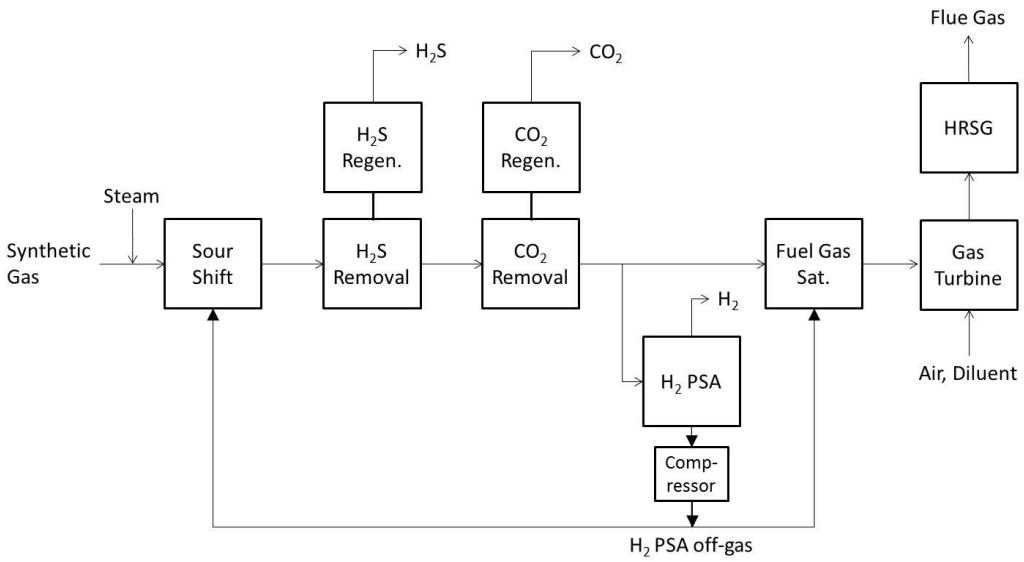

Figure 5.13: Block flow diagram of an advanced IGCC plant with a recycle of H_2 PSA tail gas to water gas shift reactors

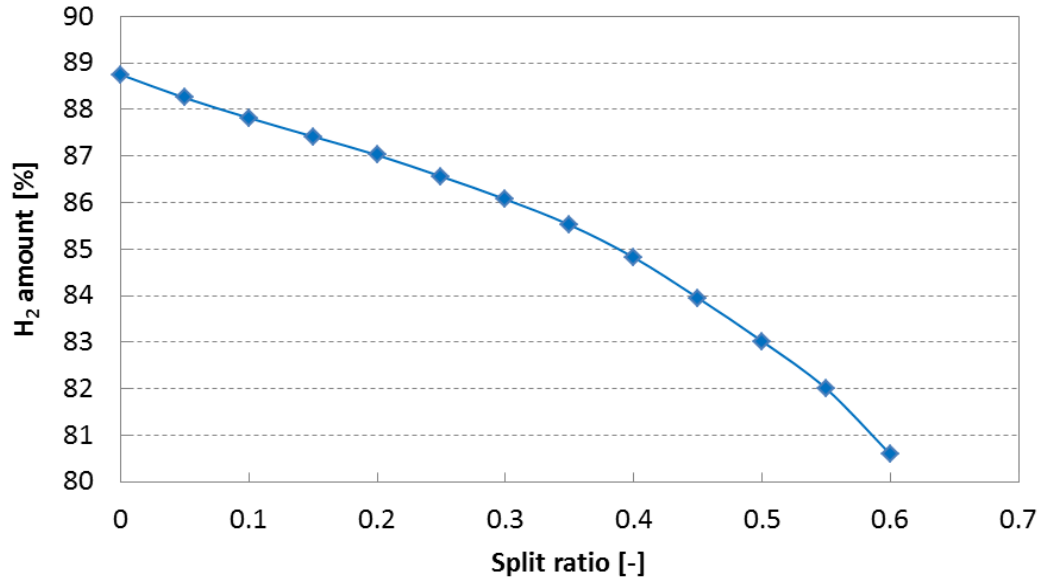

Figure 5.14: Variation of the hydrogen mole fraction percentage in the raw H_2 feed with the split ratio of the 'tail gas recycle to shift reactors' flow to total tail gas flow

It is important to see if the H_2 PSA can also be designed to achieve as high as 90% H_2 recovery even with the lowered H_2 mole fraction in the feed resulting from the recycle of a certain amount of tail gas to the shift reactors. An iterative

calculation has been conducted to evaluate a suitable split ratio of the tail gas recycle to the shift reactors to obtain a satisfactory H_2 recovery, resulting in a value of around 35% and providing a new feed composition for the integrated PSA unit of 85.40% H_2, 3.46% CO_2, 2.55% CO, 7.33% N_2 and 1.25% Ar on a molar basis. Keeping the total cycle time of 420 s, the sought target was still 99.99+ mol% of hydrogen purity with a production rate of 100 MMSCFD. As a result of the simulation study, it has been estimated that the one-column residence time for a nine-column PSA system should be increased to 130 s from 120 s in the base case without recycle, i.e., the H_2 PSA unit should be designed with larger columns to accommodate the higher feed flowrate and to remove more impurities. Accordingly, the H_2 recovery is lowered to around 89.8% from 91.3% due to the increase in the column volume. The nine-column system was selected because it corresponds to a minimum capital cost investment, as demonstrated in the previous sections of this chapter.

Figure 5.15 reports the hydrogen molar fraction along the column for the last configuration examined at the end of adsorption step and at cyclic steady state.

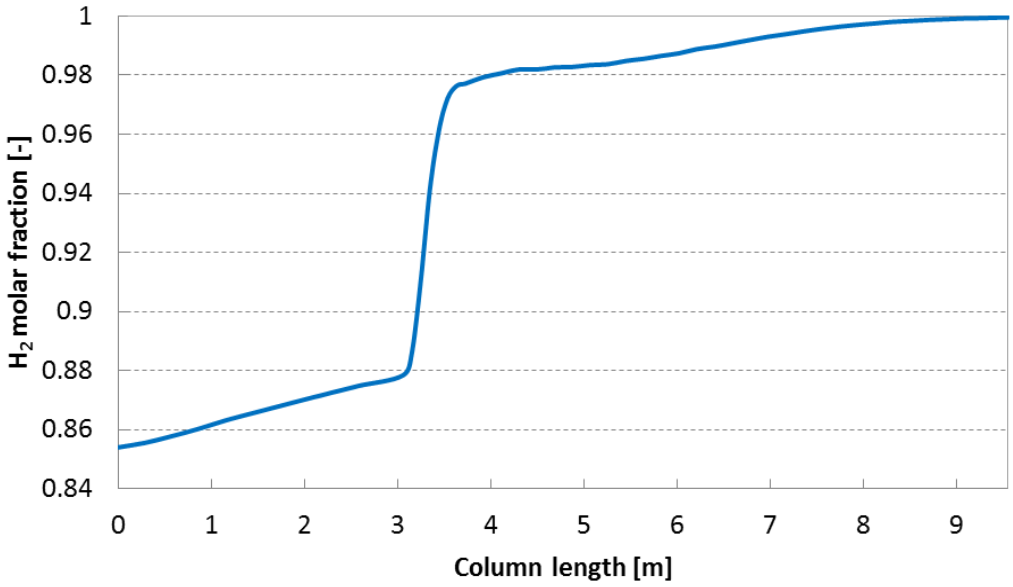

Figure 5.15: Hydrogen molar fraction profile along the column at the end of adsorption step and at CSS for the nine-column PSA system

With a one-column residence time of 130 s, the resulting column volume was 27.3 m^3 while the column length was 9.55 m (Table 5.1). It can be noticed that the hydrogen mole fraction increases progressively along the column starting from 85.4% at the feed condition until reaching the ultrapure condition at the product end (99.99%). Even if the concentration front is located at around 3.5 m in the middle of the column, the weakly adsorbed impurities continue to be gradually adsorbed along the remaining part of the bed, allowing ultrapure hydrogen to be obtained only in the proximity of z = L.

5.6 Cogenerating IGCC process improvements

As described in the previous sections, the configuration of the IGCC power plant integrated with the H_2 PSA unit is to have the H_2 PSA tail gas sent to the compressor and then to the gas turbine through the fuel gas saturator for additional power generation, as depicted in Figure 5.16, referred hereinafter as the Base case. This is because the extract stream still contains considerable amounts of hydrogen and carbon monoxide, and hence its lowering heating value can be accordingly exploited. A portion of the high-pressure clean syngas is also diverted to the coal dryer to provide the required heat to the unit (Figure 5.16).

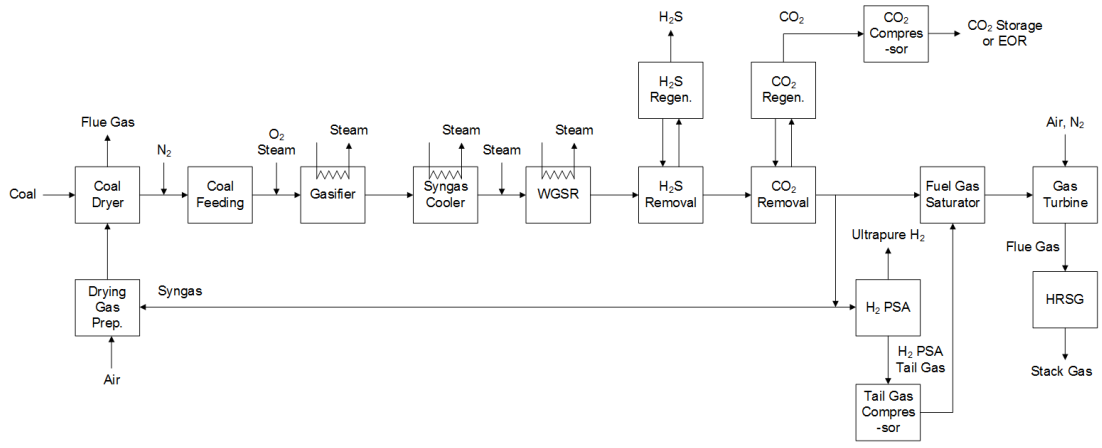

Figure 5.16: Block diagram of the Base case

The key idea of this section is to partially recycle the H_2 PSA tail gas to other units of the plant in order to increase the overall net plant efficiency. Given the fact that the power generation in the power island is fixed at 479 MW_e due to the turbomachinery installed and that the ultrapure hydrogen production rate is also kept

fixed at 100 MMSCFD, the overall plant performance can be improved through the reduction in the auxiliaries' power consumption, particularly at the dual-stage Selexol unit, the CO_2 compression train and the H_2 PSA tail gas compression train. Moreover, the overall carbon capture rate was kept constant at 90% for all the improved process configurations. In the following subsections, each change in the process diagrams from the Base case is highlighted in red.

5.6.1 Case 1: H_2 PSA tail gas recycle to water gas shift reactors

Figure 5.17 shows the configuration that was simulated in detail in section 5.5 of this chapter. A fraction of the H_2 PSA tail gas is recycled to the WGSRs to enhance the CO conversion to CO_2 and facilitate the carbon capture process. The other fraction must be sent to the gas turbine, as in the original Base case, to prevent excessive build-up of the impurities in the recycle loop. Given a mandatory requirement of a specific carbon capture rate to be achieved in the overall process (90%), the operation severity in the CO_2 removal unit could be alleviated with this H_2 PSA tail gas recycle since the feed to the CO_2 removal unit could be given a higher amount of CO_2 than when it operates without the H_2 PSA tail gas recycle. Less power consumption is also expected at the CO_2 compression train because, since the CO_2 loading is higher, the CO_2 can be regenerated at higher pressures in the flash drums. By contrast, the H_2 PSA tail gas compression power is likely to increase due to the increase of the H_2 PSA tail gas flowrate.

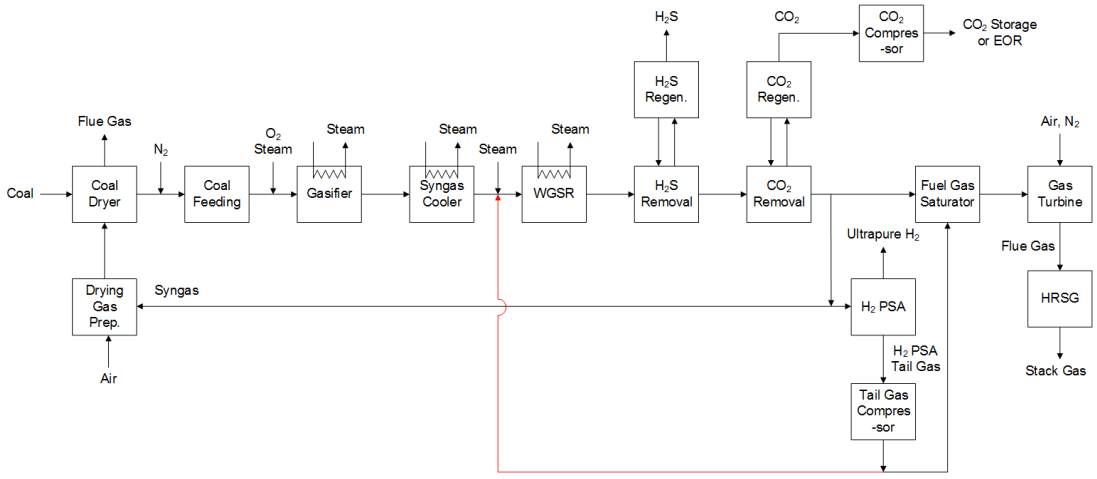

Figure 5.17: Block diagram of the Case 1 with the H_2 PSA tail gas recycle to the water gas shift reactors

5.6.2 Case 2: H_2 PSA tail gas recycle to dual-stage Selexol unit

In this configuration, the H_2 PSA tail gas is directly recycled to the CO_2 removal unit since the H_2 PSA tail gas has a substantial amount of CO_2 as well as CO, as shown in Figure 5.18. In this case, the H_2 PSA tail gas is mixed with the synthetic gas stream flowing from the H_2S removal unit to the CO_2 removal unit or it is fed to the CO_2 removal unit separately from the main synthetic gas stream. The benefit of the H_2 PSA tail gas recycle that would be expected with respect to the energy consumption reduction at both the carbon capture unit and at the CO_2 compressor must be smaller than that with the recycle to the WGSRs because no additional CO is converted to CO_2. Accordingly, the power consumption at the H_2 PSA tail gas compressor must be lower as well.

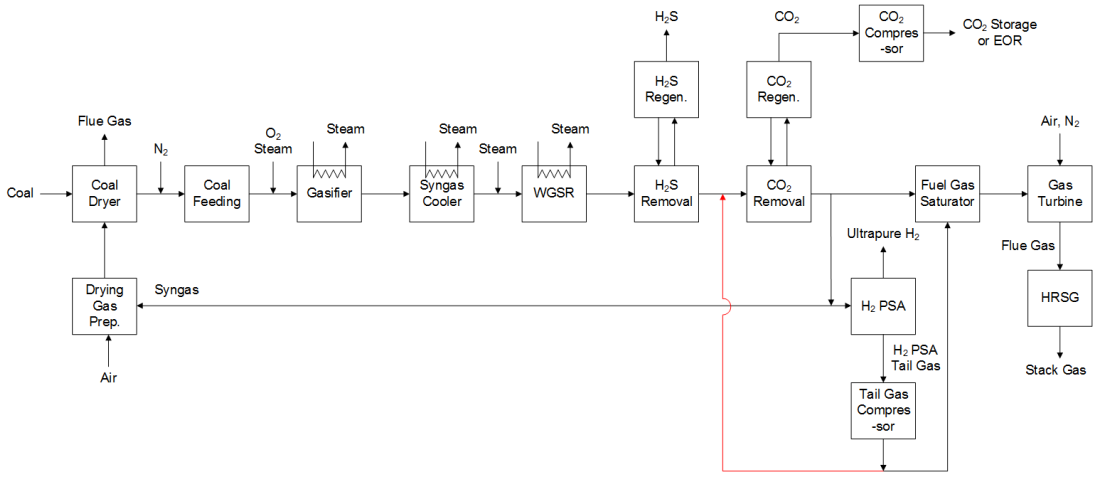

Figure 5.18: Block diagram of the Case 2 with the H_2 PSA tail gas recycle to the Selexol unit

5.6.3 Case 3: H_2 PSA tail gas recycle to coal dryer

An alternative way to exploit the value of the H_2 PSA tail gas is to send a portion of it to the drying gas preparation, where it is combusted with air to provide the heat for coal drying, as depicted in Figure 5.19. The original idea for this configuration was presented in a recent patent (Ahn et al., 2015) and relies on the fact that the H_2 PSA tail gas can be utilised to dry the coal without being recompressed, instead of the high-pressure clean syngas that would be used for power generation in the combined cycle. Providing a sufficient lowering heating

value from the H_2 PSA tail gas flow for the coal dryer, it is possible to save the power that otherwise would have been utilised to recompress this portion of tail gas. Therefore, this configuration is expected to exhibit a reduction in the tail gas compressor power compared with the Base case.

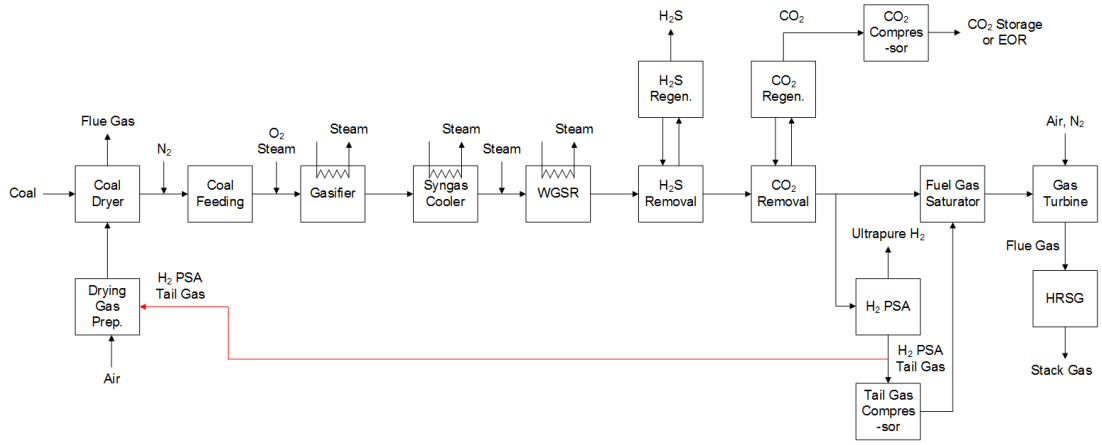

Figure 5.19: Block diagram of the Case 3 with the H_2 PSA tail gas recycle to the coal dryer

5.6.4 Case 4: Multiple alterations with H_2 PSA tail gas recycle to WGSRs and coal dryer

This case allows multiple alterations combining the process modifications proposed in the previous Cases 1 and 3 at the same time, having a portion of the H_2 PSA tail gas recycled to the water gas shift reactors and another portion recycled to the coal dryer, as shown in Figure 5.20. From the previous discussion, the H_2 PSA tail gas recycle to the dual-stage Selexol was not taken into account in this last configuration due to the lower expected benefit. It is conceivable that this case would benefit of the combined power reduction in all the three above-mentioned auxiliaries relating to the dual-stage Selexol unit, the CO_2 compression train and the H_2 PSA tail gas compression train.

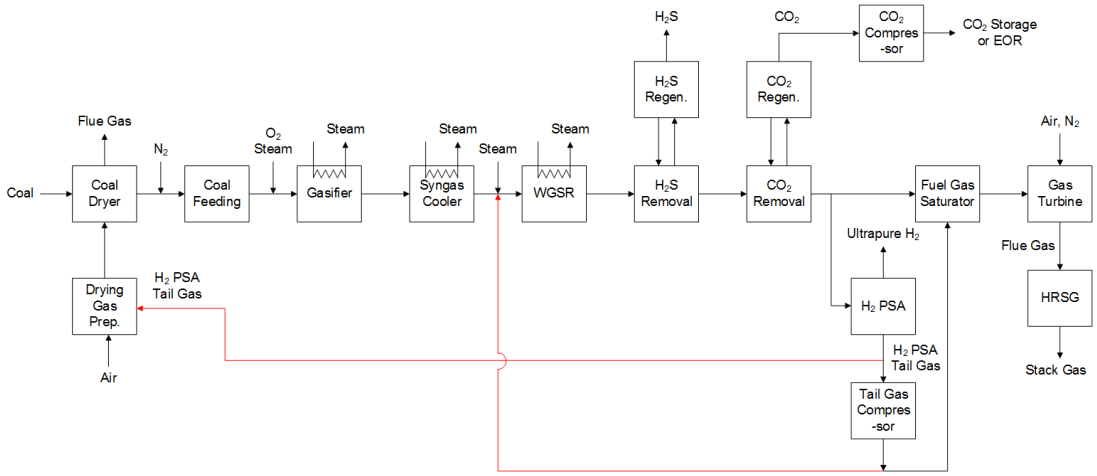

Figure 5.20: Block diagram of the Case 4 with the H_2 PSA tail gas recycle to the water gas shift reactors and the coal dryer

5.6.5 Comparison for the proposed process modifications

Table 5.12 summarises the simulation results for the proposed configurations described in the previous subsections. With a common total power output of 479 MW_e, an ultrapure hydrogen production rate of 100 MMSFCD and an overall carbon capture of 90% for all the cases, the outcome of the Base case was a net electrical plant efficiency of 18.1%. The total auxiliaries' power consumption accounted for around 185 MW_e, and therefore the resulting net power was 294 MW_e.

Case 1 showed a higher net electrical plant efficiency (18.3%) because, even with a lower PSA H_2 recovery and consequently a higher PSA tail gas compression work, the carbon capture auxiliaries and CO_2 compression works decreased significantly due to the tail gas recycle to WGSRs, which allowed less severe operation conditions in the CO_2 removal unit. In particular, the CO_2 removal unit auxiliaries decreased by 2.6% and the CO_2 compression power was reduced by 6.1%, while the H_2 PSA tail gas compression work was incremented by 23.1%. As expected, a lower improvement was seen for Case 2 where the net power was increased only by 0.6 MW_e. It should be noted that in this case both H_2 purity after the acid gas removal (86.1%) unit and H_2 recovery at the PSA unit (90.2%) were in between the values reported for the Base case and Case 1. Case 3, due to the H_2 PSA tail gas to the coal dryer, exhibited a substantial power reduction in the H_2 PSA tail gas compressor (43.6%) and a consequent increase of the overall net plant efficiency

up to 18.3%, with the same carbon capture auxiliaries' power consumptions. Eventually, the multiple alterations configuration simulated in Case 4 showed a power reduction of 2.6% in the CO_2 removal unit, of 5.5% in the CO_2 compressor and of 25.6% in the H_2 PSA tail gas compressor. The resulting net power was around 3.3 MW_e higher than that of the Base case, allowing the overall net plant efficiency to increase to 18.4%.

Another method to evaluate the net plant efficiency is to add the lowering heating value of the ultrapure hydrogen (334 MW_{th}) times its flowrate to the electricity generated and divide this sum by the coal thermal input. In this way, the net plant efficiency for the base case was estimated at 38.8% while the efficiency for Case 4 was 39.0% (Table 5.12). Of course, it is clear that the intent of such a cogenerating plant is to sell the ultrapure hydrogen to refineries that are deficient in hydrogen to operate their hydrotreater and hydrocracker units, and not to burn this valuable product.

Table 5.12: Simulation results for the cogenerating IGCC plant performances among the various cases

Plant summary	Base case	Case 1 (Base case + Tail gas to WGSRs)	Case 2 (Base case + Tail gas to Selexol unit)	Case 3 (Base case + Tail gas to coal dryer)	Case 4 (Multiple alterations: Cases 1 + 3)
Thermal input (MW_{th})	1,618	1,618	1,618	1,618	1,618
WGSR CO conversion (%)	95.7	95.5	95.7	95.7	95.5
AGR H_2 purity (%)	88.7	85.4	86.1	88.7	85.6
AGR H_2 recovery (%)	99.2	99.2	99.2	99.2	99.2
AGR H_2S recovery (%)	99.9	99.9	99.9	99.9	99.9
AGR CO_2 recovery (%)	94.1	92.2	94.0	94.1	92.3
CO_2 product purity (%)	98.5	98.5	98.5	98.5	98.5
PSA H_2 purity (%)	99.99+	99.99+	99.99+	99.99+	99.99+
PSA H_2 recovery (%)	91.3	89.8	90.2	91.3	89.9
Overall carbon capture (%)	90.0	90.0	90.0	90.0	90.0
H_2 production (MMSCFD)	100.0	100.0	100.0	100.0	100.0
AGR auxiliaries (MW_e)	18.9	18.4	18.6	18.9	18.4
CO_2 compression (MW_e)	33.0	31.0	32.1	33.0	31.2
Tail gas compression (MW_e)	3.9	4.8	4.5	2.2	2.9
Other auxiliaries (MW_e)	129.5	129.5	129.5	129.5	129.5
Total auxiliaries (MW_e)	185.3	183.7	184.7	183.6	182.0
GT power (MW_e)	324.0	324.0	324.0	324.0	324.0
ST power (MW_e)	155.0	155.0	155.0	155.0	155.0
Total power (MW_e)	479.0	479.0	479.0	479.0	479.0
Net power (MW_e)	293.7 (+334 MW_{th} H_2 LHV)	295.3 (+334 MW_{th} H_2 LHV)	294.3 (+334 MW_{th} H_2 LHV)	295.4 (+334 MW_{th} H_2 LHV)	297.0 (+334 MW_{th} H_2 LHV)
Net plant efficiency (%)	**18.1 (38.8)**	**18.3 (38.9)**	**18.2 (38.8)**	**18.3 (38.9)**	**18.4 (39.0)**

5.7 Hydrogen plant process improvements

In order to obtain a higher benefit from the process improvements proposed in the previous section, there is a need to increase the H_2 PSA tail gas flow, and hence to have different rates for the cogenerating products, favouring the production of ultrapure hydrogen over electricity. The limiting case is represented by a hydrogen plant where only ultrapure hydrogen is produced, as depicted in Figure 5.21. Keeping the same 1,618 MW_{th} coal thermal input and the same 90% overall carbon capture rate it was assumed that the H_2 PSA unit is capable to produce ultrapure hydrogen (99.99+ mol%) with a recovery of 90%. The resulting hydrogen production rate was evaluated at 286 MMSCFD for this new Base case (Ahn et al., 2015).

Table 5.13 summarises the hydrogen plant performances for the Base case and three improved cases consisting of different ways to recycle the H_2 PSA tail gas to other parts of the plant, as shown in Figure 5.21. In Case 1, 21% of the tail gas is recycled to upstream of the shift reactor and the H_2 production rate is improved by 2.4% to 293 MMSCFD from 286 MMSCFD. When recycled, the tail gas is compressed up to the pressure of main syngas stream flowing to the shift reactor, resulting in an increase of total power consumption. Case 2 is as Case 1 with the addition of a portion of the tail gas utilised to generate hot gases for the coal dryer by combustion instead of using a portion of high pressure raw H_2 feed to the H_2 PSA unit. As a result, the ultrapure hydrogen production rate was found to increase by around 1.8% in comparison to Case 1, as indicated in Table 5.13. In accordance with Case 3, beyond the partial tail gas recycle to the water gas shift reactor and the coal dryer, the remaining tail gas is sent to the dual-stage Selexol process as hot flue gas after combustion with air. In the dual-stage Selexol unit, the CO_2-laden solvents are regenerated by reducing the pressure over three flash drums in series. By heating the CO_2-laden solvents flowing to a flash vessel operating at medium pressure, more CO_2 product can be obtained at the high pressure resulting in improving the solvent working capacity and reducing the power consumption at the CO_2 compression train. The enhanced solvent working capacity leads to lowering the power consumption for CO_2 capture due to a reduced H_2 slip to the circulating solvents. By utilising 100% of the H_2 PSA tail gas at three locations upstream of the process, the production rate of

ultrapure hydrogen was found to increase by around 4.2% and the power consumptions at the dual-stage Selexol unit and the CO_2 compression train were found to reduce by around 15% and 6%, respectively. Accordingly, it is appreciated that in Case 3 the total auxiliaries' power consumption can be reduced by around 3.5% compared to the Base case.

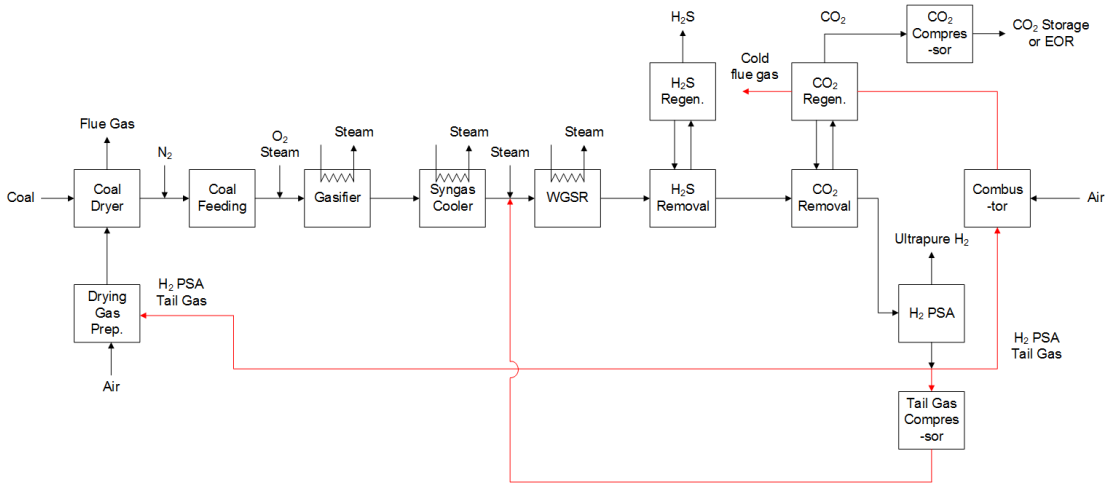

Figure 5.21: Block diagram of the hydrogen plant (HP). Red arrows define the improved cases of Table 5.13 with different ways to recycle the H_2 PSA tail gas to the water gas shift reactor, the coal dryer and the CO_2 regenerator

Table 5.13: Simulation results for the hydrogen plant (HP) performances for the various cases (Ahn et al., 2015)

Plant summary	**HP base case**	**HP Case 1 (HP base case + Tail gas to WGSRs)**	**HP Case 2 (HP Case 1 + Tail gas to coal dryer)**	**HP Case 3 (HP case 2 + Tail gas to CO_2 regen.)**
Thermal input (MW_{th})	1,618	1,618	1,618	1,618
Fuel gas flowrate (MMSCFD)	79	72	62	0
Overall carbon capture (%)	90.1	90.1	90.1	90.1
PSA H_2 purity (%)	99.99+	99.99+	99.99+	99.99+
PSA H_2 recovery (%)	90.0	90.0	90.0	90.0
H_2 production (MMSCFD)	286	293	298	298
H_2S reboiler duty (MW_{th})	14.6	14.6	14.6	11.8
AGR auxiliaries (MW_e)	20.2	19.3	19.3	17.2
CO_2 compression (MW_e)	31.7	31.7	31.7	29.8
Tail gas compression (MW_e)	N/A	3.1	3.1	3.1
Total power consumption (MW_e)	51.9	54.1	54.1	50.1

5.8 Conclusions

A detailed simulation of an advanced IGCC plant to produce power and ultrapure hydrogen simultaneously where CO_2 is intrinsically captured by a pre-combustion capture has been proposed in this chapter. The H_2 PSA unit was designed such that its H_2 recovery can be increased close to its maximum in order to avoid the excessive power consumption involved in tail gas compression and minimise the H_2 PSA feed gas flowrate. Different configurations involving from four to twelve industrial columns were investigated considering different residence times and bed sizes. It was found that at the same hydrogen purity of 99.99+ mol%, the recovery can be increased to 92% in the twelve-column system.

A comprehensive economic analysis based on four cost items – columns, adsorbent, valves, tail gas compressor – revealed that the minimum CAPEX of 20.3 million $ is associated with the nine-bed system composed of two PSA trains. The related cost fraction to the simple capture case of the IGCC was found to be as high as 1.35%.

A detailed economic analysis was also carried out considering the entire IGCC plants. For the simple capture case, the associated LCOE and cost of CO_2 avoided (AC) were evaluated at 107.7 $/MWh and 33.4 $/ton$_{CO2}$, respectively. These results are in perfect agreement with those reported by other organisations and research groups. For the cogenerating case, they were respectively found at 105.1 $/MWh and 32.1 $/ton$_{CO2}$.

The advanced cogenerating IGCC plant can be improved by implementing the H_2 PSA tail gas recycle to other units of the plant, such as the water gas shift reactors, the dual-stage Selexol unit and the coal dryer. These process modifications led to a rise in the overall net plant efficiency because they can alleviate the power consumption at the CO_2 removal unit, the CO_2 compressor and the H_2 PSA tail gas compressor. Keeping fixed the plant power output at 479 MW_e, the ultrapure hydrogen production rate at 100 MMSCFD and the overall carbon capture at 90% for all the configurations, the case where a portion of the tail gas is recycled to both the WGSRs and the coal dryer showed a net electrical plant efficiency of 18.4% against 18.1% for the base case.

Furthermore, with reference to a hydrogen plant where the ultrapure production rate and the total power consumption for the base case were evaluated at 286 MMSCFD and 51.9 MW_e, respectively, it was found that an improved configuration with the total recycle of the H_2 PSA tail gas to three locations upstream of the process – the water gas shift reactor, the coal dryer and the acid gas removal unit – could increase the ultrapure hydrogen production rate by 4.2% and reduce the total auxiliaries' power consumption by 3.5%.

References

Ahn H, Brandani S, Luberti M, Lee CH. Hydrogen production processing. WO 2015/104532 A1, 2015.

ASME's Boiler and Pressure Vessel Code (BPVC). Section VIII: Pressure Vessels. 2013; available at www.asme.org.

Bird RB, Stewart WE, Lightfoot EN. Transport Phenomena 2nd Edition, 2007.

Chemical Engineering's Plant Cost Index. 2014; available at www.che.com/pci.

DECC. UK Electricity Generation Costs Update, 2010.

DOE NETL. Roadmap on manufacturing R&D for the hydrogen economy, 2005.

DOE NETL. Cost and performance baseline for fossil energy plants, 2007.

DOE NETL. Cost estimation methodology for NETL assessments of power plant performance, 2011.

ENCAP. Periodic activity report in Sustainable Energy Systems, 2004.

EPRI. Updated cost and performance estimates for advanced coal technologies including CO_2 capture, 2009.

Fuderer A, Rudelstorfer E. US Patent No. 3986849, to Union Carbide Corporation, 1976.

GCCSI. Economic assesment of carbon capture and storage technologies, 2011.

Geankoplis CJ. Transport processes and unit operations, 1997.

General Electric. Heavy duty gas turbine products (GEA12985H). 2009; available at https://powergen.gepower.com/plan-build/products/gas-turbines/index.html.

Green DW, Perry RH. Perry's Chemical Engineering Handbook, 8th Edition, 2007.

Honeywell. UniSim Design R400, 2011.

Huang Y, Rezvani S, McIlveen-Wright D, Minchener A, Hewitt N. Techno-economic study of CO_2 capture and storage in coal fired oxygen fed entrained flow IGCC power plants. Fuel Processing Technology 2008; 89: 916-925.

IEA GHG. 2009; available at www.iea.org/publications.

IPCC. Special report on carbon dioxide capture and storage. 2005.

Li M, Rao AD, Samuelsen GS. Performance and costs of advanced sustainable central power plants with CCS and H_2 co-production. Applied Energy 2012; 91: 43-50.

Kreutz T, Williams R, Chiesa P, Consonni S. Coproduction of hydrogen, electricity and CO_2 from coal with commercially ready technology. Part B: Economic analysis. Hydrogen Energy 2005; 30: 769-784.

Luberti M, Friedrich D, Brandani S, Ahn H. Design of H_2 PSA for cogeneration of ultrapure hydrogen and power at an advanced integrated gasification combined cycle with pre-combustion capture. Adsorption 2014; 20: 511-524.

Matches' Process Equipment Cost Estimates. 2014; available at www.matche.com/equipcost.

Megyesy EF. Pressure vessel handbook. Pressure vessel publishing Inc., USA. 1995.

Mhaskar PR, Moharir AS. Heuristics for synthesis and design of pressure-swing adsorption processes. Adsorption 2012; 18: 275-295.

MIT. The future of coal, 2007.

Nikolic D, Georgiadis MC, Kikkinides ES. An optimization framework of multibed pressure swing adsorption systems. 18th European Symposium on Computer Aided Process Engineering – ESCAPE 18, 2008.

PSE Ltd. 2010; available at http://www.psenterprise.com.

Rubin ES, Chen C, Rao AB. Cost and performance of fossil fuel power plants with CO_2 capture and storage. Energy Policy 2007; 35: 4444-4454.

Rubin ES. Understanding the pitfalls of CCS cost estimates. International Journal of Greenhouse Gas Control 2012; 10: 181-190.

Rubin ES, Short C, Booras G, Davison J, Ekstrom C, Matuszewski M, McCoy S. A proposed methodology for CO_2 capture and storage cost estimates. International Journal of Greenhouse Gas Control 2013; 17: 488-503.

UOP. Recent Selexol™, PolySep™ and PolyBed™ operating experience with gasification for power and hydrogen. Gasification Technologies 2002.

UOP, 2014. Available at www.uop.com/equipment/hydrogen-separation/#pressure-swing-adsorption.

Xi'an Lvneng Purification Technology Co, Ltd, 2014, available at http://xalvneng.en.alibaba.com.

ZEP. Annual report 2009, available at www.zeroemissionsplatform.eu.

ZEP. The costs of CO_2 capture: post-demonstration CCS in the EU. 2011, available at www.zeroemissionsplatform.eu.

Chapter 6: Conclusions and directions for future work

The aim of this thesis was to explore the challenges associated with the process integration of PSA technology for hydrogen purification with an advanced IGCC power plant with pre-combustion capture. Three main subjects were discussed in this thesis: the detailed simulation of an advanced IGCC power plant (Chapter 2), the design and numerical simulation of a new PSA unit for hydrogen purification from a lab-scale perspective (Chapters 3 and 4) and the retrofit of an industrial H_2 PSA unit to the IGCC plant for cogenerating ultrapure hydrogen and power (Chapter 5). Conclusions and recommendations for future work in these areas are listed in the following sections.

6.1 IGCC power plant modelling

Integrated gasification combined cycles (IGCCs) are one of the emerging clean coal technologies that pave the way for producing power from coal with a higher net power efficiency than conventional PC-fired boiler power plants. It is also advantageous that in an IGCC power plant a carbon capture unit can be applied to a stream with a very high CO_2 partial pressure upstream of gas combustion that would not be available in the case of a PC-fired boiler power plant, leading to a lower energy penalty involved in the carbon capture.

Despite the fact that IGCC is a well-established industrial process for power generation, there is huge potential for improving its performance, hence the research effort that has been made for the last decades. However, a realistic and reliable representation of the IGCC operation is not trivial or simple to accomplish. This is due to the challenges posed by the complexity of the simulation and by the need to examine the overall performance of the plant. More than 300 units are, in fact, involved in the complete and continuous process flow diagrams developed, depending on the case examined. IGCC power plant operation and performance have received significant research interest, but only a few previous studies have presented

detailed continuous designs for IGCC power plants with carbon capture targets as high as 90%.

When it comes to retrofitting IGCC power plants with CO_2 capture processes, almost all the parts of the conventional, non-capture plant are affected. It is expected that there will be increments in the fuel that are fed to the gasifiers to operate the same gas turbine. With reference on the DOE report (2007), it was found that the IGCC power plant with Shell gasifier has a 41.1% net plant efficiency without carbon capture but this efficiency drops to approximately 31.2% when carbon capture is integrated. Water gas shift reactors are an essential addition to the IGCC power plant when it has to be operated with retrofitted carbon capture process. In order to promote the conversion of CO to CO_2, IP steam extracted from the steam cycle has to be added. The resulting conversion was around 95.7%.

The dual-stage Selexol process is the state-of-art technology to be used for IGCC in order to not only remove H_2S, but also to capture CO_2. The CO_2 compression train downstream of the CO_2 capture process is another additional component to the carbon capture IGCCs where the CO_2 product is compressed to a pressure suitable for CO_2 transport and storage. Most of the modifications necessary for the carbon capture operation of the IGCC power plant are directly connected with an effect on the performance of the plant and an energy penalty, which is interpreted as a loss in the net plant efficiency. The absorption regime occurring with DEPG solvent in the Selexol process was successfully modelled by a predictive simulation tool developed to describe the behaviour of the acid/shifted syngas in the solvent. CO_2 capture processes using DEPG in a Selexol process have been examined in detail for the IGCC power plant and were presented. One substantial improvement of the Selexol unit could be the employment of solvent warming just before phase separation in the last flash drum to enhance the solvent working capacity, leading to decreased auxiliaries and therefore increased power plant efficiency. Further work is also essential to develop power plant configurations in which solvents other than Selexol, and mixed solvents such as Sulfinol-M and Sulfinol-D, are used for AGR and CO_2 capture.

Pressure swing adsorption technology (PSA) applied to IGCC pre-combustion capture can be considered another possible research area of interest. Alike in the

post-combustion capture process, promising results are expected in terms of lower energy penalty associated to the carbon capture unit as reported in recent literature.

Other plant units were successfully simulated, such as the EP ASU, the Claus plant and the power island. One obvious, yet significant, change in the carbon capture IGCC cases is the fact that there is no potential for air integration between the GT compressor and the EP ASU. The steam cycle had to be redesigned mainly in order to provide steam to the water gas shift reactors. Specific software has to be used to develop a simulation tool capable of realistically representing the operation of the combustor, air compressor and gas turbine block.

Eventually, considering the net plant efficiency loss, the effect of the CO_2 capture process on the power plant's performance is of significant importance but it is unrealistic to assume that only the CO_2 capture process that will cause energy losses as the power plant operation is a continuous process and all plant units are interconnected.

6.2 Design of a novel H_2 PSA unit applied to an IGCC H_2-rich feed

The production of hydrogen is both a sought-after target and an appropriate environmental solution because it is commonly utilised as a feedstock in refineries as well as an energy carrier in fuel cells. It is well known, in fact, that most refining complexes face a significant deficiency in their existing hydrogen production capacity. Hydrogen is needed for operating their hydrotreating desulfurisation process, which removes mainly sulfur and other impurities from raw petroleum products and hydrocracking units to upgrade low-grade heavy residues to more valuable diesel and lube base oil. Due to the requirement for very high operational severity in both units for deep desulfurisation and improved product quality, ultrapure hydrogen with a purity of 99.99+ mol% should be utilised for the hydroprocessing.

A valid way to produce hydrogen is through IGCC with CO_2 capture. In producing ultrapure hydrogen from such a gas mixture as composed of H_2, CO_2, CO, N_2 and Ar, it is well known that pressure swing adsorption (PSA) is the only economically feasible, commercialised separation process. Therefore, it is essential

to retrofit a H_2 PSA unit to the IGCC in order to cogenerate hydrogen and power simultaneously. Knowing the maximum H_2 recovery that a H_2 PSA can produce from the raw H_2 gas is very important in evaluating the performance of the advanced IGCC plant for cogenerating power and ultrapure hydrogen. This is because the flowrate of PSA tail gas, to be determined by the H_2 recovery, should be recompressed and fed to the gas turbine along with the fuel gas. Therefore, it is essential to design a H_2 PSA such that its H_2 recovery can be maximised in order to minimise the power consumption relating to tail gas compression.

Accordingly, lab-scale simulations were carried out to increase the H_2 recovery by increasing the complexity of the PSA step configuration, which enables a PSA cycle to have a lower feed flow to one column for adsorption and more pressure equalisation steps. As a result, the H_2 recovery reached a maximum of around 93% with a Polybed H_2 PSA system with twelve columns and the step configuration containing simultaneous adsorption at three columns and four-stage pressure equalisation (Luberti et al., 2014). This result was obtained for both the cases of fixed column dimensions with varying cycle time and for fixed cycle time with varying column dimensions, at a given total flowrate. Further work would be needed to experimentally validate these results because the size of the adsorption columns in this investigation was determined to be the same as those of a lab-scale six-column PSA rig in the process-engineering laboratory at the University of Edinburgh. The rig construction has, in fact, just been completed and the rig interface work is nearly done.

An additional research direction for the future might be related to the use of novel adsorbents for the hydrogen purification process, such as metal organic frameworks (MOFs). Unlike a conventional H_2 PSA unit from SMR, in the IGCC H_2 PSA the main impurities in the raffinate stream are represented by the weakly adsorbed nitrogen and argon components. Future work should focus on synthesising novel adsorbents that, for the given range of partial pressures, would exhibit lower capacity for hydrogen and higher selectivity for N_2/H_2 and Ar/H_2, compared to the referential 5A zeolite adsorbent.

6.3 Retrofit of an industrial H_2 PSA unit to an IGCC

After the lab-scale simulations, different configurations involving from four to twelve columns were also studied considering an industrial scale H_2 PSA unit capable to produce 100 MMSCFD of ultrapure hydrogen and using different residence times and bed sizes. It was found that the recovery could be increased to 92% while the productivity was 395 $mol_{H2}/kg_{ads}/d$ for the twelve-column system. Moreover, a comprehensive economic analysis based on four cost items – columns, adsorbent, valves, tail gas compressor – revealed that the minimum CAPEX of 20.3 million $ is associated with the nine-bed system composed of two PSA trains. The related cost fraction of the simple capture case of the IGCC was found to be as high as 1.35%. A detailed economic analysis was also carried out considering the entire IGCC plant. For the simple capture case, the associated levelised cost of electricity (LCOE) and cost of CO_2 avoided (AC) were evaluated at 107.7 $/MWh and 33.4 $/ton$_{CO2}$. These results are in perfect agreement with those reported by other organisations and research groups. For the cogenerating case they were respectively found to be 105.1 $/MWh and 32.1 $/ton$_{CO2}$.

In the base case, the cogenerating IGCC is designed so that a portion of the high-pressure clean syngas is sent to the coal dryer while the entire H_2 PSA tail gas is recompressed and sent to the gas turbine. This configuration can be improved by implementing the H_2 PSA tail gas recycle to other units of the plant, such as the water gas shift reactors, the dual-stage Selexol unit and the coal dryer. These process modifications led to a rise in the overall net plant efficiency because they can alleviate the power consumption of the CO_2 removal unit, the CO_2 compressor and the H_2 PSA tail gas compressor. Keeping the power output at 479 MW_e, the ultrapure hydrogen production rate at 100 MMSCFD and 90% overall carbon capture for all the configurations, the case where a portion of the tail gas is recycled to both the WGSRs and the coal dryer showed a net electrical plant efficiency of 18.4% against the 18.1% of the base case.

Part of the proposed modifications and the related simulation results were presented in a recent patent (Ahn et al., 2015) and they may have commercial interest for companies, such as Honeywell UOP, Air Products, Air Liquide and refining

companies in general. In the limiting case where a coal gasification hydrogen plant produces only ultrapure hydrogen with a production rate of 286 MSCFD and 90% overall carbon capture, it was demonstrated that it is possible to efficiently recycle the total H_2 PSA tail gas to three locations upstream of the PSA unit, such as the water gas reactor, the coal dryer and the dual-stage Selexol unit, in order to increase the hydrogen yield by 4.2% and decrease the total auxiliaries' power consumption by 3.5%.

Future work could rely on the design and simulation of other cogenerating IGCC scenarios with different H_2/electricity production rates in order to make the IGCC plant more flexible to the market demands of these two valuable products. The ultimate, relatively low CO_2 capture cost penalty for H_2 from coal and the prospect that, even with current technology, H_2 from coal with CCS might soon become competitive compared to H_2 from natural gas with CO_2 venting, suggest that cogenerating IGCC plants have a promising future in a climate-constrained low-carbonised world if H_2 becomes a major energy carrier and if the CO_2 storage challenges can be addressed effectively.

References

Ahn H, Brandani S, Luberti M, Lee CH. Hydrogen production processing. WO 2015/104532 A1, 2015.

DOE NETL. Cost and performance baseline for fossil energy plants, 2007.

Luberti M, Friedrich D, Brandani S, Ahn H. Design of H_2 PSA for cogeneration of ultrapure hydrogen and power at an advanced integrated gasification combined cycle with pre-combustion capture. Adsorption 2014; 20: 511-524.

Appendix 1: DOE case 6 block flow diagram and data

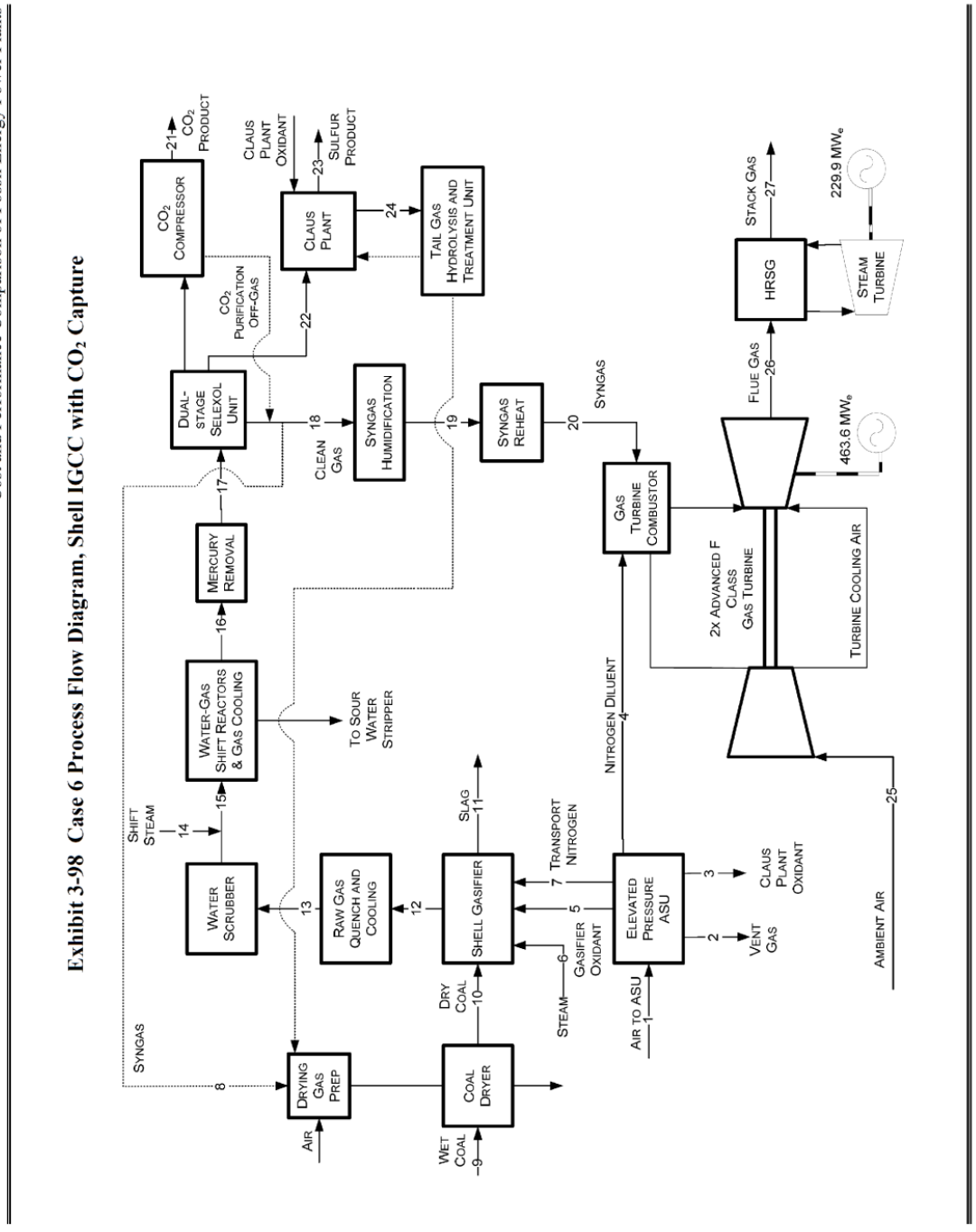

V-L Mole Fraction	**1**	**2**	**3**	**4**	**5**	**6**
Ar	0.0094	0.0263	0.0360	0.0024	0.0360	0.0000
CH_4	0.0000	0.0000	0.0000	0.0000	0.0000	0.0000
CO	0.0000	0.0000	0.0000	0.0000	0.0000	0.0000
CO_2	0.0003	0.0091	0.0000	0.0000	0.0000	0.0000
COS	0.0000	0.0000	0.0000	0.0000	0.0000	0.0000
H_2	0.0000	0.0000	0.0000	0.0000	0.0000	0.0000
H_2O	0.0104	0.2820	0.0000	0.0004	0.0000	1.0000
H_2S	0.0000	0.000	0.0000	0.0000	0.0000	0.0000
N_2	0.7722	0.4591	0.0140	0.9918	0.0140	0.0000
NH_3	0.0000	0.0000	0.0000	0.000	0.0000	0.0000
O_2	0.2077	0.2235	0.9500	0.0054	0.9500	0.0000
SO_2	0.0000	0.000	0.0000	0.0000	0.0000	0.0000
Total	1.0000	1.0000	1.0000	1.0000	1.0000	1.0000

Temperature (°F)	238	70	90	385	518	750
Pressure (psia)	190.0	16.4	125.0	460.0	740.0	740
Enthalpy (Btu/lb)	56.9	26.8	11.4	88.0	107.7	1,409.5
Density (lb/ft^3)	0.732	0.104	0.688	1.424	2.272	1.027
V-L FIowrate (lbmol/hr)	56,388	2,025	230	40,650	11,358	2,534
V-L Flowrate (lb/hr)	1,627,030	53,746	7,428	1,140,640	366,070	46,657
Solids Flowrate (lb/hr)	0	0	0	0	0	0

V-L Mole Fraction	**7**	**8**	**9**	**10**	**11**	**12**
Ar	0.0000	0.0102	0.0000	0.0000	0.0000	0.0097
CH_4	0.0000	0.0004	0.0000	0.0000	0.0000	0.0004
CO	0.0000	0.0265	0.0000	0.0000	0.0000	0.5716
CO_2	0.0000	0.0211	0.0000	0.0000	0.0000	0.0211
COS	0.0000	0.0000	0.0000	0.0000	0.0000	0.0007
H_2	0.0000	0.8874	0.0000	0.0000	0.0000	0.2901
H_2O	0.0000	0.0001	1.0000	1.0000	0.0000	0.0364
H_2S	0.0000	0.0000	0.0000	0.0000	0.0000	0.0081
N_2	1.0000	0.0543	0.0000	0.0000	0.0000	0.0585
NH_3	0.0000	0.0000	0.0000	0.0000	0.0000	0.0033
O_2	0.0000	0.0000	0.0000	0.0000	0.0000	0.0000
SO_2	0.0000	0.0000	0.0000	0.0000	0.0000	0.0000
Total	1.0000	1.0000	1.0000	1.0000	0.0000	1.0000

Temperature (^oF)	560	121	59	215	2,595	2,595
Pressure (psia)	815.0	469.6	14.7	14.7	614.7	604.7
Enthalpy (Btu/lb)	132.2	113.8	11,676.0	-	-	1,012.8
Density (lb/ft^3)	2.086	0.407	-	-	-	0.563
V-L FIowrate (lbmol/hr)	2,110	491	2,923	1,218	0	42,059
V-L Flowrate (lb/hr)	59,121	2,651	52,617	21,935	0	865,967
Solids Flowrate (lb/hr)	0	0	420,559	420,559	47,374	0

V-L Mole Fraction	**13**	**14**	**15**	**16**	**17**	**18**
Ar	0.0052	0.0000	0.0064	0.0064	0.0064	0.0102
CH_4	0.0002	0.0000	0.0002	0.0002	0.0002	0.0004
CO	0.3070	0.0000	0.0166	0.0166	0.0166	0.0265
CO_2	0.0113	0.0000	0.3771	0.3771	0.3771	0.0211
COS	0.0004	0.0000	0.0000	0.0000	0.0000	0.0000
H_2	0.1559	0.0000	0.5547	0.5547	0.5547	0.8874
H_2O	0.4826	1.0000	0.0014	0.0014	0.0014	0.0001
H_2S	0.0043	0.0000	0.0050	0.0050	0.0050	0.0000
N_2	0.0314	0.0000	0.0385	0.0385	0.0385	0.0543
NH_3	0.0018	0.0000	0.0000	0.0000	0.0000	0.0000
O_2	0.0000	0.0000	0.0000	0.0000	0.0000	0.0000
SO_2	0.0000	0.0000	0.0000	0.0000	0.0000	0.0000
Total	1.0000	1.0000	1.0000	1.0000	1.0000	1.0000

Temperature (ºF)	500	750	574	95	95	121
Pressure (psia)	564.4	825.0	544.7	482.6	472.6	469.6
Enthalpy (Btu/lb)	665.9	1,368.0	767.7	25.6	25.6	113.8
Density (lb/ft^3)	1.064	1.145	0.944	1.598	1.565	0.407
V-L FIowrate (lbmol/hr)	78, 325	11,679	89,158	63,376	63,376	39,127
V-L Flowrate (lb/hr)	1,519,300	210,400	1,714,460	1,246,470	1,246,470	211,226
Solids Flowrate (lb/hr)	0	0	0	0	0	0

V-L Mole Fraction	**19**	**20**	**21**	**22**	**23**
Ar	0.0099	0.0099	0.0000	0.0000	0.0000
CH_4	0.0004	0.0004	0.0000	0.0000	0.0000
CO	0.0256	0.0256	0.0000	0.0000	0.0000
CO_2	0.0204	0.0204	1.0000	0.3526	1.0000
COS	0.0000	0.0000	0.0000	0.0006	0.0000
H_2	0.8584	0.8584	0.0000	0.0000	0.0000
H_2O	0.0327	0.0327	0.0000	0.0502	0.0000
H_2S	0.0000	0.0000	0.0000	0.3122	0.0000
N_2	0.0526	0.0526	0.0000	0.2845	0.0000
NH_3	0.0000	0.0000	0.0000	0.0000	0.0000
O_2	0.0000	0.0000	0.0000	0.0000	0.0000
SO_2	0.0000	0.0000	0.0000	0.0000	0.0000
Total	1.0000	1.0000	1.0000	1.0000	0.0000
Temperature (°F)	213	385	156	124	352
Pressure (psia)	453.9	448.9	2,214.7	60.0	23.6
Enthalpy (Btu/Ib)	327.0	535.7	-46.4	37.9	362.5
Density (lb/ft^3)	0.365	0.288	30.929	0.343	0.080
V-L FIowrate (lbmol/hr)	40,448	40,448	22,707	1,017	0
V-L Flowrate (lb/hr)	235,031	235,031	999,309	35,657	0
Solids Flowrate (lb/hr)	0	0	11,307	0	11,825

V-L Mole Fraction	**24**	**25**	**26**	**27**
Ar	0.0074	0.0094	0.0091	0.0091
CH_4	0.0000	0.0000	0.0000	0.0000
CO	0.0792	0.0000	0.0000	0.0000
CO_2	0.2293	0.0003	0.0063	0.0063
COS	0.0003	0.0000	0.0000	0.0000
H_2	0.0417	0.0000	0.0000	0.0000
H_2O	0.4003	0.0108	0.1258	0.1258
H_2S	0.0013	0.0000	0.0000	0.0000
N_2	0.2379	0.7719	0.7513	0.7513
NH_3	0.0000	0.0000	0.0000	0.0000
O_2	0.0000	0.2076	0.1075	0.1075
SO_2	0.0026	0.0000	0.0000	0.0000
Total	1.0000	1.0000	1.0000	1.0000
Temperature (°F)	280	59	1,051	270
Pressure (psia)	23.6	14.7	15.2	15.2
Enthalpy (Btu/Ib)	362.5	13.8	364.1	150.8
Density (lb/ft^3)	0.080	0.076	0.026	0.053
V-L FIowrate (lbmol/hr)	1,603	244,799	308,019	308,019
V-L Flowrate (lb/hr)	42,962	7,062,330	8,438,000	8,438,000
Solids Flowrate (lb/hr)	0	0	0	0

Appendix 2: Design of H_2 PSA for cogeneration of ultrapure hydrogen and power at an advanced integrated gasification combined cycle with pre-combustion capture *by Luberti et al., 2014*

Adsorption (2014) 20:511–524
DOI 10.1007/s10450-013-9598-0

Design of a H_2 PSA for cogeneration of ultrapure hydrogen and power at an advanced integrated gasification combined cycle with pre-combustion capture

Mauro Luberti · Daniel Friedrich · Stefano Brandani · Hyungwoong Ahn

Received: 18 May 2013 / Accepted: 29 November 2013 / Published online: 14 December 2013

Abstract A novel hydrogen pressure swing adsorption system has been studied that is applied to an advanced integrated gasification combined cycle plant for cogenerating power and ultrapure hydrogen (99.99+ mol%) with CO_2 capture. In designing the H_2 PSA, it is essential to increase the recovery of ultrapure hydrogen product to its maximum since the power consumption for compressing the H_2 PSA tail gas up to the gas turbine operating pressure should be minimised to save the total auxiliary power consumption of the advanced IGCC plant. In this study, it is sought to increase the H_2 recovery by increasing the complexity of the PSA step configuration that enables a PSA cycle to have a lower feed flow to one column for adsorption and more pressure equalisation steps. As a result the H_2 recovery reaches a maximum around 93 % with a Polybed H_2 PSA system having twelve columns and the step configuration contains simultaneous adsorption at three columns and four-stage pressure equalisation.

Keywords IGCC · Pressure swing adsorption · Hydrogen purification · Cogeneration

Nomenclature

A_c	Internal column surface area, m^2
A_p	Pellet surface area, m^2
b_i^j	Adsorption equilibrium constant of site j for comp. i, bar^{-1}
$b_{i,0}^j$	Pre-exponential adsorption equilibrium constant coefficient of site j for comp. i, bar^{-1}
c_i	Gas concentration of component i, mol m^{-3}
c_i^m	Gas concentration of component i in the macropore, mol m^{-3}
c_T	Total gas concentration, mol m^{-3}
$c_{P,s}$	Specific heat capacity at constant pressure of the adsorbent, J kg^{-1} K^{-1}
D^L	Axial mass dispersion coefficient, m^2s^{-1}
D_c	Column diameter, m
D_m	Molecular diffusivity, m^2 s^{-1}
$D_{p,i}$	Macropore diffusivity of component i, m^2 s^{-1}
d_p	Pellet averaged diameter, m
h_w	Heat transfer coefficient at the column wall, W m^{-2} K^{-1}
H_f	Enthalpy in the fluid phase per unit volume, J m^{-3}
$\widetilde{H}_i$	Partial molar enthalpy in the fluid phase of component i, J mol^{-1}
$\Delta\widetilde{H}_i^j$	Heat of adsorption of site j for component i, J mol^{-1}
J_i	Diffusive flux of component i, mol m^{-2} s^{-1}
J_T	Thermal diffusive flux, W m^{-2}
k_g	Gas conductivity, W m^{-1} K^{-1}
$k_i^p \cdot A_p/V_p$	LDF mass transfer coefficient of component i in the pellet, s^{-1}
$k_i^{cr} \cdot 3/r_c$	LDF mass transfer coefficient of component i in the crystal, s^{-1}
L_c	Column length, m
M_{ads}	Adsorbent mass, kg
P	Pressure, bar
Pr	Prandtl number, [-]
$\bar{q}_i$	Average adsorbed concentration of component i in the crystal, mol kg^{-1}
q_i^*	Adsorbed concentration of component i at equilibrium, mol kg^{-1}
$q_{i,s}^j$	Saturation capacity of site j for comp. i, mol kg^{-1}

M. Luberti · D. Friedrich · S. Brandani · H. Ahn (✉)
Scottish Carbon Capture and Storage Centre, Institute for Materials and Processes, School of Engineering, The University of Edinburgh, Mayfield Road, Edinburgh EH9 3JL, UK
e-mail: h.ahn@ed.ac.uk

$\bar{Q}_i$	Average adsorbed concentration of component i in the pellet, mol m^{-3}
Q_{feed}	Feed flow rate, mol s^{-1}
R	Ideal gas constant J mol^{-1} K^{-1}
Re	Reynolds number, [-]
r_c	Crystal radius, m
r_p	Pellet radius, m
Sc	Schimdt number, [-]
t	Time, s
t_{cycle}	Cycle time, s
T	Temperature, K
T_f	Fluid temperature, K
T_w	Column wall temperature, K
u	Velocity, m s^{-1}
U_f	Internal energy in the fluid phase per unit volume, J m^{-3}
U_P	Internal energy in the pellet per unit volume, J m^{-3}
$U_{P,f}$	Internal energy in the macropore per unit volume, J m^{-3}
$U_{P,s}$	Internal energy in the solid phase per unit volume, J m^{-3}
v	Interstitial flow velocity, m s^{-1}
V_c	Column volume, m^3
V_p	Pellet volume, m^3
x_i, y_i	Molar fraction of component i, [-]
z	Spatial dimension, m

Greek letters

ε	External bed void fraction, [-]
ε_p	Pellet void fraction, [-]
λ^L	Axial thermal dispersion coefficient, W m^{-1} K^{-1}
μ	Viscosity, bar s
ρ_f	Fluid density, kg m^{-3}
ρ_p	Pellet density, kg m^{-3}

1 Introduction

Eight refineries in the UK are currently emitting 14.9 $MtCO_2$ which accounts for around 3 % of total UK CO_2 emission in 2009 (DECC 2009). The INEOS refining plant in Grangemouth, for example, emits around 2.2 $MtCO_2$ per annum, which is equivalent to 4 % of total CO_2 emissions in Scotland (SEPA 2008). The Committee on Climate Change (CCC) estimated that there will be a chance to curtail around 3.5 $MtCO_2$ out of 14.9 $MtCO_2$ from refineries by 2030 by improving their energy efficiency. The CCC also foresaw that beyond this target of abatement, a further reduction would be possible by deploying carbon capture units on H_2 plants and replacing combustion fuels with carbon–neutral biomass (Committee on Climate Change 2011).

It is well known that most refining complexes face a significant deficiency of their existing hydrogen production capacity. Hydrogen is needed for operating their hydrotreating desulphurisation process that removes mainly sulphur and other impurities from raw petroleum products and hydrocracking units for upgrading low-grade heavy residues to more valuable diesel and lube base oil. The need for H_2 is bound to increase due to the trends of (1) more stringent sulphur and nitrogen specification in fuel oils, (2) increasing crack spread, and (3) the rapid change of crude oil properties from 'light and sweet' to 'heavy and sour'. Due to the requirement of very high operational severity in both units for deep desulphurisation and improved product quality, ultrapure hydrogen with a purity of 99.99+ mol% should be utilised for the hydroprocessing. Accordingly, most refineries are forced to increase rapidly their hydrogen production capacities to cope with the increased H_2 demand but it is doubtful that given the upcoming carbon emission regulation conventional steam methane reforming (SMR) H_2 processes would be still the best option to meet this demand.

Most refineries have their own power plant to provide various units with the utilities such as steam and electricity. In particular, when integrated with a carbon capture unit, integrated gasification combined cycle (IGCC) power plants would have significantly lower energy penalty than coal-fired power plants since a carbon capture unit can be applied to a gas stream having higher CO_2 partial pressure in IGCC power plants. As a result, it has been reported that IGCC power plants integrated with pre-combustion capture would have notably higher net power efficiency than coal fired power plants (DOE 2007).

It should also be noted that IGCC power plants run gas turbines using H_2-rich fuel gas (88–91 mol% H_2 purity) in CO_2 capture cases instead of mixtures of CO and H_2 in non-capture cases and it is easy to produce ultrapure hydrogen product by purifying the H_2-rich fuel gas. This means that by replacing both the existing SMR H_2 plant and the coal-fired power plants with an advanced IGCC plant it would be possible to provide refining complexes with ultrapure H_2 and power simultaneously where CO_2 can be inherently captured as depicted in Fig. 1.

In producing ultrapure hydrogen (99.99+ mol%) from such a gas mixture as composed of H_2, CO_2, CO, N_2 and Ar, it is well-known that a pressure swing adsorption (PSA) is the only economically feasible, commercialised separation process. The multi-column PSA process, known as UOP Polybed, has been widely applied to SMR H_2 plants to produce ultrapure H_2 from shifted syngas. However, the conventional H_2 PSA has been designed and optimised against a feed stream of around 71 % H_2, 19 % CO_2, 4 % CO and 5 % CH_4 at 20 bar found in a SMR H_2 process. This composition and the pressure of the raw H_2 feed in a

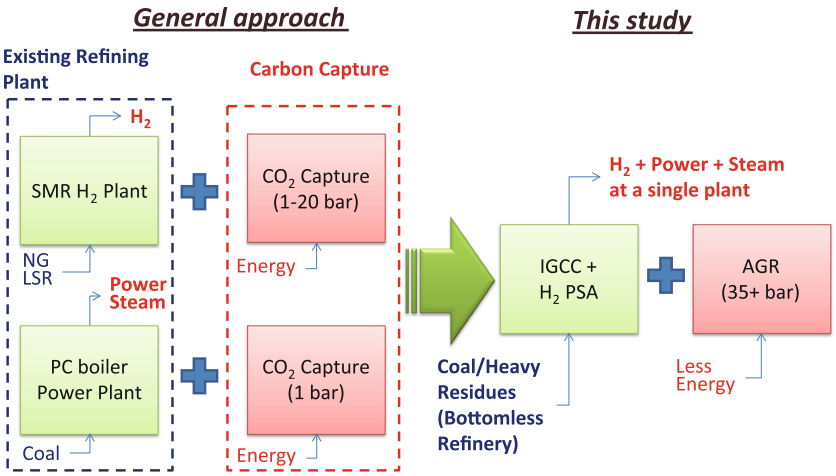

Fig. 1 A conceptual diagram to compare general approach to capture CO_2 from a SMR H_2 plant and a coal-fired power plant separately to an advanced IGCC process for cogenerating power and ultrapure hydrogen with carbon capture (this study)

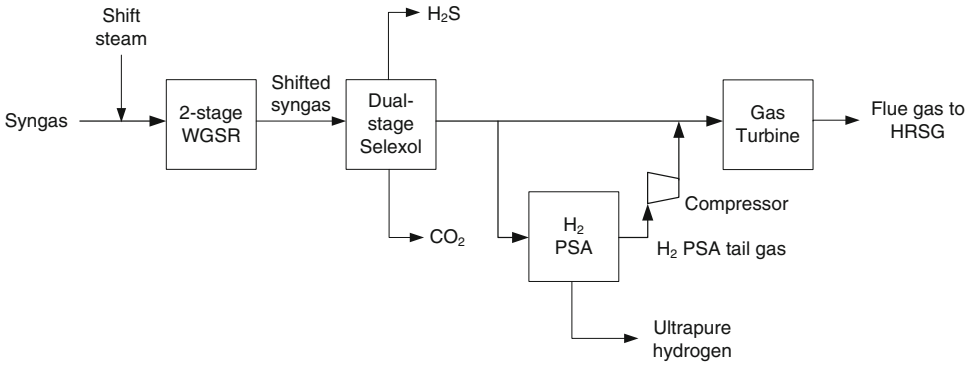

Fig. 2 Block flow diagram of an advanced IGCC process for cogenerating power and ultrapure hydrogen

SMR-based H_2 plant is quite different from the raw H_2 fuel gas in IGCC power plants with carbon capture (88.75 % H_2, 2.12 % CO_2, 2.66 % CO, 5.44 % N_2, 1.03 % Ar at 34 bar). Therefore, there is a need to revisit the design of the H_2 PSA process to estimate the H_2 recovery and productivity obtained at the operating conditions to meet the H_2 product purity as high as 99.99+ mol%.

2 Design basis of a H_2 PSA integrated with an IGCC power plant

This study is aimed at the design of a H_2 PSA system that is applicable to an advanced IGCC plant for producing both ultrapure H_2 and power. The advanced IGCC plant is a modification of a conventional IGCC power plant with carbon capture to include a new H_2 PSA unit and its block flow diagram is illustrated in Fig. 2.

The process design of the conventional IGCC power plants with carbon capture is based on an exemplary IGCC power plant using a Shell gasifier (DOE 2007; Kapetaki et al. 2013). The syngas stream from the shift reactors is fed to an acid gas removal unit (AGR), such as a dual-stage Selexol unit, to remove CO_2 as well as H_2S from the syngas. In the conventional IGCC process, the treated syngas leaving the AGR becomes saturated with water in a fuel gas saturation column and then is fed to the combustion chamber of a gas turbine. But in this study the treated syngas is split into two streams: one stream flows directly to a gas turbine for power generation and the other is sent to a H_2 PSA for ultrapure H_2 production. The H_2 PSA tail gas obtained as by-product needs to be compressed up to the operating pressure of the gas turbine and sent to the combustion chamber with the H_2-rich fuel gas.

Various H_2 PSA designs have been studied so far in order to estimate their performance when they are applied to conventional SMR H_2 plants (Ribeiro et al. 2008, 2009; Lopes et al. 2011). Even though the H_2 recovery that is expected of a commercial Polybed H_2 PSA in a SMR H_2 plant is as high as 89 %, they could obtain 52 to 80 % H_2 recovery at around 99.99 mol% H_2 purity. This is because the H_2 PSA systems in their design were configured with maximum four columns while commercial Polybed H_2 PSA systems in most cases contain seven to sixteen adsorption columns to enable enhanced hydrogen recovery. In this study, H_2 PSA systems having up to twelve columns have been simulated to see the effect of different PSA step configurations that are subject to the chosen number of

columns on the H_2 recovery using an in-house cyclic adsorption process simulator (Friedrich et al. 2013).

Given the composition and the pressure of raw H_2 feeds that previous study dealt with (Ahn et al. 2001), it was concluded that H_2 PSA designs that were configured with adsorption columns having two adsorbent layers would exhibit a better performance than those having adsorption columns packed with a single adsorbent. This is because it is unlikely to find a versatile adsorbent that has better working capacities than others for all impurities being contained in a raw H_2 feed. Therefore, a layered bed is usually configured such that an activated carbon layer near the feed end plays a role in adsorbing mainly CO_2 and CH_4 while a zeolite layer on top of the activated carbon layer removes CO and N_2. The length ratio of the carbon to zeolite layers is regarded as one of the key parameters that need to be optimised (Ahn et al. 2001, 2012; Ribeiro et al. 2008; Yang and Lee 1998; Park et al. 1998). Given the composition of the new raw H_2 feed that has relatively small CO_2 and no CH_4, however, it is plausible that an adsorption column packed with zeolite 5A performs better than those with a layered bed of activated carbon and zeolite 5A.

The production of the H_2 PSA tail gas should be minimised in order to reduce the power consumption relating to its compression before feeding it to the gas turbine. In this study the aim is to maximise H_2 recovery by adding more columns to the H_2 PSA process to enable more complicated step configurations for minimising the H_2 loss and consumption. To know the maximum hydrogen recovery that a H_2 PSA could achieve is essential in determining the mass balance around the H_2 PSA, i.e. the flowrate and the composition of both ultrapure hydrogen product and PSA tail gas. Once the mass balance is constructed at the condition of achieving the maximum H_2 recovery, it is possible to estimate the auxiliary power consumption in compressing the H_2 PSA tail gas and the power generation in the gas and steam turbines accurately.

3 H_2 PSA simulation

The dynamic behaviour of a H_2 PSA is described by a mathematical model which couples mass, momentum and energy balances over a packed bed with the appropriate boundary conditions for each step of the cycle (Friedrich et al. 2013).

Since the flow is assumed to be a dispersed plug flow the component and overall material balances along the column are given by:

$$\frac{\partial c_i}{\partial t} + \frac{(1-\varepsilon)}{\varepsilon} \cdot \frac{\partial \bar{Q}_i}{\partial t} + \frac{\partial (c_i \cdot v)}{\partial z} + \frac{\partial J_i}{\partial z} = 0 \tag{1}$$

$$\bar{Q}_i = \varepsilon_p c_i^m + \rho_p \bar{q}_i \tag{2}$$

$$J_i = -D^L c_T \frac{\partial x_i}{\partial z} \tag{3}$$

$$\frac{\partial c_T}{\partial t} + \frac{(1-\varepsilon)}{\varepsilon} \cdot \sum_i \frac{\partial \bar{Q}_i}{\partial t} + \frac{\partial (c_T \cdot v)}{\partial z} = 0 \tag{4}$$

Since the column undergoes significant temperature excursions over a cycle caused by the heat of adsorption, constitutive energy balances are coupled with the mass balance:

$$\varepsilon \frac{\partial U_f}{\partial t} + (1-\varepsilon)\frac{\partial U_P}{\partial t} + \varepsilon \frac{\partial (H_f \cdot v)}{\partial z} + \frac{\partial J_T}{\partial z} + \sum_{i=1}^{N_c} \frac{\partial (J_i \tilde{H}_i)}{\partial z} + h_w \frac{A_c}{V_c}(T_f - T_w) = 0 \tag{5}$$

$$\frac{dU_P}{dt} = \varepsilon_P \frac{dU_{P,f}}{dt} + (1-\varepsilon_P)\frac{dU_{P,s}}{dt} \tag{6}$$

$$J_T = -\lambda^L \varepsilon \frac{\partial T_f}{\partial z} \tag{7}$$

In Eq. (5), T_w is assumed to be equal to ambient temperature since a heat balance around the wall is not taken into account.

In this work the adsorption rate is represented by Linear Driving Force (LDF) model for both macropores and micropores.

$$\varepsilon_p \frac{dc_i^m}{dt} + \rho_p \frac{d\bar{q}_i}{dt} = k_i^p \frac{A_p}{V_p}(c_i - c_i^m) \tag{8}$$

$$k_i^p \frac{A_p}{V_p} = \frac{15 \cdot \varepsilon_p \cdot D_{p,i}}{r_P^2} \tag{9}$$

$$\frac{d\bar{q}_i}{dt} = k_i^{cr} \frac{3}{r_c}(q_i^* - \bar{q}_i) \tag{10}$$

The axial mass dispersion coefficient D^L and the axial thermal dispersion coefficient λ^L are estimated using the correlations by Wakao and Funazkri (1978):

$$\frac{\varepsilon \cdot D^L}{D_m} = 20 + 0.5 \cdot Sc \cdot \mathrm{Re} \tag{11}$$

$$\frac{\lambda^L}{k_g} = 7 + 0.5 \cdot \mathrm{Pr} \cdot \mathrm{Re} \tag{12}$$

The pressure drop along the column is evaluated using the Ergun equation (Ergun 1952):

$$-\frac{\partial P}{\partial z} = \frac{150\mu(1-\varepsilon)^2}{d_p^2 \varepsilon^2} v + \frac{1.75\rho_f(1-\varepsilon)}{d_p \varepsilon} v|v| \tag{13}$$

The boundary conditions for the gas phase concentrations and the enthalpies are given by the Danckwerts boundary conditions. With the conventions that the positive flow direction is from 0 (feed end) to L (product end) these can be written in a general form as:

Table 1 Isotherm parameters of dual-site Langmuir model for zeolite 5A

Gas	$q_{i,s}^1$ (mol/kg)	$q_{i,s}^2$ (mol/kg)	$b_{i,0}^1$ (bar^{-1})	$b_{i,0}^2$ (bar^{-1})	$(-\Delta H_i^1)$ (J/mol)	$(-\Delta H_i^2)$ (J/mol)
CO_2	0.7077	3.711	1.077×10^{-7}	1.233×10^{-4}	38,312	29,808
H_2	0.7077	3.711	4.227×10^{-7}	1.333×10^{-4}	19,674	9,282
CO	0.7077	3.711	2.431×10^{-8}	2.321×10^{-5}	47,736	20,994
N_2	0.7077	3.711	2.141×10^{-6}	8.987×10^{-5}	31,338	14,956
Ar	0.7077	3.711	1.399×10^{-9}	4.901×10^{-4}	50,239	11,171

$$J_T|_{z=0} = \frac{v + |v|}{2}\left(H_{f,0-} - H_{f,0}\right) \tag{14}$$

$$J_T|_{z=L_c} = \frac{v - |v|}{2}\left(H_{f,L_c+} - H_{f,L_c}\right) \tag{15}$$

$$J_i|_{z=0} = \frac{v + |v|}{2}\left(c_{i,0-} - c_{i,0}\right) \tag{16}$$

$$J_i|_{z=L_c} = \frac{v - |v|}{2}\left(c_{i,L_c+} - c_{i,L_c}\right) \tag{17}$$

Adsorption equilibrium of pure hydrogen, carbon dioxide, carbon monoxide, nitrogen and argon on zeolite 5A are reported in the literature in the range of the pressure up to 7.5 bar (Lopes et al. 2009). The adsorption equilibria are predicted by the following extended dual-site Langmuir model:

$$q_i^* = \frac{q_{i,s}^1 b_i^1 P x_i}{1 + \sum_{j=1}^{N_c} b_j^1 P x_j} + \frac{q_{i,s}^2 b_i^2 P x_i}{1 + \sum_{j=1}^{N_c} b_j^2 P x_j} \tag{18}$$

with $b_i^l = b_{i,0}^l \exp\left(\frac{-\Delta \tilde{H}_i^l}{RT}\right)$.

Experimental data (Lopes et al. 2009) are fitted using Origin 8.5 (OriginLab 2010). The isotherm parameters of dual-site Langmuir model are given in Table 1.

Cycle performances are evaluated according to the common parameters of H_2 purity, H_2 recovery and H_2 productivity defined as follows:

$$H_2\ Purity = \frac{\int_0^{t_{AD}} C_{H_2} u|_{z=L} dt}{\sum_i^{N_c} \int_0^{t_{AD}} C_i u|_{z=L} dt} \tag{19}$$

$$H_2\ Recovery = \frac{\int_0^{t_{AD}} C_{H_2} u|_{z=L} dt - \int_0^{t_{PR}} C_{H_2} u|_{z=L} dt}{\int_0^{t_{AD}} C_{H_2} u|_{z=0} dt} \tag{20}$$

$$H_2\ Productivity = \frac{\left(\int_0^{t_{AD}} C_{H_2} u|_{z=L} dt - \int_0^{t_{PR}} C_{H_2} u|_{z=L} dt\right) A_c}{t_{cycle} M_{ads}} \tag{21}$$

The aim is to design a H_2 PSA process having a capacity of 110 H_2 MMSCFD that is approximately equivalent to 1,609 H_2 mol/s. Given the H_2 mol fraction in the raw H_2 feed, the required flowrate of a raw H_2 feed flowing to the H_2 PSA would be around 2,015 mol/s assuming 90 % H_2 recovery. According to the design of the IGCC power plant with carbon capture using a Shell dry coal-fed gasifier (DOE Case 6, 2007), the advanced IGCC plant for cogeneration of power and ultrapure hydrogen would be configured such that around 40 % of the raw H_2 gas is directed to the H_2 PSA while the remaining 60 % flows to a syngas humidifier and subsequently a combustion chamber in the gas turbine just as in the conventional IGCC power plant.

Planning as a future work an experimental campaign to validate the simulation results subsequent to this study, the dimension of adsorption columns in this study was determined to be the same as those of a lab-scale six-column PSA rig as shown in Table 2. Given the column size and dimension, the feed flowrate is set at 0.002 mol/s with a scaling factor of 10^{-6}. The figures of other parameters used in the simulation are also presented in Table 2. In all the simulations, the set of the partial and ordinary differential equations and the algebraic equations were solved using the in-house CySim simulator. The discretization method for the spatial domain in the column was central finite difference method (CFDM) with 20 grid points along the column. The system of differential algebraic equations was solved with the DAE solver SUNDIALS (Friedrich et al. 2013).

4 Simulation results

Five different H_2 PSA systems have been investigated to see the change of H_2 recovery and productivity with different levels of complexity of the step configuration that is subject to the number of columns. The H_2 recovery and productivity obtained at different configurations are compared under the operating condition to meet the specification of the H_2 purity (99.99 mol%) at each configuration. First of all, a four-column H_2 PSA system was simulated and the targeted H_2 purity was obtained at a cycle time of 800 s. Since all the simulations were carried out at constant feed flowrate of 0.002 mol/s, the total cycle time became longer as more columns that are identical in size and dimension were added to configure six-, nine- and twelve-column H_2 PSA systems. This is because either more than one column can share the total feed gas for adsorption at

Table 2 List of column parameters, particle parameters, and operating conditions of H_2 PSA simulations

Column parameters	
Column length, L_c [m]	0.5
Column internal diameter, D_c [m]	0.025
External bed void fraction, ε [-]	0.391
Axial mass dispersion coefficient, D^L [m^2/s]	1.165×10^{-4}
Axial thermal dispersion coefficient, λ^L [W/m K]	1.279
Wall heat transfer coefficient, h_w [W/m^2 K]	95
Adsorbent parameters	
Pellet density, ρ_p [kg/m^3]	1,126
Pellet void fraction, ε_p [-]	0.503
Adsorbent specific heat capacity, $c_{P,s}$ [J/kg K]	920
Pellet averaged diameter, d_p [mm]	1.70
Macropore LDF coefficient, $k_i^p \times A_p/V_p$ $H_2/CO_2/CO/N_2/Ar$ [s^{-1}]	9.222/6.073/7.518/7.897/7.284
Micropore LDF coefficient, $k_i^{cr} \times 3/r_c$ $H_2/CO_2/CO/N_2/Ar$ [s^{-1}]	0.7467/0.0017/0.0332/0.1697/0.1800 (Lopes et al. 2009)
Operating conditions	
P_{ads} [bar]	34
P_{des} [bar]	1
T_{feed} [K]	303
Q_{feed} [mol/s]	0.002
Feed composition, $y_{H2}/y_{CO2}/y_{CO}/y_{N2}/y_{Ar}$ [molar]	0.8875/0.0212/0.0266/0.0544/0.0103

the same time or more steps need to be included in one cycle. To evaluate whether or not a simulation reaches its cyclic steady state (CSS), the H_2 purity and recovery at a cycle were compared with those at the previous cycle. It was assumed that a cyclic steady state would be reached if the differences of the H_2 purity and recovery between the new and previous cycles were both less than 10^{-6}.

4.1 Four-column H_2 PSA

A four-column H_2 PSA unit is designed such that a providing purge step is located between the two depressuring pressure equalisation (DPE) steps while the two pressurising pressure equalisation (PPE) steps take place in a row after the purge step as shown in Fig. 3. The step configuration was reconstructed referring to those in the literature (Cassidy 1980).

In the four-column H_2 PSA simulation, the total cycle time was fixed at 800 s with the adsorption step time equivalent to 1/4th of the cycle time as shown in Fig. 3. The purge flow is generated by reducing the column pressure starting from a pressure at the end of the first DPE step to a pressure that can be chosen at an operator's disposal. The equilibrated pressure at the start (or end) of the second DPE step (or its associated PPE step) is subject to how much purge flow is generated during the providing purge step. Accordingly, the equilibrated pressure at the end (or start) of the first DPE step (or its associated PPE step) is also affected by the amount of purge flow. The step configuration where the providing purge step is located between the two DPE steps has a clear advantage over a cycle where the providing purge step follows the two DPE steps in that it can increase the purge flowrate to a greater extent since the providing purge step can start at a higher pressure. Therefore, this configuration is capable of controlling the product purity in a wider range without having to change the cycle time. It should be noted that the pressure recovery during the pressure equalisation in this four-column H_2 PSA would decrease with an increasing purge flowrate since the equilibrated pressure at the end of each pressure equalisation stage is affected by the amount of purge flow as shown in Fig. 4. By contrast the pressure recovery can be maintained at a constant level regardless of the change of purge flowrate in the configuration where the providing purge step is located after finishing all the DPE steps.

As shown in Fig. 4, the pressure profile of a column over a cycle is varied in response to the use of the different amounts of the purge flow investigated in this study. The actual flowrate of the purge gas flowing between two columns under the providing purge and purge steps respectively must decrease with the step time since the driving

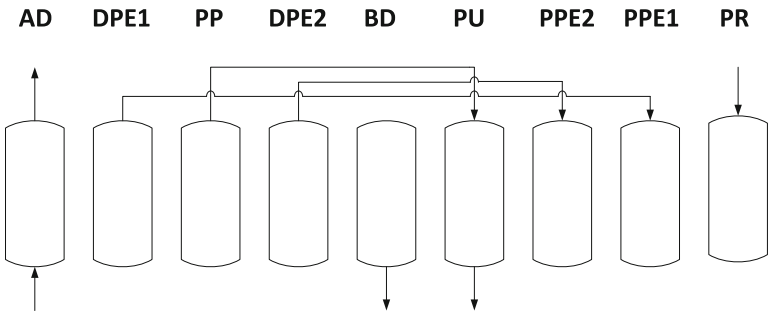

AD				DPE1	PP		DPE2	BD		PU		PPE2	PPE1	PR					
BD		PU		PPE2	PPE1		PR			AD				DPE1		PP		DPE2	
DPE1		PP		DPE2	BD		PU		PPE2	PPE1		PR			AD				
PPE1		PR			AD					DPE1		PP		DPE2	BD		PU		PPE2

Fig. 3 Step configuration of a four-column PSA cycle (*AD* adsorption, *DPE* depressurising pressure equalisation, *PP* providing purge, *BD* blowdown, *PU* purge, *PPE* pressurising pressure equalisation, *PR* product pressurisation, $t_{AD} = t_{cycle}/4$; $t_{PR} = 3t_{cycle}/16$; $t_{PP} = t_{PU} = t_{cycle}/8$; $t_{BD} = t_{DPE} = t_{PPE} = t_{cycle}/16$)

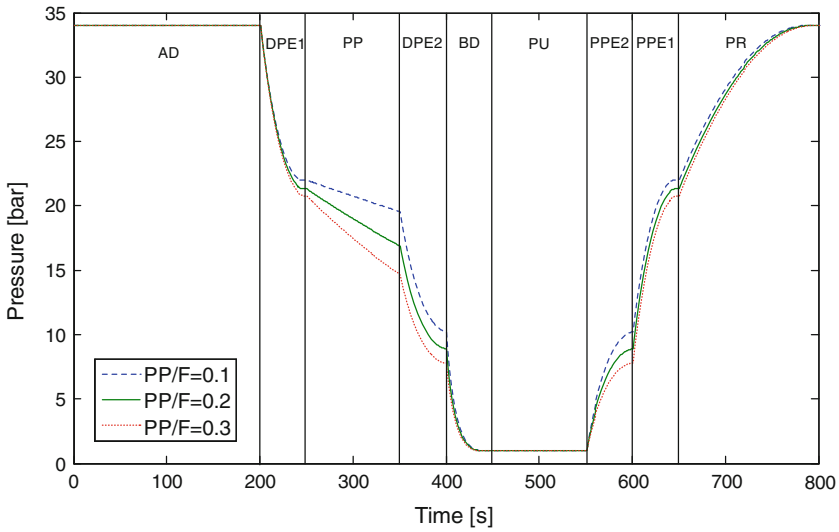

Fig. 4 Pressure profiles at the product end of a column over a cycle at the cyclic steady state of the four-column H_2 PSA unit: effect of the different amounts of purge flow

force diminishes with decreasing pressure difference between the columns. Therefore, an index of PP/F to quantify the varying purge flow as an average purge flow is introduced in this study. The PP/F denotes the ratio of an average purge flowrate being generated from one column during the providing purge step to a feed flowrate to one column for adsorption during one cycle. Note that the amount of the feed flowing to one column is not the same as the total amount of the feed flowing to a PSA system in case that more than one column share total feed flow. The different numbers of PP/F chosen at the three runs are shown in Fig. 4 and Table 3. As expected, the start and end pressures during the providing purge step becomes lower with an increase of the PP/F.

The targeted H_2 purity of 99.99+ mol% is achieved in Run 2 where during the providing purge step the column pressure changes from 21.5 to 17 bar that is equivalent to a PP/F of 0.2. At this operating condition, the H_2 recovery and productivity are 72.68 % and 162.67 mol_{H2}/kg/day, respectively.

Table 3 Performances of the four-column PSA system at different purge flow rates

Run	Adsorption time (s)	H_2 purity (%)	H_2 recovery (%)	H_2 productivity (mol_{H_2}/kg_{ads}/day)
Run 1 (PP/F = 0.1)	200	99.976	75.09	168.06
Run 2 (PP/F = 0.2)	200	99.995	72.68	162.67
Run 3 (PP/F = 0.3)	200	99.999	70.56	157.93

4.2 Six-column H_2 PSA

In the case of six-column H_2 PSA systems, two different step configurations were investigated. The first configuration (Fig. 5) features feeding the raw H_2 to two columns at the same time, that is to say, each of two columns receiving half the raw H_2 feed (Malek and Farooq 1997). Due to two columns being used for adsorption in a cycle, the first configuration cannot accommodate an additional pressure equalisation step but has the two-stage pressure equalisation that is the same as the above-mentioned four-column PSA system. Contrary to the four-column PSA system, a providing purge step is placed after the two pressure equalisation steps as shown in Fig. 5. It is anticipated that the alteration to the step configuration would be capable of improving the H_2 recovery since more pressure can be recovered during the pressure equalisation steps, that is to say, less consumption of pure hydrogen for product pressurisation and the reduced feed flowrate to one column for adsorption enables more efficient use of column due to less ingress of impurities into the product end.

In the second configuration (Fig. 6), however, only one column is taken up for high pressure adsorption in a cycle

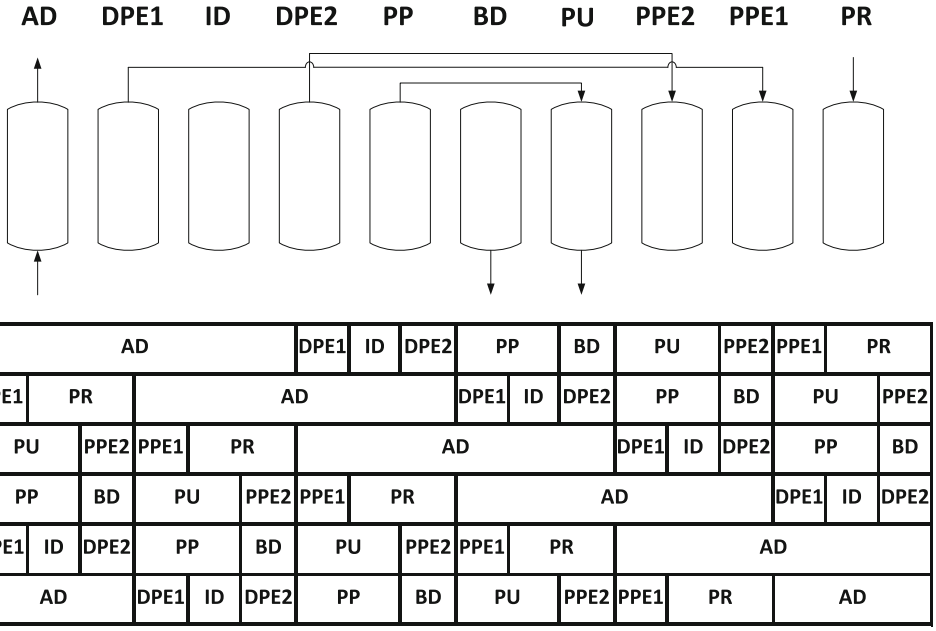

Fig. 5 Step configurations of a six-column PSA cycle with two-stage pressure equalisation (*AD* adsorption, *DPE* depressurising pressure equalisation, *ID* idle, *PP* providing purge, *BD* blowdown, *PU* purge, *PPE* pressurising pressure equalisation, *PR* pressurisation, $t_{AD} = t_{cycle}/3$; $t_{PP} = t_{PU} = t_{PR} = t_{cycle}/9$; $t_{BD} = t_{DPE} = t_{PPE} = t_{ID} = t_{cycle}/18$)

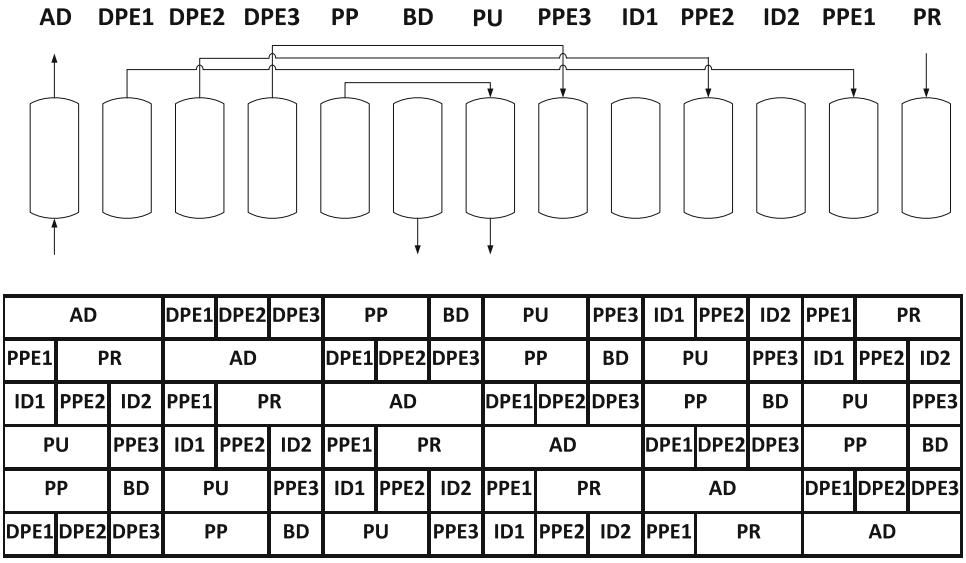

Fig. 6 Step configurations of a six-column PSA cycle with three-stage pressure equalisations (*AD* adsorption, *DPE* depressurising pressure equalisation, *PP* providing purge, *BD* blowdown, *PU* purge, *ID*: idle, *PPE* pressurising pressure equalisation, *PR* pressurisation, $t_{AD} = t_{cycle}/6$; $t_{PP} = t_{PU} = t_{PR} = t_{cycle}/9$; $t_{BD} = t_{DPE} = t_{PPE} = t_{ID} = t_{cycle}/18$)

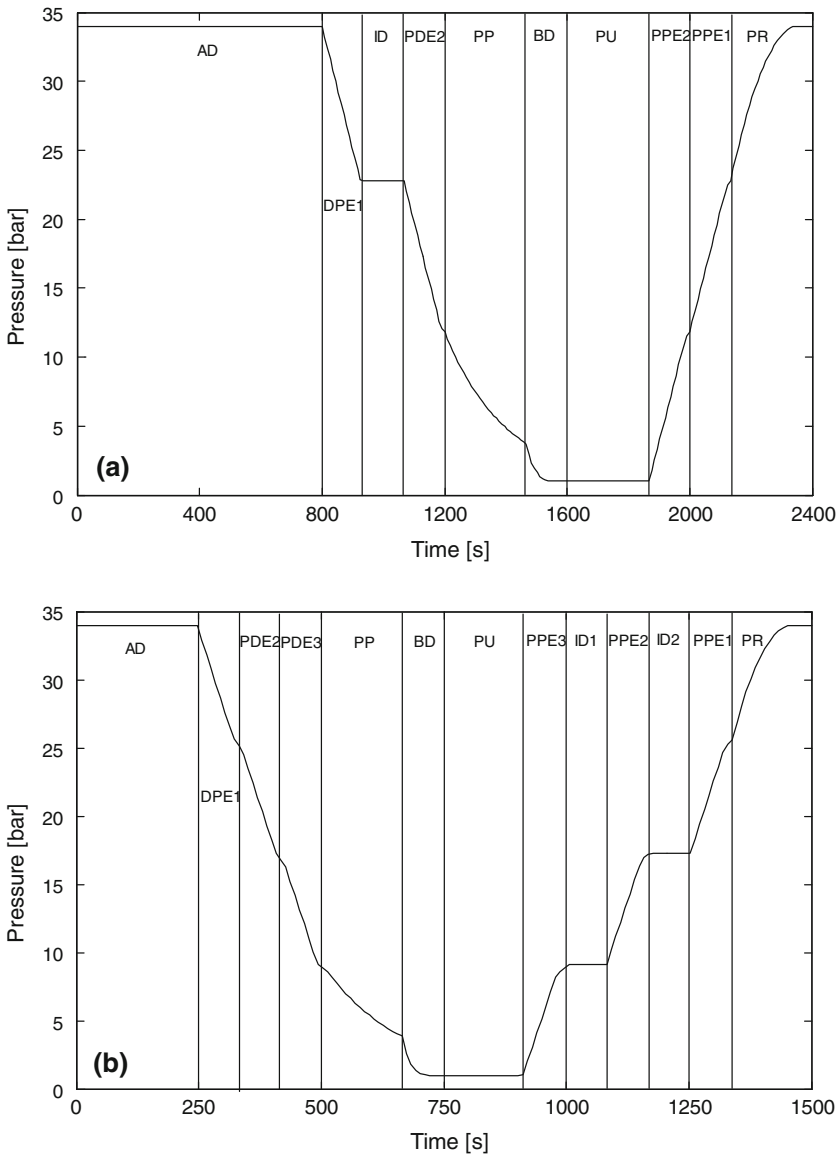

Fig. 7 Pressure profiles at the product end of a column over a cycle at the cyclic steady state of six-column H_2 PSA simulations at PP/F = 0.3 with **a** two-stage pressure equalisation (Run 6) and **b** three-stage pressure equalisation (Run 10)

just as in the four-column H_2 PSA. Therefore, it is possible to configure a PSA cycle with three-stage pressure equalisation (Xu 2002). It is generally expected that the more pressure equalisation stages a PSA cycle contains the higher hydrogen recovery can be obtained. This is because less hydrogen product is required during the product pressurisation step since the column can be pressurised to a higher pressure in advance during the PPE steps.

Figure 7 clearly exhibits the change of the pressure profile caused by adding one more pressure equalisation step to a PSA cycle. The first configuration having only two pressure equalisation steps (Fig. 7a) recovers less pressure during the pressure equalisation steps and consumes more hydrogen product during the product pressurisation step than the second configuration with three-stage pressure equalisation (Fig. 7b) does.

As observed in Table 4, the first and second configurations can achieve the targeted H_2 purity (99.99+ mol%) at the cycle times of 2,400 and 1,500 s, respectively (Run 6 and 10). The adsorption time in Run 6 (800 s) is more than three times longer than that in Run 10 (250 s) even though the feed gas entering one column for adsorption is just halved in flowrate. This can be explained by two reasons. Firstly, the reduced feed flow to one adsorption column for adsorption prevents the ingress of impurities into the product end so it can allow a cycle to have a longer adsorption time. Secondly, the first configuration with only two-stage pressure equalisation has a better working capacity than the second configuration. This is because the column can be more thoroughly regenerated by a stream having more hydrogen and pressurised by more ultrapure hydrogen during the product pressurisation step, in other

Table 4 Performance of six-column H_2 PSA simulations

Run	Adsorption time (s)	H_2 purity (%)	H_2 recovery (%)	H_2 productivity ($mol_{H2}/kg_{ads}/day$)
First configuration (two-stage pressure equalisation)				
Run 4	600	99.999	78.75	117.51
Run 5	700	99.996	81.98	122.33
Run 6	800	99.994	84.41	125.95
Run 7	900	99.975	86.29	128.75
Second configuration (three-stage pressure equalisation)				
Run 8	150	99.999	76.11	113.57
Run 9	200	99.997	82.47	123.05
Run 10	250	99.994	86.26	128.71
Run 11	300	99.969	88.79	132.48

words, the column is pressurised by gas streams coming from other columns during the pressure equalisation steps to a lesser extent. Therefore, it implies that the H_2 recovery would increase with more stages of pressure equalisation in a cycle but the working capacity of columns would deteriorate due to purging and pressurising the column with more impure gases.

It is noteworthy that the hydrogen recovery is enhanced around 12 % with the addition of two columns from four columns (Run 2) to six columns (Runs 6) only by changing the step configuration in spite of both having the same number of pressure equalisation steps. This change is not caused only by less hydrogen consumption during the product pressurisation step but also by the longer adsorption time.

At the operating condition of Run 10, the H_2 recovery increases further up to 86.26 % mainly due to enhanced pressure recovery taking place over the three-stage pressure equalisation. The stream leaving the column in the course of reducing the column pressure from 34 to 9 bar can be reused for pressurising other columns and significantly lower amount of hydrogen product is required for product pressurisation.

The H_2 productivities of both six-column H_2 PSA configurations are similar but lowered in comparison to that of the four-column H_2 PSA performance at the targeted H_2 purity. The change of the H_2 productivity can be explained with respect to the increasing number of columns (or increasing total amount of adsorbents being utilised) and the increasing H_2 recovery. The reduction of the H_2 productivity from four-column to six-column H_2 PSA is due to the increase of the H_2 recovery being less than the corresponding increase of the amount of adsorbent utilised.

4.3 Polybed H_2 PSA (nine and twelve columns)

As mentioned above, as more columns are deployed a higher hydrogen recovery would be anticipated in a H_2 PSA system. In this respect Polybed H_2 PSA processes containing seven to sixteen beds with at least three pressure equalisation steps and at least two columns receiving the feed gas for adsorption have been commercially operating for the purpose of H_2 purification (Yang 1987). In this study a nine-column eleven-step system is investigated following the step configuration found in the literature (Fuderer and Rudelstorfer 1976) as shown in Fig. 8. Figure 9 shows the pressure profile of the nine-column PSA system over a cycle at its cyclic steady state.

The nine-column eleven-step H_2 PSA system benefits from both reduced feed flowrate to one column and intensified pressure equalisation that each of the two six-column H_2 PSA systems has. The feed flowrate fed to one column for adsorption is reduced to one-third of the total feed flowrate since three out of nine columns always work for adsorption at the same time. The product pressurisation step starts at 26 bar and the providing purge step commences at 9 bar both of which are similar to those at the second configuration of six-column H_2 PSA system as shown in Figs. 7b and 9. This is because both PSA systems contain the same number of stages of pressure equalisation in their cycle.

Finally, a twelve-column thirteen-step H_2 PSA system was investigated in order to increase the H_2 recovery close to its maximum. The step configuration is presented in Fig. 10 that was originally shown in a patent (Xu et al. 2003). The step configuration features simultaneous adsorption at three columns, simultaneous providing purge and purge at two columns, and four-stage pressure equalisation. Thanks to one additional pressure equalisation step, the product pressurisation step starts at 27 bar and the providing purge step commences at 7.5 bar as shown in Fig. 11.

Table 5 lists the performance of the nine- and twelve-column H_2 PSA systems at their cyclic steady state. The nine-column H_2 PSA system can achieve the targeted H_2 purity at the adsorption step time of 1,200 s (Run 14). It should be noted that the adsorption step time of the twelve-column H_2 PSA to achieve the targeted H_2 purity (1,050 s at Run 18) is shorter than that of the nine-column H_2 PSA in spite of the same feed flowrate fed to one column, i.e. one-third of the total feed flowrate. This indicates that the column working capacity starts to deteriorate due to more incomplete regeneration by a purge flow having less hydrogen and by pressurising the column with more impure streams coming from other columns during the PPE steps instead of ultrapure hydrogen during the product pressurisation step. Nevertheless, the H_2 recovery still increases from 91.85 % at the nine-column H_2 PSA to 92.74 % at the twelve-column H_2 PSA. Since the improvement of the H_2 recovery is minimal, the H_2 productivity decreases significantly from 91.41 $mol_{H2}/kg_{ads}/day$ at the nine-column H_2

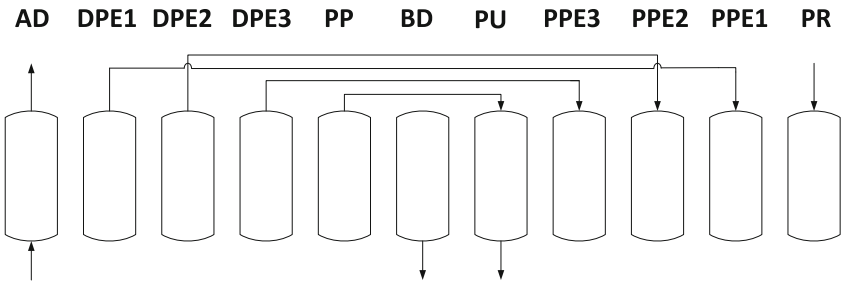

AD								DPE1	DPE2	DPE3	PP			BD	PU			PPE3	PPE2	PPE1	PR		
PPE1	PR	AD						DPE1	DPE2	DPE3	PP			BD	PU			PPE3	PPE2				
PPE3	PPE2	PPE1	PR	AD				DPE1	DPE2	DPE3	PP			BD	PU								
PU		PPE3	PPE2	PPE1	PR	AD				DPE1	DPE2	DPE3	PP			BD							
PP	BD	PU		PPE3	PPE2	PPE1	PR	AD						DPE1	DPE2	DPE3	PP						
DPE3	PP		BD	PU		PPE3	PPE2	PPE1	PR	AD								DPE1	DPE2				
DPE1	DPE2	DPE3	PP		BD	PU		PPE3	PPE2	PPE1	PR	AD											
AD		DPE1	DPE2	DPE3	PP		BD	PU		PPE3	PPE2	PPE1	PR	AD									
AD				DPE1	DPE2	DPE3	PP		BD	PU		PPE3	PPE2	PPE1	PR	AD							

Fig. 8 Step configurations of a nine-column PSA cycle (*AD* adsorption, *DPE* depressurising pressure equalisation, *PP* providing purge, *BD* blowdown, *PU* purge, *PPE* pressurising pressure equalisation, *PR* pressurisation, $t_{AD} = t_{cycle}/3$; $t_{PP} = t_{PU} = t_{cycle}/9$; $t_{BD} = t_{DPE} = t_{PPE} = t_{PR} = t_{cycle}/18$)

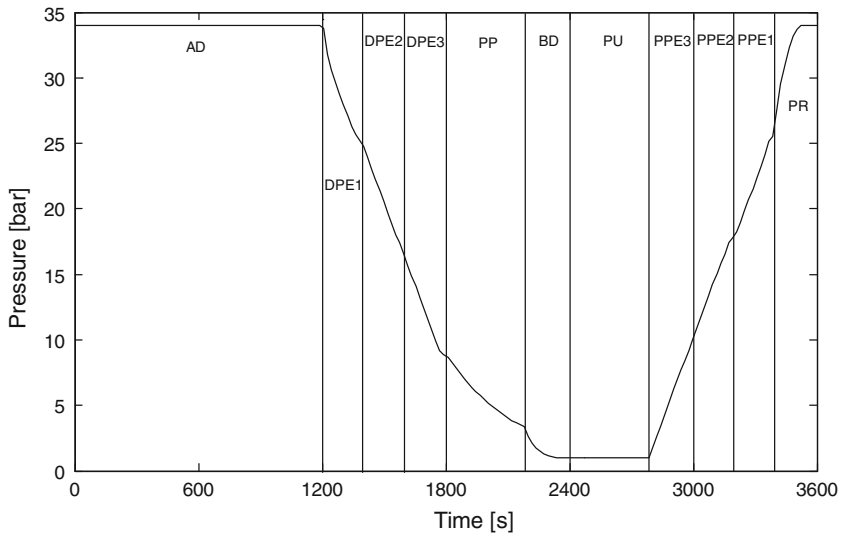

Fig. 9 Pressure profiles at the product end of a column over a cycle at the cyclic steady state of a nine-column H_2 PSA at PP/F = 0.3

PSA to 69.15 mol_{H2}/kg_{ads}/day at the twelve-column H_2 PSA.

4.4 Comparison among various PSA cycles

Up to now the H_2 recovery and productivity are compared at the targeted H_2 purity of around 99.99+ mol% among various H_2 PSA cycles having different number of columns and different step configurations. Again the H_2 productivity is reduced with the increasing number of columns while the H_2 recovery improves. All the simulation results are plotted on Fig. 12 indicating a clear trade-off between hydrogen purity and recovery.

It is expected that more-than-twelve-column H_2 PSA configuration may improve the H_2 recovery further to more than 93 % but given the trend of improving H_2 recovery with the number of columns a further improvement of H_2 recovery would be very limited. In particular, more than

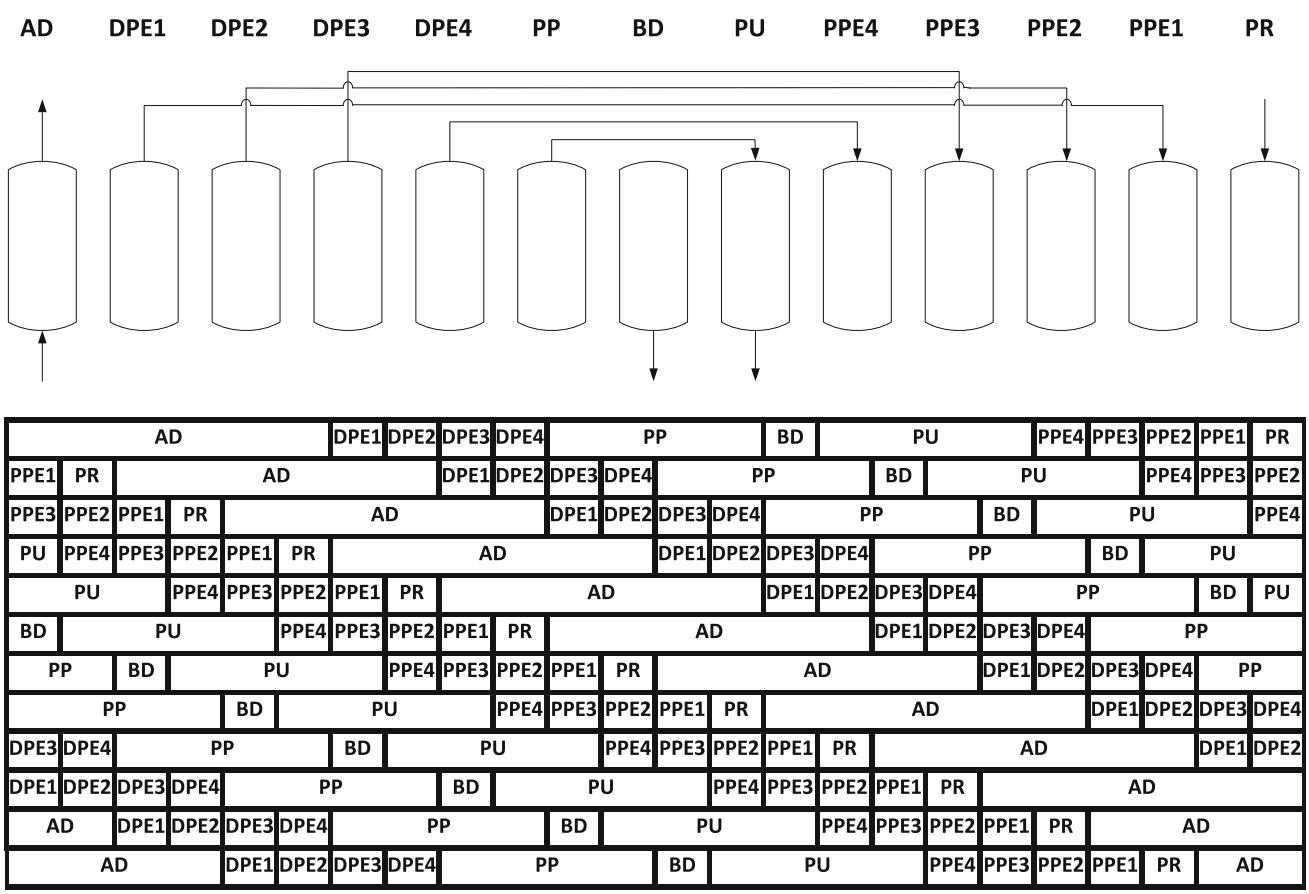

Fig. 10 Step configurations of a twelve-column PSA cycle (*AD* adsorption, *DPE* depressurising pressure equalisation, *PP* providing purge, *BD* blowdown, *PU* purge, *PPE* pressurising pressure equalisation, *PR* pressurisation, $t_{AD} = t_{cycle}/4$; $t_{PP} = t_{PU} = t_{cycle}/6$; $t_{BD} = t_{DPE} = t_{PPE} = t_{PR} = t_{cycle}/24$)

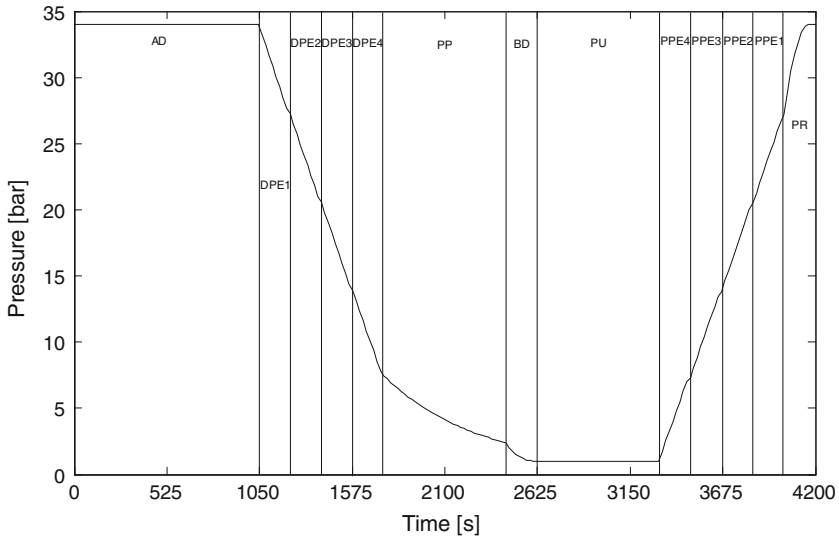

Fig. 11 Pressure profiles at the product end of a column over a cycle at the cyclic steady state of a twelve-column H_2 PSA at PP/F = 0.3

five stage pressure equalisation steps may not be necessary since the column pressure at the end of the fourth DPE (or PPE) step in the twelve-column H_2 PSA is very close to that at the end of the third DPE (or PPE) step in the nine-column H_2 PSA systems. Therefore, altering a PSA cycle to have more than five pressure equalisation steps cannot

Table 5 Performance of nine-column and twelve-column PSA simulations

Run	Adsorption time (s)	H_2 purity (%)	H_2 recovery (%)	H_2 productivity (mol_{H_2}/kg_{ads}/day)
Nine-column H_2 PSA				
Run 12	800	99.998	87.05	86.64
Run 13	1,000	99.996	89.94	89.51
Run 14	1,200	99.993	91.85	91.41
Run 15	1,300	99.974	92.58	92.14
Twelve-column H_2 PSA				
Run 16	750	99.999	89.11	66.52
Run 17	900	99.996	91.17	68.06
Run 18	1,050	99.993	92.74	69.15
Run 19	1,200	99.978	93.83	70.04

recover a notable pressure nor save the amount of ultrapure hydrogen consumed during the product pressurisation step significantly. In addition, it is likely that the working capacity of the column would be badly affected by incomplete regeneration with purge flow having less hydrogen and pressurisation of the column by more impure gas streams than the pure product streams.

Figure 13 shows the hydrogen mole fraction profile along the column at the end of the adsorption step at the cyclic steady state of all the PSA simulation investigated in this study. It clearly shows that with the reduction of the feed flow to one-column for adsorption from four-column to nine-column through six-column with two-stage pressure equalisation the PSA system allows a cycle to have longer adsorption step time so the H_2 mass transfer zone (MTZ) can progress more to the product end at the end of adsorption step. This results in less H_2 remaining at the end of the adsorption step leading to a higher H_2 recovery. The figure also shows that the twelve-column PSA has a broader H_2 MTZ than the nine-column PSA does due to worse regeneration of the column during the purge step and pressurisation with more impure stream while the column is pressurised.

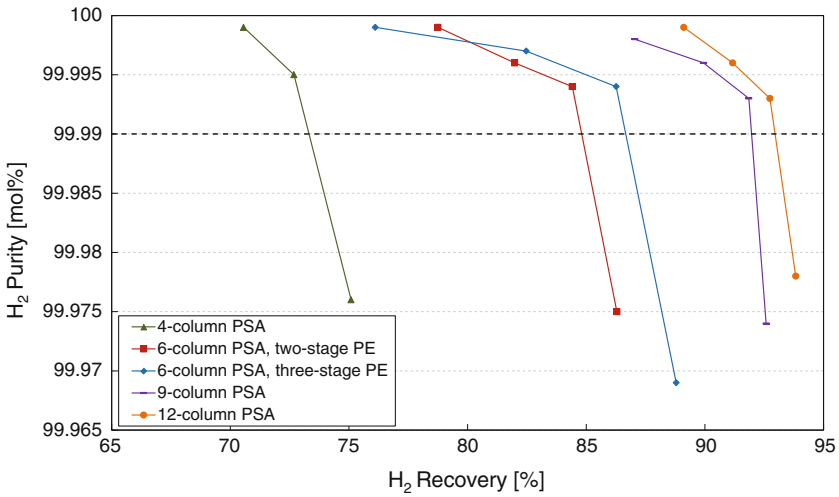

Fig. 12 Comparison of hydrogen purity and recovery at various H_2 PSA systems with the different number of columns and different step configurations

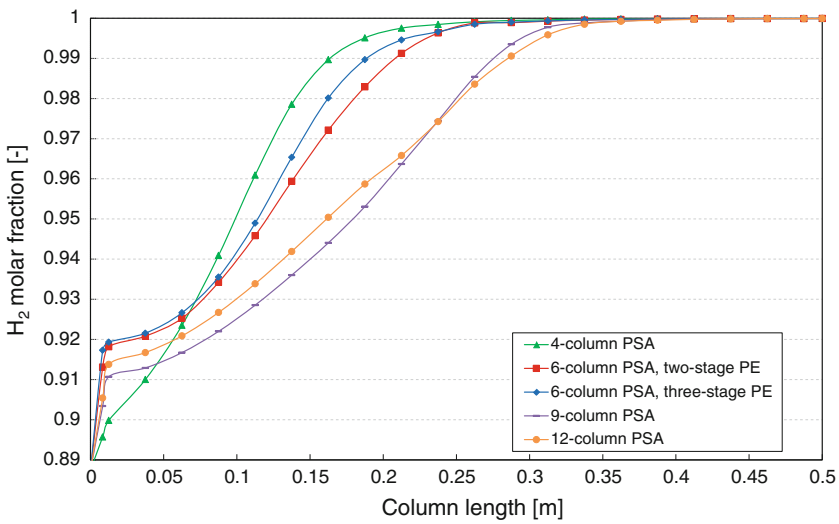

Fig. 13 Hydrogen molar fraction profiles along the column at the end of the adsorption step in various PSA cycles at around 99.99 % H_2 purity

5 Conclusions

A novel H_2 PSA system to produce ultrapure hydrogen from a raw H_2 gas generated in an advanced IGCC process has been proposed in this study. The advanced IGCC plant where CO_2 is intrinsically captured by a pre-combustion capture unit is capable of cogenerating both power and ultrapure hydrogen more economically. The advanced IGCC plant can be used in oil refineries having difficulty in sourcing ultrapure hydrogen that is required to operate hydrotreaters and hydrocrackers and intending to reduce carbon emission from their hydrogen and power plants.

To know the maximum H_2 recovery that a H_2 PSA can produce from the raw H_2 gas is very important in evaluating the performance of the advanced IGCC plant for cogenerating power and ultrapure hydrogen. This is because the flowrate of PSA tail gas, to be determined by the H_2 recovery, should be compressed up to 34 bar from the purge pressure to get the PSA tail gas fed to the gas turbine along with the fuel gas. Therefore, it is essential to design a H_2 PSA such that its H_2 recovery can be maximised in order to minimise the power consumption relating to tail gas compression.

H_2 PSA in commercial SMR hydrogen plants is capable of achieving around 89 % H_2 recovery at the 99.99+ % H_2 purity. Compared to the raw H_2 gas in the SMR hydrogen plant, the raw H_2 gas fed to the H_2 PSA in the advanced IGCC plant has a gas composition of higher hydrogen and lower impurities and the higher total pressure at which conditions the H_2 PSA is expected to perform better than the H_2 PSA in a SMR H_2 plant. As expected, the Polybed H_2 PSA having twelve columns achieves 93 % H_2 recovery at 99.99+ mol% H_2 purity.

Acknowledgments We would like to express our gratitude for the financial support from KETEP (Grant No.: 2011-8510020030) and EPSRC (Grant Nos.: EP/F034520/1, EP/G062129/1, and EP/J018198/1).

References

Ahn, H., Yang, J., Lee, C.-H.: Effects of feed composition of coke oven gas on a layered bed H_2 PSA process. Adsorption **7**, 339–356 (2001)

Ahn, S., You, Y.-W., Lee, D.-G., Kim, K.-H., Oh, M., Lee, C.-H.: Layered two- and four-bed PSA processes for H_2 recovery from coal gas. Chem. Eng. Sci. **68**, 413–423 (2012)

Cassidy, R.T.: Polybed pressure-swing adsorption hydrogen processing. ACS Symposium Series, vol. 135, Chapter 13, pp. 247–259 (1980)

Committee on climate change, reducing emissions from buildings and industry through the 2020s, Chapter 5 (2011)

DECC, Final emissions estimates by fuel type and end-user sector (2009)

DOE NETL, Cost and performance baseline for fossil energy plants (2007)

Ergun, S.: Fluid flow through packed columns. Chem. Eng. Prog. **48**, 89–94 (1952)

Friedrich, D., Ferrari, M.-C., Brandani, S.: Efficient simulation and acceleration of convergence for a dual piston pressure swing adsorption system. Ind. Eng. Chem. Res. **52**, 8897–8905 (2013)

Fuderer, A., Rudelstorfer, E.: US Patent 3986849 to Union Carbide Corporation (1976)

Kapetaki, Z., Ahn, H., Brandani, S.: Detailed process simulation of pre-combustion IGCC plants using coal-slurry and dry coal gasifiers. Energy Procedia **37**, 2196–2203 (2013)

Lopes, F.V.S., Grande, C.A., Ribeiro, A.M., Loureiro, J.M., Evaggelos, O., Nikolakis, V., Rodrigues, A.E.: Adsorption of H_2, CO_2, CH_4, CO, N_2 and H_2O in activated carbon and zeolite for hydrogen production. Sep. Sci. Technol. **44**, 1045–1073 (2009)

Lopes, F.V.S., Grande, C.A., Rodrigues, A.E.: Activated carbon for hydrogen purification by pressure swing adsorption: multicomponent breackthrough curves and PSA performance. Chem. Eng. Sci. **66**, 303–317 (2011)

Malek, A., Farooq, S.: Study of a six-bed pressure swing adsorption process. AIChE J. **43**, 2509–2523 (1997)

OriginLab: Data analysis and graphing software. Origin **8**, 5 (2010)

Park, J.-H., Kim, J.-D., Yang, R.T.: Adsorber dynamics and optimal design of layered beds for multicomponent gas adsorption. Chem. Eng. Sci. **53**, 3951–3963 (1998)

Ribeiro, A.M., Grande, C.A., Lopes, F.V.S., Loureiro, J.M., Rodrigues, A.E.: A parametric study of layered bed PSA for hydrogen purification. Chem. Eng. Sci. **63**, 5258–5273 (2008)

Ribeiro, A.M., Grande, C.A., Lopes, F.V.S., Loureiro, J.M., Rodrigues, A.E.: Four beds pressure swing adsorption for hydrogen purification: case of humid feed and activated carbon beds. AIChE J. **55**, 2292–2302 (2009)

SEPA's National Air Quality Report (2008)

Wakao, N., Funazkri, T.: Effect of fluid dispersion coefficients on particle-to-fluid mass transfer coefficients in packed beds. Chem. Eng. Sci. **33**, 1375–1384 (1978)

Xu, J., Weist, E.L.: US Patent 6454838 B1 to Air Products and Chemicals Inc (2002)

Xu, J., Rarig, D.L., Cook, T.A., Hsu, K.K., Schoonover, M., Agrawal, R.: US Patent 6565628 B2 to Air Products and Chemicals Inc (2003)

Yang, R.T.: Gas separation by adsorption processes. Butterworth Publishers (1987)

Yang, J., Lee, C.-H.: Adsorption dynamics of a layered bed PSA for H_2 recovery from coke oven gas. AIChE J. **44**, 1325–1334 (1998)

Appendix 3: A novel strategy to produce ultrapure hydrogen from coal with pre-combustion carbon capture *by Luberti et al., 2014*

Available online at www.sciencedirect.com

ScienceDirect

Energy Procedia 63 (2014) 2023 – 2030

Energy Procedia

GHGT-12

A novel strategy to produce ultrapure hydrogen from coal with pre-combustion carbon capture

Mauro Luberti, Daniel Friedrich, Dursun Can Ozcan, Stefano Brandani, Hyungwoong Ahn*

Scottish Carbon Capture and Storage Centre, School of Engineering, The University of Edinburgh, Edinburgh, EH9 3JL, UK

Abstract

Integrated Gasification Combined Cycles (IGCCs) are one of the emerging clean coal technologies which paves the way for producing power from coal with a higher net power efficiency than conventional PC-fired boiler power plants. It is also advantageous that in an IGCC power plant a carbon capture unit can be applied to a stream having a very high CO_2 partial pressure upstream of gas combustion that would not be available in case of a PC-fired boiler power plant, leading to less energy penalty involved in the carbon capture. In this study it is aimed to design a cogeneration process where a Hydrogen Pressure Swing Adsorption (H_2 PSA) unit is retrofitted to an IGCC power plant with pre-combustion capture for producing ultrapure hydrogen (99.99+ vol%). The ultrapure hydrogen is commonly utilised as feedstock for deep desulphurisation and hydrocracking units at refineries as well as H_2 fuel cells. It is found that, at the same H_2 purity of 99.99+%, the hydrogen recovery could be improved up to 93% with the increasing number of columns. Improving the H_2 recovery at the H_2 PSA to its maximum can contribute to reducing the power consumption for compressing the H_2 PSA tail gas by minimizing the yield of the H_2 PSA tail gas by-product. Furthermore, it is demonstrated that the H_2 PSA can also be designed to achieve 90% H_2 recovery even when a portion of the tail gas is recycled to the shift reactors in order to improve the overall advanced IGCC performance by increasing the H_2 yield and by reducing the auxiliary power consumption at carbon capture unit.

Peer-review under responsibility of the Organizing Committee of GHGT-12

Keywords: IGCC; Ultrapure hydrogen; Cogeneration; Pressure swing adsorption; Process simulation

* Corresponding author. Tel.: +44-131-650-5891; fax: +44-131-650-6551.
E-mail address: H.Ahn@ed.ac.uk

Peer-review under responsibility of the Organizing Committee of GHGT-12
doi:10.1016/j.egypro.2014.11.217

1. Introduction

Strong dependency on crude oil and natural gas and their associated soaring price and supply chain risk increase the need for efficient utilization of fossil fuel energy sources of being exhausted. The rising concentration in the atmosphere of various pollutants known as greenhouse gases (GHG) is identified as one of the key factors contributing to global warming effect. However, it is agreed that the fossil fuels will retain a major position in supplying heat and power in the near future before alternative technologies using renewable sources become mature enough to be substituted for conventional fossil fuels. In this respect, CCSU (Carbon Capture, Storage, and Utilisation) research has been stimulated as a pre-emptive way of sustaining fossil-fuel based economic growth without devastating the environment. Among various industrial CO_2 emitters, it is anticipated that the first commercial CCSU plant will be deployed to one of the fossil fuels fed power plants that currently account for approximately 30% of the global anthropogenic CO_2 emission [1].

The UK has set in its 2008 Climate Change Act a target to reduce its GHG emission up to 80% of 1990 levels in 2050, which will lead to allowed emissions of 150 $MtCO_2e$ per year. This target can be met only if all the industries including refining and petrochemical plants, cement plants, iron and steel manufacture as well as power stations are decarbonised. As regards refining and petrochemical industries, the Committee on Climate Change (CCC) estimated that the abatement of CO_2 emission would be possible partly by improving the energy efficiency of refining and petrochemical industries [2]. In addition it also proposed further reduction in CO_2 emission would be available by deploying carbon capture units on H_2 plants and replacing combustion fuels with carbon-neutral biomass. In particular, most of refining complexes need to increase their hydrogen production capacities to cope with the increased H_2 demand for their hydrotreating desulphurisation process that removes mainly sulphur and other impurities and hydrocracking units, which is to upgrade low-grade heavy residues to more valuable diesel and lube base oil. Given imminent carbon emission regulation, however, it is doubtful that conventional Steam Methane Reforming (SMR) process would be still the best option to produce ultrapure hydrogen.

In this study, it is aimed to design an advanced Integrated Gasification Combined Cycle (IGCC) to produce power and ultrapure hydrogen simultaneously from the coal where CO_2 is captured inherently for producing the ultrapure H_2. It has been reported that coal is reserved most abundantly and is distributed most evenly over the globe among the fossil fuels [3]. IGCC plants can be potentially operated with other carbonaceous feedstock such as biomass, low quality petroleum residues and MSW.

Regardless of choice of a process producing synthetic gas, it is well-known that a pressure swing adsorption (PSA) is the only economically feasible, commercialised separation process to produce ultrapure hydrogen (99.99+ vol.%) from a synthetic gas. Various works have been published on hydrogen purification using H_2 PSA but they have been mainly based on feed gases originated from SMR reactors and COGs [4-9]. Therefore, it is required to redesign the H_2 PSA based on the condition of feed gas originated from coal gasifiers.

In this study, a H_2 PSA has been simulated using an in-house dynamic simulator while an exemplary IGCC plant is simulated using Honeywell UniSim Design R400. The in-house H_2 PSA simulator was successfully imported into Honeywell UniSim environment and integrated with the IGCC simulation that enables us to carry out various process configuration studies. The aim of this work is to design a cogeneration process capable to produce ultrapure hydrogen (100 H_2 MMSCFD) and power achieving 90% carbon capture.

2. Integrated gasification combined cycle (IGCC) with pre-combustion carbon capture simulation

Firstly a process simulation for a conventional IGCC power plant integrated with a pre-combustion carbon capture has been constructed using Honeywell UniSim R400 based on DOE report [10] in order to estimate the net power generation. Subsequently the IGCC power plant simulation is modified to an advanced IGCC plant to produce power and ultrapure hydrogen simultaneously (Figure 1). In the advanced IGCC plant, the H_2-rich fuel gas is split into two streams and one of two is fed to a H_2 PSA for producing ultrapure hydrogen. The split ratio is determined so as to generate the ultrapure hydrogen at the flowrate of 100 MMSCFD. The H_2 PSA tail gas needs to be compressed up to the pressure of the H_2 fuel gas for feeding it to a high pressure gas cycle. This strategy of utilising the H_2 PSA tail gas can augment the power generation at the combined cycle. Therefore, the net power generation from the advanced IGCC should take into account additional power consumption at the H_2 PSA tail gas compressors and power generation at the combined cycle relating to the H_2 PSA tail gas in addition to the H_2 fuel gas.

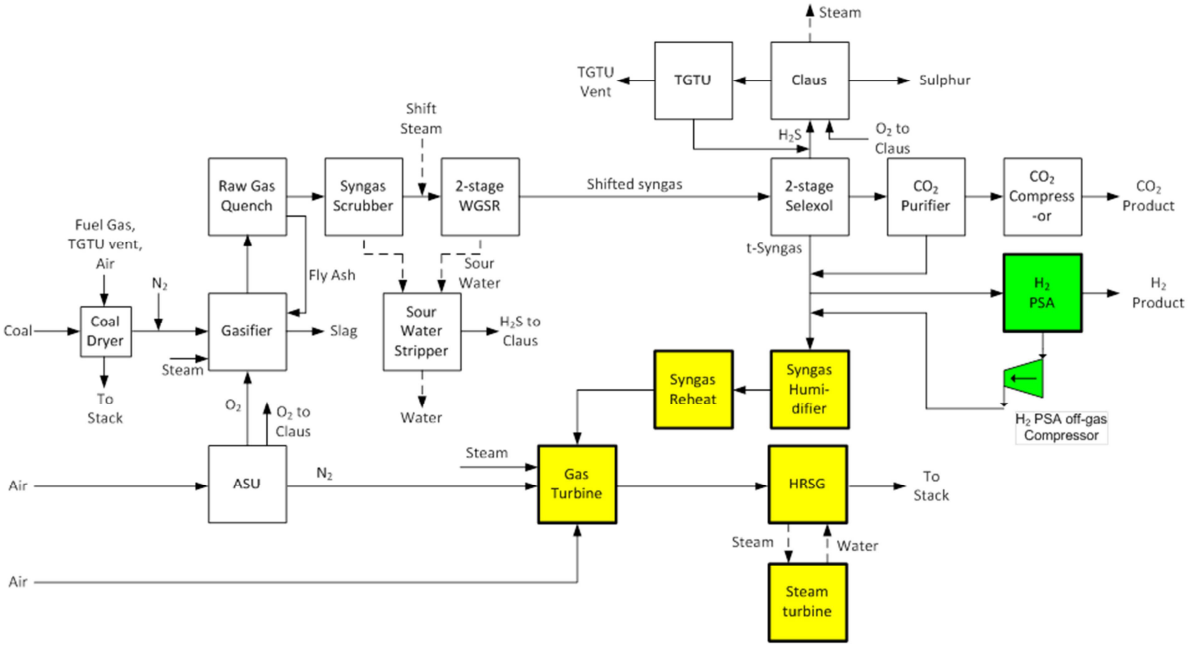

Fig. 1. Block flow diagram of an advanced IGCC plant to produce power and ultrapure hydrogen.

2.1. Gasifier and Syngas Cooler

The Shell gasifier, fed by the Illinois No.6 bituminous dry coal transported by nitrogen, 95% oxygen with nitrogen and argon balanced, and 400ºC steam, was simulated with conversion reactor where the conversion rate of each reaction was adjusted to match the mass balance as reported in the reference [11]. The Shell gasifier operates at 1,424ºC and 4.2 MPa producing some HP steam in the steam jacket with the carbon conversion rate set as 99.5%. An Elevated Pressure (EP) ASU produces 95% oxygen from air for its use in the gasifier and the Claus sulphur plant. The hot syngas from the gasifier is subsequently quenched by water to have the syngas contain steam. After the water quench, the syngas is cooled to generate the HP and IP steams in series and then flows to the syngas scrubber where water-soluble impurities are removed.

2.2. Water Gas Shift Reactors (WGSR)

Additional steam is added to this stream before being fed to the two shift reactors in series operating at the high

and low temperatures, respectively. Given the operating conditions of the two shift reactors (Gibbs reactor), the CO conversion rate was estimated to be 95.7% in total that is consistent with the reference study. It should be noted that the Shell gasifier generates a syngas having around 0.5 of H_2/CO ratio compared to around 1.0 in the GEE gasifier, so the Shell IGCC would require greater amount of CO to be converted to CO_2 in order to achieve 90% carbon capture. The higher load in shift reaction requires more steam consumption in shift reaction, obviously leading to higher energy penalty in the Shell IGCC when it is integrated with carbon capture unit [11].

2.3. Acid Gas Removal (AGR) Unit

The syngas stream from the shift reactors is fed to a dual-stage Selexol unit to recover CO_2 and H_2S separately from the syngas. This commercialised acid gas removal (AGR) process has two absorbers where the lean solvent from the steam stripper is fed to a CO_2 absorber and then part of the CO_2-laden solvent subsequently captures more reactive H_2S in a H_2S absorber. While the H_2S rich solvent is regenerated by the steam stripper, pure CO_2 comes off the CO_2-laden solvent by successive two flash drums at the different pressures. The treated syngas from the AGR unit becomes saturated with water in a fuel gas saturation column and then is fed to combustion chamber. But in case of advanced IGCC plant the treated syngas is split into two streams: one stream flows to the gas turbine and the other flows to a H_2 PSA. The treated syngas is composed of 88.75% H_2, 2.12% CO_2, 2.66% CO, 5.44% N_2, 1.03% Ar at 34 bar in this study. The initial simulations based on the values of the H_2S and CO_2 solubilities in Selexol included in the UniSim Design database led to inconsistent results. Gas-liquid equilibria have been improved modifying the Henry constants obtained by regressing experimental data found in literature [12,13].

2.4. Combined Cycle

Two identical advanced F class gas turbines, each having 232 MWe of net power generation, were taken into account where the combustion chamber is simulated with an adiabatic Gibbs reactor. The exhaust flue gas, exiting the gas turbine at 602ºC, enters the Heat Recovery Steam Generator (HRSG) to recover the large quantity of thermal energy that it contains. The steam cycle was designed with 12.4MPa/538ºC/538ºC of which the HP and IP temperatures are slightly lower than those in non-capture case due to the lowered heating value of syngas. The flue gas finally exits the HRSG at 132 ºC and is sent to the atmosphere.

3. Design of H_2 PSA at advanced IGCC

The hydrogen PSA unit produces ultrapure hydrogen (99.99+ vol%) at 34 bar while it discharges the tail gas at 1 bar. Since the H_2 PSA tail gas contains a considerable amount of hydrogen and CO, it should be utilised for power generation by feeding it to a combined cycle. To do this, the H_2 PSA tail gas needs to be recompressed before it being sent to a high pressure combustion chamber. Given the fact that the tail gas compression involves significant power consumption, it is essential to increase the hydrogen recovery at the H_2 PSA close to its maximum in order to minimise the required H_2 PSA feed flowrate and the tail gas compression work at the same time. Once the mass balance around the H_2 PSA is determined based on the required product flowrate and the maximum H_2 recovery achievable, it is possible to estimate net power generation taking into account the tail gas compression work.

In our previous work [14], an in-depth study on design of H_2 PSA integrated with an IGCC power plant was carried out to maximize H_2 recovery at the H_2 PSA unit. The study demonstrated that the H_2 recovery could be increased by increasing the complexity of the PSA step configuration that enables a PSA cycle to have a lower feed flow to one column for adsorption and to accommodate more pressure equalization steps. In the study, the column dimensions were kept constant in all the PSA configurations so the total cycle time increases considerably and the bed productivity decreases with increasing number of columns from four to twelve. This is because more than one column undergo simultaneously the adsorption step so the total flowrate is reduced to half or one third. In this work the PSA simulations were performed at constant total cycle time of 1200 s regardless of the various configurations. As a result, the bed productivity can be almost kept constant. Note that with the increasing number of columns, the volume of one column should be reduced at the constant total cycle time but the ratio of column length to diameter is kept constant at 20.

Table 1. Effect of the one-column residence time during adsorption step on hydrogen purity, recovery and productivity at different H_2 PSA configurations.

One-Column Residence time [m^3·s/mol]	Column length [m]*	Column diameter [m]*	H_2 purity [%]	H_2 recovery [%]	H_2 productivity [mol_{H2}/kg_{ads}/day]
Four-Column PSA with two-stage pressure equalisation					
0.100	0.467	0.0233	99.979	78.25	218.39
0.1225	0.500	0.0250	99.993	75.28	171.51
0.150	0.535	0.0267	99.996	71.85	133.69
0.175	0.563	0.0281	99.998	68.42	109.12
Six-Column PSA with two-stage pressure equalisation					
0.100	0.371	0.0185	99.976	86.38	321.44
0.1225	0.400	0.0200	99.993	83.43	253.44
0.150	0.424	0.0212	99.997	80.32	199.26
0.175	0.447	0.0223	99.999	75.93	161.46
Nine-Column PSA with three-stage pressure equalisation					
0.100	0.324	0.0162	99.971	92.79	345.12
0.1225	0.346	0.0173	99.992	91.48	277.78
0.150	0.371	0.0185	99.995	89.71	222.56
0.175	0.390	0.0195	99.998	86.96	184.39
Twelve-Column PSA with four-stage pressure equalisation					
0.100	0.324	0.0162	99.983	93.41	260.57
0.110	0.334	0.0167	99.992	92.94	235.92
0.1225	0.346	0.0173	99.994	92.52	210.71
0.150	0.371	0.0185	99.997	90.48	168.35

*Note that the column dimensions were estimated based on the feed flowrate scaled down with a factor of 10^{-6}.

It has been explored at which one-column residence time during the adsorption step ($\tau = V/F$) the H_2 PSA can achieve the target H_2 purity of 99.99+ vol%. Table 1 shows the effect of residence time on the performance of each H_2 PSA configuration with respect to hydrogen purity, recovery and productivity (see [14] for step configuration of each H_2 PSA configuration). It is expected that with increasing residence time the H_2 purity can be improved as a sacrifice of H_2 recovery and productivity. In the four-, six- and nine-column systems the targeted H_2 purity is obtained with a H_2 PSA run having a column size to give a residence time in the vicinity of 0.1225 m^3·s/mol. This is because as the feed flowrate to one column during adsorption step is reduced from total feed flowrate at the four-column PSA to the one third at the nine-column PSA through the one half at the six-column PSA, the required volume of one adsorption column is reduced almost at the same ratio. However, the residence time is notably reduced to 0.110 m^3·s/mol from nine-column PSA to twelve-column PSA since the feed flowrate to one column during adsorption step does not change but the adsorption step time decreases from the one third to the one fourth of cycle time, i.e. the total amount of feed to be treated by one column during adsorption step is reduced.

It is clearly demonstrated that given the targeted H_2 purity of 99.99+vol% the H_2 recovery increases from 75% to 93% with increasing number of columns as shown in Tables 1 and 2. Along with the change in the H_2 recovery, the required ratio of H_2 PSA feed to total H_2 fuel gas and the required tail gas compression work are also changed significantly. As the ultrapure hydrogen product rate was determined a priori, the required feed flowrate for the H_2 PSA decreases with the increasing H_2 recovery and simultaneously the tail gas compression work decreases as well (Table 2). Moreover, the lower PSA feed flowrate resulting from the higher H_2 recovery can contribute to augmented power generation at the combined cycle since more H_2 fuel gas can be sent to the gas turbine at constant coal feed rate.

Table 2. Flowrate ratios of PSA feed to total H_2 fuel gas and tail gas compression works among various H_2 PSA configurations at the condition of 99.99+vol% H_2 purity and total cycle time of 1200 s.

H_2 PSA configuration	H_2 recovery [%]	Ratio of H_2 PSA feed to total H_2 fuel gas [%]	Tail gas compression work [MW]
Four-Column PSA with two-stage pressure equalisation	75.28	41.85	8.08
Six-Column PSA with two-stage pressure equalisation	83.43	37.62	5.70
Nine-Column PSA with three-stage pressure equalisation	91.48	34.43	3.82
Twelve-Column PSA with four-stage pressure equalisation	92.94	33.91	3.52

4. Improving the performance by recycling H_2 PSA tail gas to shift reactors

It has been reported that the ultrapure hydrogen yield could be improved by recycling the H_2 PSA tail gas to shift reactors [15] as shown in Figure 2. This is because the CO contained in the tail gas can be converted to CO_2 and H_2 in reaction with steam. This modification can also lead to reduce the energy penalty involved in carbon capture.

However, it should be noted that it is not possible to recycle the entire tail gas to the shift reactors due to a build-up of impurities in the recycle loop being proportional to the amount of tail gas recycle. It implies that it is essential to bleed a portion of the tail gas out of the recycle loop by sending it to the gas turbine as shown in Figure 2. Therefore, it is important to see if the H_2 PSA can also be designed to achieve as high as 90+% H_2 recovery even with the lowered H_2 mole fraction in the feed resulting from the recycle of a certain amount of the tail gas to the shift reactors.

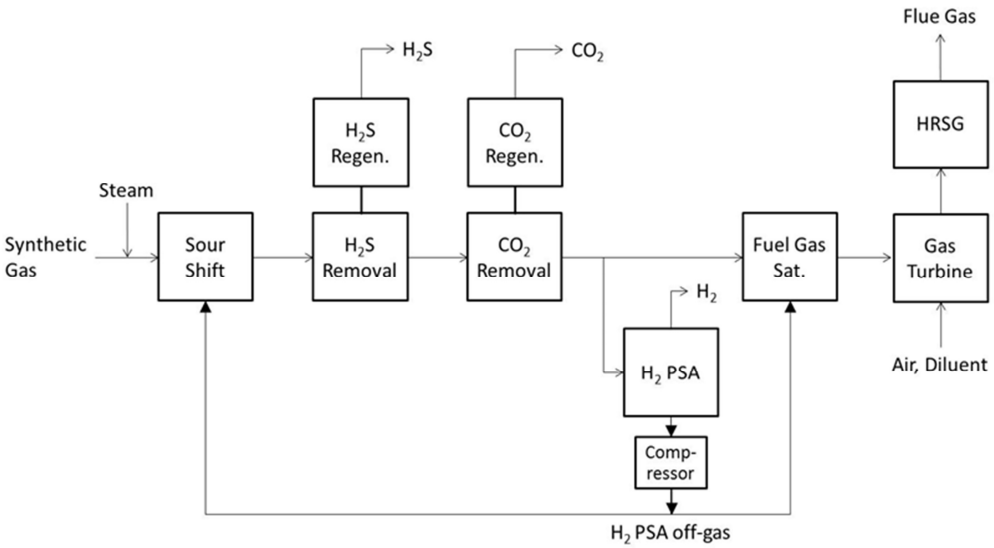

Fig. 2. Block flow diagram of an advanced IGCC plant with a recycle of H_2 PSA tail gas to shift reactors.

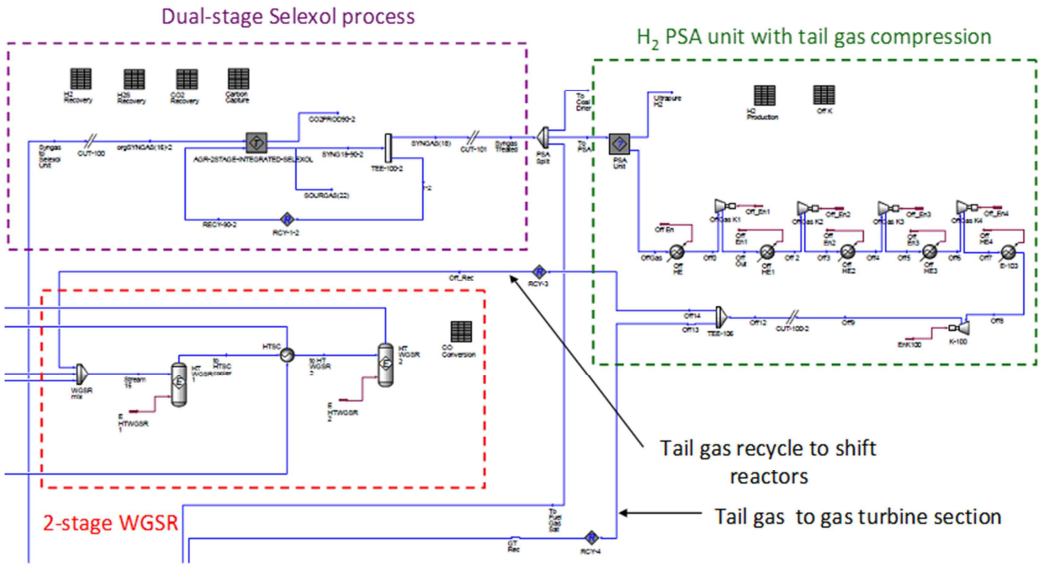

Fig. 3. UniSim PFD of an advanced IGCC plant with a recycle of H_2 PSA tail gas to shift reactors where the dynamic simulation (H_2 PSA with tail gas recycle) is integrated with Honeywell UniSim simulation (IGCC power plant simulation).

In this study, the adsorption column volume of the nine-column H_2 PSA with the total cycle time of 1200 s is sought to give the targeted 99.99 vol% H_2 purity when the H_2 mole fraction in feed is lowered to 0.85 due to the tail gas recycle. To do this study, it is prerequisite to construct an integrated process simulation where the in-house dynamic H_2 PSA simulator is imported into the UniSim IGCC simulation as shown in Figure 3. As a result of the simulation study, it is estimated that the one-column residence time should be increased to 0.140 $m^3 \cdot s/mol$ from 0.1225 $m^3 \cdot s/mol$, i.e. the H_2 PSA unit should be designed with a larger column to accommodate the higher feed flowrate and to remove more impurities. Accordingly the H_2 recovery is lowered to around 90% from 91.5% due to the increase in the column volume.

5. Conclusions

A detailed simulation of an advanced IGCC plant to produce power and ultrapure hydrogen simultaneously where CO_2 is intrinsically captured by a pre-combustion capture has been proposed in this study. The H_2 PSA is designed such that its H_2 recovery can be increased to its maximum in order to avoid the excessive power consumption involved in tail gas compression and minimise the H_2 PSA feed gas flowrate.

The advanced IGCC for cogeneration can be improved by implementing the tail gas recycle to shift reactors since it can improve the H_2 product yield and the overall power generation and can alleviate the power consumption at pre-combustion carbon capture process.

Acknowledgements

We would like to express our gratitude for the financial support from EPSRC (Grants No.: EP/F034520/1, EP/G062129/1, and EP/J018198/1) and KETEP (Grant No.: 2011-8510020030).

References

[1] Chiesa P, Consonni S, Kreutz T, Williams R. Co-production of hydrogen, electricity and CO_2 from coal with commercially ready technology. Part A: Performance and emissions. *Int J Hydrogen Energy* 2005; **30**: 747-767.

[2] Committee on Climate Change, Chapter 5: Reducing emissions from buildings and industry through the 2020s, 2011.

[3] Emun F, Gadalla M, Majozi T, Boer D. Integrated gasification combined cycle (IGCC) process simulation and optimization. *Computers and Chemical Engineering* 2010; **34**: 331-338.

[4] Yang J, Lee CH. Adsorption dynamics of a layered bed PSA for H_2 recovery from coke oven gas. *AIChE Journal* 1998; **44**: 1325-1334.

[5] Ahn H, Lee C-H, Seo B, Yang J, Baek K. Backfill cycle of a layered bed H_2 PSA process. *Adsorption* 1999; **5**: 419-433.

[6] Park JH, Kim JN, Cho SH. Performance analysis of a four-bed H_2 PSA process using layered beds. *AIChE Journal* 2000; **46**: 790-802.

[7] Ribeiro AM, Grande CA, Lopes FVS, Loureiro JM, Rodrigues AE. A parametric study of layered bed PSA for hydrogen purification. *Chemical Engineering Science* 2008; **63**: 5258-5273.

[8] Ribeiro AM, Grande CA, Lopes FVS, Loureiro JM, Rodrigues AE. Four beds pressure swing adsorption for hydrogen purification: case of humid feed and activated carbon beds. *AIChE Journal* 2009; **55**: 2292-2302.

[9] Lopes FVS, Grande CA, Rodrigues AE. Activated carbon for hydrogen purification by pressure swing adsorption: Multicomponent breackthrough curves and PSA performance. *Chemical Engineering Science* 2011; **66**: 303-317.

[10] DOE NETL. Cost and Performance baseline for fossil energy plants, 2007.

[11] Kapetaki Z, Ahn H, Brandani S. Detailed process simulation of pre-combustion IGCC plants using coal-slurry and dry coal gasifiers. *Energy Procedia* 2013; **37**: 2196-2203.

[12] Xu Y, Schutte RP, Hepler LG. Solubilities of Carbon Dioxide, Hydrogen Sulfide and Sulfur Dioxide in Physical Solvents. *The Canadian Journal of Chemical Engineering* 1992; **70**: 569-573.

[13] Burr B, Lyddon L. A comparison of physical solvents for acid gas removal. 87th Annual GPA Convention, 2008.

[14] Luberti M, Freidrich D, Brandani S, Ahn H. Design of a H_2 PSA for cogeneration of ultrapure hydrogen and power at an advanced integrated gasification combined cycle with pre-combustion capture. *Adsorption* 2014; **20**: 511-524.

[15] UOP. Recent Selexol^{TM}, PolySep^{TM} and PolyBed^{TM} Operating Experience with Gasification for Power and Hydrogen. Gasification Technologies 2002.

Appendix 4: Hydrogen production processing *by Ahn et al., 2015*

(12) INTERNATIONAL APPLICATION PUBLISHED UNDER THE PATENT COOPERATION TREATY (PCT)

(19) World Intellectual Property Organization
International Bureau

(43) International Publication Date
16 July 2015 (16.07.2015)

WIPO | PCT

(10) International Publication Number
WO 2015/104532 A1

(51) International Patent Classification:
C10J 3/02 (2006.01) *C01B 3/56* (2006.01)
C10K 1/00 (2006.01) *B01D 53/047* (2006.01)
C10K 3/04 (2006.01)

(21) International Application Number:
PCT/GB2014/053843

(22) International Filing Date:
24 December 2014 (24.12.2014)

(25) Filing Language: English

(26) Publication Language: English

(30) Priority Data:
1400260.4 8 January 2014 (08.01.2014) GB

(71) Applicants: **THE UNIVERSITY COURT OF THE UNIVERSITY OF EDINBURGH** [GB/GB]; Old College, South Bridge, Edinburgh, Midlothian EH8 9YL (GB). **YONSEI UNIVERSITY** [KR/KR]; 262, Seongsan-no, Seodaemun-gu, Seoul 120-749 (KR).

(72) Inventors: **AHN, Hyungwoong**; c/o Sanderson Building, The King's Buildings, University of Edinburgh, Mayfield Road, Edinburgh Central Scotland EH9 3JL (GB). **BRANDANI, Stefano**; c/o Sanderson Building, The King's Buildings, Univeristy of Edinburgh, Mayfield Road, Glasgow Central Scotland EH9 3JL (GB). **LUBERTI, Mauro**; c/o Sanderson building, The Kings Buildings, Univeristy of Edinburgh, Mayfield Road, Edinburgh Central Scotlans EH9 3JL (GB). **LEE, Chang-Ha**; c/o Dept of Chemical & Biomolecular Eng, Yonsei University, 50 Yonse-ro, Seodaemun-gu, Seoul 120-749 (KR).

(74) Agent: **FLAHERTY, Annette**; Delta House, 50 West Nile Street, Glasgow Central Scotland G1 2NP (GB).

(81) Designated States *(unless otherwise indicated, for every kind of national protection available)*: AE, AG, AL, AM, AO, AT, AU, AZ, BA, BB, BG, BH, BN, BR, BW, BY, BZ, CA, CH, CL, CN, CO, CR, CU, CZ, DE, DK, DM, DO, DZ, EC, EE, EG, ES, FI, GB, GD, GE, GH, GM, GT, HN, HR, HU, ID, IL, IN, IR, IS, JP, KE, KG, KN, KP, KR, KZ, LA, LC, LK, LR, LS, LU, LY, MA, MD, ME, MG, MK, MN, MW, MX, MY, MZ, NA, NG, NI, NO, NZ, OM, PA, PE, PG, PH, PL, PT, QA, RO, RS, RU, RW, SA, SC, SD, SE, SG, SK, SL, SM, ST, SV, SY, TH, TJ, TM, TN, TR, TT, TZ, UA, UG, US, UZ, VC, VN, ZA, ZM, ZW.

(84) Designated States *(unless otherwise indicated, for every kind of regional protection available)*: ARIPO (BW, GH, GM, KE, LR, LS, MW, MZ, NA, RW, SD, SL, ST, SZ, TZ, UG, ZM, ZW), Eurasian (AM, AZ, BY, KG, KZ, RU, TJ, TM), European (AL, AT, BE, BG, CH, CY, CZ, DE, DK, EE, ES, FI, FR, GB, GR, HR, HU, IE, IS, IT, LT, LU, LV, MC, MK, MT, NL, NO, PL, PT, RO, RS, SE, SI, SK, SM, TR), OAPI (BF, BJ, CF, CG, CI, CM, GA, GN, GQ, GW, KM, ML, MR, NE, SN, TD, TG).

Published:

— *with international search report (Art. 21(3))*

(54) Title: HYDROGEN PRODUCTION PROCESSING

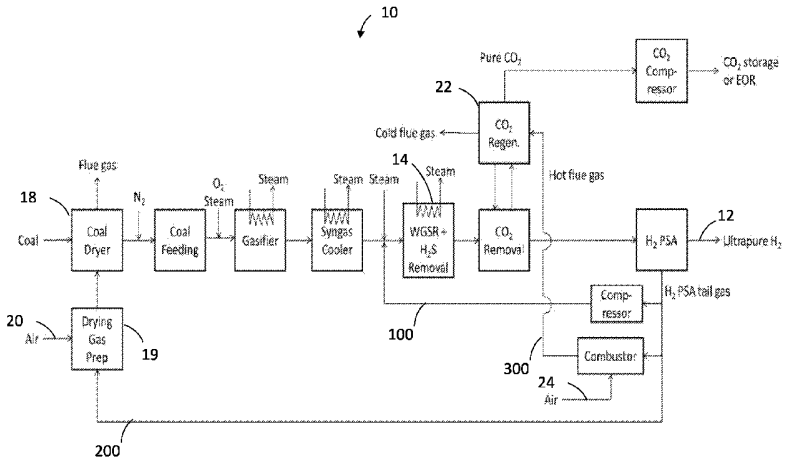

Figure 2

(57) Abstract: A hydrogen production process and production plant (10) operable to produce, at least, Hydrogen and Carbon dioxide, the process comprises a recycle loop, wherein tail gas (100, 200, 300) produced downstream in the process is used upstream of the process at a shift reactor and at least one of providing heat for drying coal (18) and providing heat for regenerating CO_2 (22).

WO 2015/104532 A1

HYDROGEN PRODUCTION PROCESSING

FIELD OF INVENTION

The present invention relates to a hydrogen production process and a hydrogen production plant which utilises downstream tail gas for use at one or more upstream stages in the process to improve hydrogen production rate and reduce energy consumption involved.

BACKGROUND TO THE INVENTION

Gasification is the conversion of an organically derived, carbonaceous material by partial oxidation into a gaseous product, synthesis gas ("syngas") comprising hydrogen (H_2), carbon monoxide (CO), carbon dioxide (CO_2), methane (CH_4), Nitrogen (N_2) and other hydrocarbons and impurities. Reactions are generally carried out at elevated temperatures and atmospheric or elevated pressures.

Hydrogen Pressure Swing Adsorption (H_2 PSA) is an example of a gas purification process, which is considered unique in the field of producing ultrapure hydrogen. For example a system having two to twenty columns per one train and having each column interconnected can produce an ultrapure hydrogen product continuously with high product recovery and productivity. The system is considered capable of producing/outputting a very high purity of hydrogen suitable for use as a refinery hydrotreater, hydrocracker and as fuel cells from a H_2-enriched synthetic gas feed. The H_2-enriched synthetic gas feed is usually generated by steam, partial oxidation, or auto-thermal reforming of gas or gasification of solid carbonaceous raw material followed by shift reaction.

Demand for clean fuels is increasing in present society and as such Hydrogen is becoming increasingly important as a clean fuel component that is obtainable from the refining process.

Honeywell UOP have commercialised a cogeneration plant to produce, at the same time, ultrapure hydrogen and power. The Honeywell's process was configured such that the hydrogen PSA off-gas or tail gas is sent to a power island of combined cycle power plants.

Accordingly, it is desirable to provide an improved hydrogen and power generating system and process.

It is also desirable to improve carbon capture from a hydrogen and power generating system.

It is desirable to obtain a capture rate of carbon dioxide in excess of 90%.

SUMMARY OF THE INVENTION

Accordingly, a first aspect of the present invention provides a hydrogen production process operable to produce, at least, hydrogen and carbon dioxide, the process comprises a recycle loop, wherein tail

gas that is produced downstream in the process is used upstream of the process at a shift reactor and for at least one of providing heat for drying coal and providing heat for regenerating CO_2.

The process includes a pressure swing adsorption (PSA) process to produce an ultrapure hydrogen (99.99+%) from the H_2-rich syngas stream. At present the PSA process is a commercially-available process capable of producing ultrapure hydrogen (99.99+%) from the H_2-rich syngas stream.

The process may comprise directing downstream tail gas to an upstream location of the process and providing heat for drying coal and providing heat for regenerating CO_2.

The process may further comprise combusting tail gases at the location of coal drying.

The process may further comprise combusting tail gases at the location of regenerating CO_2.

The process may further comprise feeding air to the location of coal drying and/or the location of regenerating CO_2.

Substantially 100% of tail gas may be reused to provide heat to the upstream units or mixed with a main syngas stream upstream of the process.

A predetermined proportion of tail gas may be captured and reused to provide heat upstream of the process.

A predetermined proportion of tail gas may be transported and mixed with the main syngas stream flowing to the shift reactor.

A predetermined proportion of tail gas may be transported to provide heat to dry coal. A predetermined proportion of tail gas may be transported to provide heat to regenerate CO_2. A further aspect of the present invention provides a hydrogen production plant comprising at least means for drying coal, gasifying means, gas cooling means, means of removing and regenerating carbon dioxide and pressure swing adsorption means operable to separate and exhaust hydrogen from the plant, wherein the plant operates according to the process as claimed in any preceding claim.

The production plant may further comprise means of upstream communication, by which means tail gas is transported to a shift reactor and at least one of the means for drying coal and the means of removing and regenerating carbon dioxide.

The production plant may further comprise means of combusting tail gas proximate the at least one of the means for drying coal and the means of removing and regenerating carbon dioxide and means of imparting heat produced by combusting the tail gas to the at least one of the means for drying coal and the means of removing and regenerating carbon dioxide.

The production plant may further comprise means of proportioning a quantity of tail gas being fed to each of the shift reactor and at least one of the means for drying coal and the means of removing and regenerating carbon dioxide.

Aspects of the invention relate to hydrogen production integrated with carbon capture.

The production plant may comprise carbon capture units, including, but not limited to, a wet absorption, solid-looping fluidised bed process, and fixed-bed adsorption in order to produce CO_2 products of sufficiently high purity for use in, for example, CO_2 storage, the food/beverage industry, enhanced oil/gas recovery and CO_2 utilisation to synthesise valuable chemicals. Gas feed to the H_2 PSA unit normally has an enriched H_2 mole fraction balanced with carbon monoxide (CO), Carbon dioxide (CO_2), Nitrogen (N_2), Argon (Ar), Methane (CH_4) and trace amounts of water vapour and other hydrocarbons.

Adsorption columns of a H_2 PSA process are typically packed with one or more layers of alumina, silica, zeolite, activated carbon and their ion-exchanged forms. The H_2 PSA process operates continuously to produce a product stream of high purity H_2 by selectively adsorbing the impurities during adsorption steps.

Following the adsorption step, each adsorption column experiences one or more stages of depressurising, providing purge, blowdown, purge, one or more stages of repressurising and feed or product pressurisation steps so that the residual hydrogen can be recovered thoroughly and the adsorbents in the column can be regenerated efficiently in order to get the column to recover the adsorption capacity during the adsorption step of the following cycle.

During the blowdown and purge steps gas effluents contain high amounts of CO and CO_2 as well as H_2, N_2, Ar, CH_4 and trace amounts of water vapour and other hydrocarbons. In most cases the H_2 tail gases are utilised as fuel gas since they contain high calorific values. For example, Steam Methane Reforming (SMR) H_2 plants make use of the entire tail gases as fuel gases for endothermic steam reformers.

In a recent publication (UOP, Gasification Technologies 2002) relating to Selexol™, PolySep™ and PolyBed™ operating experience with gasification for power and hydrogen, an advanced process configuration was presented where tail gas is recycled to existing shift reactors to boost the overall H_2 yield in H_2 plants. However, it was identified that increasing the amount of tail gas recycled to shift reactors results in a lower hydrogen mole fraction of the raw H_2 feed due to a build-up of impurities in the recycle loop as indicated in the graph of Figure 1. Figure 1 illustrates the variation of hydrogen mole fraction percentage in the raw H_2 feed with a split ratio of 'tail gas recycle to shift reactors' flow to total tail gas flow. Therefore, such a process configuration would only be possible when a substantial amount of impurities is removed from the recycle loop and where the level of impurities can be maintained at a minimum level such that the downstream H_2 PSA unit can achieve, at the same time,

satisfactory H_2 purity and recovery. Impurities can be reduced, for example by adding a separation process to remove impurities or by bleeding a proportion of tail gas out of the recycle loop.

A process and plant according to aspects of the present invention provide various benefits over existing arrangements. For example, there is lower energy consumption at carbon capture units. This relates to the working capacity at a CO_2 capture unit, wherein by adding thermal energy to the CO_2 regenerator, from the combustion of tail gases, the CO_2 capture plant can be operated with a improved working capacity. Reduced energy consumption and a reduction in size of the equipment in a carbon capture unit is the result.

A further benefit from an increased and more efficient utilisation of the tail gases is increased yield of H_2 in the overall H_2 plant. Generally, part of the synthetic gas leaving a carbon capture unit is being used as a fuel gas for coal drying, which inevitably results in the loss of H_2 product overall. By utilising the tail gas as a fuel gas for coal drying, the loss of the valuable synthetic gas can be avoided. In addition, since the CO_2 capture plant can be operated using less sorbents/solvents because of the improved working capacity, the slip of H_2 into sorbents/solvents at the carbon capture unit can also be reduced.

In addition, the thermal CO_2 regeneration in addition to the depressurised CO_2 regeneration results in reduced power consumption at CO_2 compression. In the event that solvents/sorbents regeneration is done by depressurisation, the heating of the CO_2-laden solvents/sorbents by hot, combusted, tail gas makes it possible to increase CO_2 production at a flash drum operating at an elevated pressure which results in reducing power consumed for CO_2 compression.

Where the aim is to produce high purity CO_2 and ultrapure H_2 with the recoveries of both products as high as 90% in the overall H_2 plant and the H_2 PSA respectively with a tail gas recycle to shift reactors put in place, it is inevitable that part of the tail gas must be bled out or an impurities separator must be utilised because impurities cannot be included in both the pure CO_2 and ultrapure hydrogen products.

The present invention relates to improving the performance of ultrapure hydrogen production plants using dry coal-fed gasification which is integrated with a carbon capture unit with an aim to achieve a capture rate of CO_2 of over 90% and to utilise substantially 100% of tail gases in the production process.

BRIEF DESCRIPTION OF THE DRAWINGS

For a better understanding of the invention and to show how the same may be carried into effect reference will now be made by way of example to the accompanying drawings in which:

Figure 1 is a graphical representation of variation of the hydrogen mole fraction percentage in the raw H_2 feed with the split ratio of the 'tail gas recycle to shift reactors' flow to total tail gas flow;

Figure 2 is a schematic representation of a hydrogen plant using coal gasification with a carbon capture unit in accordance with embodiments of the present invention; and

Figure 3 is a table providing a comparison of the performance of a known H_2 plant and recycle process compared with an H_2 plant and process according to embodiments of the present invention.

DESCRIPTION OF EMBODIMENTS OF THE INVENTION

As discussed above, present technology, which is capable of obtaining a 90% carbon capture rate from a H_2 plant, using coal gasification uses recycled tail gas fed only to shift reactors. However, as illustrated above a problem with this method can be impurities. Therefore, to continue with a process utilising only recycle feed of tail gases to the shift reactors requires additional means to physically remove impurities or means to reduce the quantity of tail gas recycled, by for example bleeding off some tail gas as fuel gases. By such means excessive build-up of the impurities in the recycle loop can be avoided.

Figure 2 illustrates an example system 10 of a H_2 production plant composed of coal gasification, gas conditioning, a carbon capture unit and H_2 Pressure Swing Adsorption (PSA) technology according to embodiments of the present invention where substantially 100% of tail gas is utilised by diverting tail gas upstream to three locations. The illustrated system 10 utilises recycled tail gas at two additional locations compared with the example discussed above.

The production plant comprises carbon capture units such as wet absorption, a solid-looping fluidised bed process, and fixed-bed adsorption in order to produce CO_2 products of sufficiently high purity for use in, for example, CO_2 storage, the food/beverage industry, enhanced oil/gas recovery and CO_2 utilisation to synthesise valuable chemicals. Gas feed to the H_2 PSA unit normally has an enriched H_2 mole fraction balanced with carbon monoxide (CO), Carbon dioxide (CO_2), Nitrogen (N_2), Argon (Ar), Methane (CH_4) and trace amounts of water vapour and other hydrocarbons.

Adsorption columns of a H_2 PSA process are typically packed with one or more layers of alumina, silica, zeolite, activated carbon and their ion-exchanged forms. The H_2 PSA process operates continuously to produce a product stream of high purity H_2 12 by selectively adsorbing the impurities during adsorption steps.

Following the adsorption step, each adsorption column experiences one or more stages of depressurising, providing purge, blowdown, purge, one or more stages of repressurising and feed or product pressurisation steps so that the residual hydrogen can be recovered thoroughly and the adsorbents in the column can be regenerated efficiently in order to get the column to recover the adsorption capacity during the adsorption step of the following cycle.

During blowdown and purge steps, gas effluents contain high amounts of CO and CO_2 as well as H_2, N_2, Ar, CH_4 and trace amounts of water vapour and other hydrocarbons.

According to embodiments of the present invention the H_2 tail gases are utilised upstream to increase the output of ultra pure H_2.

Firstly, a quantity of tail gas 100 is directed upstream to the shift reactor 14 where the tail gas 100 is mixed with the syngas stream flowing from the syngas cooler to improve the hydrogen product yield.

Secondly a quantity of tail gas 200 is directed upstream to the drying gas preparation section 19 where the tail gas 200 is combusted with air 20 to provide heat for drying the coal at the coal dryer 18.

Thirdly, a quantity of the tail gas 300 is directed to a carbon capture unit 22. Again, the tail gas 300 is combusted with air 24 to provide heat, in this case, for CO_2 regeneration.

In the embodiments of the invention substantially 100% of tail gas is recycled with a proportion being fed upstream to the shift reactors 14, a proportion being fed to the drying coal preparation section 19 and a proportion being fed to the CO_2 regenerator 22. According to an embodiment of the present invention, as illustrated in Figure 2, the tail gas is split into three streams 100, 200, 300. One stream 100 is recycled to the shift reactors to boost the H_2 yield at the H_2 PSA. The second stream 200 is sent to 'drying gas preparation' where it is combusted with air to provide the heat for coal drying. The third stream 300 is directed to a CO_2 regenerator of a carbon capture unit, where the tail gas is combusted with air to produce the heat required for more efficient regeneration of CO_2-laden solvents or sorbents. In the illustrated example 21% of tail gas is fed to the shift reactor, 12% of tail gas is sent to drying gas preparation 19 and 67% of tail gas is fed to the CO_2 regenerator.

As explained above, an excessive tail gas recycle to the shift reactors can reduce the H_2 concentration in the raw H_2 stream. As such, the entire quantity of tail gas cannot be recycled to the shift reactors due to the impurities. Therefore, only a proportion of tail gas is fed to the shift reactors; 21% being used in the illustrated example.

The proportion of tail gas recycled to the coal dryer can also be variable because water content in coal can vary with coal type. Therefore, the required amount of tail gas for coal drying will vary depending on the type of coal used in the system and it will be appreciated that it may be possible to use 100% of tail gas for coal drying. It is most likely that a proportion of tail gas will be used. In the illustrated example 12% of tail gas was sent for coal drying purposes.

With further reference to figure 2 and figure 3, the improvement in performance of the H_2 plant according to embodiments of the present invention can be demonstrated. A base case simulation was constructed where the synthetic gas by coal gasification was converted to a H_2-rich stream by shift reaction and subsequently ultrapure hydrogen is produced at the H_2 PSA unit at 286 million standard cubic feet per day (MMSCFD).

Referring to the table illustrated in Figure 3, in Case 1, 21% of tail gas is recycled to upstream of the shift reactor. With the recycle put in place, the raw H_2 feed to the H_2 PSA is as low as 84.5%, which is

lower than 87.1% in the base case (see Figure 3). But the H_2 production rate was improved by 2.4% to 293 MMSCFD from 286 MMSCFD. When recycled, the tail gas is compressed up to the pressure of main syngas stream flowing to the shift reactor, resulting in an increase of total power consumption.

In this example, a conventional dual-stage Selexol™ unit was used to capture Hydrogen Sulphide (H_2S) and CO_2 at the same time. As discussed above, to maintain the H_2 mole fraction in the raw H_2 feed as high as 84.5%, part of the tail gas is removed from (bled out of) the recycle loop and used, for example as fuel gases for other processes. In this example part of the synthetic gas leaving the carbon capture unit is fed to the coal dryer section to provide heat after combustion. This example is referenced as Case 2 in the table of figure 3. In accordance with this embodiment of the present invention, represented as case 2 in figure 3, a portion 200 of the tail gas is utilised for generating hot gases for a coal dryer 18 by combustion while a portion of raw H_2 feed to the H_2 PSA is used as described above. As a result, the ultrapure hydrogen production rate was found to increase by around 1.8% in comparison to Case 1 as indicated in the table of Figure 3.

In accordance with a further embodiment of the invention, represented as case 3 in figure 3, the remainder of the tail gas 300, after its use in the coal dryer, is sent to a dual-stage Selexol™ process. In the dual-stage Selexol™ unit, the CO_2-laden solvents are regenerated by reducing the pressure over two or more flash drums in series. By heating the CO_2-laden solvents flowing to a flash vessel operating at a medium pressure, more CO_2 product can be obtained at the high pressure resulting in improving the solvent working capacity and reducing the power consumption at the CO_2 compression train.

The enhanced solvent working capacity leads to lowering the power consumption for CO_2 capture due to a reduced amount of solvent being pumped and improving the H_2 production rate due to reduced H_2 slip to the circulating solvents.

By utilising substantially 100% of the tail gas at three locations upstream of the process, the production rate of ultrapure hydrogen was found to increase by around 4.2% and the power consumptions at the dual-stage Selexol unit and the CO_2 compression unit was found to reduce by around 15% and 6%, respectively.

Accordingly, it will be appreciated that the total auxiliary power consumption can be reduced by around 8% by the embodiments of the present invention compared with the performances of a system and process where only a limited proportion of the tail gases is recycled for use only with the shift reactors.

While the invention is susceptible to various modifications and alternative forms, specific embodiments are shown by way of example in the drawings and are herein described in detail. It should be understood, however, that drawings and detailed description thereto are not intended to limit the invention to the particular form disclosed.

CLAIMS

1. A hydrogen production process operable to produce, at least, Hydrogen and Carbon dioxide, the process comprises a recycle loop, wherein tail gas produced downstream in the process is used upstream of the process at a shift reactor and at least one of providing heat for drying coal and providing heat for regenerating CO_2.

2. A process as claimed in claim 1, comprising directing downstream tail gas to an upstream location of the process and providing heat for drying coal and providing heat for regenerating CO_2.

3. A process as claimed in any of claims 1 or 2, further comprising combusting tail gases at the location of coal drying.

4. A process as claimed in any preceding claim, further comprising combusting tail gases at the location of regenerating CO_2.

5. A process as claimed in any preceding claim, further comprising feeding air to the location of coal drying and/or the location of regenerating CO_2.

6. A process as claimed in any preceding claim, wherein substantially 100% of tail gas is reused to provide heat to the upstream units or mixed with a main syngas stream upstream of the process.

7. A process as claimed in any preceding claim, wherein a predetermined proportion of tail gas is captured and reused to provide heat upstream of the process.

8. A process as claimed in any preceding claim, wherein a predetermined proportion of tail gas is transported and mixed with a main syngas stream flowing to the shift reactor.

9. A process as claimed in any preceding claim, wherein a predetermined proportion of tail gas is transported to provide heat to dry coal.

10. A process as claimed in any preceding claim, wherein a predetermined proportion of tail gas is transported to provide heat to regenerate CO_2.

11. A hydrogen production plant comprising at least means for drying coal, gasifying means, gas cooling means, means of removing and regenerating carbon dioxide and pressure swing adsorption means operable to separate and exhaust hydrogen from the plant, wherein the plant operates according to the process as claimed in any preceding claim.

12. A hydrogen production plant as claimed in claim 11, further comprising means of upstream communication, by which means tail gas is transported to a shift reactor and at least one of the means for drying coal and the means of removing and regenerating carbon dioxide.

13. A hydrogen production plant as claimed in claim 11 or 12, further comprising means of combusting tail gas proximate the at least one of the means for drying coal and the means of removing and regenerating carbon dioxide and means of imparting heat produced by combusting the tail gas to the at least one of the means for drying coal and the means of removing and regenerating carbon dioxide.

14. A hydrogen production plant as claimed in any of claims 11 to 13, further comprising means of proportioning a quantity of tail gas into proportions being fed to each of the shift reactor and at least one of the means for drying coal and the means of removing and regenerating carbon dioxide.

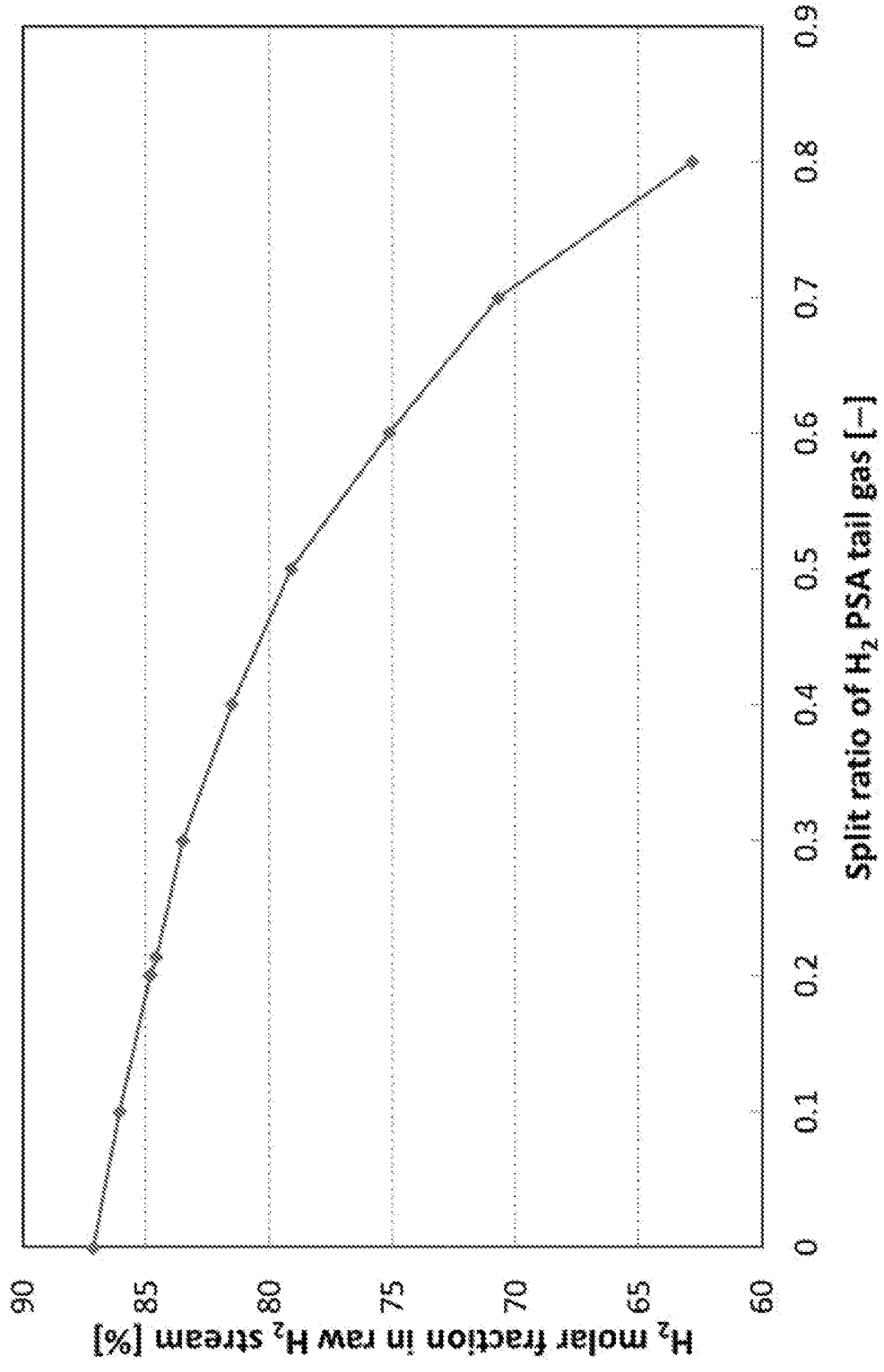
H2 molar fraction in raw H2 stream [%]
90
85
80
75
70
65
60
Split ratio of H2 PSA tail gas [–]
0
0.1
0.2
0.3
0.4
0.5
0.6
0.7
0.8
0.9

Figure 1

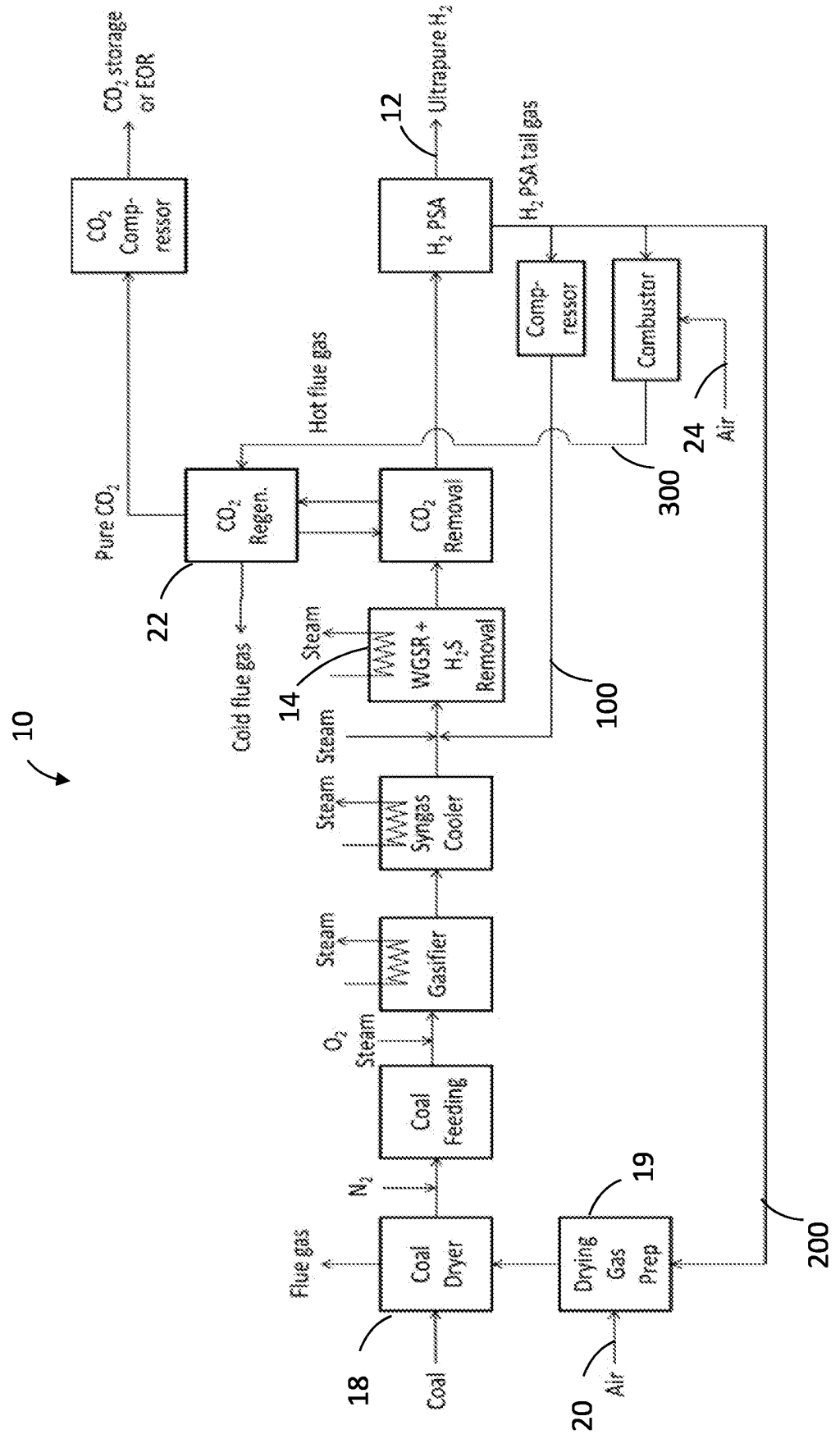
10
CO_2 storage or EOR
CO_2 Comp-ressor
Pure CO_2
CO_2 Regen.
22
Cold flue gas
Hot flue gas
CO_2 Removal
Steam
WGSR + H_2S Removal
14
Steam
Steam
Syngas Cooler
Steam
Gasifier
O_2
Steam
Coal Feeding
N_2
Flue gas
Coal Dryer
18
Coal
Drying Gas Prep
19
20
Air
12
Ultrapure H_2
H_2 PSA
H_2 PSA tail gas
Comp-ressor
Combustor
24
Air
300
100
200

Figure 2

	Base case	*Case 1 (Base case + Tail gas recycle to shift reactors)*	*Case 2 (Case 1 + Tail gas recycle to coal drier)*	*Case 3 (Case 2 + Tail gas recycle to Selexol unit)*
Thermal input [kWt]	1,617,772	1,617,772	1,617,772	1,617,772
Overall CO conversion rate at shift reactors [%]	97.8	97.7	97.7	97.7
Fuel Gas flowrate [MMSCFD]	79	72	62	0
H_2 purity of treated syngas at Selexol unit [%]	87	85	85	85
H_2 recovery of treated syngas at Selexol unit [%]	99.1	99.0	99.0	99.0
H_2S recovery at Selexol unit [%]	99.8	99.8	99.8	99.8
CO_2 recovery at Selexol unit [%]	90.1	90.1	90.1	90.1
CO_2 product purity [%]	97.3	97.1	97.1	97.2
H_2 purity at H_2 PSA [%]	99.99+	99.99+	99.99+	99.99+
H_2 recovery at H_2 PSA [%]	90.0	90.0	90.0	90.0
Ultrapure H_2 production rate [MMSCFD]	**286**	**293 (+2.4%)**	**298 (+4.2%)**	**298 (+4.2%)**
H_2S reboiler duty at Selexol unit [MWt]	14.6	14.6	14.6	11.8 (–19.2%)
Power consumption at Selexol unit [MWe]	**20.2**	**19.3 (–4.5%)**	**19.3 (–4.5%)**	**17.2 (–14.9%)**
Power consumption for CO_2 Compression [MWe]	**31.7**	**31.7**	**31.7**	**29.8 (–6.0%)**
Power consumption at tail gas compressor [MWe]	N/A	3.1	3.1	3.1
Total power consumption [MWe]	**51.9**	**54.1 (+4.4%)**	**54.1 (+4.4%)**	**50.1 (–3.5%)**

Figure 3

INTERNATIONAL SEARCH REPORT

International application No
PCT/GB2014/053843

A. CLASSIFICATION OF SUBJECT MATTER
INV. C10J3/02 C10K1/00 C10K3/04 C01B3/56 B01D53/047
ADD.

According to International Patent Classification (IPC) or to both national classification and IPC

B. FIELDS SEARCHED

Minimum documentation searched (classification system followed by classification symbols)
C10J C10K C01B B01D

Documentation searched other than minimum documentation to the extent that such documents are included in the fields searched

Electronic data base consulted during the international search (name of data base and, where practicable, search terms used)

EPO-Internal, WPI Data

C. DOCUMENTS CONSIDERED TO BE RELEVANT

Category*	Citation of document, with indication, where appropriate, of the relevant passages	Relevant to claim No.
X	DE 198 07 224 A1 (LINDE AG [DE]) 26 August 1999 (1999-08-26) figures 1-5 columns 1-4 claims 1-13	1-14
A	WO 2008/157433 A2 (WORMSER ENERGY SOLUTIONS INC [US]; WORMSER ALEX [US]) 24 December 2008 (2008-12-24) figure 8	1-14
A	US 2011/168605 A1 (BLEVINS RANDY [US] ET AL) 14 July 2011 (2011-07-14) figure 1	1-14

-/--

[X] Further documents are listed in the continuation of Box C.

[X] See patent family annex.

* Special categories of cited documents :

"A" document defining the general state of the art which is not considered to be of particular relevance

"E" earlier application or patent but published on or after the international filing date

"L" document which may throw doubts on priority claim(s) or which is cited to establish the publication date of another citation or other special reason (as specified)

"O" document referring to an oral disclosure, use, exhibition or other means

"P" document published prior to the international filing date but later than the priority date claimed

"T" later document published after the international filing date or priority date and not in conflict with the application but cited to understand the principle or theory underlying the invention

"X" document of particular relevance; the claimed invention cannot be considered novel or cannot be considered to involve an inventive step when the document is taken alone

"Y" document of particular relevance; the claimed invention cannot be considered to involve an inventive step when the document is combined with one or more other such documents, such combination being obvious to a person skilled in the art

"&" document member of the same patent family

Date of the actual completion of the international search	Date of mailing of the international search report
4 March 2015	11/03/2015

Name and mailing address of the ISA/	Authorized officer
European Patent Office, P.B. 5818 Patentlaan 2 NL - 2280 HV Rijswijk Tel. (+31-70) 340-2040, Fax: (+31-70) 340-3016	Lachmann, Richard

INTERNATIONAL SEARCH REPORT

International application No
PCT/GB2014/053843

C(Continuation). DOCUMENTS CONSIDERED TO BE RELEVANT

Category*	Citation of document, with indication, where appropriate, of the relevant passages	Relevant to claim No.
A	US 2012/003145 A1 (GROVER BHADRA S [US] ET AL) 5 January 2012 (2012-01-05) figures 1-6 paragraph [0029] -----	1-14
A	WO 2013/062800 A1 (RENTECH INC [US]; JIANG WEIBIN [US]; MCCOMISH BRUCE E [US]; BORUM BRYA) 2 May 2013 (2013-05-02) paragraphs [0047], [0095] claims 3,69 paragraphs [0077] - [0083] -----	1-14

INTERNATIONAL SEARCH REPORT

Information on patent family members

International application No
PCT/GB2014/053843

Patent document cited in search report	Publication date	Patent family member(s)	Publication date
DE 19807224 A1	26-08-1999	CA 2261412 A1	20-08-1999
		DE 19807224 A1	26-08-1999
WO 2008157433 A2	24-12-2008	AR 070943 A1	19-05-2010
		AU 2008265954 A1	24-12-2008
		CA 2727267 A1	24-12-2009
		CN 102083947 A	01-06-2011
		EP 2183339 A2	12-05-2010
		TW 200920933 A	16-05-2009
		US 2010281878 A1	11-11-2010
		WO 2008157433 A2	24-12-2008
US 2011168605 A1	14-07-2011	US 2011168605 A1	14-07-2011
		US 2012020846 A1	26-01-2012
		WO 2012087504 A2	28-06-2012
US 2012003145 A1	05-01-2012	US 2012003145 A1	05-01-2012
		WO 2012003158 A1	05-01-2012
WO 2013062800 A1	02-05-2013	CA 2852761 A1	02-05-2013
		EP 2771435 A1	03-09-2014
		US 2013109765 A1	02-05-2013
		WO 2013062800 A1	02-05-2013